SKB

TECHNICAL REPORT 94-04

Final report of the AECL/SKB Cigar Lake Analog Study

Jan Cramer (ed.)[1], John Smellie (ed.)[2]

1 AECL, Canada
2 Conterra, Uppsala, Sweden

May 1994

SVENSK KÄRNBRÄNSLEHANTERING AB
SWEDISH NUCLEAR FUEL AND WASTE MANAGEMENT CO
BOX 5864 S-102 40 STOCKHOLM
TEL. 08-665 28 00 TELEX 13108 SKB S
TELEFAX 08-661 57 19

FINAL REPORT OF THE AECL/SKB CIGAR LAKE ANALOG STUDY

Jan Cramer (ed.)[1], John Smellie (ed.)[2]

1 AECL, Canada
2 Conterra, Uppsala, Sweden

May 1994

AECL Research

FINAL REPORT OF THE AECL/SKB CIGAR LAKE ANALOG STUDY

Edited by
J.J. Cramer (AECL)
and
J.A.T. Smellie

Whiteshell Laboratories
Pinawa, Manitoba, Canada R0E 1L0
1994

AECL-10851
COG-93-147
SKB TR 94-04

PREFACE

This report summarizes the results of the Cigar Lake Analog Study, a 3-year collaborative program (1989-1992) between Atomic Energy of Canada Limited (AECL), with support from Ontario Hydro under the auspices of the Candu Owners Group, and the Swedish Nuclear Fuel and Waste Management Company (SKB). It also includes a contribution from the Los Alamos National Laboratory, which started collaboration with AECL in 1991 with funding from the United States Department of Energy.

The report represents a summary of the effort of a large group of writers from different countries and organizations, and covers a variety of technical disciplines. No attempt has been made to harmonize the style, format, spelling or technical terminology. Editorial changes were made to ensure clarity, and introductions were written for each major section.

FINAL REPORT OF THE AECL/SKB CIGAR LAKE ANALOG STUDY

Edited by
J. Cramer (AECL) and J. Smellie

ABSTRACT

The Cigar Lake uranium deposit is located in northern Saskatchewan, Canada. The 1.3-billion-year-old deposit is located at a depth of about 450 m below surface in a water-saturated sandstone at the unconformity contact with the high-grade metamorphic rocks of the Canadian Shield. The uranium mineralization, consisting primarily of uraninite (UO_2), is surrounded by a clay-rich halo in both sandstone and basement rocks, and remains extremely well preserved and intact. The average grade of the mineralization is ~8 wt.% U; locally grades are as high as ~55 wt.% U.

The Cigar Lake deposit has many features that parallel those being considered within the Canadian concept for disposal of nuclear fuel waste. The study of these natural structures and processes provides valuable insight toward the eventual design and site selection of a nuclear fuel waste repository. The main feature of this analog is the absence of any indication on the surface of the rich uranium ore 450 m below. This indicates that the combination of natural barriers has been effective in isolating the uranium ore from the surface environment. More specifically, the deposit provides analog information relevant to the stability of UO_2 fuel waste, the performance of clay-based barriers, radionuclide migration, colloid formation, radiolysis, fission-product geochemistry and general aspects of water-rock interaction. The main geochemical studies on this deposit focus on the evolution of groundwater compositions in the deposit and on their redox chemistry with respect to the uranium, iron and sulphide systems.

Since 1984, through cooperation from the owners of the Cigar Lake deposit, analog studies have been conducted. AECL, with support from Ontario Hydro under the auspices of the CANDU Owners Group, initiated international participation in 1989 through collaboration with the Swedish Nuclear Fuel and Waste Management Company (SKB) and, more recently, with the Los Alamos National Laboratory (LANL). This report gives the results of the various studies carried out during the 3-year collaboration between AECL and SKB, as well as a summary of the LANL study. It provides detailed information on the generated databases and models, and integrates this information into conclusions for use in safety assessment of the Canadian, Swedish and United States disposal concepts.

AECL Research
Whiteshell Laboratories
Pinawa, Manitoba, Canada R0E 1L0
1994

AECL-10851
COG-93-147
SKB TR 94-04

RAPPORT DÉFINITIF D'ÉTUDE DE L'ANALOGUE DE CIGAR LAKE EFFECTUÉE PAR EACL ET SKB

Révisé par
J. Cramer (EACL) et J. Smellie

RÉSUMÉ

Le gisement d'uranium de Cigar Lake est situé dans le nord de la Saskatchewan au Canada. Ce gisement de 1,3 milliard d'années se trouve à une profondeur d'environ 450 m, sous la surface, dans un grès saturé d'eau au contact de la discordance avec les roches métamorphiques Précambriennes du Bouclier canadien. Le minerai d'uranium, qui contient principalement de l'uraninite (UO_2), est entouré d'un halo riche en argile aussi bien dans le grès que dans le socle, reste très bien conservé et intact. La teneur moyenne du minerai est d'environ 8 % en poids d'U; localement, la teneur peut atteindre d'environ 55 % en poids d'U.

Le gisement de Cigar Lake comporte de nombreux éléments qui sont équivalents à ceux en cours d'examen dans le contexte du concept canadien de stockage permanent des déchets de combustible nucléaire. L'étude de ces structures et processus naturels donne un aperçu précieux de la conception et de la sélection d'un site de dépôt de déchets de combustible nucléaire qui s'ensuivraient. La principale caractéristique de cet analogue est l'absence de tout indice sur la surface du minerai riche en uranium situé à 450 m de profondeur. Ceci indique que la combinaison des barrières naturelles a isolé efficacement le minerai d'uranium de l'environnement de surface. De façon plus particulière, cet analogue apporte des renseignements quant à la stabilité des déchets de combustible d'UO_2, aux performan-ces des barrières à base d'argile, à la géochimie des produits de fission et aux aspects de l'interaction eau-roche. Les principales études géochimiques de ce gisement portent sur l'évolution de la composition des eaux souterraines et sur la chimie des phénomènes d'oxydo-réduction dans celles-ci en fonction de l'uranium, du fer et du sulfure.

Des études de cet analogue sont menées, depuis 1984, par la coopération des propriétaires du gisement de Cigar Lake. EACL, avec le soutien d'Ontario Hydro sous les auspices du Groupe des propriétaires de réacteurs CANDU, a lancé la participation internationale en 1989 par la collaboration avec la Société suédoise de gestion du combustible et des déchets nucléaires (SKB) et, tout récemment, avec le Los Alamos National Laboratory (LANL). Le présent rapport donne les résultats des diverses études effectuées au cours des 3 ans de collaboration entre EACL et SKB ainsi qu'un résumé de l'étude effectuée par LANL. Il donne des renseignements précis sur les bases de données et modèles produits et intégre ces renseignements sous forme de conclusions à utiliser pour l'évaluation, quant à la sûreté, des concepts canadiens, suédois et americains (E-U) de stockage permanent.

EACL Recherche
Laboratoires de Whiteshell
Pinawa, Manitoba, Canada R0E 1L0
1994

AECL-10851
COG-93-147
SKB TR 94-04

CONTENTS

CONTENTS (concl.)

1. EXECUTIVE SUMMARY

(J. Cramer and J. Smellie)

1.1 INTRODUCTION

AECL has conducted natural analog studies on the Cigar Lake uranium deposit in northern Saskatchewan since 1984, as part of the Canadian Nuclear Fuel Waste Management Program. This deposit has a number of features analogous to aspects being considered in the performance assessment of concepts for disposal of nuclear fuel waste at depth in crystalline rock. In particular, the analogy with the excellent long-term isolation of UO_2-ore in this deposit is of great interest to both Canada and Sweden, who are developing similar concepts (both considering granite as a host rock) for disposal of UO_2-based fuel waste. AECL's studies on the deposit from 1984 to 1988, with the generous co-operation of COGEMA Canada Ltd. and the Cigar Lake Mining Corporation, concentrated on the characterization of the relatively undisturbed mineralization and its surrounding host rocks, prior to the onset of mining-related activities, which started in 1988. In 1989, AECL, with support from Ontario Hydro under auspices of the Candu Owners Group, and the Swedish Nuclear Fuel and Waste Management Company (SKB) started a collaborative three-year program (the "**Cigar Lake Analog Study**") to extend and focus the analog studies on the Cigar Lake deposit.

This report provides background information and summarizes the results of the Cigar Lake Analog Study. The emphasis is on the analog aspects and the implications of modelling activities related to the performance assessment of disposal concepts for nuclear fuel wastes developed in both Canada and Sweden.

1.2 OBJECTIVES

The two main objectives of the Cigar Lake Analog Study were:

- to obtain an understanding of the processes involved in, and the effects of, steady-state water-rock interaction in the deposit; and

- to obtain an understanding of the processes involved in, and the effects of, trace-element migration in and around the deposit (including paleo-migration processes since the deposit was formed).

To achieve these objectives, databases and models were produced with the aim of addressing the following four issues related to performance assessment of the disposal concepts:

1- The evaluation of equilibrium thermodynamic codes and databases.

2- The evaluation of the role of colloids, organics and microbes in transport processes for radionuclides (near- to far-field analogy).

3- The evaluation of UO_2 stability and the influence of radiolysis on UO_2 dissolution and radionuclide migration (near-field analogy).

4- The evaluation of generic mass-transport models for potential radionuclide migration through clay-based sealants (near-field analogy).

1.3 THE CIGAR LAKE URANIUM DEPOSIT

The 1.3-Ga-old uranium deposit at Cigar Lake is located near Waterbury Lake in northern Saskatchewan, Canada, and is one of the many unconformity-related uranium deposits found in the Athabasca Sandstone Basin. The uranium mineralization is found inside the clay-rich matrix of the hydrothermally altered sandstone at a current depth of 450 m below surface, at the contact between the sandstone and the underlying older basement rocks (Figure 1.1).

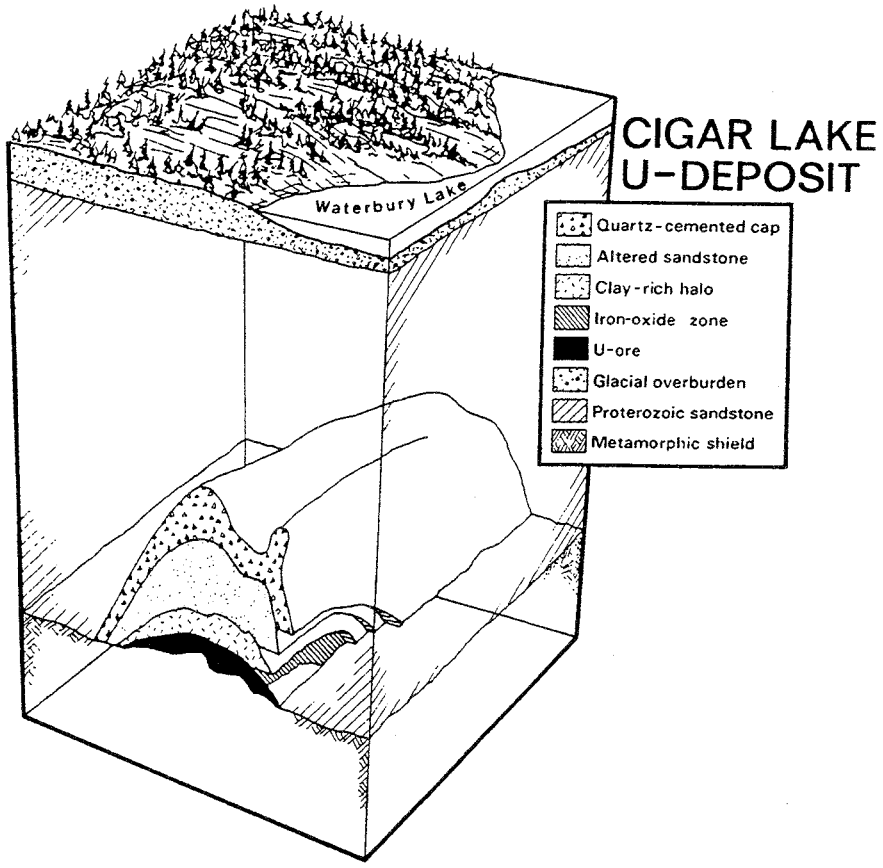

FIGURE 1.1 A three-dimensional block diagram showing the Cigar Lake uranium deposit located on the contact between the sandstone host rocks and the underlying metamorphic basement.

The uranium mineralization, comprised primarily of uraninite (UO_2) and pitchblende (amorphous UO_2) with subordinate coffinite ($USiO_4$), was orginally formed at a depth of >3 km below surface. The average grade of the deposit is ~ 8 wt.% U, with local concentrations reaching values as high as 60 wt.% U. The clay matrix in which the uranium mineralization occurs consists of illite and chlorite, changing upward and outward to illite and kaolinite.

Three groundwater flow regimes have been identified in the local stratigraphy at Cigar Lake (Figure 1.2). The uppermost Local Regime is unconfined and includes waters of the glacial overburden. The Intermediate Regime, in the upper sandstone unit, is confined between the Local Regime above and the Semi-Regional Regime in the lower sandstone unit below. The Semi-Regional Regime is confined below by the altered top ("regolith") of the basement and the clay-rich halo surrounding the uranium ore in the deposit. The groundwater flow direction in the Semi-Regional Regime is from southwest to northeast, intersecting the deposit through the highly permeable altered sandstone overlying the clay and ore zones (Figure 1.2).

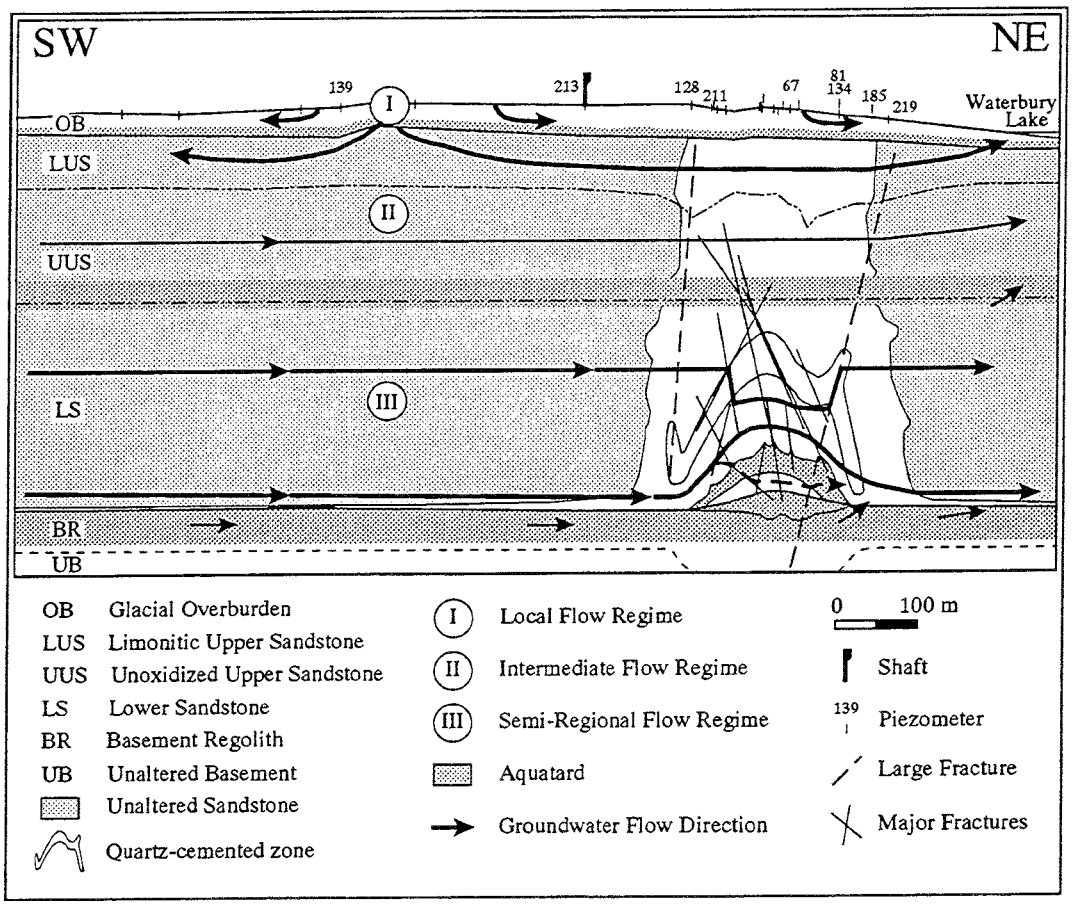

FIGURE 1.2 Cross section paralell to the direction of regional groundwater flow. Flow lines are illustrated on the diagram, and although hypothetical, they are constrained by the available hydrologic and geologic data.

The clay-rich matrix and halo surrounding the uranium mineralization play an important role in the long-term preservation of the main ore zone in this deposit. The clay-rich rocks and zones have relatively low hydraulic conductivities, compared with the altered and unaltered sandstone of the overlying main aquifer, thereby effectively sealing the ore zone from bulk groundwater flow through this zone. In addition, the clay-rich rocks and the hydrothermally altered sandstones are enriched in pyrite/marcasite (iron-sulphides), providing efficient redox buffering in the undisturbed system.

1.4 ANALOG FEATURES OF THE DEPOSIT

The Cigar Lake uranium deposit has a number of features analogous to aspects considered in the performance assessment (PA) of concepts for the disposal of nuclear fuel waste deep in crystalline rock . In what may be termed a "worse-case scenario", the Cigar Lake ore has been well-preserved inside a natural aquifer without specially designed man-made barriers, and without showing any direct evidence of its existence at the present-day surface. Since the current topography and overburden were formed during the last glaciation, any potential migration of radionuclides from the ore has not reached the surface environment during at least 10^4 a. This time frame is in accordance with the quantitative predictions in performance assessment required by regulatory guidelines (10^4 a in Canada and 10^6 a in Sweden). Thus, the spatial arrangement of the UO_2 ore surrounded by natural barriers, including a clay zone and several hundreds of metres of host rock in a tectonically stable formation, is similar to that of the disposal scenario in the concepts being considered in both Canada and Sweden.

In addition to this general analogy, many analogous processes and materials can be found and studied in more detail in the Cigar Lake deposit. These include both processes that occur in the present-day system and those that occurred during the ~1-Ga history of the deposit since its formation. For example, current processes that have been studied include water-rock interaction, evolution of groundwater compositions, redox geochemistry, stability and dissolution of uranium and clay minerals, sealing by clay, formation and properties of colloids, activity and role of microbes etc. On the other hand, paleo-processes that can be studied from the geological record include the effects of erosion, uplift and glaciation, paleo-hydrology, water-rock interaction, redox buffering, mineral stability and radionuclide mass transport. A comprehensive record of the studies carried out on many of these processes is given in the various sections under Chapter 3 of this report.

1.5 STUDY APPROACH

The program of the joint Cigar Lake Analog Study was subdivided into a number of Tasks, with each Task covering one particular discipline or related disciplines (Figure 1.3). The goal for each Task was to produce specific databases and conceptual models, and to carry out modelling to further improve the understanding of the observed processes in each discipline. The main databases and conceptual models produced are:

- the geological database and conceptual model,
- the hydrogeological database and conceptual model,
- the mineralogical and lithogeochemical database, and
- the hydrogeochemical database and the geochemical conceptual models for evolution of groundwater compositions and redox geochemistry.

In addition, the various databases and conceptual models were subsequently integrated in modelling for the four PA-related objectives (see Section 1.2), as illustrated in Figure 1.3.

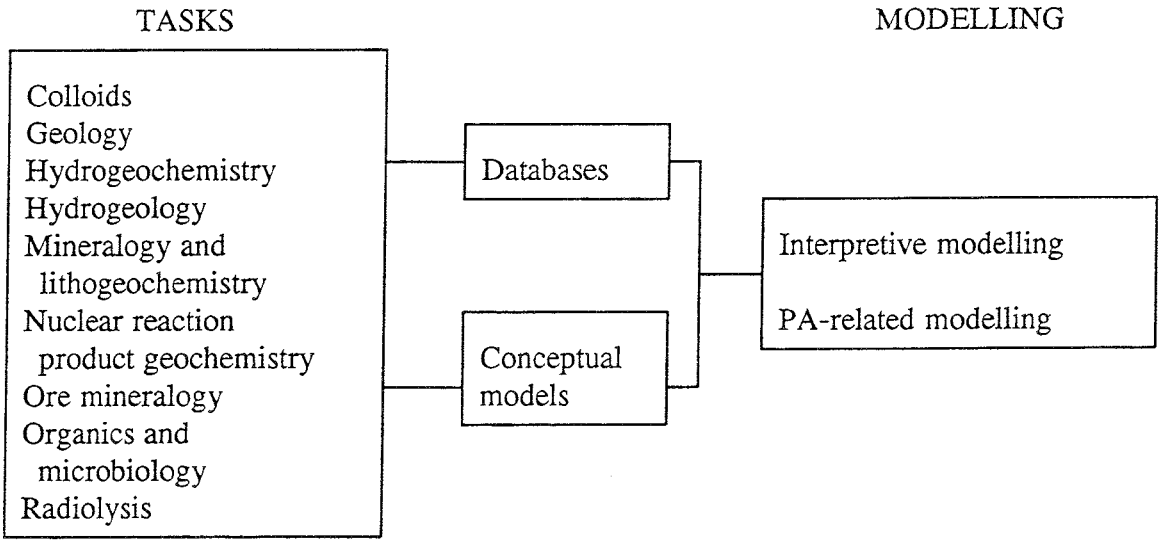

FIGURE 1.3 Relationship between Tasks and Modelling activities in the Cigar Lake Analog Study.

1.6 GENERAL CONCLUSIONS

The Cigar Lake Analog Study has provided valuable information and insight on a number of performance assessment aspects common to the disposal concepts in both Canada and Sweden. The important general conclusions can be summarized as follows:

1- UO_2 dissolution and stability:
- UO_2 is stable under reducing conditions over geological time;
- little dissolution of UO_2 occurred during 100 Ma; and
- congruent dissolution of UO_2 is controlled by surface alteration.

2- Clay sealing:
- clay (in this case illite) can provide effective, long-term sealing;
- illite is stable under suitable conditions over geological time; and
- clay is an efficient barrier to radionuclide and colloid migration.

3- Colloids:
- colloid and particle contents in groundwater are generally lowest in competent rock and highest in friable rock;
- only a small fraction of radionuclides in water is attached to colloids;
- colloids can be effectively sealed in by clay-rich rocks; and
- colloids were not important in radionuclide migration at Cigar Lake, at least on a time scale of 10^4 a.

4- Organics and Microbes:
   - low humic contents in dilute water are unlikely to play a significant role in either speciation or mobilization of radionuclides;
   - microbes can survive in radiation fields, and they can mediate in redox control and buffering; and
   - organics and microbes are unlikely to adversely affect radionuclide migration in the near field.

5- Groundwater chemistry:
   - interactions with clay minerals control the bulk composition of groundwater;
   - redox geochemistry is strongly controlled and buffered by the iron and sulphur redox couples; and
   - the evolution of groundwater compositions can be predicted by existing geochemical codes.

6- Radiolysis:
   - radiolytic-oxidation models for UO_2 dissolution appear overly conservative in SKB's current PA code; and
   - dissolved Fe^{2+} is an important scavenger of radiolytic oxidants.

7- Radionuclide migration:
   - natural hydrologic barriers and appropriate geochemical conditions in a relatively open, natural system are effective in limiting radionuclide migration over any significant distance; and
   - clay sealing is an important barrier to radionuclide migration.

2. INTRODUCTION

(J. Cramer and J. Smellie)

2.1 BACKGROUND AND OBJECTIVES

AECL has been conducting natural analog studies on the Cigar Lake uranium deposit in northern Saskatchewan since 1984, as part of the Canadian Nuclear Fuel Waste Management Program. This deposit has a number of features analogous to aspects considered in the performance assessment (PA) of concepts for disposal of nuclear fuel waste at depth in crystalline rock (Cramer 1986, 1994; Cramer et al. 1987; Goodwin et al. 1989). In particular, the analogy with the excellent long-term isolation of UO_2-ore in this deposit is of great interest for disposal of UO_2-based fuel waste. AECL's studies on the deposit from 1984 to 1988 concentrated on the characterization of the relatively undisturbed mineralization and its surrounding host rocks prior to the onset of mining-related activities, which started in 1988. A considerable amount of data and information on the deposit was already available in 1988 with the mining company, Cigar Lake Mining Corporation (CLMC), the exploration company, COGEMA Canada Ltd, and from AECL's work.

In 1989, AECL and SKB started a collaborative three-year program (the "Cigar Lake Analog Study") to extend and focus the analog studies on the Cigar Lake deposit. The Los Alamos National Laboratory (LANL) joined the program in 1991, with funding from the United States Department of Energy, to work specifically on the geochemistry of nuclear reaction products formed in this deposit.

The two main objectives of the Cigar Lake Analog Study were:

- to obtain an understanding of the processes involved in, and the effects of, steady-state water-rock interaction in the deposit, and

- to obtain an understanding of the processes involved in, and the effects of, trace-element migration in and around the deposit (including paleo-migration processes since the deposit was formed).

To achieve these objectives, databases and models were produced with the aim of addressing the following four issues related to performance assessment of the disposal concepts:

1- The evaluation of equilibrium thermodynamic codes and databases.

2- The evaluation of the role of colloids, organics and microbes in transport processes for radionuclides (near- to far-field analogy).

3- The evaluation of UO_2 stability and the influence of radiolysis on UO_2 dissolution and radionuclide migration (near-field analogy).

4- The evaluation of generic mass-transport models for potential radionuclide migration through clay-based sealants (near-field analogy).

2.2 STUDY APPROACH AND ACTIVITIES

The program of the joint Cigar Lake Analog Study was subdivided into a number of Tasks, with each Task covering one particular discipline or related disciplines (Figure 2.1). The goal for each Task was to produce specific databases and conceptual models, and to carry out modelling to further improve the understanding of the observed processes in each discipline. The following primary databases and conceptual models were produced:

- the geological database and conceptual model,
- the hydrogeological database and conceptual model,
- the mineralogical and lithogeochemical database, and
- the hydrogeochemical database and the geochemical conceptual models for evolution of groundwater compositions and redox geochemistry.

The various databases and conceptual models were subsequently integrated in modelling for the four PA-related objectives (see Section 2.1).

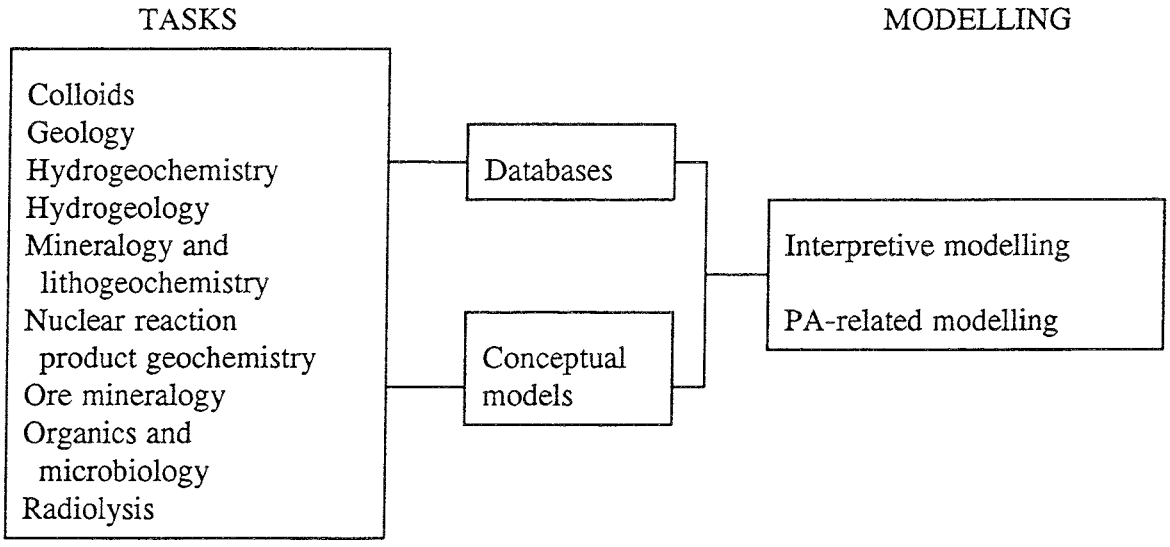

FIGURE 2.1 Relationship between Tasks and Modelling activities in the Cigar Lake Analog Study.

The Project activities were planned to achieve the two main objectives as outlined in Section 2.1. The main activities included fieldwork, meetings and workshops, as summarized in Table 2.1. In addition, many small meetings, discussions and consultations took place between Project participants, CLMC and subcontractors.

TABLE 2.1
MAIN ACTIVITIES OF THE AECL/SKB CIGAR LAKE ANALOG STUDY

DATE	ACTIVITY
1989 May-June	Fieldwork: drilling of 2 holes, installation of 6 piezometers, hydrologic tests and measurements, sampling of waters, colloids and core (including the ore zone in hole 220).
1989 November	Fieldwork: sampling of waters and colloids, hydrologic measurements.
1990 March	Fieldwork: sampling of core.
1990 April	First Annual Workshop in Pinawa, Canada. Steering Committee meeting.
1990 May	Fieldwork: sampling of waters and colloids, hydrologic measurements.
1990 October-November	Fieldwork: sampling of waters, colloids and organics, hydrologic measurements.
1990 December	Review Meeting on Hydrogeochemistry in Pinawa, Canada.
1991 January	Fieldwork: sampling waters at surface and underground from ore zone, sampling for microbiology.
1991 April	Fieldwork: installation of continuous water-level logging system.
1991 April-May	Second Annual Workshop in Saskatoon, Canada, including a fieldtrip to Cigar Lake. Steering Committee meeting.
1991 June	Fieldwork: sampling of core from freeze hole (FH-18) in ore zone.
1991 August	Work Meetings on Speciation Code testing and Mass Transport modelling in Pinawa, Canada. Review Meeting on Mineralogy and Lithogeochemistry in Pinawa, Canada. Work Meeting on Modelling in Stockholm, Sweden.
1991 September	Fieldwork: sampling of waters, colloids, organics and microbes.
1991 October	Official start of LANL involvement on Nuclear Reaction Product geochemistry.
1991 December	Review Meetings on Hydrogeology and Modelling in Forsmark, Sweden. Steering Committee meeting.
1992 April	Fieldwork: sampling of frozen ore from mining test.
1992 June	Third Annual Workshop in Winnipeg, Canada.

Achievement of the two main objectives required comprehensive studies of the uranium mineralization and its surroundings, involving a multidisciplinary and integrated approach to understand and conceptualize the complex systems that had been operating in the past as well as those that are currently in operation. Achieving the first objective required the following:

- Determination of the speciation and solubility of trace elements in groundwater and associated rocks and minerals in the main units of the deposit. Specific trace elements of interest in performance assessment included U, Th, Pb, V, Mo, Ni, Co, Zn, Cu, Sn, Zr, Se, Ra, Pd, Tc, Pu, and I.

- Determination of the redox chemistry in the groundwater and associated rocks and minerals in the ore and clay zones. The processes taken into consideration include radiolysis and microbial activity, and the role of dissolved and solid organic phases.

- Determination of the uranium-mineral stability and dissolution. This includes the composition, structure and stability of surface alteration on uranium minerals (uraninite and coffinite) and the processes affecting dissolution of these phases.

- Determination of the present hydrogeology of the deposit. This involves the modelling of the hydraulic characteristics of the deposit, particularly of the ore and clay zones, and includes boundary conditions, flow directions and budget.

Achievement of the second objective required the following:

- Determination of the hydrogeologic conditions involved in trace-element migration. This includes reconstruction of the paleo-hydrogeology where possible.

- Determination of trace-element migration in the ore and clay zones and in the host rocks surrounding the mineralization. This involves the determination of retention and fixation processes and parameters for mobile trace elements such as U, Ra, Pb, Ni, Co, Zn, Cu, V, actinides, nuclear reaction products and uranium series nuclides.

- Determination of colloid stability, migration and fixation of trace elements. This includes the aquisition of background data to develop models for the role of colloids in migration of any of the trace elements mentioned above.

- Determination of organic-phase stability, migration and complexation of trace elements. This includes the evolution of both dissolved and solid organic phases, the role of the organics in microbial activity and development of models for the role of organics in trace-element migration.

2.3 STRUCTURE AND MANAGEMENT

The Cigar Lake Analog Study commenced on 1989 April 1 and continued until 1992 June. Project administration and management were provided by AECL. The structure of the Project included three entities (Figure 2.2): a Steering Committee, a Technical Committee and a Principal Investigators Group. The Principle Investigators Group was subdivided into a number of Tasks, each including a distinct discipline or a combination of related topics (see Table 2.2).

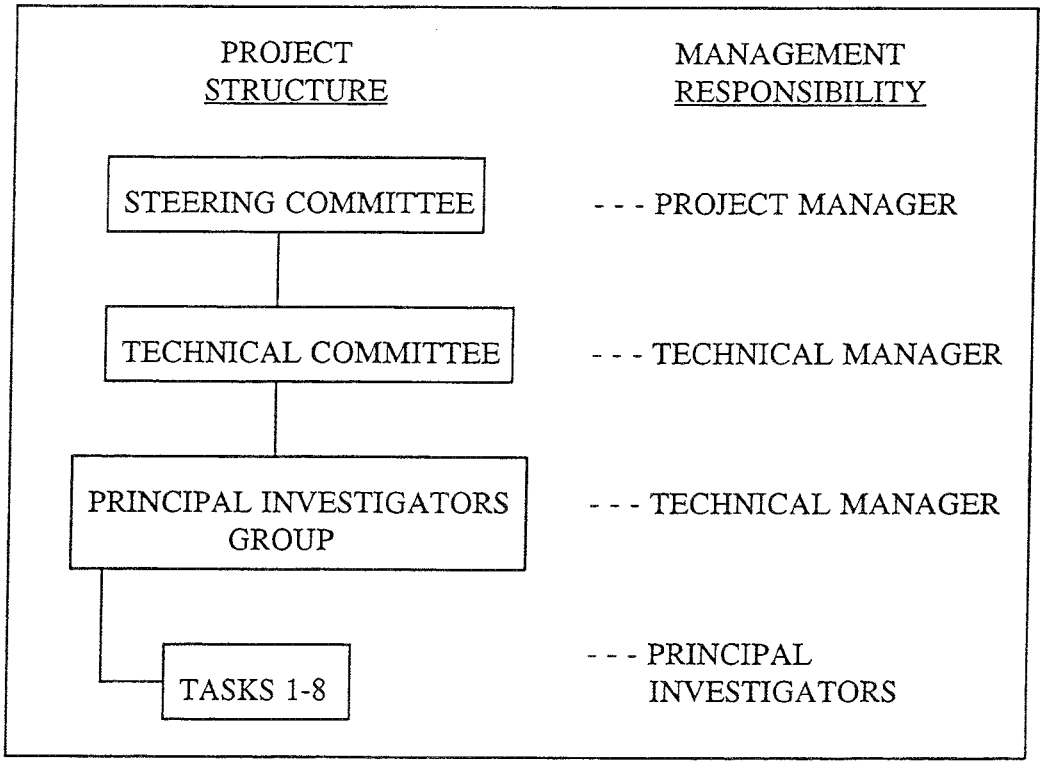

FIGURE 2.2 Structure of the AECL/SKB Cigar Lake Analog Study.

The **Steering Committee** was responsible for the administration and management of the Project, including, but not limited to, a review of all scientific, technical and financial aspects. The Committee consisted of four members:

Peter Sargent	AECL	Project Manager	(Chairman)
Fred Karlsson	SKB	Managerial Representative	
Jan Cramer	AECL	Technical Manager	
John Smellie	SKB	Technical Representative	(Secretary)

Neil Chapman (Intera, U.K.) acted as an advisor to the Steering Committee.

The **Principal Investigators Group** (Table 2.2) was responsible for the execution of the technical program, including, but not limited to, field and laboratory work, collaboration between individual Tasks, and reporting. In addition, two modelling co-ordinators, Jordi Bruno and Jan Cramer, were responsible for the co-ordination and integration of the various modelling activities of the Project, in Europe and in North America respectively. The modelling co-ordinators, together with John Smellie, formed a **Technical Committee**, which was responsible for the regular review of the modelling aspects of the various Tasks.

TABLE 2.2
TASKS AND PRINCIPAL INVESTIGATORS
FOR THE CIGAR LAKE ANALOG STUDY

Task #	Topic	Principal Investigators
1	Hydrogeochemistry	Jan Cramer
2	Colloids	Peter Vilks
3	Hydrogeology	Doug Stevenson Anders Winberg
4	Rock mineralogy and geochemistry	John Smellie, Jan Cramer Jeanne Percival
5	Ore and Nuclear Reaction Product geochemistry	Sham Sunder, Jan Cramer, Rod Ewing, June Fabryka-Martin
6	Organic geochemistry and microbiology	Bert Allard, Peter Vilks, Sim Stroes-Gascoyne
7	Radiolysis	Hilbert Christensen
8	Integrated modelling	Jordi Bruno, Ivars Neretnieks Jan Cramer, Wayne Nesbitt

Jan Cramer was the Technical Manager for the Project, and was responsible for the general co-ordination of all of the activities of the Project, including execution of fieldwork, reporting to the Steering Committee and liaison with CLMC. John Smellie was the Technical Representative from SKB and was responsible for liaison between SKB and AECL. He acted as secretary at the Steering Committee meetings and, together with the Technical Manager, prepared reports on the Project's activities and results.

The Steering Committee met on an annual basis, usually in conjunction with the Annual Workshop or a review meeting. Meetings of the Principal Investigators Group, in addition to any Workshops, were held at regular intervals as required and at least once a year.

When necessary, workshops were scheduled throughout the duration of the Project to provide a forum for evaluation of progress and for planning program activities. These workshops were important mechanisms to co-ordinate all the Tasks and their investigators, in order to integrate data requirements for the objectives of the Project. The first Annual

Workshop was held in 1990, April 18 to 20, in Pinawa, to review progress and plan future activities. The second Annual Workshop was held in 1991, April 29 to May 3, in Saskatoon. This Workshop included a fieldtrip to the Cigar Lake site. The third and final Annual Workshop was held in 1992, June 3 to 5, in Winnipeg.

Project status was reported in comprehensive progress reports, each covering a period of about four months. These reports comprised a brief summary from each Task stating the work carried out, the key results obtained, and an indication of future intentions. When applicable, any publications and any proceedings resulting from Workshops and Review Meetings were appended. Each spring, after completion of each Project Year, which ran from April 1st to March 31st, a comprehensive Annual Report was produced. These Annual Reports included results and conclusions for the year just completed, as well as the proposed program and schedule for the following year. Review Meetings, devoted to a more specialized integration of data and exchange of ideas within one or a restricted number of Tasks, were held periodically as the need arose. Such meetings, involving both modellers and data-gathering groups, were more frequent as conceptual modelling of the Tasks and their eventual integration into performance-assessment-related modelling became necessary.

2.4 REFERENCES

CRAMER, J.J. 1986. A natural analog for a fuel waste disposal vault. In: 2nd International Conference on Radioactive Waste Management, Winnipeg, Sept. 1986. Can. Nucl. Soc. Proc., 697-702.

CRAMER, J.J. 1994. Natural analogs in support of the canadian concept for nuclear fuel waste disposal. Atomic Energy of Canada Ltd. Rep., **AECL-10291**, 109p.

CRAMER, J.J., VILKS, P. and LAROCQUE, J.P.A. 1987. Near-field analog features from the Cigar Lake uranium deposit. In: Natural Analogues in Radioactive Waste Disposal. Eds: B. Côme and N.A. Chapman. Com. Europ. Commun. Rep., **EUR 11037-EN**, 59-72.

GOODWIN, B.W., CRAMER, J.J. and McCONNELL, D.B. 1989. The Cigar Lake uranium deposit: An analogue for nuclear fuel waste diposal. In: Natural Analogues in Performance Assessments for the Disposal of Long Lived Radioactive Wastes. Int. Atom. Ener. Agency Tech. Rep., **304**, App. B, 37-45.

3 TASKS

3.1 GEOLOGY
(J. Cramer)

3.1.1 Geological setting

The Cigar Lake uranium deposit (Figure 3.1) is located in northern Saskatchewan at the southwestern tip of Waterbury Lake. The deposit is of hydrothermal origin and Proterozoic age, and is one of many unconformity-type, sandstone-hosted uranium deposits that characterize the Athabasca Basin uranium province (Fouques et al. 1986; Bruneton 1987, 1993). These deposits are all relatively high-grade, with some containing average ore grades of several percent uranium. The Cigar Lake deposit is notable because it is located well below the surface at a depth of about 430 m, and the deposit has no direct surface signatures to indicate its presence.

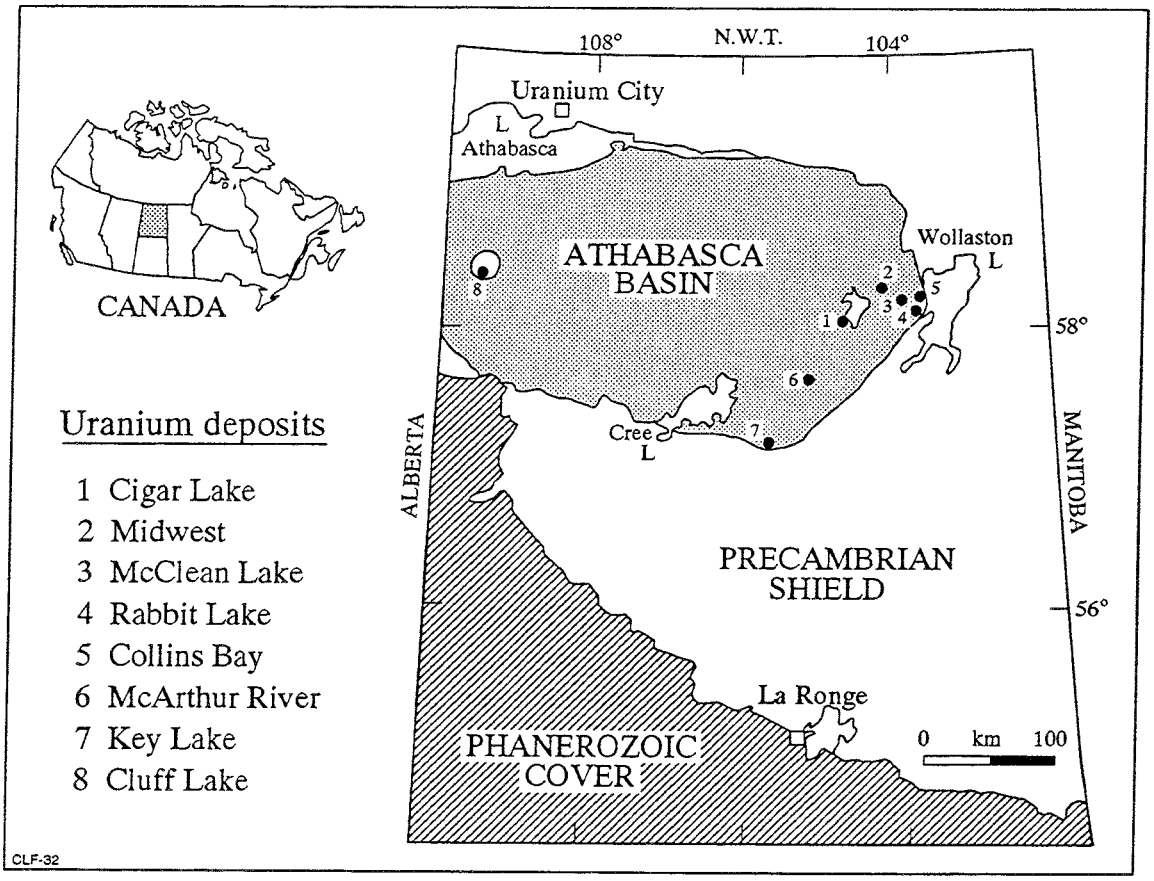

FIGURE 3.1 Location map showing uranium deposits of the Athabasca Basin in northern Saskatchewan, Canada.

The mineralization, consisting primarily of uraninite and pitchblende, with subordinate coffinite, formed about 1.3 Ga ago (Cumming and Krstic 1992) at an estimated depth of more than 3 km below surface in hydrothermally altered sandstone. The mineralization is

located at the unconformity contact of the host sandstone of the Athabasca Group and the metamorphic Precambrian basement (metapelites and calc-silicate gneisses), and is currently situated at a depth of ~430 m below the surface, following millions of years of erosion. The uranium mineralization occurs in a clay matrix and is shaped like an irregular lens that measures approximately 2000 m long, 20 to 100 m wide and 1 to 20 m thick. The average grade of the total mineralization is around 8 wt.% U, with local concentrations reaching values as high as 55 wt.% U. The geological reserve has been calculated to be 1.5×10^5 Mg U. The Cigar Lake deposit has many features in common with the other unconformity-type deposits in the region, which all tend to consist of long linear deposits that overly graphitic metapelites subcropping at the unconformity (Hoeve and Quirt 1984; Sibbald et al. 1990).

3.1.2 Basement

The Athabasca Group sediments unconformably overly a deeply weathered surface (regolith) developed on the Precambrian basement. The unweathered crystalline basement rocks consist of Archean and Lower Proterozoic metamorphosed rocks that, in the Cigar Lake area, include mainly graphitic metapelitic gneisses with intercalations of calc-silicate gneisses and meta-arkoses (Bruneton, 1993). The most characteristic feature of the graphitic metapelite is its highly sheared fabric and the occurrence of abundant graphite and pyrite in the foliation surrounding K-feldspar and cordierite "augen". This rock occurs primarily below the Cigar Lake deposit and extends for about 2 km with a width of between 50 and 100 m.

In addition to the metapelitic gneisses, the calc-silicate-bearing meta-arkosic gneisses occur in the area. Pegmatites and anatectic mobilizates are common in the form of veinlets, lenses and irregular-shaped bodies, and migmatitic fabric is also widespread. The mineralogy of the metapelitic rocks indicates that metamorphism peaked in the upper amphibolite grade, probably as part of the regional Hudsonian metamorphism.

The structure and orientation of the basement rocks in the Cigar Lake area are dominated by large northeast-southwest lineaments and east-west structural corridors. The basement rocks under the deposit form an east-west belt in which the units have a steeply southward dip (Figure 3.2); a major discontinuity is noticeable to the west of Cigar Lake where it corresponds to the western termination of the overlying uranium mineralization.

The deposit lies above a well-defined high in the topographic surface of the basement. The correlation between the narrow belt of augen gneiss with mylonitic textures (including abundant graphitic lubricant) and this topographic high suggests a tectonic control in the formation of this ridge. Such a ridge has been observed at other unconformity uranium deposits in the eastern Athabasca Basin.

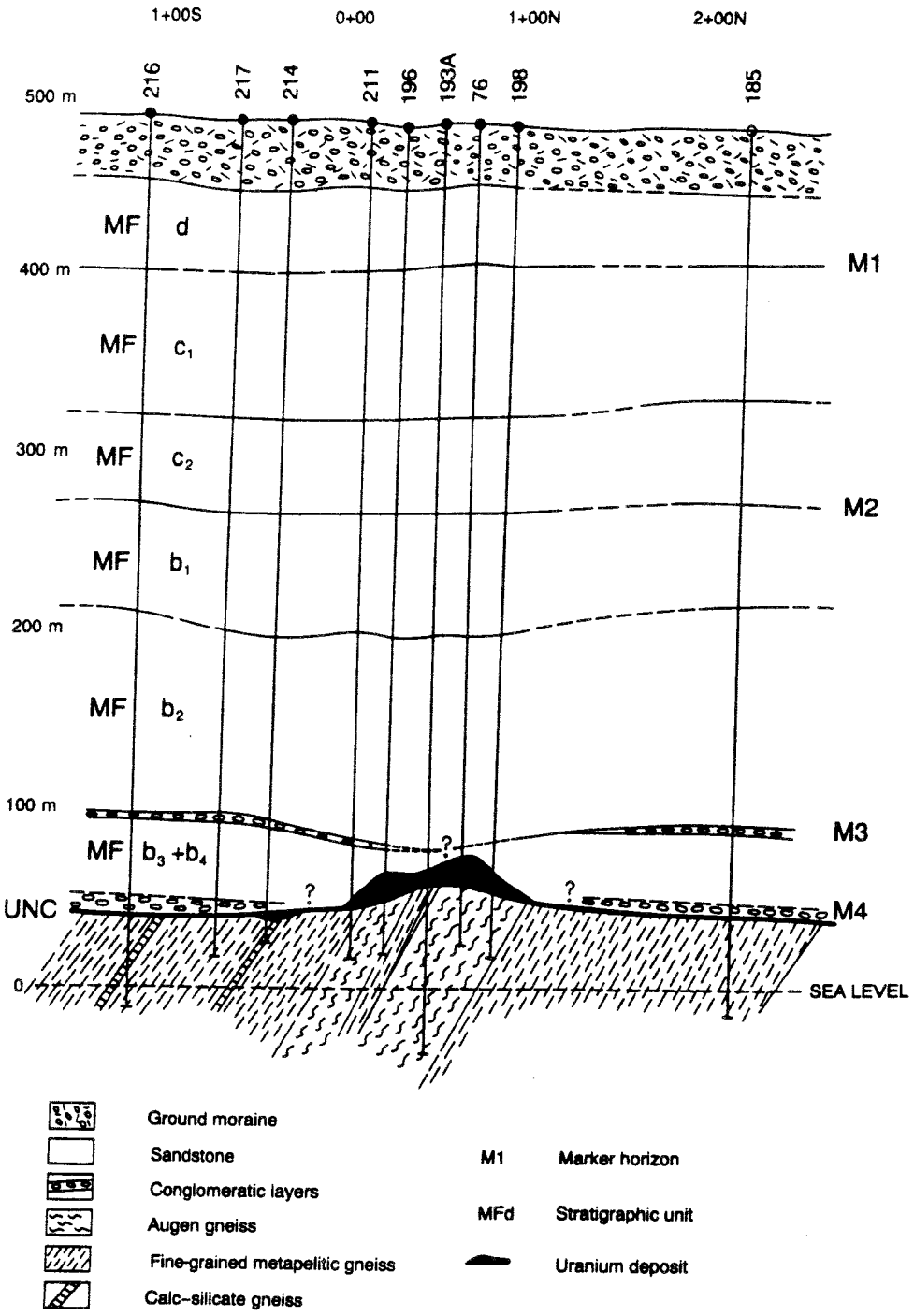

FIGURE 3.2 Geological cross section through the Cigar Lake deposit (from Bruneton, 1993).

Alteration of the basement rocks in the Cigar Lake area includes three distinct types (Bruneton, 1993): retrograde metamorphism, paleo-weathering and hydrothermal alteration. The limited retrograde greenschist-type alteration of the high-grade metamorphic rocks is characterized by a green colouration of the rocks due to dominant chloritization and sericitization. The development of the regolith to a depth of 40 to 50 m into the basement

resulted from extensive lateritic weathering of the basement surface prior to subsidence and basin formation. The regolith typically has two distinctly coloured zones, reflecting the paleo redox-interface between the reduced basement lithologies and the overlying oxidizing systems of, first, surface exposure, and, second, red-bed-type sediments. The hydrothermal alteration (contemporaneous with the formation of the uranium mineralization) is characterized by a late, white- to pale-green colouration of the basement rocks, which obliterates the characteristic colour zonation in the regolith, and by the absence of graphite in the metapelitic gneiss. The extent and degree of this hydrothermal alteration is also related to the occurrence of mineralization at the unconformity: it disappears laterally beyond the known terminations of the deposit, and the degree of hydrothermal alteration in the basement rocks roughly correlates with the grade of the mineralization.

3.1.3 Sandstone

The main member of the Proterozoic Athabasca Group sediments in the eastern part of the Athabasca Basin is the Manitou Falls Formation. The sandstones in the Cigar Lake area are all part of this formation, in which Ramaekers (1981) has distinguished three stratigraphic units (MFd, MFc and MFb in Figure 3.2). The uppermost MFd unit is characterized by a homogeneous fine- to medium-grained texture with intercalated clay clasts and horizons. The rock is affected by a surface-derived alteration (bleaching and limonitization) extending to the base of this unit. The MFc unit contains medium- to coarse-grained sandstones with micro-conglomeratic layers. The MFb unit is characterized by sandstones that are more coarse-grained than those in the MFc unit, and it contains gritty and conglomeratic layers. The top of this unit is marked by a prominent increase in pebble content and in conglomerate layers thicker than 2 cm (Bruneton, 1993). The 5 to 15-m-thick, coarse basal conglomerate directly overlies the unconformity contact with the basement regolith.

The unaltered sandstones of units MFc and MFb are characterized by the ubiquitous content of hematite, showing in the pink-to-red-to-purple colours of the rocks. The general increase in grain size of the rocks from unit MFd to MFb also corresponds with an increase in total radioactivity of the rock, which in turn can be correlated with the occurrence of heavy minerals concentrated in the conglomeratic layers (Bruneton, 1993). These heavy minerals include Fe-Ti oxides, rutile, zircon, monazite, tourmaline and phosphates. The bulk of the sandstones is made up of poorly sorted quartz grains (>80 %) within a clay matrix (2 to 20 %) in which kaolinite is more abundant than illite (Bruneton, 1993).

The mainly fluvial sandstones in the Cigar Lake area are flat-lying and generally increase in thickness in a westerly direction, reflecting the regional gradient (9 m/km towards the west) of the unconformity contact in the eastern Athabasca Basin. Local deformations and discontinuities in this horizontal sandstone stratigraphy are due to post-depositional faulting. This faulting represents either refractions of reactivated basement faults or responses to volume adjustments in the sandstone during its hydrothermal alteration and mineralization. The reactivation of older basement lineaments caused mainly block faulting along steeply SE- and S-dipping fractures, whereas the faulting in response to the hydrothermal alteration of the sandstone caused a secondary set of subvertical fractures over the length of the deposit (Bruneton, 1987).

3.1.4 Sandstone alteration

The hydrothermal event associated with the formation of the Cigar Lake uranium mineralization was responsible for the characteristic alteration of the host sandstones (Figure 3.3). Hydrothermal fluids passing through the basement, where they became reducing upon contact with the graphite-bearing metapelitic rocks in the basement, were discharged along a ridge on the basement topography into the sediment basin. Where these reducing fluids interacted with the more oxidizing diagenetic uranium-bearing solutions of the red-bed-type sandstones, uranium minerals were deposited comtemporaneously with the hydrothermal water-rock interaction.

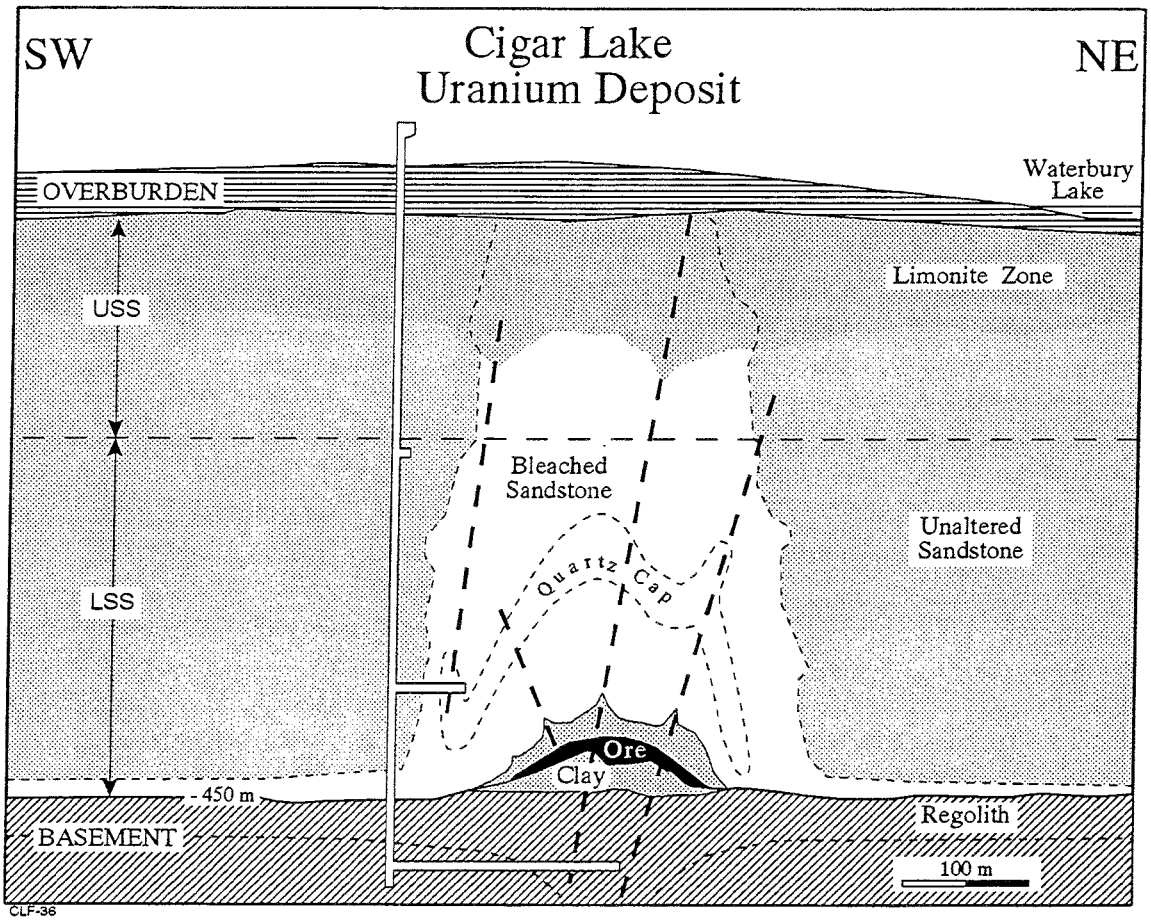

FIGURE 3.3 Schematic cross section through the Cigar Lake deposit showing the uranium mineralization and its host rocks, including the lithologic characteristics related to hydrothermal alteration and weathering. (USS= upper sandstone; LSS= lower sandstone).

The resulting alteration of the sandstone (at temperatures between 150 and 200 °C) includes the following characteristic features: a) reduction of Fe(III) from hematite to Fe(II) in marcasite/pyrite, forming a nearly symmetrical plume of "bleached" sandstone above and parallel to the axis of the deposit; b) dissolution and mobilization of quartz from the sandstone, causing a progressive enrichment of refractory clay and accessory minerals

toward the high-temperature side and reprecipitation of the dissolved silica toward the cooler side of the hydrothermal system; and c) fracturing caused by volume readjustments in response to the quartz redistribution mentioned under (b). Thus, with increasing depth and lateral proximity to the host sandstone, alteration of the sandstone is characterized by increasing clay-mineral contents, reaching 80 to 100% locally in and around the mineralized zone. However, a quartz-cemented zone (or "quartz cap") marks the location of the silica reprecipitation in the altered sandstone before the zone reaches a clay-mineral content of about 30 %. Below this quartz cap, the altered sandstone is highly permeable, densely fractured and locally friable until the clay-mineral content reaches about 60 % in the so-called clay-rich halo (or "clay zone"). This clay zone is 5 to 30 m thick, contains elevated uranium contents and surrounds the high-grade uranium mineralization. The hydrothermal alteration also affected the basement rocks underneath the mineralization, extending the clay-rich zone past the unconformity into the basement regolith. This alteration and the paleo-weathering (producing the ~50-m-thick regolith) of the basement resulted in local obliteration of the original metamorphic textures and mineral assemblages. The effects of hydrothermal alteration extend upwards about 300 m into the sandstone and down into the basement to about 100 m below the unconformity.

At present, the different lithologies are characterized as follows (Bruneton 1987):

1- The pink/red-to-purple relatively **unaltered sandstone** is competent and hard, contains hematite, subequal amounts of illite and kaolinite, and has a clay-mineral content of about 5 to 10 %.

2- The ~100-m-thick **limonite zone** (unit MFd) at the top of the sandstone bedrock (Figure 3.3) is a late alteration (glacial and post-glacial) superimposed on both unaltered and bleached sandstones. It represents a zone in which downward infiltration of oxidizing, surface-derived waters causes precipitation of ferrihydrites (including limonite), giving the rocks a pale orange colour.

3- The grey-white **bleached sandstone** is competent and hard, and contains finely disseminated marcasite/pyrite, local accumulations of solid hydrocarbons, more illite than kaolinite, and may have a clay-mineral content >15 % (however, intercalated beds and zones of less-altered (less "bleached") sandstone do occur within this unit).

4- The grey **quartz-cemented zone** is highly fractured, contains euhedral quartz on fracture surfaces, in cavities and interstitially in the matrix, and is somewhat lower in clay-mineral content than the surrounding bleached sandstone.

5- The grey **altered sandstone** is less competent, even soft and friable in places, is intensely fractured and contains generally up to 30 % clay-minerals both in the matrix and in fractures, with illite dominating over kaolinite. The presence of faults may be indicated by layers or pockets of massive clay, very friable sandstone or sand.

6- The pink-grey/white **clay zone** is almost entirely composed of clay and some quartz with rare sandstone remnants. Localized oxidized areas are common (faults?). Illite is the dominant clay mineral with minor amounts of kaolinite, and chlorite appearing toward the ore zone. Siderite and marcasite/pyrite are common constituents. This zone has elevated uranium contents and is mineralized locally (up to 1 % U).

7- The **clay-ore contact** is relatively sharp (both upper and lower contacts of the ore zone) with respect to the uranium content. However, the clay-to-ore transition is characterized by the gradual disappearance of kaolinite and by a marked increase in chlorite content. The upper clay-ore contact is red-green in colour and may be 1 to 3 m thick, with the greater thickness localized along fractures. This upper contact obtains its reddish colouration from Fe(III) phases including both hematite and amorphous to poorly-crystallized ferrihydrites. Very locally, siderite may form up to 50 % of the rock.

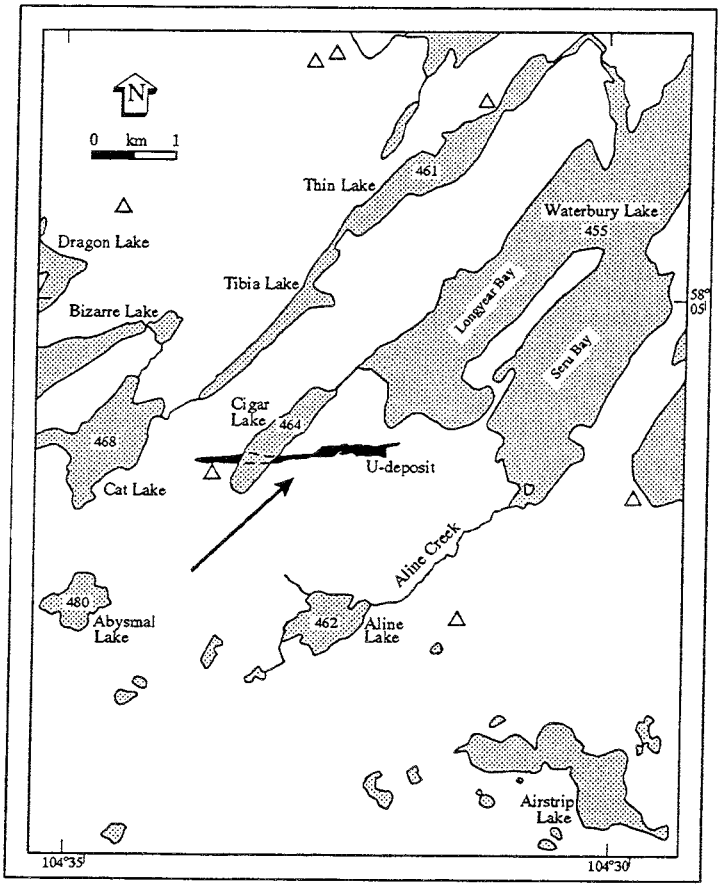

FIGURE 3.4 Plan view of the Cigar Lake area, showing the projected outline of the uranium deposit, the direction of regional groundwater flow (arrow) and the numerous bodies of surface water (numbers indicate elevation in metres above sea level). Also marked are locations where sandstone outcrops at surface (Δ).

3.1.5 Overburden

The Quaternary overburden in the Cigar Lake area consists of Pleistocene glacial sediments, overlying the relatively flat surface of the sandstone bedrock. The topography is dominated by drumlins and eskers, and sandy ground moraine is the dominant surficial deposit in the area. The thickness of the unconsolidated overburden ranges between 0 and 55 m, with bedrock only observed in several isolated exposures in the Cigar Lake area (Figure 3.4). Larger areas without overburden cover occur further to the south of Cigar Lake, in the upland area of the regional Waterbury Lake catchment (e.g., in the Close Lake - MacArthur River area).

The overburden stratigraphy is very similar to that described for areas immediately to the north (Schreiner, 1983) and east (Geddes, 1982). This stratigraphy is characterized by alternating horizons of silt- or sand-dominated composition, with glacially-transported boulders interspersed throughout and on top of the sediments. These boulders predominantly consist of sandstone but boulders of high-grade metamorphic basement rocks also occur. The sandy sediments are underlain by a dense basal lodgement till (>35,000 a old, Schreiner 1983) with ablation textures occurring locally. In the area around the deposit, this basal till ranges in thickness between 2 and 4 m.

3.1.6 Uranium mineralization

The Cigar Lake uranium mineralization occurs in a very clay-rich matrix that is dominated by illite and chlorite with minor carbonates (siderite and calcite) and accessory phases (e.g., zircon, rutile, phosphates etc.). In addition to uranium, the ore deposit contains elevated concentrations of sulphides, arsenides and sulph-arsenides incorporating a broad suite of elements (e.g., Ni, Co, Mo, Pb (radiogenic), Zn, Mn and Fe). Three stages of mineralization can be recognized (Bruneton 1987), of which at least the first two are considered to be of a hydrothermal nature:

I- euhedral uraninite and pitchblende associated with primary As-S minerals of Ni, Co and Fe;

II- pitchblende associated with secondary As-S minerals, in addition to Cu, Mo, Pb, Zn and Fe sulphides; and

III- pitchblende and coffinite associated with ferrihydrites.

The first stage produced the bulk of the Cigar Lake mineralization, whereas the last stage occurred on a local and uneconomic scale, dispersing uranium above (perched mineralization along fractures) and also below (minor basement mineralization) the primary ore body. The first two stages have been dated at 1362 Ma and 1287 Ma respectively (Cumming and Krstic 1992). The last stage of mineralization is characterized by a low-temperature assemblage, and is much younger, dated at 293 Ma ago (Cumming and Krstic 1992).

The bulk of the uranium mineralization (>95 %) occurs in the sandstone directly overlying the unconformity contact with the basement. The perched mineralizations have been encountered as small pockets along fractures in drillholes at elevations of up to 300 m above the main mineralization. These perched mineralizations have a simple pitchblende/uraninite mineralogy. The minor uranium mineralization (also containing some basemetal sulphides and arsenides) in the basement rocks immediately below the main deposit occurs as fracture-controlled veinlets and irregular intercalations to a depth of several tens of metres. The main uranium mineralization consists of a rich wide part in the east (about 800 m long) and a narrower western extension (about 1200 m long) containing both a lower grade and reserve of U. The main exploration, characterization and development activities by the exploration and mining companies have focussed on the rich eastern part of the deposit.

3.1.7 Underground exploration

The activities by the mining company since 1988 include the sinking of a 500-m-deep shaft and the excavation of horizontal drifts at several levels (Figure 3.3) for underground exploration and for testing of potential mining techniques. This excavation and exploration drilling have provided additional information to that obtained from surface drilling, as well as providing closer access to the deposit for direct sampling and measurements.

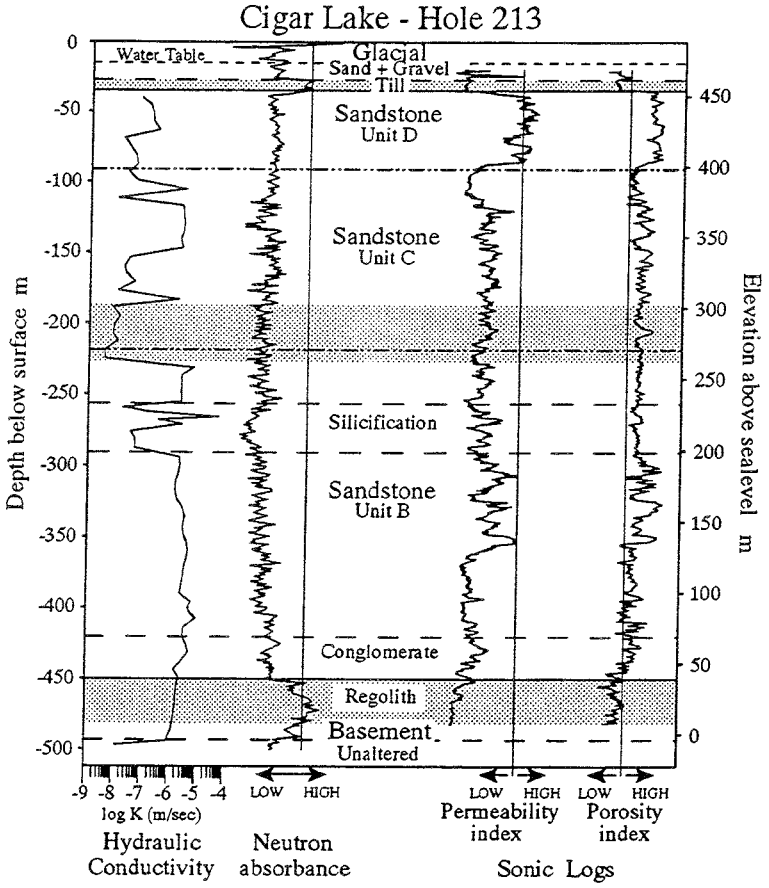

FIGURE 3.5 Vertical profile at shaft Hole 213 showing results of various in-hole measurements.

The information obtained from both drillcore and in-hole measurements in the pilot hole for the shaft (Hole 213, Figure 3.5) correlated well with the lithologic and hydraulic observations obtained during shaft sinking. The shaft has been excavated in essentially unaltered sandstone outside the hydrothermal alteration halo, although locally some of the intersected sandstone showed signs of bleaching. Excavation for the concrete collar of the shaft extended down through the overburden to a depth of 41 m below surface. Subsequent excavation of the shaft through the Upper Sandstone and the upper part of the Lower Sandstone, to a depth of 309 m below surface, did not require grouting of the rock to control inflow of water from the sandstone. The intersection of a steeply north-dipping fracture system, over a distance of about 30 m just below the base of the limonitic sandstone Unit D (MFd), did not produce elevated inflows of water compared with the unfractured sandstone. Grouting was needed to control water inflow from a depth of 309 m down to the unconformity.

No grouting was required for any of the excavations below the unconformity in basement rocks. Although results from hydraulic testing and measurements of the neutron absorbance in Hole 213 suggested both a high hydraulic conductivity and water content for the regolith, shaft excavation encountered essentially dry rock with minimal water inflow. This latter observation corresponds with the information on the permeability and porosity of the regolith as obtained from sonic logging in Hole 213 (Figure 3.5). The elevated water content of the regolith indicated by the neutron absorbance data can be correlated with the relatively high content of clay minerals containing structure-bound water. Further test-mine development in the basement underneath the deposit showed that all the excavated basement rocks had no significant groundwater permeability. In fact, additional hydraulic testing underground confirmed the hydraulic conductivity values for the basement rocks (1 to 5 $x10^{-9}$ m/s) obtained from measurements in boreholes drilled from surface. Maximum water inflows from fractures intersected in the basement excavations measured only several litres per minute, which also suggests an apparent lack of significant hydraulic connection with the overlying sandstone along these fractures.

The basement rocks strike east-west, dip steeply south at 60 to 90°, and constitute a mass that is at least 400 m thick stratigraphically. On the basis of available geological and geophysical data, the basement rock mass is interpreted to be reasonably homogeneous and continuous in the east-west direction and highly variable in the north-south direction. The vertical section in Figure 3.6 shows the observed distribution of major fractures and of the different types of basement and sandstone rocks encountered during excavation and drilling for the test-mine development. A noticeable feature is the funnel-shaped zone of hydrothermally altered basement rock which also overprints the older regolithic alteration immediately underneath the unconformity. This hydrothermal alteration is characterized by a weakening of the rock strength through shearing and foliation dominated by clay-mineral development. Within this formation, many discreet, steeply-dipping, conformable zones of highly altered rock exist within less altered rock. Many of these are weakly mineralized with uranium, arsenides and sulphides, and they are interpreted to be fault zones that may have acted as pathways for ascending, chemically reducing fluids. Some of these mineralized zones are known to extend down to at least 50 m below the deposit.

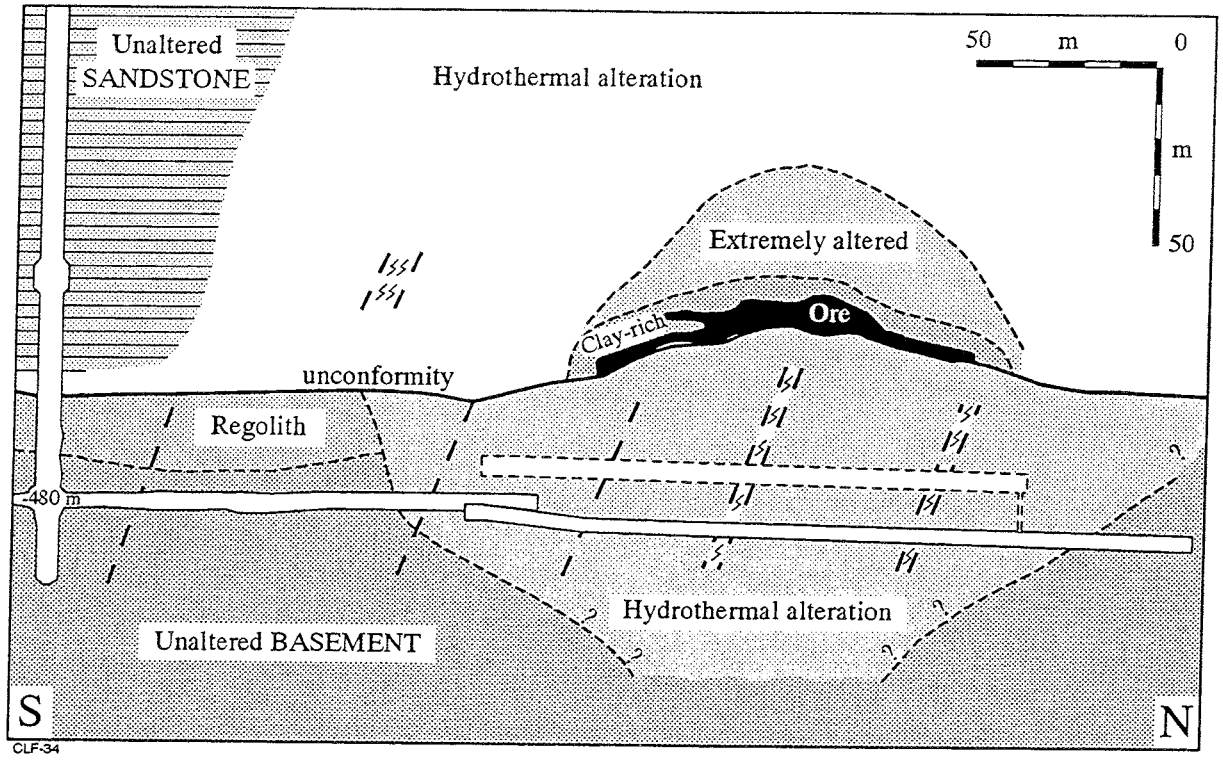

FIGURE 3.6 Schematic geological section (10750E) through the Cigar Lake deposit showing the different rock types and major fractures (heavy dashed lines) encountered during excavation and drilling.

3.1.8 References

BRUNETON, P. 1987. Geology of the Cigar Lake uranium deposit (Saskatchewan, Canada). In *Economic Minerals of Saskatchewan* (ed. C.F. Gilboy and L.W. Vigrass). Sask. Geol. Soc. Spec. Publ., **8**, 99-119.

BRUNETON, P. 1993. Geological environment of the Cigar Lake uranium deposit. Can. J. Earth Sci., **30**, 653-673.

CUMMING, G.L. and KRSTIC, D. 1992. The age of unconformity-related uranium mineralization in the Athabasca Basin, northern Saskatchewan. Can. J. Earth Sci., **29**, 1623-1639.

FOUQUES, J.P., FOWLER, M., KNIPPING, H.D. and SCHIMANN, K. 1986. The Cigar Lake uranium deposit: Discovery and general characteristics. In *Uranium deposits of Canada* (ed. E.L. Evans). Can. Inst. Min. Metall. Spec. Vol., **33**, 218-229.

GEDDES R.S. 1982. The Vixen Lake indicator train northern Saskatchewan. In *Propecting in areas of glaciated terrain - 1982* (ed. P.H. DAVENPORT). Can. Inst. Min. Metall. Publ., 264-283.

HOEVE, J. and QUIRT, D. 1984. Mineralization and host rock alteration in relation to clay mineral diagenesis and evolution of the Middle-Proterozoic, Athabasca Basin, northern Saskatchewan, Canada. Sask. Res. Council Tech. Rep., **187**, 187p.

RAMAEKERS, P. 1981. Hudsonian and Helikian basins of the Athabasca Region, northern Saskatchewan. In *Proterozoic Basins of Canada* (ed. F.H.A. CAMPBELL). Geol. Surv. Can. Pap., **81-10**, 219-233.

SCHREINER B.T. 1983. Quaternary geology of the NEA/IAEA Athabasca test area. In *Uranium exploration in Athabasca Basin, Sasktachewan, Canada* (ed. E.M. CAMERON). Geol. Surv. Can. Pap., **82-11**, 27-32.

SIBBALD, T.I.I., QUIRT, D.H. and GRACIE, A.J. 1990. Uranium deposits of the Athabasca Basin, Saskatchewan. Geol. Surv. Can. Open File, **2166**, 56p.

3.2 MINERALOGY AND LITHOGEOCHEMISTRY

3.2.1 Introduction
(J. Cramer)

The Cigar Lake deposit is unique among the unconformity-related deposits in the Athabasca Basin because of its location inside a fairly symmetrical stratigraphic arrangement of hydrothermally altered host rocks. This halo of altered host rocks is not only an important exploration feature: its preservation provides an opportunity to study the effects of long-term water-rock interaction on the primary and secondary dispersion halos of trace elements in these rocks. In addition, the study of the composition, distribution and trace-element fixation properties of the different clay minerals throughout the whole deposit is important in understanding the evolution of hydrologic flowpaths, water-rock interaction and radionuclide migration.

A number of initial observations indicated that much of the current mineral and trace-element distributions in the host rocks originated from the hydrothermal event associated with the ore deposition. Extensive work by the exploration company (COGEMA) was carried out to study the distribution patterns of major and trace elements in the sandstones overlying the deposit. This information and that reported by Clark (1987) was used to obtain a 3-dimensional picture of the distribution of uranium, thorium and lead in the overlying sandstones. The resulting distribution patterns in the top of the sandstone bedrock, occurring >350 m vertically above the mineralization, show a good correlation between the abundance of these elements and the outline of the uranium mineralization. Such patterns indicate that at least the distribution of uranium is predominantly of primary origin, because these patterns vertically transect the horizontal lithological and hydrological stratigraphies, and their abundances of thorium and lead correlate with a radiogenic origin from decay of the corresponding uranium.

To further investigate these preliminary conclusions, two studies were undertaken. One study was aimed at establishing the mechanism of fixation of uranium in the host rocks, in particular uranium associated with the clay minerals, and the other to evaluate evidence for more recent migration of uranium and its daughter radionuclides. The first study, initiated prior to the start of the AECL/SKB collaboration in 1989, included a detailed study on the clay mineralogy and geochemistry, and on the uranium fixation mechanisms by means of selective extraction techniques. This work constituted the Ph.D. study of Jeanne Percival at Carleton University in Ottawa, which was funded by AECL and completed at the end of 1989. The second study, undertaken as part of the AECL/SKB collaboration, involved the measurement of activity ratios for isotopes from the uranium and thorium decay series in core samples from selected locations in the deposit.

The results of the first study have been reported in a number of publications (Percival, 1990; Percival and Kodama, 1989; Percival et al., 1990, 1993), whereas Section 3.2.3 of this report gives results of the ongoing work on uranium fixation mechanisms and their occurrence in different geological systems. The results of the second study are reported in

Section 3.2.2. The observed correlation between the fixation of dissolved uranium and various iron-mineral phases, as well as the importance of some of these latter phases in the redox geochemistry at Cigar Lake, led to the review of the thermodynamic data for the Fe-O-C-S-H system, as reported in Section 3.2.4.

References

CLARK, L.A. 1987. Near-surface lithogeochemical halo as an aid to discovery of deeply buried unconformity-type uranium deposits, Athabasca Basin, Canada. J. Geochem. Explor., **28**, 71-84.

PERCIVAL, J.B. 1990. Clay mineralogy, geochemistry and partitioning of uranium within the alteration halo of the Cigar Lake uranium deposit, Saskatchewan, Canada. Carleton University, Ottawa, Canada, Ph.D. Thesis, 343p.

PERCIVAL, J.B. and KODAMA, H. 1989. Sudoite from Cigar Lake, Saskatchewan. Can. Mineral. **27**, 633-641.

PERCIVAL, J.B., TORRANCE, J.K. and BELL, K. 1990. On the development of a sequential extraction procedure with application to leachability problems. In *Acid Mine Drainage Designing for Closure* (ed. J.W. Gadsby, J.A. Malick and S.J. Day). BiTech Publishers Ltd., Vancouver, 51-62.

PERCIVAL, J.B., TORRANCE, J.K. and BELL, K. 1993. Clay mineralogy and isotope geochemistry of the alteration halo at the Cigar Lake uranium deposit. Can. J. Earth Sci., **30**, 689-704.

3.2.2 Geochemical and isotopic features of the host sandstones and clay halo
(J. Smellie, J. Cramer and A. MacKenzie)

3.2.2.1 Introduction

One of the key questions surrounding interpretation of the Cigar Lake rock geochemistry is whether observed trace-element variations in the sandstones around the ore body reflect primary hydrothermal or younger secondary patterns. They may be associated with the ore formation (dated to around 1.3 Ga), or younger secondary remobilization (in the range of 200-300 Ma ago), as indicated by the perched uranium occurrences along fracture paths emanating from the ore body. Alternatively, these variations may have resulted from recent low-temperature mobilization and redistribution processes, i.e., within the last million years or so. Clarifying these issues has an important bearing on several of the repository performance assessment (PA) modelling exercises as defined by the Cigar Lake analog study, for example, the potential application of coupled chemical/transport modelling of radionuclide migration (or other trace elements) to the hydrogeochemical system. If the lithogeochemical patterns are hydrothermal in origin, then the system is, and has been, relatively closed since ore emplacement, and therefore no major groundwater mobilization or transportation of chemical species is presently occurring at ambient temperatures. Additionally, if the red iron oxide-rich zone located marginally to the massive uranium ore in the clay horizon is associated with radiolysis, small-scale evidence of recent uranium mobilization should also be measureable.

Most evidence to date suggests that the system has remained largely closed since hydrothermal activity associated with ore emplacement ceased. However, there is evidence of younger, secondary "perched mineralizations", observed within older fractures that radiate outwards from the ore body; in these cases remobilized uranium has in some instances extended to 150 m above the ore body (Bruneton, 1987). Furthermore, variable uranium distributions in the highly altered zone of the Lower Sandstone formation suggest that some uranium may have been removed from the more permeable stratigraphic horizons above the level of the ore body.

There are also indications of variations in uranium content within the clay-rich zone surrounding the uranium ore, apparently in association with disseminated Fe-oxyhydroxides. As to whether these distributions are the result of hydrothermal, or more recent secondary processes at low temperature, is still uncertain.

Three main objectives guided the sample selection for this study:

a- to study the geochemical behaviour of uranium and its daughter nuclides within recent time scales (< 1 Ma),
b- to provide support for some of the hydrogeochemical concepts, and
c- to provide data that could be integrated with PA-related modelling objectives.

Measurements of uranium-decay series isotopes in whole-rock samples were carried out on rock profiles extending from the clay/ore interface to the sandstone bedrock surface to

investigate whether recent (≤ 1 Ma) mobilization has taken place. Disequilibria within the decay series can result from water-rock interaction processes; secular equilibria on the other hand suggests a closed system. These data have been complemented by whole-rock major-element and selected trace-element analyses, including Mössbauer analysis to assess the degree of oxidation using the Fe_{III}/Fe_T ratio.

3.2.2.2 General geological background

The Cigar Lake uranium deposit is hosted by the Manitou Falls Formation, and is described in detail by Fouques et al. (1986) and Bruneton (1987). This formation generally consists of a monotonous sequence of red, fine- to coarse-grained hematitic sandstones, somewhat conglomeratic, varying from well- to poorly-sorted and becoming progressively finer grained towards the top of the sequence. Accessory minerals tend to be either dispersed or concentrated in thin bands that increase towards the bottom of the sequence. In addition to this increase in accessory minerals, which is reflected in an increase in the trace-element content (e.g., REEs, Th and U), there is also some enrichment of illite and chlorite in the basal 10 to 20 m. Although this may also be a stratigraphic feature, it appears more likely to be the result of diagenesis under conditions of a significant geochemical gradient between the MgO- and K_2O-rich basement and the MgO- and K_2O-poor sandstones.

Hydrothermal emplacement of the uranium deposit was accompanied by extensive alteration of the sandstones. This hydrothermal alteration, characterized by reducing conditions, resulted in bleaching the sandstone and producing a ferrous iron mineralogy. Alteration extends down into the basement rocks underlying the deposit to a depth of about 100 m, and up into the sandstones to about 300 m. At the bedrock surface (i.e., glacial overburden-sandstone contact), the hydrothermal signature is most obvious as enhancements of uranium (>2 ppm) and the presence of illite. From the bedrock surface to depths of around 100 m, the bleached sandstones (and the more regionally unaltered sandstones) have been subsequently subjected to a recent, surface-derived, low-temperature alteration producing limonite.

Closer to the deposit the sandstones are grey in colour because of the microdissemination of Fe-sulphides (pyrite, marcasite $\pm$ hydrocarbons). At greater depths, a grey quartz zone is encountered, which resulted from the precipitation and overgrowth of quartz, mostly as fracture fillings. Below this zone the sandstones become increasingly altered due to the dissolution of silica and illitization processes. Illite also occurs as a matrix mineral in the sandstones, in addition to being a major fracture-filling component. Closer to the ore deposit, the clay content (dominantly illite) increases progressively (up to 30 vol.% of the rock) and the sandstones become increasingly more friable, locally producing unconsolidated layers and pockets. This altered sandstone zone finally grades into the massive clay that surrounds the ore body.

Alteration of the sandstones above the ore body, and the formation of the quartz cap, have been greatly facilitated by an extensive system of vertical and sub-vertical faults that extend upwards from the basement through the deposit. Most of these faults have been produced prior to the mineralization process.

The massive clay zone (locally up to 12 m thick), in contact with and surrounding the ore body, can be subdivided into an outer white bleached zone and a narrow inner red ferric-rich zone (in reality a combination of hematite and Fe-oxyhydroxides). It is almost entirely composed of clay minerals with rare quartz remnants (both altered and more competent varieties). In addition to the massive clay zone being commonly ferric-rich, siderite is locally abundant either as aggregates of euhedral crystals or as irregular layers and veins. The clay is generally weakly mineralized (0.01 to 1.0 wt.% U), but local concentrations of up to several percent U are present.

The red ferric-rich massive clay occurs along the clay/ore interface and generally indicates a total Fe content (measured as Fe_2O_3) of greater than 4 wt.%. This iron oxide enrichment is mostly pervasive, and the transition to the white bleached clay is gradational and outwards from the ore body. Occasionally, enrichments are concentrated along and marginal to some fractures, which may suggest conducting pathways through the clay. The bleached clay (<4 wt.% Fe_2O_3) forms the bulk of the massive clay zone.

The massive ore zone has sharp contacts with the clay zone above and the highly argillized basement below. The outstanding feature of the zone is the uranium content, which may exceed 40 wt.% U over several metres. The massive uraninite/pitchblende is brecciated and associated with sulphides and arseno-sulphides. The zone is heterogeneous, with portions of the massive, competent high-grade ores sharply grading into lower grade ores and intermixed with dark grey to green clay-rich lenses and horizons. Enrichments of iron oxides tend to be limited to faults and fractures.

3.2.2.3 Sampling

Drillcore samples were selected from existing exploration and underground drilling materials. All samples collected represent profiles or specific horizons located within the zone of hydrothermal alteration. The heterogeneity of the sandstone sequence, particularly in the vicinity of the ore body, was taken into account (i.e., sandstone, sandy clay, clayey sandstone and clay horizons); when samples of the clay horizon were selected, special emphasis was put on the red iron oxide layers and on locating potentially conducting fractures or more porous zones. These were often, but not always, lined or impregnated with iron oxides. The material sampled is described in detail below.

Drillcore 44A

Borehole 44A, located within the eastern part of the mineralization (along fence 7+50E), intersects the massive ore at around 422 m depth. The clay-rich layer extends from 410 to 420 m and is typically heterogeneous, consisting of alternations of clay and sandy horizons in the upper transition part and clay and ore in the lower transition part. The samples selected (Figure 3.7) represent splits of rock sections mineralogically and geochemically described earlier by Percival (1990). The samples generally represent the transition from the altered sandstone to the bleached clay, including the iron oxide-rich horizon in the clay layer adjacent to the ore body. Some of the clay bands may either be clay-rich layers or,

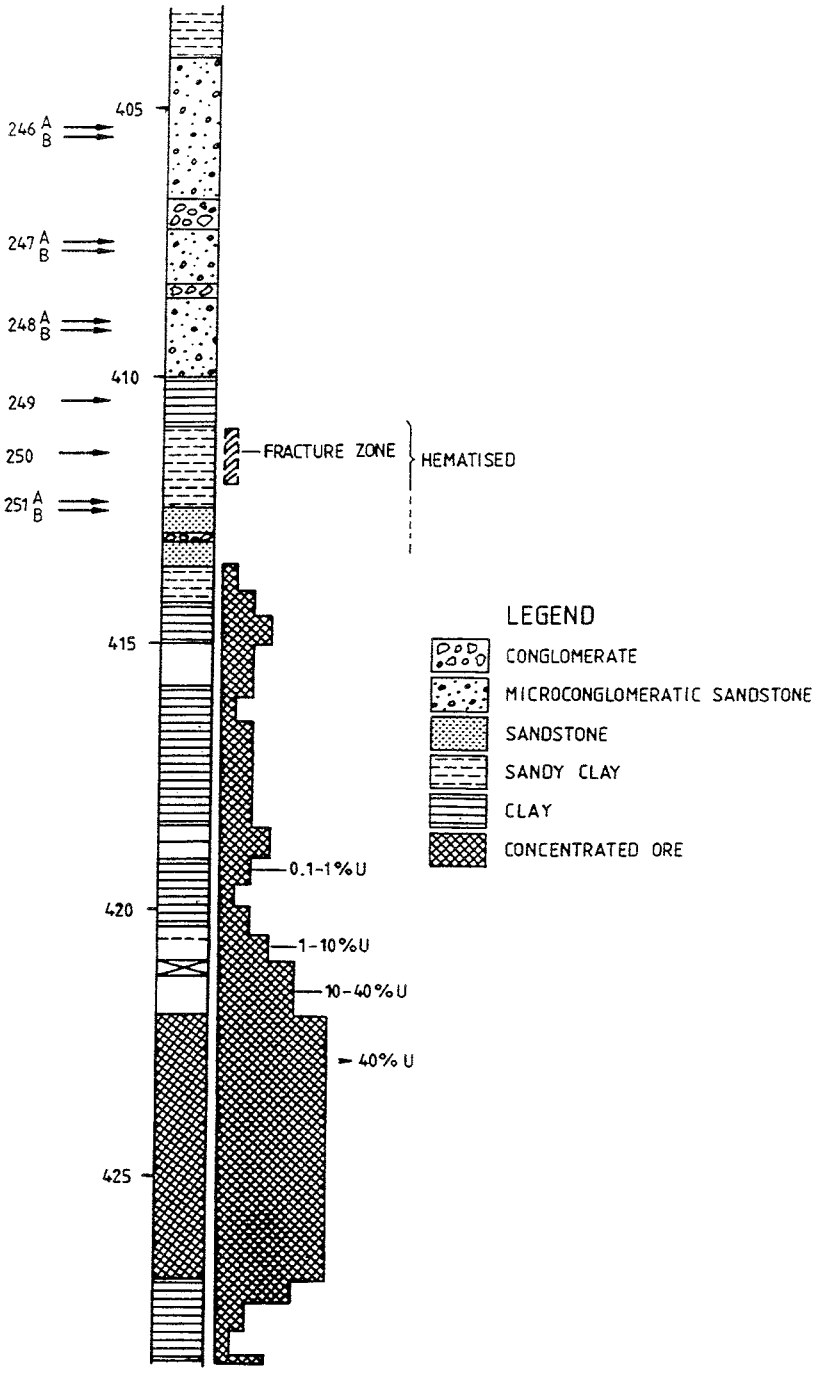

FIGURE 3.7 Geological log of drillcore 44A showing the transition from massive ore, through the clay layer and out into the altered sandstone sequence. Alongside the core is shown: a) a graphical illustration of the uranium contents, b) the location of an open ferric-rich fracture, c) the position of the ferric-rich zone, and d) the positions of the samples studied, i.e. those nearest to the clay/ore interface.

equally likely, represent intersections with clay-infilled fractures that accompanied hydrothermal activity. The red iron oxide zone extends for some 3 m from the ore body contact and affects sandstone, sandy clay and clay layers alike. Located within the sandy clay layer is a more strongly iron-rich zone identified as a probable "open" fracture. In comparison with the profile as a whole, this fracture zone was considered to represent the most likely point where any migration of radionuclides in solution would pass, either to or from the ore body.

Drillcore 196

Borehole 196 is also located in the eastern sector of the mineralization (along fence 7+75E) and forms a part of the cross-section illustrated in Figure 3.8. The sampled profile is in the Lower Sandstone formation and extends from 270 m down to the clay/sandstone interface at 390 m depth. This area of sampled sandstone was chosen because it represents, as determined from the uranium distribution plot (Figure 3.8), a region of uranium "depletion", which may or may not reflect active uranium removal by groundwater. Drillcore material consisting of both sandstone and sandy clay varieties were collected.

Drillcore 76

Borehole 76 lies north of hole 196 and forms part of the same cross-section (Figure 3.8); it traverses a perched fracture mineralization at 270 m. In order to test for evidence of recent groundwater movement associated with uranium remobilization along these established pathways, samples were selected to represent a profile extending from the mineralized fracture out into the adjacent sandstone. This profile was also used to establish the extent of matrix radionuclide diffusion into the sandstone from the fracture.

Drillcore FH-18

Borehole FH-18 (one of the underground freeze holes) extends from the gallery below the ore body up through the ore itself and includes some of the surrounding clay horizon above the ore. This provided an excellent opportunity to study a new profile through the ferric-rich and bleached clay horizons. In particular, the larger core diameter (6 cm) allowed samples to be removed that had not been in contact with the drilling water. This ensured, for example, that any measured isotopic disequilibrium was real, thus excluding the possibility of uranium removal by water flushing during drilling. Furthermore, the core contained several fracture zones, some characterized by Fe-oxyhydroxides, which were thought to represent groundwater flow paths through the otherwise quite impermeable clay. Details of the location of the clay zone samples selected for analysis are shown in Figure 3.9.

Miscellaneous

An additional four samples from drillcore 76 were selected from different parts of the Cigar Lake deposit to check for recent uranium remobilization. Two samples (CS500, CS501; Figure 3.8) were taken from the limonitic sandstones, one sample (CS537) from just above the clay/ore interface in the iron oxide zone, and one sample from the basement clay underlying the ore body (CS540). A further core sample from drillhole 113 (CS313) was selected from a metre-thick zone of bleached clay just above the ore zone at 408.3 m depth.

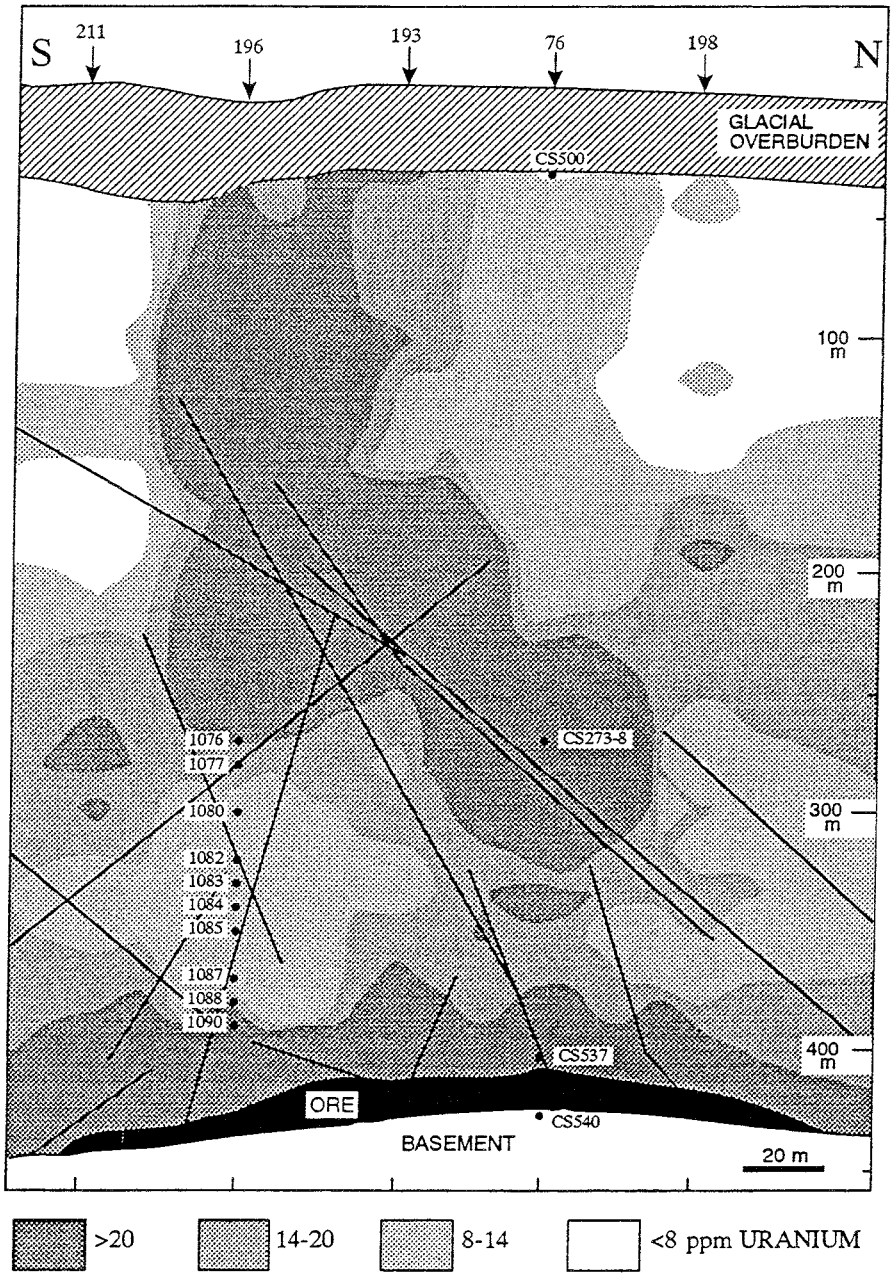

FIGURE 3.8 Section through the main ore body (Fence 7+75E) showing the distribution of uranium in the sandstone host rock above the mineralization and the distribution of major fractures. Note the position of borehole 196, the area of uranium "depletion" (8-14 ppm) above the ore body and the location of the Lower Sandstone samples. Also shown are the sample locations for the perched mineralization (CS273-8), for the limonite zone (CS500) and for the upper and lower contacts of the ore zone (CS537 and CS540).

3.2.2.4 Sample preparation and analysis

Samples from drillcores 44A, 196 and 76 were initially sectioned for microscopy and the remaining material was then milled to powders; various splits were analysed using different methods and procedures. Whole-rock X-ray fluorescense (XRF) analyses of the major and minor elements were available from earlier studies by J. Cramer (AECL), and stable isotope determinations on some samples, using the clay separate (<2 μm) fractions, are reported by Percival (1990). In these whole-rock studies U was analysed by direct neutron counting (DNC) and Th by instrumental neutron activation analysis (INAA). For this present study, whole-rock powdered splits were analysed for the uranium- decay series using established radiometric methods, i.e., α-spectrometry for U and Th and direct gamma counting for Ra. Using gamma spectroscopy to determine ^{226}Ra is not the best method available, and there is some doubt about accepting radium concentrations at face value; interpretation was therefore restricted to the major trends indicated and to the $^{226}Ra/^{230}Th$ activity ratios. Powdered splits were also analysed by Mössbauer spectroscopy to determine the Fe_{III} and Fe_{II} contents and hence the Fe_{III}/Fe_T oxidation ratio.

3.2.2.5 Results and discussion

The analytical results are tabulated in Tables 3.1 to 3.3 and illustrated in Figures 3.10 to 3.18.

3.2.2.5.1 General geochemistry and mineralogy

The variation in rock type (i.e., clay, sandstone, clayey sandstone etc.) is readily observed in the major- and trace-element geochemistry along drillcore 44A (Table 3.1; Figures 3.7 and 3.10). In general the clay samples predictably have less SiO_2 but more Al_2O_3, Fe_2O_3 and K_2O; minor increases in TiO_2 are also common. All the trace elements, including U and Th, show increased contents in association with the clay. These chemical trends are well established in the near-vicinity of the uranium mineralization and are common to many of the unconformity-type deposits in the Athabasca Basin (Cramer, 1986). These trends reflect the hydrothermal alteration of the sandstone, which has resulted in the dissolution and removal of quartz, accompanied by the formation of clay (mostly illite) and a residual concentration of accessory Zr-, Ti-, Th- and REE- bearing minerals.

Distinctive geochemical alteration trends are also locally apparent marginal to radiating fracture zones that channelled and dispersed younger, lower temperature solutions up and through the sandstones surrounding the main ore deposit. Figure 3.11 illustrates a profile selected through one of these fracture zones from drillcore 76. The chemical trends indicate the extent of the alteration, in general 1-2 cm from the fracture edge. Only the decrease in Al_2O_3, K_2O and Sr is anomalous compared with the major patterns.

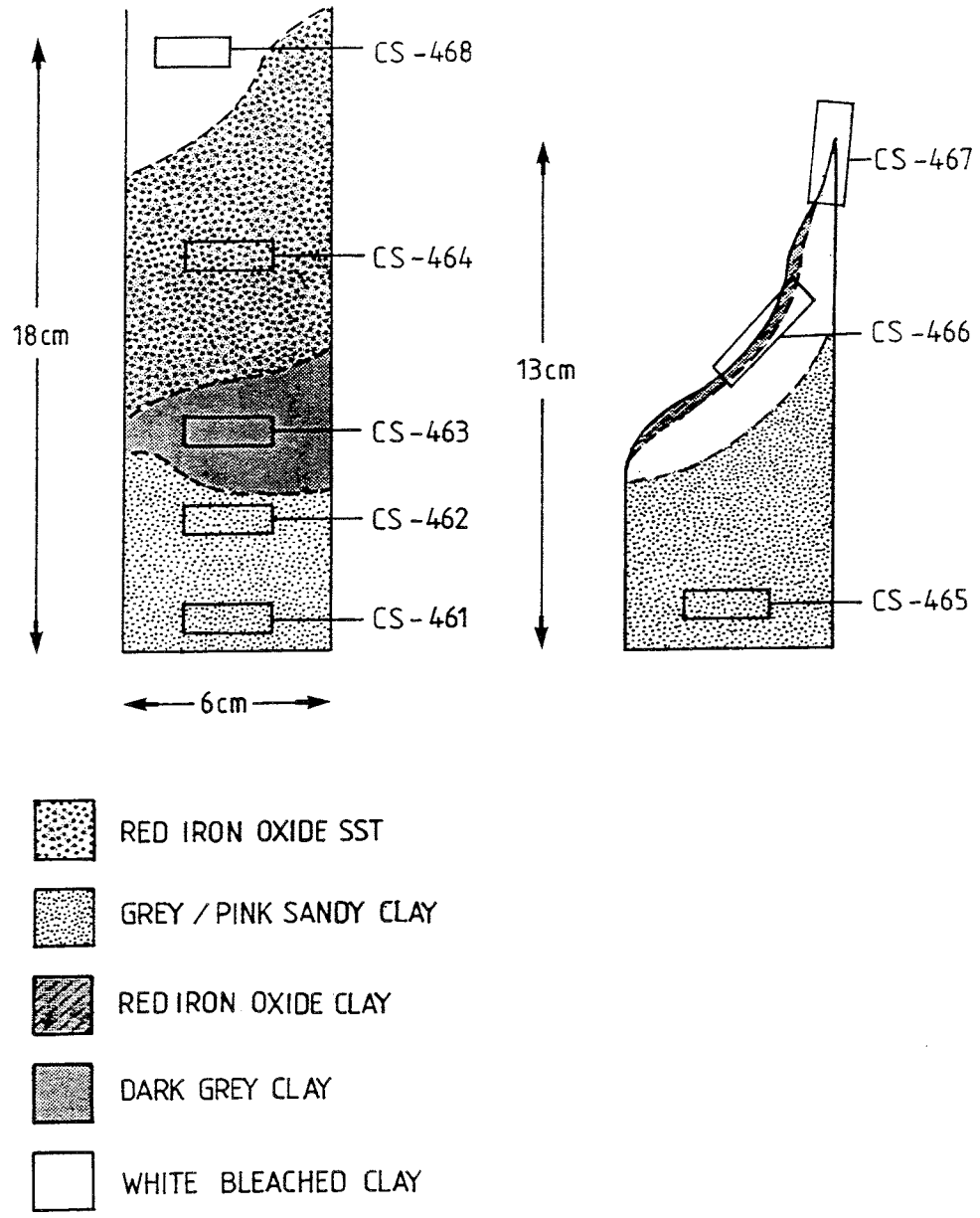

FIGURE 3.9 Sample locations of massive clay and fracture material from drillcore FH-18.

3.2.2.5.2 Distribution of iron

The total iron contents (Table 3.1) of those samples located further than 2.5 m from the orebody are very low (mostly within the range of 0.08-0.52 wt.%), even in the clay-rich sandstones. It is only when the ferric-rich zone is approached (samples CS 250/251) that the iron contents increase significantly (from 4.38 to 30.50 wt.%). Although this is most apparent for the clay samples, the sandstone nearest the orebody (CS251A) also contains appreciable amounts of iron (10.10 wt.%).

TABLE 3.1
WHOLE-ROCK MAJOR AND TRACE ELEMENT ANALYSES FROM DRILLCORE 44A
(See Figure 3.7 for some of the sample locations)

Sample CS-		240	241	242	243	244	245	246A*	246B	247A	247B	248A	248B	249	250	251A	251B
SiO_2	wt%	95.00	93.70	86.30	94.00	87.30	59.90	88.80	86.00	93.30	59.70	92.90	66.10	43.40	34.60	81.50	29.50
TiO_2		0.12	0.15	0.36	0.08	0.65	1.50	0.13	0.32	0.36	1.42	0.24	0.69	1.33	0.60	0.06	0.59
Al_2O_3		2.33	2.77	7.93	2.58	6.33	24.50	5.99	7.96	3.21	24.00	3.71	20.60	32.40	25.10	1.97	20.40
Fe_2O_3		0.10	0.10	0.24	0.08	0.20	0.45	0.15	0.28	0.21	1.32	0.09	0.52	4.38	21.50	10.10	30.50
MnO		<0.01	<0.01	<0.01	<0.01	<0.01	0.01	<0.01	<0.01	<0.01	<0.01	<0.01	<0.01	0.03	0.08	0.04	0.11
MgO		0.12	0.14	0.24	0.09	0.21	0.76	0.17	0.27	0.09	0.70	0.09	0.62	1.01	1.07	0.33	1.18
CaO		0.01	0.01	0.02	0.01	0.03	0.07	0.01	0.03	0.02	0.06	0.01	0.06	0.12	0.26	0.11	0.26
Na_2O		0.31	0.22	0.26	0.20	0.26	0.32	0.28	0.28	0.24	0.31	0.23	0.27	0.27	0.03	0.20	0.26
K_2O		0.62	0.72	2.18	0.71	1.80	7.19	1.72	2.25	0.88	6.88	1.04	5.97	9.42	7.49	0.54	6.35
P_2O_5		0.04	0.04	0.11	0.04	0.11	0.23	0.04	0.09	0.05	0.18	0.05	0.15	0.30	0.22	0.03	0.18
LOI		0.85	0.85	1.85	0.47	1.62	4.23	1.23	1.85	0.93	5.16	0.77	4.08	7.23	9.23	4.62	10.90
Cr	ppm	<10.0	<10.0	<10.0	4.3	13.0	58.2	6.6	20.9	9.4	50.3	6.4	49.7	53.7	47.9	4.0	51.5
Rb		20	20	30	<10	40	80	30	70	30	80	10	60	90	70	30	60
Sr		140	120	530	110	520	1130	130	420	200	890	180	710	1680	720	50	460
Y		10	30	110	10	60	180	<10	10	20	80	10	30	30	10	<10	<10
Zr		140	300	610	70	1020	2740	130	390	420	1810	260	840	1910	1180	60	920
Nb		<10	20	30	20	20	50	<10	10	<10	20	<10	10	20	40	10	30
Hf		3.7	8.2	16.0	2.6	28.8	74.3	4.1	11.5	10.9	50.7	7.6	26.0	52.8	27.8	2.1	24.5
Ta		5.2	2.5	2.3	2.1	3.6	5.0	1.4	2.2	3.0	4.7	3.1	3.4	4.0	2.4	1.0	2.7
Sc		0.7	0.9	1.9	0.5	2.8	9.4	1.1	2.6	1.2	9.2	1.4	6.7	10.3	7.0	0.6	6.3
Co		102.7	34.6	28.8	35.1	31.4	32.4	25.0	30.7	35.9	36.9	46.5	27.3	19.9	10.4	18.5	8.9
Cs		n.d**	0.2	0.5	n.d	0.7	0.9	n.d	0.8	n.d	1.3	0.3	0.6	0.4	0.2	0.2	0.5
U		4.4	9.4	10.3	5.7	31.1	100.7	8.6	128.7	136.5	220.0	39.2	141.7	198.2	79.8	72.9	99.8
Th		6.1	7.3	17.6	4.5	87.2	124.7	6.0	25.3	34.5	113.8	30.2	79.5	140.8	79.9	4.2	70.8
La		20.1	17.6	69.8	19.5	64.6	164.6	22.1	67.1	32.9	133.1	29.6	110.9	187.4	168.6	10.9	152.3
Ce		37.9	26.6	131.1	39.3	128.6	332.2	44.0	132.4	50.4	252.5	54.9	224.7	369.0	337.2	1.6	306.9
Nd		10.8	9.7	37.4	14.5	56.8	144.2	18.5	n.d	22.6	n.d	22.8	n.d	150.7	n.d	n.d	n.d
Sm		1.6	1.8	11.9	2.8	12.0	33.0	3.5	24.2	20.6	42.1	7.9	33.3	48.2	30.1	10.7	31.5
Eu		0.4	0.3	1.2	0.3	1.0	2.5	0.4	1.1	0.4	1.9	0.4	1.4	3.0	2.2	0.2	1.9
Tb		0.5	0.5	2.0	1.0	0.8	3.3	0.1	0.6	0.2	1.7	0.1	n.d	1.5	n.d	n.d	n.d
Yb		0.4	0.6	0.6	0.5	n.d	n.d	0.4	1.6	0.8	n.d	0.9	2.0	4.9	n.d	0.3	3.7
Lu		n.d	n.d	0.3	n.d	0.4	1.4	n.d	n.d	n.d	0.6	n.d	n.d	0.7	n.d	n.d	n.d

* "A" sample represents sandstone fraction; "B" sample represents clay-rich fraction.

** n.d= not detected.

Apart from minor amounts associated with accessory minerals and interstitial iron minerals in the bleached, non-mineralized samples, most of the iron near the orebody is in the form of dispersed hematite and Fe-oxyhydroxides, resulting in a characteristically red colouration. The concentration of these phases is, for the most part, fairly heterogeneously distributed. In places it is most marked in and adjacent to identified fracture and more porous zones; contrastingly it can also occur in the more massive, impermeable, bleached clay layers. Some iron is also bound up in silicate phases (e.g., chlorite) and siderite.

The Mössbauer data (Table 3.2) for drillcore 44A (plus one sample from drillcore 113) show oxidation ratios varying from 0.17 to 0.94 (a ratio of unity indicates that all the iron is in the ferric state). Greater oxidation is therefore indicated for the two samples furthest from the orebody (CS245 and 246B). In contrast, the least oxidized sample (CS251A; Fe_{III}/Fe_T = 0.17) also happens to be from the sandstone nearest the orebody (also in the near-vicinity of the fracture zone), which would be expected to be more porous than the oxidized clay samples (e.g., CS250 and 251B at 0.67 and 0.54, respectively) taken from either side of the sandstone. However, because the data refer to bulk sample analyses, rather than mineral fraction separates, it is still not clear how much of the Fe_{II} and Fe_{III} is bound up in discrete mineral phases, compared with how much may be introduced into the rock by oxidation processes, whether through early hydrothermal alteration or later processes.

3.2.2.5.3 Distribution of uranium and thorium

Uranium and thorium in drillcores 44A and 113 have been analysed using two different methods, DNC and α-spectroscopy (Table 3.2). There is a good general correlation for the uranium data, but thorium values between the two methods are in some cases highly variable; in these cases the α-spectrometry values are preferred. The distribution of U and Th along the drillcore 44A profile is illustrated in Figure 3.10.

The clay samples generally contain higher concentrations of uranium and thorium than adjacent clay-rich sandstones and less- or unaltered sandstones. This is attributable primarily to the fact that the clays are a direct result of hydrothermal processes and therefore have been in contact with mineralizing solutions. Furthermore, because clays are known to be efficient scavengers of trace elements, so later absorption of uranium cannot be ruled out. The samples farthest from the orebody (CS-244 to 240) contain low amounts of U and Th (4.4-30.0 ppm and 2.6-83.0 ppm respectively); this may in part be a function of distance, but more realistically it probably reflects different rock types and mineralogy (samples are mostly clay-rich sandstone rather than clays). Towards the orebody (CS-244 to 251B) both the U and Th contents and the proportion of clay in the samples increase (76.9-220.0 ppm U and 30.5-150.5 ppm Th); the clay-rich sandstones and sandstones continue to exhibit low values (e.g., CS246A, 248A), although CS246B and 247A have significantly higher U contents. In conclusion, some of the uranium contents of the samples, and almost all of the thorium contents, reflect variations of accessory mineral phases. Most of the uranium, on the other hand, occurs as discrete uranium phases (uraninite/pitchblende) and as surface coatings absorbed on clays (or even bound up in the crystal lattices; see Percival, 1990) and/or Fe-oxyhydroxide phases.

TABLE 3.2
URANIUM-DECAY SERIES AND MÖSSBAUER MEASUREMENTS FOR DRILLCORE 44A FROM CIGAR LAKE

Sample CS-	Rock type*	Depth m	U ppm	Th ppm	$^{234}U/^{238}U$	$^{230}Th/^{234}U$	$^{226}Ra/^{230}Th$	Fe^{3+}/Fe_T **
240	S/C	385.6	a 7.5	6.8	0.98±0.01	1.00±0.005	1.22±0.07	ne
			b 4.4	6.1				
241	S/C	389.6	12.1	9.3	0.92±0.01	1.05±0.04	1.00±0.04	ne
			9.5	7.3				
242	S/C	393.2	16.4	2.6	0.96±0.01	1.09±0.04	1.60±0.08	ne
			10.3	17.6				
243	S/C	396.5	5.1	7.4	1.21±0.05	1.05±0.05	1.17±0.06	ne
			5.8	4.5				
244	S/C	400.5	29.9	82.3	1.00±0.01	0.97±0.05	1.31±0.07	ne
			31.1	87.2				
245	C	402.6	99.7	143.3	1.00±0.01	1.04±0.04	0.96±0.05	0.81
			100.7	124.7				
246A	S	405.3	8.6	7.2	0.92±0.03	1.09±0.05		ne
			8.6	6.0				
246B	S/C	405.3	116.9	30.5	0.96±0.01	1.11±0.04	0.28±0.01	0.94
			128.7	25.3				
247A	S	407.5	140.7	42.5	0.81±0.03	1.32±0.04		ne
			136.5	34.5				
247B	C	407.5	211.2	131	0.98±0.01	1.05±0.03	1.54±0.06	1.00
			220.0	113.8				
248A	S	409.2	38.6	29	1.07±0.01	0.99±0.03	1.24±0.06	ne
			39.5	30				
248B	C	409.2	144.9	101.3	0.83±0.01	1.08±0.05	2.45±0.10	0.54
			142	79.5				
313	C	408.3	179.3	150.5	0.90±0.01	1.04±0.04	1.06±0.05	ne
			152	49				
249	C	410.6	183.2	137	0.86±0.02	1.19±0.04		0.15
			198.2	141				
250	C_H	411.7	76.9	104	0.96±0.03	1.12±0.04		0.67
			79.8	80				
251A	S_H	412.5	-					0.17
			72.9					
251B	C_H	412.4	91.7	74	1.02±0.03	0.92±0.03		0.54
			99.8	71				

* C= Clay; S= Sandstone; S/C= Clay-rich Sandstone; C_H, S_H= Ferric-rich.
** Fe by Mössbauer analysis; ne= no estimate possible due to low iron content
a U and Th by α-Spectrometry; Ra by direct γ-Counting.
b U by Delayed n-Counting; Th by Instrumental Neutron Activation.

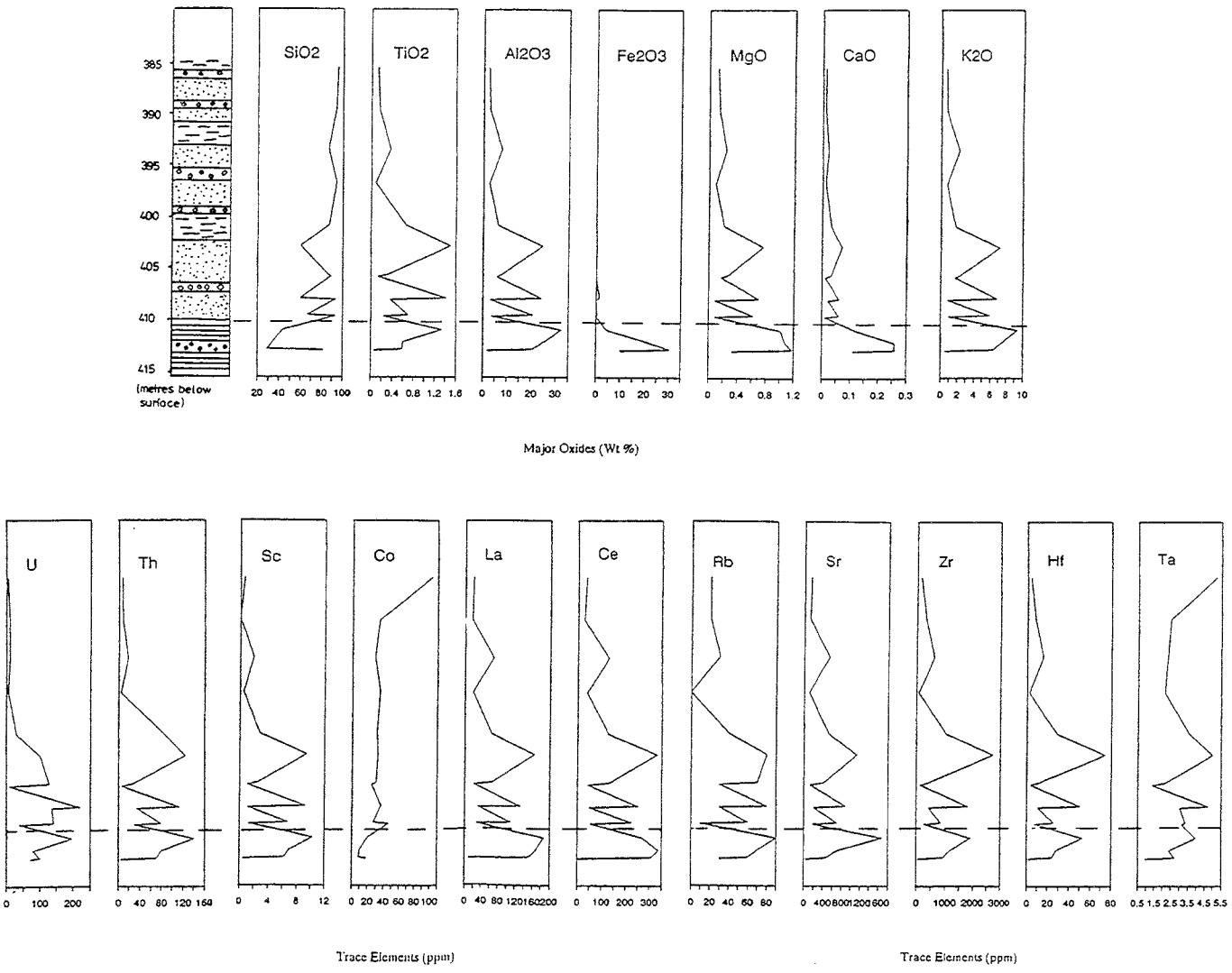

FIGURE 3.10 Whole-rock, major- and trace-element geochemical profiles along drillcore 44A (XRF data from Table 3.1; see also Figure 3.7).

Increases in U and Th are also indicated at hydrothermally altered fracture margins (Figure 3.11). Although the major part of the uranium discussed is hydrothermal in origin, some of the more minor uranium distributions measured may also be the result of remobilization due to recent groundwater-rock interaction; this is discussed in more detail below.

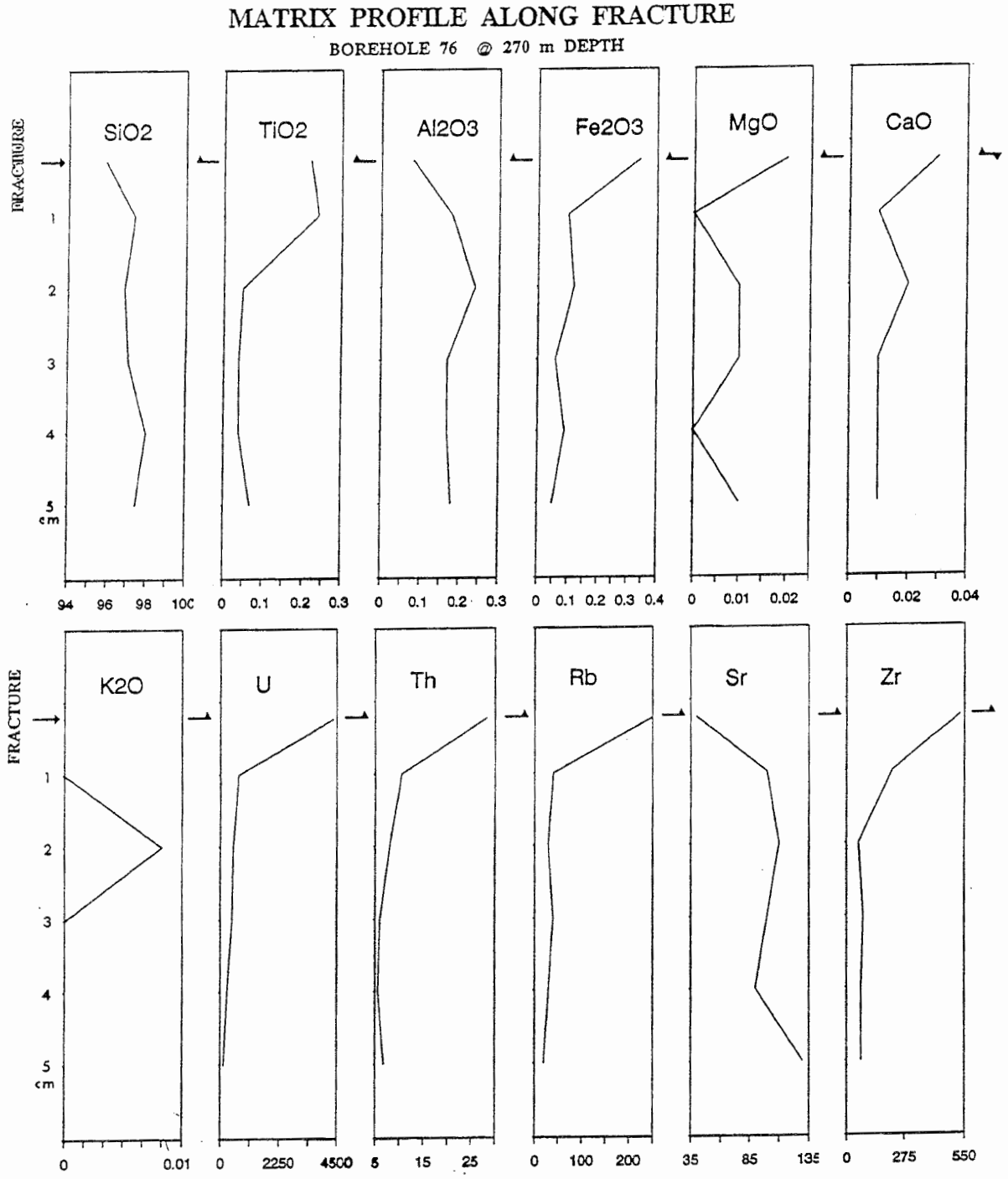

FIGURE 3.11 Major (wt.%) and selected trace (ppm) element contents in whole-rock samples from the matrix profile transecting the secondary perched mineralization in drillcore 76 (XRF data).

3.2.2.5.4 Uranium decay series

Drillcore 44A

The uranium-decay-series measurements are presented in Table 3.2 and illustrated in Figure 3.12. The $^{234}U/^{238}U$ activity ratios show very little deviation from secular equilibrium. Exceptions are samples CS248B and CS313, based on higher U-content and therefore better counting statistics, and CS243, based on very-low uranium contents. The $^{230}Th/^{234}U$ activity ratios are similarly equilibrated with only four exceptions (CS246B, 247A, 249 and 250). The $^{226}Ra/^{230}Th$ activity ratios, in contrast, show marked isotopic disequilibria apart from three samples (CS241, 245 and 313).

At face value little significant mobilization of uranium is apparently occurring, but radium is highly mobile and moving through the system. It is interesting to note, however, that for samples CS243, 248B and 313, near-secular equilibrium is indicated for the $^{230}Th/^{234}U$ activity ratios but not for the corresponding $^{234}U/^{238}U$ ratios. This suggests that where ^{234}U (from α-recoil loss) is quickly removed from these locations before the ^{234}U has time to decay to ^{230}Th, which would otherwise result in $^{230}Th/^{234}U$ ratios greater than unity. Furthermore, the high $^{226}Ra/^{230}Th$ ratios of two of these samples (exception being CS313) indicate that radium is moving through these locations and becoming deposited, most likely absorbed, onto the clay particles. There are indications, therefore, that there may be active conductive pathways existing through the "clay" layer adjacent to the orebody, but they are limited in extent.

For the two samples located at either side of the fracture zone (CS250 and 251B), where water-rock reaction processes would most likely occur and where isotopic data are available, only the $^{230}Th/^{234}U$ activity ratio for CS250 indicates isotopic disequilibria, suggesting a fairly recent removal of ^{234}U.

Using a Thiel plot (Figure 3.12), and allowing for conservative (10 %) analytical errors (boxed-in area), there is an overall impression that some uranium removal may be occurring. Those samples showing clear uranium removal are CS247A, 248B and 249. Sample CS243 plots within the complex field.

Drillcore 196

The Lower Sandstone samples represented by this profile (Table 3.3; Figure 3.13) show generally low but variable uranium (10.0-20.9 ppm) and thorium (8.2-22.2 ppm) concentrations; the thorium variation is believed to be due to mineralogical heterogeneity in the sandstone/clay. With respect to uranium and radium, there is no clear evidence for uranium movement, but in most cases radium has been preferentially mobilized and removed from within the sandstones, i.e., within a time scale of $< 10^3$ a.

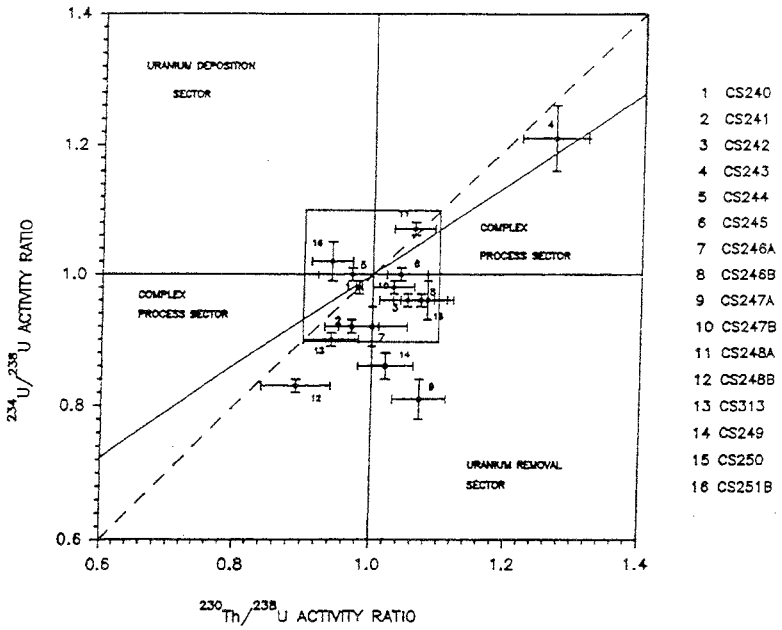

FIGURE 3.12 Thiel diagram for drillcore 44A and 113 samples. The boxed-in area includes isotopic ratios which can, based on a conservative judgement, be considered near or at secular equilibrium, given the uncertainties (10 %) of the analytical methods used.

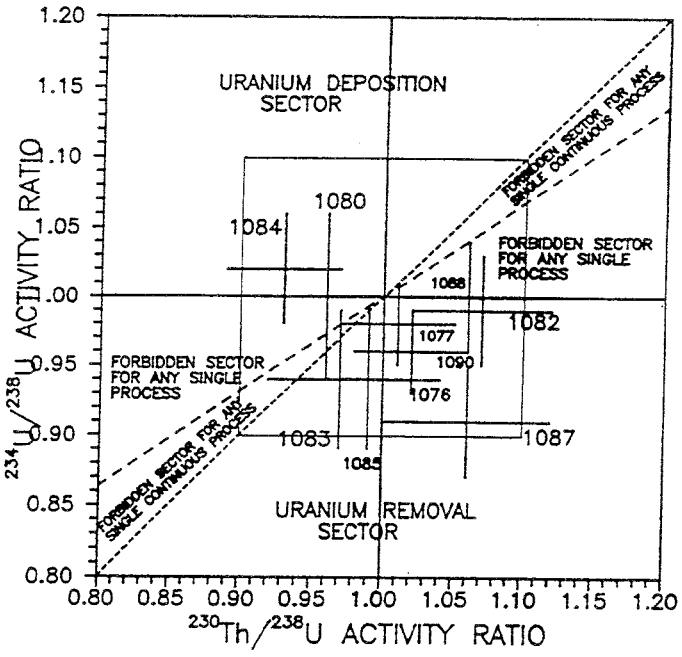

FIGURE 3.13 Thiel diagram of Lower Sandstone formation samples from drillcore 196.

TABLE 3.3
URANIUM-DECAY-SERIES MEASUREMENTS FOR
SELECTED ROCK SAMPLES FROM CIGAR LAKE

Sample #	Depth m	U ppm	Th ppm	$^{234}U/^{238}U$ Act.Ratio	$^{230}Th/^{234}U$ Act.Ratio	$^{226}Ra/^{230}Th$ Act.Ratio
		Limonitic Horizon - Hole 76				
CS-500	33.55	7.4±0.2	2.8±0.2	0.88±0.03	1.10±0.04	0.77
CS-501	40.50	7.9±0.2	4.7±0.1	0.87±0.03	1.29±0.06	0.80
		Sandstone Profile - Hole 196				
1076	270	15.3±0.4	16.6±0.7	0.94±0.03	1.06±0.04	0.89
1077	280	20.9±0.5	22.2±0.7	0.98±0.03	1.03±0.04	0.82
1080	300	11.2±0.5	9.1±0.2	1.00±0.06	0.96±0.04	0.76
1082	320	10.0±0.2	10.1±0.5	0.99±0.04	1.08±0.05	0.77
1083	330	16.3±0.6	9.6±0.7	0.94±0.05	1.03±0.05	
1084	340	10.6±0.3	13.6±0.7	1.02±0.04	0.91±0.04	
1085	350	13.9±0.5	8.2±0.5	0.94±0.05	1.05±0.05	1.01
1087	370	11.4±0.3	8.7±0.5	0.91±0.04	1.17±0.06	
1088	380	13.7±0.4	14.1±0.7	1.00±0.04	1.06±0.05	0.97
1090	390	15.6±0.4	11.4±0.2	0.96±0.03	1.06±0.04	0.75
		Perched Mineralization - Hole 76				
CS-273	270.0	5054±162	100 ±14	0.92±0.04	1.24±0.06	
CS-274	270.0	859±15	32 ±3	0.86±0.02	1.17±0.04	
CS-275	270.0	551±14	10.6±0.2	0.91±0.02	1.21±0.03	
CS-276	270.0	573±14	36 ±2	0.96±0.03	0.99±0.03	0.57
CS-277	270.0	292±7	5.4±1.5	0.96±0.03	1.08±0.05	0.76
CS-278	270.0	138±4	10.4±1.5	0.99±0.04	0.84±0.04	1.25
		Red Clay-Ore Contact - Hole 76				
CS-537	400.1	2.9±0.2	6.9±0.3	0.98±0.06	0.90±0.05	1.21
		New Ore+Clay Core - Hole FH-18				
CS-461	430.21	705±17	33 ±5	0.93±0.03	1.04±0.03	0.72
CS-462	430.18	518±12	21.5±3	1.03±0.03	0.94±0.03	1.40
CS-463	430.15	322±11	85 ±8	1.06±0.05	0.94±0.05	0.99
CS-464	430.11	147±5	18.3±2	1.26±0.06	1.08±0.05	1.10
CS-465	430.19	6440±109	76 ±16	1.00±0.02	0.74±0.03	0.26
CS-466	430.11	321±9	82 ±5	1.03±0.04	0.87±0.03	
CS-467	430.07	2252±70	138 ±9	0.91±0.04	1.05±0.04	
CS-468	430.03	456±10	79 ±5	0.97±0.03	1.07±0.04	1.20
CS-469	432.90	26730±535	2890 ±225	0.99±0.03	0.99±0.03	0.69
CS-470	429.48	737±16	55 ±4.5	0.98±0.03	1.03±0.04	1.24
CS-471	429.48	4431±22	353 ±47	1.01±0.07	0.93±0.05	0.34
		Basement at Unconformity - Hole 76				
CS-540	430.1	126±4	49 ±5	1.00±0.04	1.10±0.06	0.77

Drillcore 76

Comparison of uranium and thorium data (Table 3.3) using different methods of determination show a good correlation for uranium (by DNC and α-spectrometry) but a less satisfactory agreement for thorium (by XRF and α-spectrometry). For the discussion below the α-spectroscopy values are preferred in each case.

In general, the major- and trace-element data across the whole-rock profile (samples CS273-278; Table 3.3; Figure 3.11) indicate that the first 2-3 cm of the rock matrix surrounding the fracture have been affected by water-rock interaction, introducing or removing selected elements. The uniform trends for all elements in the matrix beyond this zone suggest that the extent of water-rock interaction was limited to clay mineral transformation (probably illite to kaolinite) within ~ 3 cm from the fracture.

The analysed profile through the small perched U-mineralization (samples CS273-278) indicates that uranium and thorium concentrations (coeval with mineralization) decrease with distance from the fracture into the adjacent sandstone (Figure 3.11; Table 3.3). Uranium, after an initial high of 5054 ppm U at the fracture margin, shows a more regular decrease from 859 to 138 ppm, and thorium concentrations, after an initial sharp reduction from 100 to 32 ppm within the first 1 cm, become more irregular, probably reflecting local variations in Th-bearing accessory mineral phases.

Subsequent radionuclide movement, as indicated by the uranium-decay-series data (Figure 3.14), shows, with three exceptions (CS276, 277 and 278), uranium loss, mostly within recent times ($< 10^5$ a). Sample 278, located farthest from the mineralized fracture edge, shows uranium gain close to equilibrium. Radium data (Table 3.3), available only for samples 276-278, (i.e., 3-5 cm from the fracture edge), suggest movement on a 10^3 a time scale for these samples, with ^{226}Ra deposition at sample CS278.

These data suggest that recent active groundwater interaction is occurring along and adjacent to these old mineralized faults, remobilizing both uranium and radium within a distance of 5 cm from the fracture surface in the rock matrix.

Of the four miscellaneous samples from drillcore 76, samples CS500/501 from the upper limonitic horizon (Table 3.3) clearly show a removal of uranium (CS500 over time scales of 10^5 to 10^6 a, and CS501 more recently) and radium ($< 10^3$ a). This supports the hydrogeochemical conceptual model: it shows that marginally oxidizing groundwaters permeate to depths of at least 100 m, resulting in the formation of limonite, partly at the expense of Fe-sulphides, in the upper part of the bleached sandstone succession.

Of the other two samples (Table 3.3; Figure 3.15), CS537 from the red clay/ore contact shows uranium deposition under near-equilibrium conditions and also recent deposition of radium. Sample CS540 from the basement near the unconformity contact shows recent near-equilibrium removal of uranium ($< 10^5$ a, similar to CS501) and radium removal ($< 10^3$ a). The results for these samples are significant as they indicate that recent water-rock interactions are occurring under and above the ore zone. More data, however, are required before this can be evaluated as being a general or only an isolated occurrence.

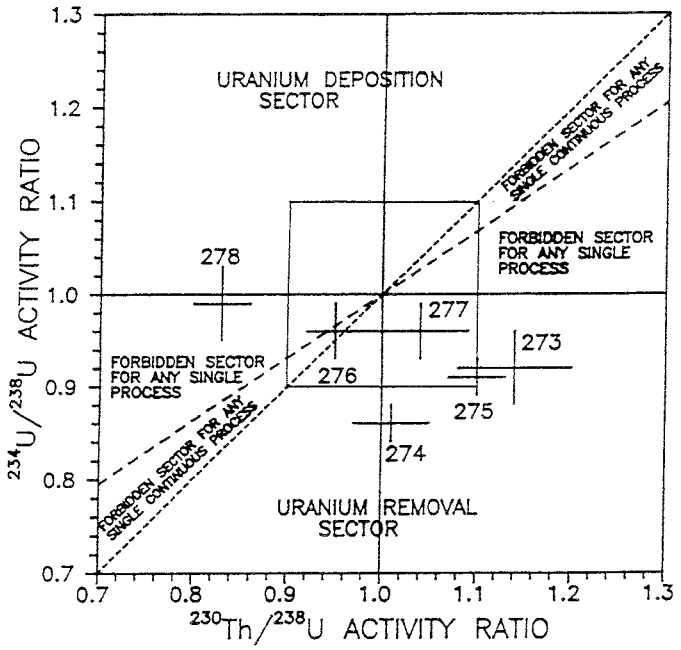

FIGURE 3.14 Thiel diagram of secondary perched mineralisation profile from drillcore 76.

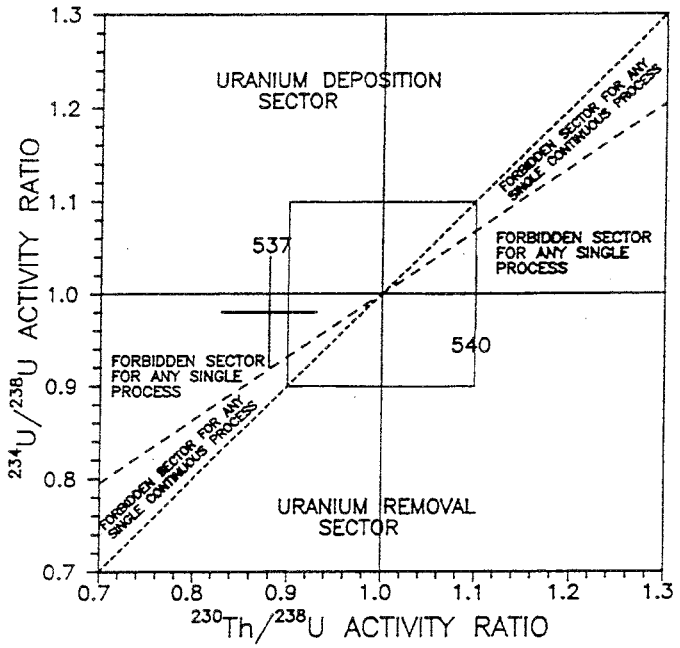

FIGURE 3.15 Thiel diagram of miscellaneous samples CS537 (ferric-rich clay/ore contact) and CS540 (basement clay at unconformity) from drillcore 76.

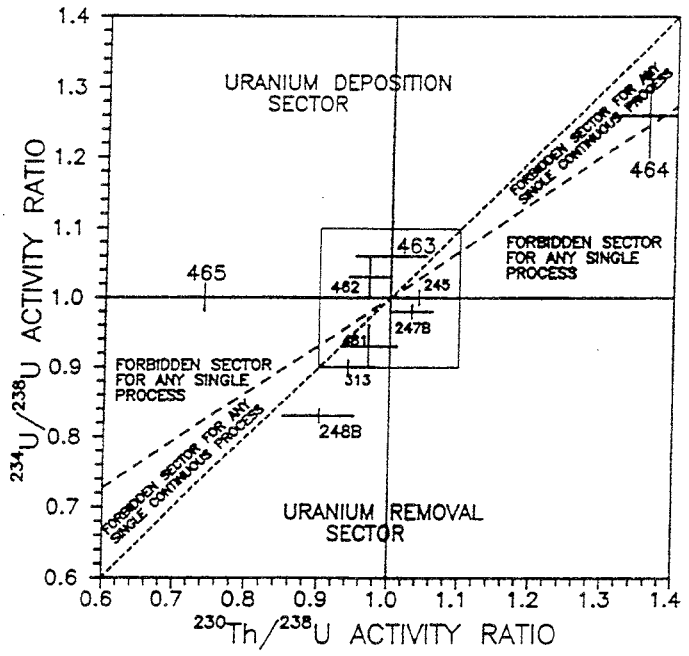

FIGURE 3.16 Thiel diagram of massive clay/sandy clay varieties, both ferric-rich and non-ferric-rich from drillcore FH-18.

Drillcore FH-18

The drillcore data from the massive clay zone (Table 3.3) are presented in terms of homogeneous rock samples and fracture surface/adjacent host rock samples, i.e., those samples where water-rock interaction should be at a minimum and those most likely to show interaction. Comparisons are made with similarly located samples from drillcore 44A.

Figure 3.16 illustrates samples selected from unfractured core portions that were uniform in colour and texture (see also Figure 3.9): reddish sandy clay (CS461, 462 and 465), grey-white bleached clay (CS463 and 468; CS247B and 248B) and red sandstone (CS464). In general, the samples plot close to isotopic equilibrium; the major deviations are shown by samples CS465 (equilibrium deposition) and CS248B (removal during the last 1 Ma). Sample CS464 plots in a position that could be taken to show deposition of uranium in a "single event" at some time in the past (i.e., 10^5 a), with the system subsequently remaining undisturbed and returning towards equilibrium. Radium, on the other hand, shows both significant deposition (CS462, 247B and 248B) and also removal (CS465) on a 10^3-a time scale; samples CS463 and 464 show equilibrium.

For comparison, Figure 3.17 shows selected data from drillcore 44A. It represents texturally uniform rock or alteration types outside the massive clay zone devoid of Fe-oxyhydroxides, e.g., bleached clay/sandstone (CS241, 243, 244 and 248A), bleached sandstone (CS242 and 246A) and bleached clay (CS240). With the exception of CS243, which shows deposition of uranium in a "single event", in common with sample CS464 above (Figure 3.16), the other samples show close to equilibrium values, indicating insignificant uranium removal during the last 1 Ma.

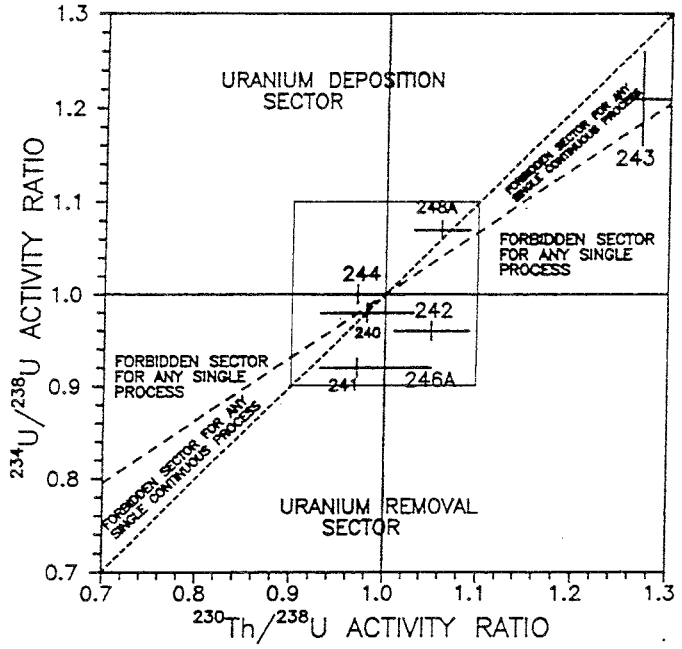

FIGURE 3.17 Thiel diagram of massive clay/sandy clay varieties, both ferric-rich and non-ferric-rich from drillcore 44A and 113.

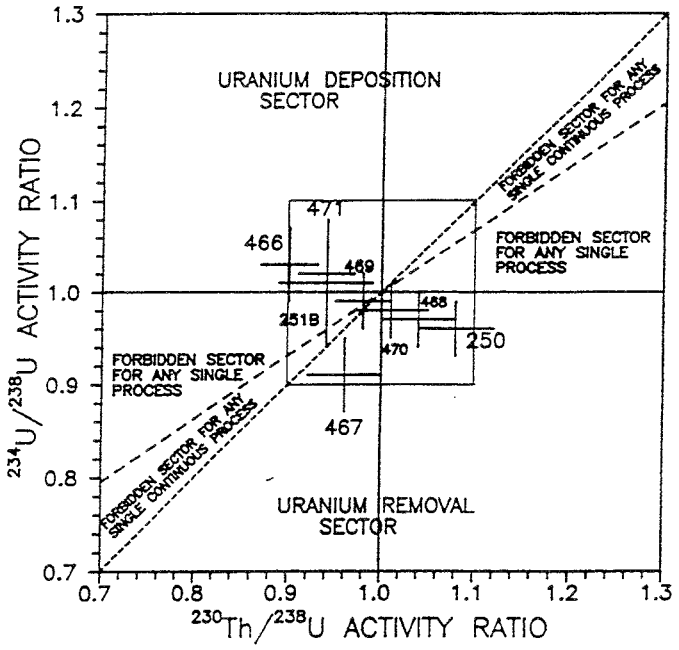

FIGURE 3.18 Thiel diagram of clay fracture surface samples, both ferric-rich and non-ferric-rich from drillcore FH-18.

3.2.2.6 Conclusions

In summary, even though the data are insufficient to draw far-reaching conclusions, the uranium-decay-series measurements show in general that, with a few exceptions, the samples from within the deposit (i.e., altered sandstone, clay and ore zones) have close to secular equilibrium activity ratios for $^{234}U/^{238}U$ and $^{230}Th/^{234}U$. This suggests that bulk dissolution of uranium from these rocks is not presently occurring. This is supported by the low concentrations of dissolved uranium and the prevailing reducing conditions in the groundwaters collected from these same rock units. Contrastingly, the $^{226}Ra/^{230}Th$ activity ratios show both radium removal and deposition on a 10^3 a time scale.

When considering all the results from the different lithologies in more detail, however, the following features become apparent:

a) Massive clay layer:
   - In the massive clay zone, uranium and radium may both be removed (somewhat preferentially) and deposited. There is no obvious "lithological control", i.e., ferric-rich versus non-ferric-rich or sandy versus clay-rich.

   - At the ferric-rich clay/ore contact above the ore body, deposition of uranium and radium is sometimes observed, which contrasts with the removal of these radionuclides at the clay/basement contact underlying the ore body.

   - Along the clay fracture surfaces (both ferric-rich and bleached varieties), uranium removal and loss may occur: there is also some evidence that the clay-filled fractures dating back to hydrothermal activity do not presently conduct groundwater; the only sample showing true secular isotopic equilibrium was from such a location.

b) Sandstone formations:
   - Small amounts of uranium and radium may be removed (preferentially) as well as deposited within the Lower Sandstone formation; this appears to be limited in extent and may depend on localized redox excursions.

c) Limonite zone:
   - Uranium and radium removal is clearly occurring in the upper limonitic zone.

d) Perched secondary mineralization:
   - There is evidence of recent active groundwater interaction occurring along and adjacent to these old mineralized faults, remobilizing both uranium and radium within a distance of 5 cm from the fracture surface.

The uranium-decay-series results indicate that uranium and radium removal (preferential) and deposition may occur within the clay layer. This includes the massive "impermeable" bleached and ferric-rich varieties, the heterogeneous "permeable/impermeable" clay types, and the more "permeable" clay-rich sandstone and sandstone transition sequences. Fractures and more permeable zones, in some cases ferric-rich, also suggest removal and deposition. The only sample to show true secular isotopic equilibrium comes from a clay-filled hydrothermal fracture, which helps to underline how efficiently hydrothermal activity has generally "sealed" the clay layer subsequent to mineralization. Uranium remobilization would imply a time scale from 10^6 to 10^5 a to recent, and for radium a time scale of 10^4 a.

There is evidence suggesting irregular patterns of uranium and radium removal and deposition from contrasting (e.g., ferric-rich vs. bleached) yet homogeneous (i.e., fracture-free) clay types. The absence of any obvious "pathways" further suggests that radionuclide diffusion is the dominant process occurring in this case. Furthermore, the heterogeneity of the removal/deposition patterns point to movement on a localized scale (0.01 to 0.1 m).

Studies of the more porous/fractured clay samples point to a more "advective", less restricted movement of radionuclides within and through the massive clay layer, often associated with pathways within both the bleached and ferric-rich clay types. In two of the best examples studied (chosen for being ferric-rich and potentially conducting), preferential "advective" removal of uranium and radium may well have occurred at the fracture surfaces, whereas diffusion of these radionuclides may have occurred simultaneously from the fractures into the host media, culminating in marginal deposition within 1-2 cm from the fracture surface.

Evidence for radiolysis has tended to focus in on the red ferric-rich horizons located at and near the clay/ore interface, on the assumption that oxidation of ferrous iron has been caused by groundwater oxidant transfer (accompanied by dissolved uranium) from radiolytic reactions occurring in the ore zone. This would result in a co-precipitation of Fe_{III} and uranium. Mössbauer studies of the ferric-rich vs. non-ferric-rich clay zones (Table 3.2) support the fact that oxidation has indeed occurred, but it is still not clear how much of the Fe_{II} and Fe_{III} is bound up in discrete mineral phases, compared with what may be introduced into the rock by oxidation processes. Moreover, the enhancement of uranium associated with the ferric phases need not indicate co-precipitation; uranium could quite as easily have been (or is being) scavenged at any later stage by the high concentrations of associated Fe-oxyhydroxides.

The recent mobility of uranium discussed above obviously points to a localized removal and deposition of uranium not only within the massive clay layer as a whole, but also within the ferric-rich horizons. Some removal can be explained by the transport of ^{234}U (derived from α-recoil processes) under groundwater reducing conditions, but other uranium-decay data suggest leaching of ^{234}U, possibly under less reducing conditions. This latter mechanism may be used to support the presence of radiolysis.

3.2.2.7 References

BRUNETON P. 1987. Geology of the Cigar Lake uranium deposit (Saskatchewan, Canada). In *Economic Minerals of Saskatchewan* (ed. C.F. GILBOY and L.W. VIGRASS). *Sask. Geol. Soc. Spec. Publ.* **8**, 99-119.

CRAMER J.J. 1986. Sandstone-hosted uranium deposits in northern Saskatchewan as natural analogs to nuclear fuel waste disposal vaults. *Chem. Geol.* **55**, 269-279.

FOUQUES J.P., FOWLER M., KNIPPING H.D. and SCHIMANN K. 1986. The Cigar Lake uranium deposit: Discovery and general characteristics. In *Uranium deposits of Canada* (ed. E.L. EVANS). *Can. Inst. Min. Metall. Spec. Vol.* **33**, 218-229.

PERCIVAL J.B. 1990. Clay mineralogy, geochemistry and partitioning of uranium within the alteration halo of the Cigar Lake uranium deposit, Saskatchewan, Canada. Ph.D. dissertation, Carleton Univ., Ottawa, Canada.

3.2.3 Clay mineralogy and geochemistry
(J. Percival)

3.2.3.1 Introduction

Engineered clay barriers in a nuclear fuel waste disposal system are expected to impede, or retain by sorption, the outward movement of released radionuclides in the event of canister corrosion and leakage. The Cigar Lake deposit, with a clay-rich halo marginal to the orebody (near-field implications) and an abundance of clay minerals in the surrounding host sandstone (far-field implications), provides a unique opportunity to study the movement and dispersion of uranium and its daughter nuclides during both the initial hydrothermal events and the later low-temperature groundwater/rock interaction processes.

A detailed Ph.D. study on the clay mineralogy and geochemistry of the clay-rich rocks in the Cigar Lake deposit has been carried out at Carleton University in Ottawa (Percival, 1990). Results of this study have been reported in the following documents:

1988	Abstract Clay Mineralogical Society of America, Poster	Percival, Torrance and Bell
1989	Paper Canadian Mineralogist on sudoite from Cigar Lake	Percival and Kodama
1990	PhD thesis	Percival
1993	Paper in Canadian Journal of Earth Sciences	Percival, Torrance and Bell

In addition, some mineralogical and geochemical work on clay minerals from the Cigar Lake deposit has also been carried out by COGEMA in France, as part of the general petrological characterization of the deposit geology. The study carried out by Percival (1990) is a comprehensive study focussed on the origin and alteration of the clay minerals and their association with uranium mineralization. The main points from this study are summarized below.

The high-grade, unconformity-type Cigar Lake uranium deposit occurs wholly in the sandstones close to the unconformity contact. An alteration halo grades outwards from the deposit through zones characterized by:

1- Fe-chlorite + illite $\pm$ carbonate $\pm$ uraninite $\pm$ gersdorffite;

2- sudoite + illite $\pm$ hematite $\pm$ sulphides;

3- illite + hematite; and

4- illite $\pm$ kaolinite $\pm$ hematite.

Detrital kaolinite was almost completely transformed to illite. Illite polytypes grade from $3\underline{T}$-$2\underline{M}_1$ mixtures near the ore, to $2\underline{M}_1$, to $2\underline{M}_1$-$1\underline{M}$ mixtures in overlying sandstone. In the alteration zone, Kübler indices of illite crystallinity indicate high-grade diagenetic to anchimetamorphic, with local epizonal, conditions.

Although the alteration to illite extends upwards and outwards hundreds of metres, U and trace elements are concentrated only within 50 m of the ore. Many of these elements have been passively concentrated by removal of silica from the original sandstone rock matrix. Mass balance calculations indicate possible volume changes of up to 94 %.

Stable isotopic measurements for illite-rich samples indicate little disturbance to the alteration halo since primary mineralization, about 1.3 Ga ago. Average δD (-82 o/oo) and δ^{18}O (+10 o/oo) values for illite-rich clay are comparable to similar samples from other Athabasca U deposits, indicating fluids of regional extent. Illite K-Ar dates range from 1255 ± 28 to 1148 ± 28 Ma, suggesting either recrystallization or resetting by hydrothermal fluids, possibly related to the emplacement of the MacKenzie dyke swarm about 1267 Ma ago. A more recent event is recorded in a sudoite + illite mixture from the basement, at 815 ± 30 Ma, which corresponds with a regional event recorded elsewhere in the basin. An Fe-chlorite-bearing ore sample shows evidence for interaction with present-day meteoric waters.

Data on contents of uranium and of rare earth elements (REE) in the clay samples show overall higher values for the clay-size fractions (<2 μm) than for the coarser-size fractions. Carbonate, uraninite, amorphous Fe-oxides, crystalline Fe-oxides, and residual silicate phases were analyzed for U using selective sequential extraction. About one-third of the extractable U occurs as uraninite, and between 4 and 60 % is associated with the clay minerals. It is likely that any uranium dispersed as a result of initial hydrothermal alteration was adsorbed by the neoformed clay minerals and incorporated in the clay mineral lattice. In iron-rich samples uranium is also associated with crystalline iron-oxides; in iron-poor samples, it is associated with amorphous iron-oxides. The restricted distributions of U and other elements, which mimic radionuclides of concern in nuclear fuel waste disposal, indicate that the illite-rich materials have provided an effective sorptive/retentive barrier for about 1.3 Ga.

The following sections summarize work carried out on selected clay mineral samples during the period 1989-1992, and a comparative study of selective extraction on Cigar Lake clay samples and samples from two different open pit mines. This latter study contrasts the different modes of uranium fixation between that in the red clay-ore contact in the Cigar Lake deposit with that in the oxidizing surface environments of the open pits at the Cluff Lake and Rabbit Lake deposits.

3.2.3.2 Clay-rich samples from 1991 freeze-hole cores

Seven clay-rich core samples were selected for detailed chemical and mineralogical analyses. These samples, taken from three boreholes, form a transect across the alteration halo above the ore zone (Table 3.4). One sample, CS454 was taken at the contact between the massive clay and ore zones. The samples exhibit variable degrees of alteration. They consist of 50

to 80 % clay matrix dominated by illite, with subordinate chlorite ± kaolinite; 0 to 30 % detrital quartz; 5 to5 % detrital mica; trace to 30 % Fe-oxides (hematite, goethite and ferrihydrite); trace to 5 % disseminated pyrite, and trace amounts of zircon, leucoxene, rutile, pyrrhotite and a U-rich mineral (unidentified). Quartz occurs as floating grains with highly corroded grain boundaries in sample CS452. In other samples, quartz is present only in trace amounts as remnant grains. More details will be available following SEM and microprobe analyses.

TABLE 3.4
CLAY-RICH SAMPLES FROM 1991 FREEZE-HOLE CORES (60 mm OD)

Sample/Drillhole #	Depth m	Description/Comments
CS452/FH-18	430.09-430.22	massive clay; pale reddish-brown
CS435/FH-18	430.34-430.44	dense clay and hard sandstone band; pinkish-grey
CS454/FH-18	432.89-432.99	soft clay-like material; pale reddish- brown
CS485/FH-16	437.00-437.06	massive clay; light greenish-grey
CS488/FH-16	433.94-434.00	massive clay; yellowish-grey
CS490/FH-16	432.89-432.93	massive clay; pale greenish yellow
CS491/FH-17	435.69-435.77	massive clay; yellowish-grey

Major- and trace-element chemistry is presented in Table 3.5. The samples have SiO_2, Al_2O_3 and K_2O in amounts that are typical of the massive clay zone, with the exception of CS452 (altered sandstone) and CS454 (Fe-oxide- and U-rich sample). Arsenic, Co, Cu, Li, Mo, Pb, Rb, Th and U are elevated in sample CS452 relative to the other samples. Lithium contents range from 88 to 540 ppm, with an average about 340 ppm, reflecting the abundance of clay minerals in these samples.

Cation exchange capacity (CEC) and exchangeable cations (Ca, Mg, Na and K) were determined on bulk samples by extraction with NH_4HOAc adjusted to pH 7, following the method outlined in Sheldrick (1984) (Norwest Labs, Winnipeg). Results are shown in Table 3.6. In addition, Na exchangeable percentage (ESP), total exchange capacity (TEC) and base saturation are given. Base saturation is defined as TECx100/CEC. The high percentages (> 100 %) indicate the presence of soluble salts (e.g., gypsum) in the samples.

Semi-quantitative clay mineral analysis of the <2 μm fraction is in progress. Bulk samples and clay-size separates will be selectively leached to determine partitioning of U, Pb and ^{226}Ra.

TABLE 3.5
MAJOR- AND TRACE-ELEMENT COMPOSITION OF ROCK SAMPLES FROM THE CIGAR LAKE CLAY-RICH ALTERATION HALO

	CS452	CS453A	CS453B	CS454	CS485	CS488	CS490	CS491
SiO_2 wt%	85.6	43.3	42.6	32.5	44.9	44.9	46.4	44.4
TiO_2	0.30	1.69	1.46	2.19	1.33	0.93	1.33	0.47
Al_2O_3	8.09	28.3	28.5	22.4	32.7	32.6	33.5	33.0
Fe_2O_3	1.35	4.07	5.06	7.03	2.65	4.89	2.00	2.12
MnO	0.01	0.03	0.02	0.03	0.03	0.02	0.03	0.01
MgO	0.39	1.99	1.90	1.97	0.98	1.30	1.29	0.91
CaO	<0.01	0.17	0.20	0.46	0.04	0.07	0.02	0.04
Na_2O	0.03	0.39	0.18	0.17	0.27	0.12	0.26	0.09
K_2O	2.04	6.94	7.82	3.95	8.08	8.63	8.09	9.15
P_2O_5	0.06	0.19	0.24	0.28	0.19	0.16	0.16	0.09
LOI	1.62	9.23	10.2	13.9	6.15	6.54	6.15	8.85
SUM	99.6	96.9	98.7	85.5	97.8	100.5	99.8	99.3
Ag ppm	0.5	0.5	0.5	37	0.5	0.5	1.5	0.5
As	25	150	140	370	32	23	39	53
Ba	119	433	297	408	160	135	181	87
Co	12	90	52	317	27	31	101	23
Cd	<1	1	1	4	<1	<1	1	<1
Cr	20	138	150	179	61	32	63	19
Cu	51	88	91	5580	24	14	30	12
Li	88	410	360	540	240	300	440	350
Mo	4	15	15	3750	12	10	14	11
Nb	10	<10	<10	<10	44	<10	74	<10
Ni	39	347	251	249	16	75	64	110
Pb	43	358	281	15700	128	144	133	93
Rb	53	244	186	1140	125	198	112	103
Sr	221	1150	1290	898	829	569	762	244
Th	18	93	95	160	68	43	82	61
U	393	1870	391	20000	189	2220	128	754
Y	26	46	35	<10	76	<10	74	28
Zn	30	161	87	821	75	61	203	30
Zr	526	2190	2110	2210	2010	2060	26700	1120

Note: Total Fe reported as Fe_2O_3.

TABLE 3.6
CATION EXCHANGE CAPACITY, EXCHANGEABLE CATIONS AND BASE SATURATION OF ROCK SAMPLES FROM THE CIGAR LAKE CLAY-RICH ALTERATION HALO

Sample #	CEC* mEq/100g	Ca ppm	Mg ppm	Na ppm	K ppm	ESP* %	TEC* mEq/kg	% Base Saturation
CS452	3.51	300	280	368	2930	12.4	129	367
CS453A	18.8	1570	1156	284	--	--	--	--
CS453B	14.6	2340	1680	910	8970	6.2	641	439
CS454	21.4	2580	1455	665	7130	6.3	460	215
CS485	6.32	470	298	128	2950	4.3	129	204
CS488	9.27	560	398	105	3450	3.0	154	166
CS490	9.55	945	360	100	4090	2.3	186	195
CS491	6.60	330	898	100	2928	2.5	170	258

* CEC= cation exchange capacity; ESP= exchangeable Na percentage; TEC= total exchange capacity (sum of exchangeable bases).

3.2.3.3 Uranium fixation in two contrasting environments

3.2.3.3.1 Introduction

Within the alteration halo of the Cigar Lake deposit, the uranium distribution appears to result from primary ore-forming processes rather than secondary, hydromorphic alteration. Evidence for this, based on sequential extraction experiments, includes:

1- low concentrations (< 10 ppm) of U in the overlying and distal sandstones to the ore, except along fracture zones containing perched mineralization;
2- low concentrations of easily-leached forms of U associated with exchangeable and carbonate-bound sites;
3- the occurrence of U as uraninite in relatively constant proportions;
4- abundance of extractable U associated with residual silicates, primarily the clay minerals; and
5- a decrease with depth of the proportion of extractable U associated with the residual silicates (Percival, 1990).

Sequential extraction procedures provide a means of identifying the chemical forms and mineral associations of heavy metals of environmental concern. Information about the origin, mode of occurrence, bioavailability, physicochemical availability, mobilization and transportation potential of the metals can also be determined (Tessier et al., 1979). Although commonly used in exploration studies to enhance geochemical anomalies (Sondag, 1981; Tessier et al., 1982; Chao, 1984), the use of selective extraction techniques in environmentally-related studies is on the increase.

Sequential extraction procedures consist of a series of single, partial extraction methods that attack the samples with increasing severity. Selection of an individual extraction method to be used in a sequential extraction procedure is dependent upon the nature of the material (e.g., mineralogy). In addition, the criteria for selection should ensure that the procedure is:

1- selective or mineral-specific;
2- robust, such that it is independent of small changes in concentration, extraction time or temperature; and
3- rapid, simple and reproducible (Borggaard, 1988).

3.2.3.3.2 Analytical methods and materials

In this study a sequential extraction procedure (Figure 3.19) was used to determine the partitioning of U in:

1- carbonates (easily-acid-soluble and exchangeable sites);
2- uraninite (may include sulphide- and organic-bound);
3- amorphous Fe-oxides;
4- crystalline Fe-oxides; and
5- residual silicates.

Detailed information about the partial extraction methods used and their testing on the samples is given in Percival (1990) and Percival et al. (1990).

Uranium, in extractant solutions, was analyzed by DNC at Atomic Energy Radiochemical Company (now called Nordion International) following the method of Boulanger et al. (1975). This technique was selected over others because it is relatively inexpensive, reproducible, and not prone to matrix interference. In this method, it is assumed that the ratio of U isotopes is consistent with their natural abundance (i.e., the U-decay series is in equilibrium).

Because of low U concentrations in the extractant solutions, the supernatant solutions were concentrated. Solutions were passively evaporated to dryness using a heat lamp. Residues were then dissolved in about 5 to 10 mL of 4 M HNO_3 and the U was analyzed by DNC. Difficulties arose in concentrating the dithionite-citrate solutions because of excessive amounts of dissolved solids. In the current study on the wallrock samples from the open-pit uranium mines, U in the extractant solutions was analyzed by inductively-coupled plasma mass-spectrometry (ICP-MS) at the Geological Survey of Canada.

The sequential extraction procedure was applied to 17 bulk and 13 clay-size samples. Uranium in the extractant solutions was analyzed using the INAA-DNC method by Nordion Limited. The extractant solutions were passively concentrated to dryness and redissolved in a small volume of 4 M HNO_3 before analysis.

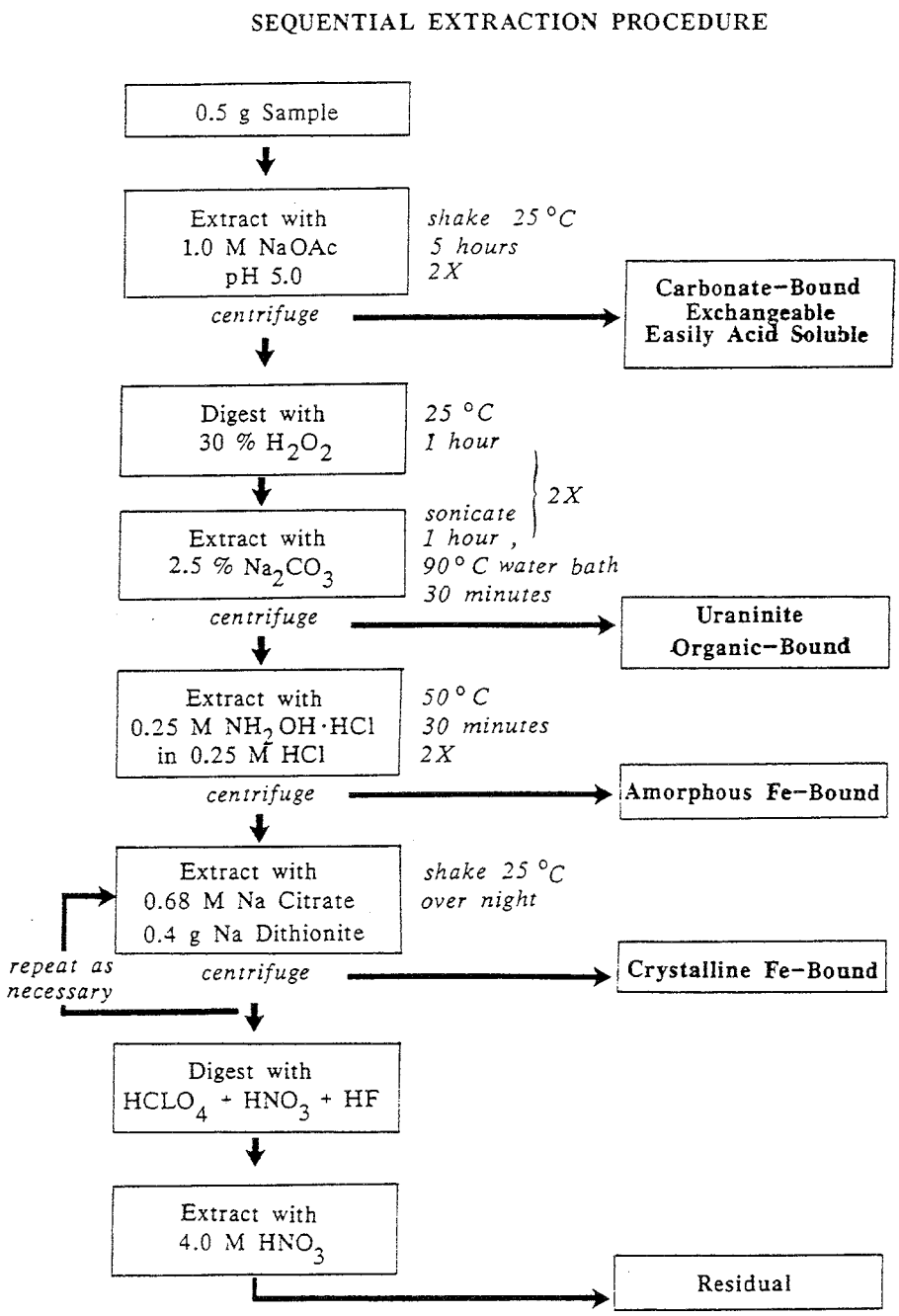

FIGURE 3.19 Sequence of reagents used to partition U in Cigar Lake samples.

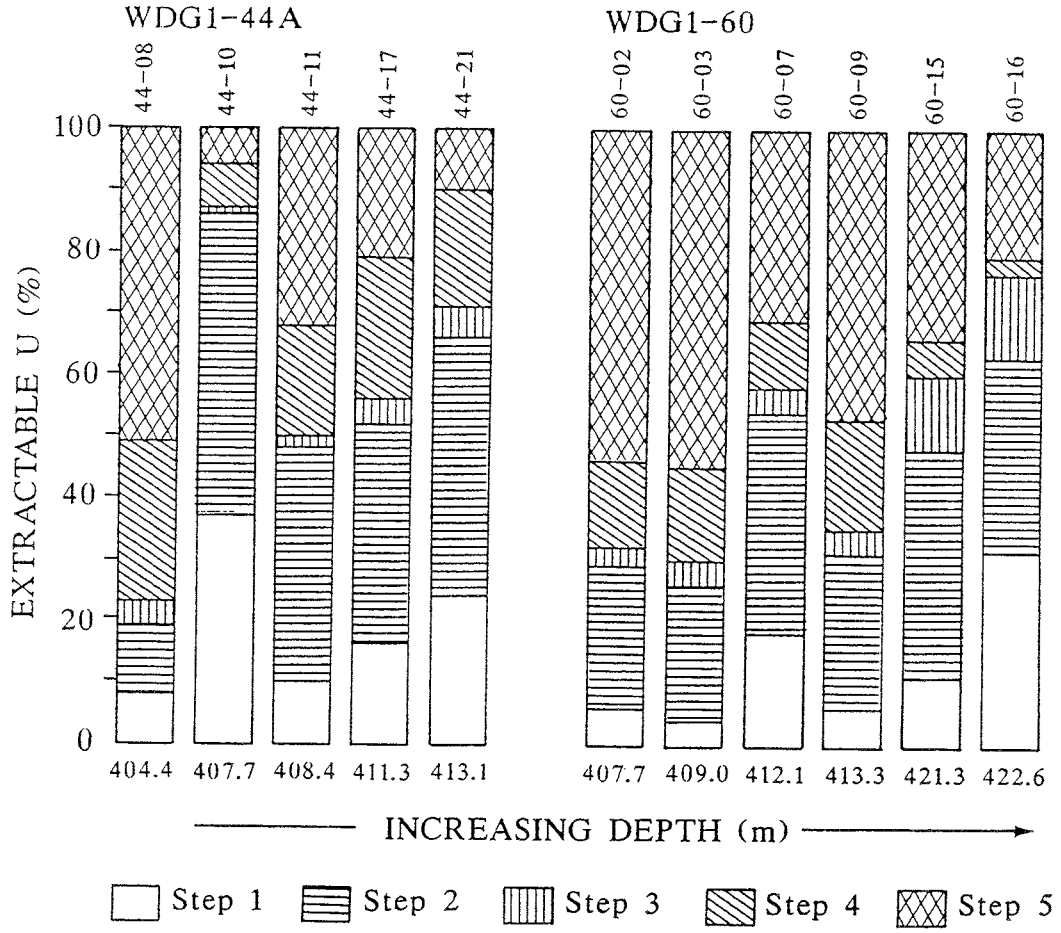

FIGURE 3.20 Relationship between extractable U and depth for bulk samples from boreholes WDG1-44A and WDG1-60. Sample numbers are listed on top of each bar, and the depth is listed underneath.

3.2.3.3.3 Results and discussion

Results are presented in Tables 3.7 and 3.8 and Figure 3.20. The proportion of U extracted by step 1 is variable, ranging from 4 to 37 % of the total U. Uranium associated with this fraction is probably the most mobile form in these samples. Uranium extracted by step 2 ranged from 10 to 49 % for bulk samples and 13 to 68 % for clay-size samples. The U extracted by step 3 formed the lowest proportion. The few exceptions (samples 60-15, 60-16 and 103-05) may represent dissolution of Fe-chlorite present in samples 60-15 and 60-16, and amorphous Fe-oxides in sample 103-05. Uranium extracted by step 4 is highly variable, ranging from 3 to 39 % for bulk samples and 2 to 54 % for clay-size samples. Uranium extracted during step 5 is associated with the residual minerals, which include the clay minerals illite, sudoite and kaolinite, as well as zircon, apatite, goyazite and rutile. The amount extracted by this step ranged from 4 to 60 %, with the highest proportions extracted from illite-rich samples. In all cases there was no apparent correlation between the amount

extractable by any step and the total U or Fe_2O_3 contents of the samples.

The relationship between U extracted in each step and depth is shown in Figure 3.20 for bulk samples from two boreholes. The importance of U associated with the residual minerals (step 5) appears to decrease with depth toward the ore. Sample 44-10 is anomalous, in that the U extracted by steps 1 and 2 is high relative to other samples, about 35 and 49 % respectively. The remaining fractions account for only 14 % of the total extractable U. The high proportion of readily-extractable U (step 1) indicates secondary dispersion. This sample may represent late-stage remobilization of the ore.

The sequential extraction procedure is being applied to wall-rock samples from open pits in the Athabasca basin. In the surface weathering environment, low-grade ore remaining in the wall-rock of the pits is a potential contaminant to surface and ground waters. It is hoped that the application of this procedure may enable prediction of the proportion of the metals (e.g., As, Ni and U) that could be easily leached by the surface waters and groundwater seeps. To differentiate between exchangeable and carbonate-bound metals, the procedure was slightly modified for this study. As $MgCl_2$ is less aggressive than HOAc (step 1 in Figure 3.19), the samples were initially leached by $MgCl_2$ (1 M, pH 7.0, room temperature). The samples include aluminous and graphitic gneiss and sandstone samples from three open pits in the Cluff Lake mine camp (D-pit, Claude and Dominique-Janine) and one from the Rabbit Lake mine camp (Collins Bay B-Zone).

Results from two of the open pits are presented in Tables 3.9 and 3.10. The proportion of U extractable by steps 1 (exchangeable), 3 (uraninite-bound) and 4 (amorphous-Fe-oxide-bound) is very low (<16 %) for the bulk samples and more variable (up to 24 %) for the clay-size samples. Step 2-extractable U (easily-acid-soluble/carbonate-bound) is proportionally high for the B-Zone bulk samples (35-76 %) and moderately high for the clay-size samples (23-39 %). Uranium extractable by step 5, associated with the crystalline Fe-oxide phase, is variable, ranging from 0 to 59 %. The Al-bearing gneiss samples from D-Pit and the sandstone samples from B-Zone pit contain low concentrations of total U (<30 ppm) but have the largest proportion associated with the residual minerals (step 6).

In contrast to the clay samples from the Cigar Lake deposit, the samples from the surface environment have a higher proportion of U that is readily available for migration. This higher proportion resulted from steps 1 and 2 in the modified procedure, which account for, on average, up to 40 % of the extractable U. In the Cigar Lake study, step 1 accounted for only 15 % of the extractable U. The mafic and graphitic gneiss samples also tend to have a large proportion of extractable U associated with these more available forms. These data supports very limited oxidation and hydromorphic transport of U in the Cigar Lake alteration halo samples relative to the open-pit wallrock samples.

3.2.3.3.4 Summary

Preliminary data from the open-pit sandstone samples indicate that less U is associated with the residual silicates and accessory phases and more is associated with uraninite and Fe-

oxides, relative to the Cigar Lake samples. About 40 % of the U is readily available (exchangeable and easily acid-soluble/carbonate forms) from the open-pit samples in contrast to < 15 % for the Cigar Lake samples. This increase is likely due to weathering of the open-pit samples in the near-surface environment. The gneissic samples appear to have a large proportion (up to 76 %) of extractable U in readily available (leachable) sites (exhangeable and easily acid-soluble/carbonate forms).

3.2.3.4 Acknowledgements

Special thanks to S. Phaneuf for the sequential extraction experiments and general laboratory assistance, and N. Bertrand for U analyses of extractants (wallrock samples).

3.2.3.5 References

BORGGAARD, O.K. 1988. Phase identification by selective dissolution techniques. In *Iron in Soils and Clay Minerals* (ed. J.W. Stucki, B.A. Goodman and U. Schwertmann). Reidel Publishing Co., Dordrecht, Holland, 83-98.

BOULANGER, A., EVANS, D.J.R. and RABY, B.F. 1975. Uranium analysis by neutron activation delayed neutron counting. In *Proceedings of the 7th Annual Symposium Canadian Mineral.* Analysts, Thunder Bay, Ontario, 10p.

CHAO, T.T. 1984. Use of partial dissolution techniques in geochemical exploration. J. Geochem. Explor. **20**, 101-135.

PERCIVAL, J.B. 1990. Clay mineralogy, geochemistry and partitioning of uranium within the alteration halo of the Cigar Lake uranium deposit, Saskatchewan, Canada. Carleton University, Ottawa, Canada, Ph.D. Thesis, 343p.

PERCIVAL, J.B. and KODAMA, H. 1989. Sudoite from Cigar Lake, Saskatchewan. Can. Mineral. **27**, 633-641.

PERCIVAL, J.B., TORRANCE, J.K. and BELL, K. 1990. On the development of a sequential extraction procedure with application to leachability problems. In *Acid Mine Drainage Designing for Closure* (ed. J.W. Gadsby, J.A. Malick and S.J. Day). BiTech Publishers Ltd., Vancouver, 51-62.

PERCIVAL, J.B., TORRANCE, J.K. and BELL, K. 1993. Clay mineralogy and isotope geochemistry of the alteration halo at the Cigar Lake uranium deposit. Can. J. Earth Sci., **30**, 689-704.

SHELDRICK, B.H. (ed). 1984. Analytical Methods Manual 1984. Land Resources Res. Inst., Agric. Canada, Ottawa, Ontario, LRRI Contr., **84-30**.

SONDAG, F. 1981. Selective extraction procedures applied to geochemical prospecting in an area contaminated by old mine workings. J. Geochem. Expl., **15**, 645-652.

TESSIER, A., CAMPBELL, P.G.C. and BISSON, M. 1979. Sequential extraction procedure for speciation of particulate trace metals. Anal. Chem. **51**, 844-851.

TESSIER, A., CAMPBELL, P.G.C. and BISSON, M. 1982. Particulate trace metal speciation in stream sediments and relationships with grain size: implications for geochemical exploration. J. Geochem. Explor. **16**, 77-104.

TABLE 3.7
EXTRACTABLE URANIUM FROM BULK SAMPLES BY
STEPS 1 - 5 OF THE SEQUENTIAL EXTRACTION PROCEDURE

Sample #	Step 1 %	Step 2 %	Step 3 %	Step 4 %	Step 5 %	U_{TOT} ppm	Fe_2O_3 wt%
	CIGAR LAKE:						
	Clayey Sandstone						
44-08	8	11	4	26	51	245	0.53
60-15	11	37	12	6	34	131	8.52
103-05	15	31	7	39	8	61	55.00
	Claystone						
44-10	37	49	1	7	6	1920	2.26
44-11	10	38	2	18	32	233	0.67
44-17	16	36	4	23	21	713	13.43
44-21	24	42	5	19	10	2160	9.25
49-12	6	24	1	11	58	318	1.16
57-02	12	10	5	24	49	105	9.68
60-02	6	23	3	14	54	106	0.56
60-03	4	22	4	15	55	71	0.61
60-07	18	36	4	11	31	322	2.27
60-09	6	25	4	18	47	88	3.05
113-02	7	32	2	18	41	1294	0.69
119-30	22	22	3	10	43	149	18.40
	Ore						
60-16	31.5	31.5	13.5	3	0.5	137000	5.83
	Basement						
53-15	7	10	7	16	60	52	1.07

Step 1: NaOAc + HOAc-extractable/carbonate-bound, exchangeable and easily acid-soluble
Step 2: H_2O_2 + Na_2CO_3-extractable/uraninite, organic- and sulphide-bound
Step 3: $NH_2OH.HCl$-extractable/amorphous Fe-oxide-bound
Step 4: Dithionite-Citrate-extractable/crystalline Fe-oxide-bound
Step 5: HF + $HClO_4$ + HNO_3-extractable/residual minerals

TABLE 3.8
EXTRACTABLE URANIUM FROM CLAY-SIZE SAMPLES BY
STEPS 1 - 5 OF THE SEQUENTIAL EXTRACTION PROCEDURE

Sample #	Step 1 %	Step 2 %	Step 3 %	Step 4 %	Step 5 %	U_{TOT} ppm	Fe_2O_3 wt%
	CIGAR LAKE:						
	Clayey Sandstone						
44-08	13	35	1	17	34	638	0.72
60-15	6	46	3	18	27	130	-
103-05	9	13	14	54	10	130	-
	Claystone						
44-11	6	35	2	36	21	574	1.24
49-12	12	28	1	13	46	1215	1.42
57-02	13	23	5	27	32	35	31.86
60-02	6	41	2	6	45	145	0.70
60-03	3	35	1	9	52	349	0.86
60-07	12	33	3	16	36	233	2.14
60-09	2	33	2	19	44	278	4.38
119-30	16	48	3	10	23	147	7.52
	Ore						
60-16	23	68	3	2	4	33100	6.24
	Basement						
53-15	13	31	4	10	42	1356	1.40

Step 1: NaOAc + HOAc-extractable/carbonate-bound, exchangeable and easily acid-soluble
Step 2: H_2O_2 + Na_2CO_3-extractable/uraninite, organic- and sulphide-bound
Step 3: $NH_2OH.HCl$-extractable/amorphous Fe-oxide-bound
Step 4: Dithionite-Citrate-extractable/crystalline Fe-oxide-bound
Step 5: HF + $HClO_4$ + HNO_3-extractable/residual minerals

TABLE 3.9
EXTRACTABLE URANIUM FROM BULK SAMPLES BY
STEPS 1 - 6 OF THE MODIFIED SEQUENTIAL EXTRACTION PROCEDURE

Sample #	Lithology *	Step 1 %	Step 2 %	Step 3 %	Step 4 %	Step 5 %	Step 6 %	U_{TOT} ppm
COLLINS BAY: B-Zone								
CB-1	Sst	3	64	9	12	0	12	13
CB-2	Sst	5	76	4	3	0	12	62
CB-5	Gr-Gn	1	75	7	2	0	14	24
CB-6	ASst	2	35	16	11	27	9	105
CB-6	BSst	2	37	11	14	29	7	123
PNA90-34	Sst	6	67	20	1	1	5	1100
PNA90-35	Gr-Gn	1	20	25	10	5	39	10
PNA90-43A	Sst	0	16	9	9	3	63	15
PNA90-43D	Sst	1	14	15	6	4	59	30
PNA90-46	Clst	0	9	11	1	2	76	230
PNA90-47A	Gr-Gn	1	35	21	4	2	38	26
PNA90-47B	Gr-Gn	1	51	10	5	2	31	27
PNA90-49	Ma-Gn	0	70	27	0	0	2	9500
CLUFF LAKE: D-Pit								
PNA89-3	Al-Gn	0	0	0	3	59	38	3.7
PNA89-5	Al-Gn	0	0	0	3	52	45	3.4
PNA90-9	Al-Gn	0	0	0	2	45	53	5.7
PNA90-1	Al-Gn	0	5	5	4	3	83	11
PNA90-2	Ft-Gg	0	27	48	3	4	17	94
PNA90-3	Gn	1	36	18	3	4	39	14
PNA90-4	Ft-Gg	1	12	5	8	7	67	6.1
PNA90-5	Gn	1	6	21	1	7	65	2.8

Step 1: $MgCl_2$-extractable/exchangeable
Step 2: NaOAc + HOAc-extractable/carbonate-bound and easily acid-soluble
Step 3: H_2O_2 + Na_2CO_3-extractable/uraninite, organic- and sulphide-bound
Step 4: $NH_2OH.HCl$-extractable/amorphous Fe-oxide-bound
Step 5: Dithionate-Citrate-extractable/crystalline Fe-oxide-bound
Step 6: HF + $HClO_4$ + HNO_3-extractable/residual minerals
* Al-Gn= Aluminous Gneiss; ClSt= Claystone; Ft-Gg= Fault Gouge; Gn= Gneiss; Gr-Gn= Graphitic Gneiss; Ma-Gn= Mafic Gneiss; Sst= Sandstone.

TABLE 3.10
EXTRACTABLE URANIUM FROM CLAY-SIZE SAMPLES BY
STEPS 1 - 6 OF THE MODIFIED SEQUENTIAL EXTRACTION PROCEDURE

Sample #	Lithology *	Step 1 %	Step 2 %	Step 3 %	Step 4 %	Step 5 %	Step 6 %	U_{TOT} ppm
COLLINS BAY: B-Zone								
CB-1	Sst	16	32	0	15	18	19	52
CB-2	Sst	19	34	12	4	3	28	264
CB-5	Gr-Gn	18	39	24	3	5	10	61
CB-6A	Sst	11	27	11	8	33	10	719
CB-6B	Sst	12	23	17	8	27	13	964
PNA90-34	Sst	2	62	27	1	2	6	-
PNA90-35	Gr-Gn	1	23	27	8	5	37	-
PNA90-43A	Sst	1	14	9	8	3	65	-
PNA90-43D	Sst	3	3	45	20	14	14	-
PNA90-46	Clst	0	13	15	2	8	61	-
PNA90-47A	Gr-Gn	2	51	27	5	2	13	-
PNA90-47B	Gr-Gn	1	51	26	5	1	16	-
CLUFF LAKE: D-Pit								
PNA89-3	Al-Gn	7	0	0	6	0	87	2.8
PNA89-5	Al-Gn	0	0	0	4	57	39	3.1
PNA89-9	Al-Gn	0	47	0	4	41	8	10
PNA90-1	Al-Gn	0	22	8	8	5	57	-
PNA90-2	Ft-Gg	2	28	43	4	5	18	-
PNA90-3	Gn	3	55	23	2	3	14	-
PNA90-4	Ft-Gg	1	20	10	11	7	52	-
PNA90-5	Gn	1	43	5	4	10	37	-

Step 1: $MgCl_2$-extractable/exchangeable
Step 2: NaOAc + HOAc-extractable/carbonate-bound and easily acid-soluble
Step 3: H_2O_2 + Na_2CO_3-extractable/uraninite, organic- and sulphide-bound
Step 4: $NH_2OH.HCl$-extractable/amorphous Fe-oxide-bound
Step 5: Dithionate-Citrate-extractable/crystalline Fe-oxide-bound
Step 6: HF + $HClO_4$ + HNO_3-extractable/residual minerals

* Al-Gn= Aluminous Gneiss; ClSt= Claystone; Ft-Gg= Fault Gouge; Gn= Gneiss; Gr-Gn= Graphitic Gneiss; Ma-Gn= Mafic Gneiss; Sst= Sandstone.

3.2.4 The Fe-O-C-S-H system
(D. Kettlewell)

3.2.4.1 Introduction

The study of phase equilibria and redox chemistry for the Fe-O-C-S-H system in the Cigar Lake uranium deposit has identified the need for an internally consistent thermodynamic database for this system, upon which all future modelling calculations for the iron system can be based. Having internally consistent Gibbs energy data is a necessity for various modelling calculations. It is important that once the Gibbs energy of a component species (ie. $Fe^{2+}_{(aq)}$) is defined, the Gibbs energy values for the remaining ferrous iron species should have that value. Much of the data used by previous authors in modelling iron phase relationships was obtained from various sources such as the National Bureau of Standards (NBS) compilation tables (Wagman et al. 1982, although Fe-data were compiled in 1966), or the U.S. Geological Survey (USGS) Bulletin 1452 (Robie et al. 1979). These compilations may not include the most recent free energy values for the iron system. The standard Gibbs free energies of formation ($\Delta G°_f$) that were compared in this study are shown in Table 3.11.

3.2.4.2 Free Energies of Fe^{2+} and Fe^{3+}

Fe^{2+}

The standard free energies of formation of Fe^{2+} compared in this study range from -78.87 to -91.21 kJ/mol (Table 3.11). Values from the USGS (Robie et al. 1979) and the NBS (Wagman et al. 1982) compilations give values that range from -78.87 to -78.90 kJ/mol for Fe^{2+} respectively. These values are very close, and it is not surprising that Robie et al. (1979) ultimately reference their value from an earlier NBS compilation of Wagman et al. (1969). Although the data of Wagman et al. (1982) compared in this study were retrieved from the 1982 NBS tables, the iron data were compiled in 1966. The sources of the data are not listed in the NBS tables, so it is difficult to verify these values. Larson et al. (1968) report values for Fe^{2+} that are substantially lower (-91.21 $\pm$ 2.09 kJ/mol) than those quoted by Wagman et al. (1982) and Robie et al. (1979). Larson et al. (1968) calculated heats of formations ($\Delta H°_f$) and entropies ($\Delta S°$) from the solubility of $FeSO_4 \cdot 7H_2O$ (c) (melanterite). The value for $\Delta H°_f$ was found to be -92.5 kJ/mol, which is much more negative than the value of -89.1 kJ/mol reported by Wagman et al. (1982). Larson et al. (1968) also considered other data that supported the lower heat of formation value. Sadiq and Lindsay (1979, 1981) conducted an extensive review of the thermodynamic data available for Fe^{2+}, and adopt the Gibbs energy value of Larson et al. (1968). Their rationale was that Larson et al. (1968) used the most current reliable data in their calculations. This study adopts the free energy value proposed by Larson et al. (1968). This value of $\Delta G°_f$= -91.21 kJ/mol for Fe^{2+} was also accepted by Langmuir (1969), Tremaine et al. (1977), Tremaine and LeBlanc (1980), and Taylor and Owen (1993).

Fe^{3+}

The free energy of formation values for Fe^{3+} compared here range from -16.82 to -4.6 kJ/mol (see Table 3.11). These values are based upon calculations of the Fe^{2+}/Fe^{3+} electrode potential. Currently, the best available data for the oxidation potential of the

Fe^{2+}/Fe^{3+} electrode leads to a value of 0.770 V (Whittemore and Langmuir 1972). From the relationship:

$$\Delta G^\circ_f = -nFE^\circ$$

and the adopted value for the free energy of Fe^{2+}, a value of ΔG°_f=-16.92 kJ/mol is obtained for Fe^{3+}. This is the free energy value for Fe^{3+} adopted in this study.

3.2.4.3 Other Fe-species

To maintain internal consistency in the thermodynamic parameters for the remaining iron species, the free energies of Fe^{2+} and Fe^{3+} adopted here, along with the appropriate equilibrium constants for individual formation reactions, must be used in calculating their free energies. This has been done by Sadiq and Lindsay (1979), who went to much trouble to generate an internally consistent database for iron species (among other elemental species). In some cases, however, more recent equilibrium constants or solubility products are available, and these were used here to calculate more up-to-date internally consistent free energy values (Table 3.11). Also, recently published calorimetric data for hematite and magnetite have been used for these minerals (Hemingway 1990). The data listed are considered only for 298.15 °K and 100 kPa.

Hydrated Ferrous Iron Species
The hydrated ferrous iron species of interest include:

$Fe(OH)^+$	logK= -9.5	(Baes and Mesmer 1976; Nordstrom et al. 1990)
$Fe(OH)_{2(aq)}$	logK= -20.6	(Baes and Mesmer 1976)
$Fe(OH)_3^-$	logK= -31	(Baes and Mesmer 1976)

The equilibrium constants for these species are based upon the general reaction:

$$Fe^{2+} + xH_2O \Leftrightarrow Fe(OH)_x^{2-x} + xH^+.$$

When calculating the free energies for these species from the above equilibrium constants and using the free energy for Fe^{2+} adopted in this study, the following values are obtained: -274.16 kJ/mol, -447.97 kJ/mol and -625.77 kJ/mol for $Fe(OH)^+$, $Fe(OH)_{2(aq)}$, and $Fe(OH)_3^-$, respectively. Tremaine and Leblanc (1980) derived free energy values for these species from experimental work on the solubility of magnetite. However, to maintain internal consistency within this compilation, the above calculated free energies are selected. Sadiq and Lindsay (1979) preferred the logK for $Fe(OH)_{2(aq)}$ of Hem and Cropper (1959) over that of Baes and Mesmer (1976), yet did not give a specific reason for their preference.

$Fe(OH)_2$ (solid)
The free energy for $Fe(OH)_{2(s)}$ was reported as -491.95 kJ/mol by Sadiq and Lindsay (1979). This was based on the reaction:

$$Fe(OH)_{2(s)} \Leftrightarrow Fe^{2+} + 2OH^-$$

with a logK value of -15.1. This logK value was the average equilibrium constants of several different studies. Baes and Mesmer (1976) report an equilibrium constant of logK= 12.85 for the reaction:

$$Fe(OH)_{2(s)} + 2H^+ \Leftrightarrow Fe^{2+} + 2H_2O.$$

The free energy of $Fe(OH)_{2(s)}$ calculated using this logK, along with the adopted free energy of Fe^{2+} (Table 3.11), gives a free energy value of -492.84 kJ/mol. This free energy will be accepted in this study.

Hydrated Ferric Iron Species

The hydrated ferric iron species of interest include:

$Fe(OH)^{2+}$	logK= -2.19	(Baes and Mesmer 1976; Nordstrom et al. 1990)
$Fe(OH)_2^+$	logK= -5.67	(Baes and Mesmer 1976)
$Fe(OH)_{3(aq)}$	logK= <-12	(Baes and Mesmer 1976)
	logK= -12.07	(Hem and Cropper 1959; Sadiq and Lindsay 1979; Langmuir 1969)
	logK= -12.56	(Nordstrom et al. 1990)
$Fe(OH)_4^-$	logK= -21.6	(Baes and Mesmer 1976; Nordstrom et al. 1990)

The equilibrium constants for these species are based on the general equation:

$$Fe^{3+} + xH_2O \Leftrightarrow Fe(OH)_x^{3-x} + xH_2O.$$

For the species $Fe(OH)_{3(aq)}$, the equilibrium constant used in this compilition has the value logK= -12.07 (Hem and Cropper 1959), which has been accepted by Sadiq and Lindsay (1979) and Langmuir (1969). Baes and Mesmer (1976) report a general value of logK <-12, while Nordstrom et al. (1990) report a value of logK= -12.56. However, Nordstrom et al. (1990) reference this value from Baes and Mesmer (1976). Therefore, the value put forth by Nordstrom et al. (1990) may be erroneous. Calculating the free energies from the above equilibrium constants and the adopted free energy for Fe^{3+} leads to the values -241.60 kJ/mol, -458.91 kJ/mol, -659.55 kJ/mol and -842.33 kJ/mol for the species $Fe(OH)^{2+}$, $Fe(OH)_2^+$, $Fe(OH)_{3(aq)}$, and $Fe(OH)_4^-$, respectively. These values are adopted for this compilation.

$Fe(OH)_3$ (ferrihydrite)

Nordstrom et al. (1990) report logK values of 3.0 to 5.0 for microcrystalline to amorphous $Fe(OH)_3$ respectively for the reaction:

$$Fe(OH)_{3\ (s)} + 3H^+ \Leftrightarrow Fe^{3+} + 3H_2O.$$

Sadiq and Lindsay (1979) distinguished two $Fe(OH)_{3(s)}$ phases: one for amorphous material and one for soil material. These phases are distinguished as amorphous ferrihydrite (about 4 days old) with a logK of 3.54, and soil ferrihydrite (found in natural soils) with a logK of 2.70, respectively. The occurrence of soil ferrihydrite is reported by Lindsay (1979) and Norvell and Lindsay (1982). This "soil-Fe" can be thought of as a phase with a greater

degree of structural order than the phases referenced by Nordstrom et al. (1990). It is unclear what the exact structure of "soil-Fe" is, but, because it occurs naturally in soils, it may more closely reflect the ferrihydrite present in natural environments such as Cigar Lake. The three forms of ferrihydrite reported here include the amorphous and microcrystalline varieties as reported by Nordstrom et al. (1990), and the soil variety as reported by Lindsay (1979). These are denoted as amorphous (am), microcrystalline (mc), and soil (soil). Using a logK of 5.0 for amorphous ferrihydrite (Nordstrom et al. 1990), along with the free energy of Fe^{3+} adopted here (Table 3.11), the free energy is calculated as -699.83 kJ/mol. Using a logK of 3.0 for microcrystalline ferrihydrite (Nordstrom et al. 1990), and the free energy of Fe^{3+} adopted here (Table 3.11), the free energy is calculated as -711.24 kJ/mol. Finally, using a logK of 2.70 for "soil-Fe" (Norvell and Lindsay 1982), and the free energy of Fe^{3+} adopted here (Table 3.11), the free energy for soil-ferrihydrite is calculated as -712.95 kJ/mol. These values are presented in Table 3.11.

α-FeOOH (goethite)

Gibbs energy values for goethite (α-FeOOH) range from -488.55 kJ/mol to -491.29 kJ/mol (Robie et al. 1979; Sadiq and Lindsay 1979). Sadiq and Lindsay (1979) calculated their value of -491.29 kJ/mol, from the reaction:

$$0.5\alpha\text{-}Fe_2O_{3(c)} + 0.5H_2O \Leftrightarrow \alpha\text{-}FeOOH_{(c)}$$

with the value for ΔG°_r of this reaction from Schmalz (1959). Nordstrom et al. (1990) reports an equilibrium constant for the reaction:

$$\alpha\text{-}FeOOH + 3H^+ \Leftrightarrow Fe^{3+} + 2H_2O$$

of logK= -1.0. This value originated from Langmuir and Whittemore (1971). Using this logK value and the revised free energy data for Fe^{3+} accepted in this study, recalculation leads to a free energy value of -496.89 kJ/mol. This free energy is adopted in this study.

α-Fe_2O_3 (hematite)

Hematite (α-Fe_2O_3) free energy values in this comparison range from -742.20 to -744.12 kJ/mol. Sadiq and Lindsay (1979) report a value -744.12 kJ/mol calculated from ΔH°_f= -826.05 kJ/mol and S°= 87.44 J/deg.mol (Stull et al. 1971, and Grønvold and Westrum 1959, respectively). Hemingway (1990) reports a free energy value for hematite as ΔG°_f= -744.273 kJ/mol from calorimetric studies. This value is used by Taylor and Owen (1993). The free energy value for hematite from Hemingway (1990) is adopted in this study.

Fe_3O_4 (magnetite)

The reported free energy values for magnetite (Fe_3O_4) range from -1012.57 to -1018.68 kJ/mol. Sadiq and Lindsay (1979) reported a value of -1018.68 kJ/mol, which was calculated from ΔH°_f= 1120.43 kJ/mol (Salmon, 1961) and S°= 150.75 J/deg.mol (Grønvold and Westrum 1962). Hemingway (1990) reports a free energy for synthetic magnetite of -1012.57 kJ/mol, which is equivalent to the value reported by Robie et al. (1979) and was used by Taylor and Owen (1993). The free energy of magnetite from Hemingway (1990) is adopted in this study.

TABLE 3.11
COLLECTED STANDARD FREE ENERGIES OF FORMATION ($\Delta_f G°$ kJ/mol)

Species *	Robie et al. 1978	Wagman et al. from 1966	Larson et al. 1968	Sadiq and Lindsay 1979	**This Study**
Fe^{2+}	-78.87±1.0	-78.90	-91.21±2.09	-91.21	-91.21[1]
Fe^{3+}	-4.6±1.0	-4.70	-16.74±2.2	-16.82	-16.83[2]
$Fe(OH)^{2+}$		-277.4		-289.91	-274.16[3]
$Fe(OH)_2(aq)$				-474.01	-447.97[3]
$Fe(OH)_3^-$		-614.9		-620.15	-625.77[3]
$Fe(OH)_2(s)$		-486.5		-491.95	-492.24[3]
$Fe(OH)^{2+}$		-229.41		-241.50	-241.60[4]
$Fe(OH)_2^+$		-438.0		-458.69	-458.91[4]
$Fe(OH)_3(aq)$		-659.3		-653.62	-659.55[4]
$Fe(OH)_4^-$				-842.32	-842.33[4]
$Fe(OH)_3$ (am)		-696.5		-708.14	-699.93[5]
$Fe(OH)_3$ (mc)					-711.34[5]
$Fe(OH)_3$ (sl)				-712.95	-713.05[6]
$FeCO_3$ (Sd)	-666.70±2.09	-666.67		-677.60	-680.79[7]
FeS_2 (Py)	-160.23±1.72	-166.9		-162.26	-162.26[6]
α-FeOOH(Go)	-488.55±0.75			-491.29	-496.99[4]
α-Fe_2O_3 (He)	-742.68±1.3	-742.2		-744.12	-744.27[8]
Fe_3O_4 (Mg)	-1012.57±2.13	-1015.4		-1018.68	-1012.57[8]
S°	0.00	0.00		0.00	0.00
HS^-	12.10±0.85	12.08		12.18	12.18[6]
$H_2S(aq)$		-27.83		-27.91	-27.91[6]
SO_4^{2-}	-744.63±0.12	-744.53		-744.54	-744.54[6]
$CO_2(g)$		-394.36		-394.38	-394.38[6]
CO_3^{2-}	-527.90±0.12	-527.81		-527.94	-527.94[6]
HCO_3^-	-586.85±0.12	-586.77		-586.89	-586.89[6]
$H_2CO_3(aq)$	-623.17±0.12	-623.08		-623.21	-623.21[6]
H^+	0.00	0.00		0.00	0.00
OH^-	-157.33±0.09	-157.244		-157.29	-157.29[6]
H_2O	-237.14±0.08	-237.129		-237.18	-237.18[6]

* (am)= amorphous; (mc)= micro-crystalline; (sl)= ferrihydrite variety in soils; (Sd)= siderite; (Py)= pyrite; (Go)= goethite; (He)= hematite; (Mg)= magnetite

1 from Larson et al. (1968)

2 recalculated from the Fe^{2+}/Fe^{3+} electrode potential 0.770 V (Whittemore and Langmuir, 1972) and $\Delta_f G°$ for Fe^{2+} adopted above

3 recalculated using $\Delta_f G°$ for Fe^{2+} adopted above and equilibrium constants from Baes and Mesmer (1976)

4 recalculated using $\Delta_f G°$ for Fe^{3+} adopted above and equilibrium constants from Baes and Mesmer (1976)

5 recalculated using $\Delta_f G°$ for Fe^{3+} adopted above and equilibrium constants from Nordstrom et al. (1990)

6 from Sadiq and Lindsay (1979)

7 recalculated using $\Delta_f G°$ for Fe^{2+} adopted above and solubility data from Bruno et al. (1992)

8 from Hemingway (1990)

$FeCO_3$ (siderite)

The free energy of siderite is reported as -666.70 and -666.67 kJ/mol by Robie et al. (1979) and Wagman et al. (1982, compiled in 1966), respectively. Sadiq and Lindsay (1979) report the lower value of -677.60 kJ/mol. This is calculated from a logK value of 10.24 (Singer and Stumm 1970) for the reaction:

$$FeCO_3 \Leftrightarrow Fe^{2+} + CO_3^{2-}$$

for synthetic siderite. Nordstrom et al. (1990) give a range of solubility product constants for siderite, based upon the above reaction. These are logK = -10.89 and -10.45 for crystalline to (freshly?) precipitated siderite respectively. The range in siderite solubility depends upon the "degree of crystallization." This refers to particle size effects, order-disorder phenomena and defect structures of the mineral (in this case, siderite) (Nordstrom et al. 1990). Braun (1991) measured solubilities of synthetic siderite from 30 to 80 °C, and calculated the linear expression for the variation of solubility with temperature as:

$$pK_{sp} = 0.0314T + 10.20 \quad (T \text{ in } °C).$$

Substitution of 25 °C into this expression yields a $logK_{sp}$ = -10.99, which compares favourably with the value given by Nordstrom et al. (1990) for crystalline siderite. The free energy calculated from the solubility of Braun (1991) is -681.67 kJ/mol, which is similar to the value of Sadiq and Lindsay (1979). Bruno et al. (1992) report a solubility constant for the above reaction as $logK_{sp} = -10.8 \pm 0.2$. Recalculating the free energy then gives $\Delta G°_f$ = -680.79 kJ/mol (utilizing the adopted free energy of Fe^{2+}). All values are very similar and this study adopts the solubility of Bruno et al. (1992), resulting in the free energy of $\Delta G°_f$ = -680.79 kJ/mol (Table 3.11).

FeS_2 (pyrite)

Wagman et al. (1982) report a $\Delta G°_f$ value of -166.9 kJ/mol for FeS_2 (pyrite). Robie et al. (1979) report a $\Delta G°_f$ of -160.23 kJ/mol, which originated from Toulmin and Barton (1964). Sadiq and Lindsay (1979) have adopted a $\Delta G°_f$ of -162.26 kJ/mol. This was calculated from $\Delta H°_f$ = -173.64 kJ/mol and S° = 52.93 J/deg.mol from Grønvold and Westrum (1976) and Grønvold and Westrum (1962) respectively. The free energy value reported by Sadiq and Lindsay (1979) is adopted in this study.

3.2.4.4 Sulphur species

The important sulphur species in the study of the Fe-O-C-S-H system include minerals, such as pyrite, and the aqueous species S°, HS^-, $H_2S_{(aq)}$, and SO_4^{2-}. Comparison of the free energy values reported by Robie et al. (1979), Wagman et al. (1982), and Sadiq and Lindsay (1979) show very little variance (see Table 3.11). For HS^- and SO_4^{2-}, the differences fall well within the uncertainty given by Robie et al. (1979). The difference between the $H_2S_{(aq)}$ free energy of Wagman et al. (1982) and that of Sadiq and Lindsay (1979) is only <0.10 kJ/mol. Therefore, this study adopts the values given by Sadiq and Lindsay (1979).

3.2.4.5 Other Carbonate species

The important carbonate species in the study of the Fe-O-C-S-H system include the mineral siderite, the aqueous species $CO_3^{=}$, HCO_3^{-}, and $H_2CO_{3(aq)}$, and the gas $CO_{2(g)}$. The free energy for siderite has already been discussed. The aqueous carbonate species have very well defined free energy values (Table 3.11), and for all cases these values fall within the error limits proposed by Robie et al. (1979). $CO_{2(g)}$ free energies reported by Wagman et al. (1982) and Sadiq and Lindsay (1979) are very close. Therefore, this study adopts the values given by Sadiq and Lindsay (1979).

3.2.4.6 Water

The free energies for OH^- and $H_2O_{(aq)}$ (Table 3.11) show very little difference. In fact, any difference falls within the error ranges proposed by Robie et al. (1979). All the values adopted by Sadiq and Lindsay (1979) were taken from CODATA (1976). These values are also adopted for this study.

3.2.4.7 References

BAES, C.F. Jr. and MESMER, R.E. 1976. *The Hydrolysis of Cations.* John Wiley & Sons, 489p.

BRAUN, R.D. 1991. Solubility of iron(II) carbonate at temperatures between 30 and 80°. Talanta, **38**, 205-211.

BRUNO, J., WERSIN, P. and STUMM, W. 1992. On the influence of carbonate in mineral dissolution: II. The solubility of $FeCO_3$ (s) at 25°C and 1 atm total pressure. Geochim. Cosmochim. Acta, **56**, 1149-1155.

CODATA 1976. Report of the CODATA task group on key values of thermodynamics. CODATA Bull., **17**.

GRØNVOLD, F. and WESTRUM, E.F. Jr. 1959. α-ferric oxide. Low temperature, heat capacity, and thermodynamic functions. J. Am. Chem. Soc., **81**, 1780-1783.

GRØNVOLD, F. and WESTRUM, E.F. Jr. 1962. Heat capacities and thermodynamic functions of iron disulfide (pyrite), iron diselenide, and nickel diselenide from 5 to 350°K. The estimation of standard entropies of transition metal chalcogenides. Inorg. Chem., **1**, 36-48.

GRØNVOLD, F. and WESTRUM, E.F. Jr. 1976. Heat capacity of iron sulfides. Thermodynamics of markasite from 5 to 700°K, pyrite from 300 to 780°K and the transformation of markasite to pyrite. J. Chem. Thermo., **8**, 1039-1048.

HEM, J.D. and CROPPER, W.H. 1959. Survey of ferrous-ferric chemical equilibria and redox potentials. U.S. Geol. Sur. Water Supply Paper, **1459-A**.

HEMINGWAY, B.S. 1990. Thermodynamic properties for bunsenite, NiO, magnetite, Fe_3O_4, and hematite, Fe_2O_3, with comments on selected oxygen buffer reactions. Amer. Miner., **75**, 781-790.

LANGMUIR, D. 1969. The Gibbs free energy of substances in the system Fe-O_2-H_2O-CO_2 at 25°C. U.S. Geol. Surv. Prof. Paper, **650-B**, B180-B184.

LANGMUIR, D. and WHITTEMORE, D.O. 1971. Variation in the stability of precipitated ferric oxyhydroxides. In *Proc. Symp. Nonequilibrium Systems in Natural Water Chem.* (ed. J.D. Hem). Advances in Chemistry Series No. 106. Amer. Chem. Soc., 209-234.

LARSON, J.W., CERUTTI, P., GARBER, H.K. and HEPLER, L.G. 1968. Electrode Potentials and Thermodynamic Data for Aqueous Ions. Copper, Zinc, Cadmium, Iron, Cobalt, and Nickel. J. Phys. Chem., **78**, 2902-2907.

LINDSAY, W.L. 1979. *Chemical Equilibria in Soils.* John Wiley & Sons, 449p.

NORDSTROM, D.K., PLUMMER, L.N., LANGMUIR, D., BUSENBERG, E., MAY, H.M., JONES, B.F. and PARKHURST, D.L. 1990. Revised Chemical Equilibrium Data for Major Water-Mineral Reactions and Their Limitations. In *Chemical modelling of aqueous systems II* (ed. D.C. Melchior and R.L. Bassett). Amer. Chem. Soc. Symp. Series, **416**, 489-413.

NORVELL, W.A. and LINDSAY, W.L. 1982. Estimation of iron(III) solubility from EDTA chelate equilibria in soils. Soil Sci. Soc. Am. J., **46**, 710-715.

ROBIE, R.A., HEMINGWAY, B.S. and FISHER, J.R. 1979. Thermodynamic properties of minerals and related substances at 290.15K and one bar (10^5 pascals) pressure and at higher temperatures. U.S. Geol. Surv. Bull., **1452**, 456p.

SADIQ, M. and LINDSAY, W.L. 1979. Selection of standard free energies of formation for use in soil chemistry. Colorado State Univ. Experim. Station Tech. Bull., **134**, 1069p.

SADIQ, M. and LINDSAY, W.L. 1981. Standard free energy of formation of some chemical species: Discrepancies and selections. Arabian J. Sci. Eng., **6**, 95-104.

SALMON, O.N. 1961. High temperature thermodynamics of the iron oxide system. J. Phys. Chem., **65**, 550-556.

SCHMALZ, R.F. 1959. A note on the system Fe_2O_3-H_2O. Geophys. Res. J., **64**, 575-579.

SINGER, P.C. and STUMM, W. 1970. The solubility of ferrous iron in carbonate-bearing water. J. Am. Chem. Soc., **62**, 198-202.

STULL, D.R. and others. 1971. *JANAF thermochemical tables.* 2nd Ed. Dow Chemical Company, Midland, Michigan.

TAYLOR, P. and OWEN, D.G. 1993. Oxidation of magnetite in aerated aqueous media. Atomic Energy of Canada Ltd. Rep., **AECL-10821** and **COG-93-81.**

TOULMIN, P. III and BARTON, P.B. Jr. 1964. Thermodynamic study of pyrite and pyrrhotite. Geochim. Cosmochim. Acta, **28**, 641-671.

TREMAINE, P.R. and LEBLANC, J.C. 1980. The solubility of magnetite and the hydrolysis and oxidation of Fe^{2+} in water to 300°C. J. Sol. Chem., **9**, 415-442.

TREMAINE, P.R., VON MASSOW, R. and SHERMAN, G.R. 1977. A calculation of Gibbs free energies for ferrous ions and the solubility of magnetite in H_2O and D_2O to 300°C. Thermochim. Acta, **19**, 287-300.

WAGMAN, D.D., EVANS, W.H., PARKER, V.B., HALOW, I., BAILEY, S.M. and SCHUMM, R.H. 1969. Selected values of chemical thermodynamic properties. Nat. Bur. Std. Tech. Note, **270-4.**

WAGMAN, D.D., EVANS, W.H., PARKER, V.B., SCHUMM, R.H., HALOW, I., BAILEY, S.M., CHURNEY, K.L. and NUTTAL, R.L. 1982. The NBS tables of chemical thermodynamic properties. Selected values for inorganic and C_1 and C_2 organic substances in SI units. J. Phys. Chem. Ref. Data, **11 (supp. 2)**, 392p.

WHITTEMORE, D.O. and LANGMUIR, D. 1972. Standard Electrode Potential of $Fe^{3+} + e^- = Fe^{2+}$ from 5-35°C. J. Chem. Eng. Data, **17**, 288-290.

3.3 ORE MINERALOGY AND GEOCHEMISTRY

3.3.1 Introduction

(J. Cramer)

Laboratory studies on the mechanism of UO_2-fuel dissolution in groundwater have shown that the dissolution strongly depends on the redox conditions. The laboratory experiments for these studies were performed under chemically-controlled conditions to determine the effect of different parameters on the dissolution kinetics of UO_2 fuel, and they were of limited duration. Information about the long-term dissolution and oxidation behaviour of used nuclear fuel in a disposal vault can be obtained by investigating the composition of suitable uranium minerals and their environment in appropriate natural systems.

The initial observations at Cigar Lake indicated that reducing conditions dominated the water-rock/ore interaction processes throughout much of this deposit, with the exception of the red contact zone of the clay halo overlying the mineralization. Whereas ferrous mineral phases (such as sulphides (pyrite and marcasite) and carbonate (siderite)) dominate the iron mineralogy inside the halo of hydrothermally altered host rock, ferric phases (such as oxide (hematite) and oxihydroxides (ferrihydrite, goethite)) occur in this red contact zone and in parts of the main mineralization. These observations led to the speculation that radiolysis of groundwater in contact with the uranium minerals inside the mineralization may produce an oxidation potential resulting in a "redox front" characterized by the ferric phases.

The preservation of vast amounts of UO_2 (uraninite) and $USiO_4$ (coffinite) in this deposit for ~ 1 Ga, despite the potential effects of radiolysis, necessitated a detailed study of the mineralogy, geochemistry and, in particular, the surface composition of the uraninite phases. Information on the composition of the mineral surfaces having exposure to groundwater can then be further compared with measured contents of dissolved uranium and Eh values for present-day groundwaters from the mineralization. Information from the ore characterization studies and from the hydrogeochemical characterization provide the strongest link between this analog study and the modelling of the long-term stability of UO_2-fuel waste.

The initial ore-characterization work included X-ray diffraction (XRD), scanning electron microprobe (SEM) and X-ray photoelectron spectroscopy (XPS) studies carried out at the Whiteshell Laboratories in Pinawa. The results of this work have been summarized in Sections 3.3.2 and 3.3.3, with the XPS measurements providing important data on the U^{6+}/U^{4+} ratios of uraninite mineral surfaces. Further detailed characterization of the uranium ore minerals has been carried out at the University of New Mexico in Albuquerque. This work includes detailed electron microprobe (EMP) studies on uranium mineralogy, and the results are summarized in Section 3.3.4. Data obtained from this latter study provided important information on phase relationships and actual mineral compositions.

3.3.2 Characterization of ore samples
(J. Cramer, S. Sunder and P. Taylor)

3.3.2.1 Introduction

The characterization of the Cigar Lake ore samples, carried out by AECL, is summarized in this section: it includes the XPS, SEM and XRD findings on the same or similar samples to those described in Section 3.3.4.

In the paper on Cigar Lake uraninite by Sunder et al. (1988), it was stated that XRD peak profiles were observed that resembled those reported for synthetic UO_2 that had been partly oxidized to α-U_3O_7. On the basis of this observation it was concluded that the uraninite samples contained a hyperstoichiometric phase, "most likely α-U_3O_7". In retrospect, that wording (and some of the subsequent discussion) is stronger than was justified by the available data, although the conclusion falls short of any categorical claim for the existence of U_3O_7 in the examined specimens.

The possibility that the complex uraninite diffraction-line profiles may arise from partitioning of Pb and other elements between two uraninite phases was not considered, and this possibility cannot be ruled out. However, subsequent XRD and XPS results (see below) do support the conclusion that two uraninite phases **with different average uranium oxidation states** are present; the XPS data confirm an upper limit of 0.5 for the U^{6+}/U^{4+} ratio. The quality of the XRD data are insufficient to distinguish between a tetragonal phase and some assemblage of cubic phases (again, see below). This is a reflection of the crystallinity of the material. The X-ray data are "limited" primarily by poor crystallinity and consequent peak-broadening.

3.3.2.2 Samples and methodology

The XPS analyses were performed on the rough sample surfaces obtained by breaking ~4-mm-thick coupons under anaerobic conditions. The coupons were cut from the original diamond-drill core, using a high-speed diamond-blade saw and tapwater for cooling and washing. The same coupon and, where possible, the same surface of this coupon used for the XPS analysis was also analyzed subsequently by SEM and XRD. All coupons were stored in an anaerobic chamber immediately following their cutting from the core and upon completion of each analysis.

There are significant differences in the type of information and data obtained by these three instrumental techniques, depending mainly on the excitation and detection parameters (such as depth of penetration and diameter of the source beam, etc.). Whereas the XPS analysis provides information on only the 1- to 3-nm-thick surface layer of a specimen, the penetration depth of the X-rays used in XRD is much greater, and is therefore less suitable for characterization of surface layers < 1 μm thick. However, optical SEM analysis is excellent for characterizating such sample surfaces. Furthermore, the energy- and wavelength-dispersive spectrometry (EDS and WDS) analyzes used with the SEM provide generally only semi-quantitative data on composition of sub-micron features, because of the penetration depth of the electron beam and resulting X-rays.

3.3.2.3 XPS findings

The XPS results described in Section 3.3.3 and in Sunder et al. (1988, 1992) show several compositions less oxidized than U_3O_7-equivalent, and none significantly more oxidized. The main point of Sunder et al. (1988) is that the ore oxidation has not proceeded beyond the $UO_{2.33}$ stage. Three samples showed U^{6+}/U^{4+} ratios of 0.24, 0.36 and 0.37, respectively, well below 0.5 - a value expected for $UO_{2.33}$. The other two samples had U^{6+}/U^{4+} ratios of 0.47 and 0.57, i.e., values close to that for $UO_{2.33}$ (within experimental error).

The XPS analyses were carried out on 24 samples from 4 different boreholes (Table 3.12, Section 3.3.3). The measured U^{6+}/U^{4+} ratios for the ore samples from holes 69 and 145 are in general higher than for the samples from holes 220 and FH-18. One possible explanation may be the much longer time ($\sim$5 a) that the cores from holes 69 and 145 were exposed to the atmosphere before the XPS samples were cut and analyzed. The cores from holes 220 and FH-18, on the other hand, were sampled for the XPS coupons as soon as was feasible following the drilling of these cores. Furthermore, the core from hole FH-18 was packaged and stored under N_2 gas on-site, immediately following the extraction from the core barrel.

We have observed signals for both Pb^{2+} and (more recently) S^{2-} in our XPS spectra, and PbS has been identified by both XRD and SEM. However, the relative intensities of the Pb and S peaks in the XPS spectra are such that PbS cannot account for all the Pb signal. Therefore we have to suggest that some Pb^{2+} is present in a phase other than PbS. Hence the statement in Sunder et al. (1988, p.470) that "**much of the lead is in a form other than PbS**". One such form would be as Pb(II) substituted in the uraninite (hence, a Pb(II) oxide). The point is that the lead is +2, not elemental, and probably in an oxide environment; this gave some clue as to a lower limit for the redox conditions, although we do not know the PbO activity in the uraninite.

3.3.2.4 SEM findings

The SEM analyses were performed on a ISI model DS-130 instrument equipped with a Tracor Northern EDS system. The images were obtained with a 15 kV excitation voltage and typical magnifications were in the range of 1000 to 7000 times. Beam diameters for EDS and WDS spot analyses were in the range of 10 to 100 nm.

Figures 3.21 and 3.22 show the SEM images for the two samples CS615 and CS620, respectively. Crystals of uraninite, without any visible surface alteration, are embedded in a matrix of clay minerals (Figure 3.21A) or surrounded by galena (Figure 3.21B) in the dense sample CS615. The clean break-surfaces are typical for the large uraninites in this sample, and the UO_2 grain boundaries and cavity surfaces are devoid of visible reaction zones or layers containing micro-crystals that are rooted in the uraninite matrix. Small cavities in the uraninites or on grain boundaries are typically filled with fine-grained coffinite ($USiO_4$) and galena (PbS) (Figures 3.21C and 3.21D). The occurrence of an oxidation layer locally on the uraninite surfaces and in cavities, similar to that found more abundantly in sample CS620, is restricted to a more porous part of sample CS615. This latter observation

indicates that the oxidation is secondary, and would have required access to a larger aqueous reservoir in which conditions, such as redox, could change significantly compared with the isolated pockets of aqueous solution trapped in the cavities of the less porous part of the sample.

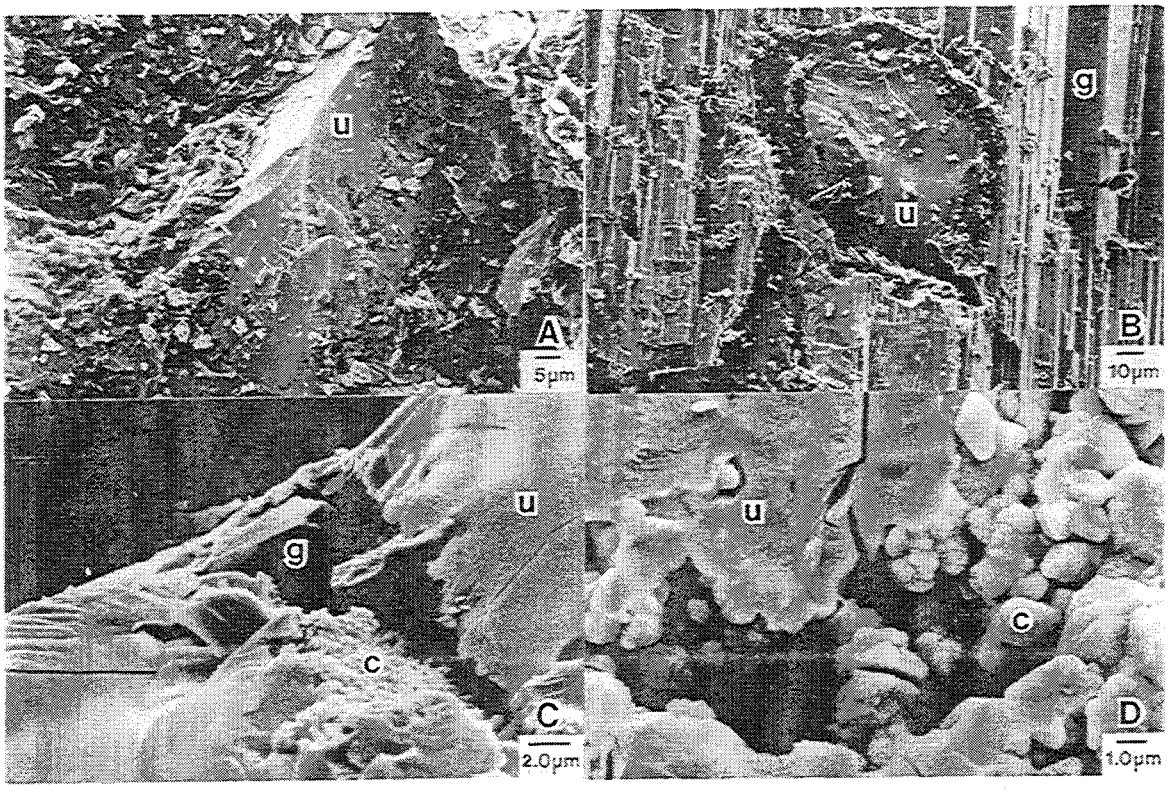

FIGURE 3.21 SEM microphotographs of uranium ore sample CS615 from drillhole 220 in the Cigar Lake deposit. The enlargements in C and D show details of cavities in the host uraninite (u) crystals, containing galena (g) and coffinite (c).

In comparison, the uraninite in the friable sample CS620 has a different appearance, showing abundant evidence for deformation and alteration (Figure 3.22A), including reaction rims and surface layers consisting of very fine-grained crystals (Figure 3.22B). These latter micro-crystals, in the micron to sub-micron size range, contain a mixture of both cavity-filling and cavity-lining minerals. The cavity-filling minerals are galena and coffinite, whereas most of the cavity-lining crystals are well rooted in the uraninite matrix (Figure 3.22C and 3.22D). The EDS and WDS spectra for these latter crystals show the presence of only uranium and oxygen, indicating that they are likely a uranium oxide. The structure of the micro-crystals resembles the tetragonal dipyramids of U_3O_7 described by George et al. (1986). The presence of U_3O_7 in these uranium ore samples would be consistent with the information obtained by XRD on the same samples, as well as with the hydrogeochemical data for groundwater from the ore zone of the Cigar Lake deposit.

Comparing these SEM observations with the XPS results shows that sample CS-615 has both low U^{6+}/U^{4+} ratios and is devoid of visible reaction zones or layers containing micro-crystals that are rooted in the uraninite matrix. On the other hand, the more oxidized sample CS-620 has higher U^{6+}/U^{4+} ratios and shows abundant evidence of reaction rims and surface layers at intergrain boundaries and around cavities in uraninite and coffinite. The presence of uranium oxide among the rooted micro-crystals on the uraninite and coffinite surfaces suggest the secondary formation of higher oxides of uranium, possibly U_4O_9 and U_3O_7.

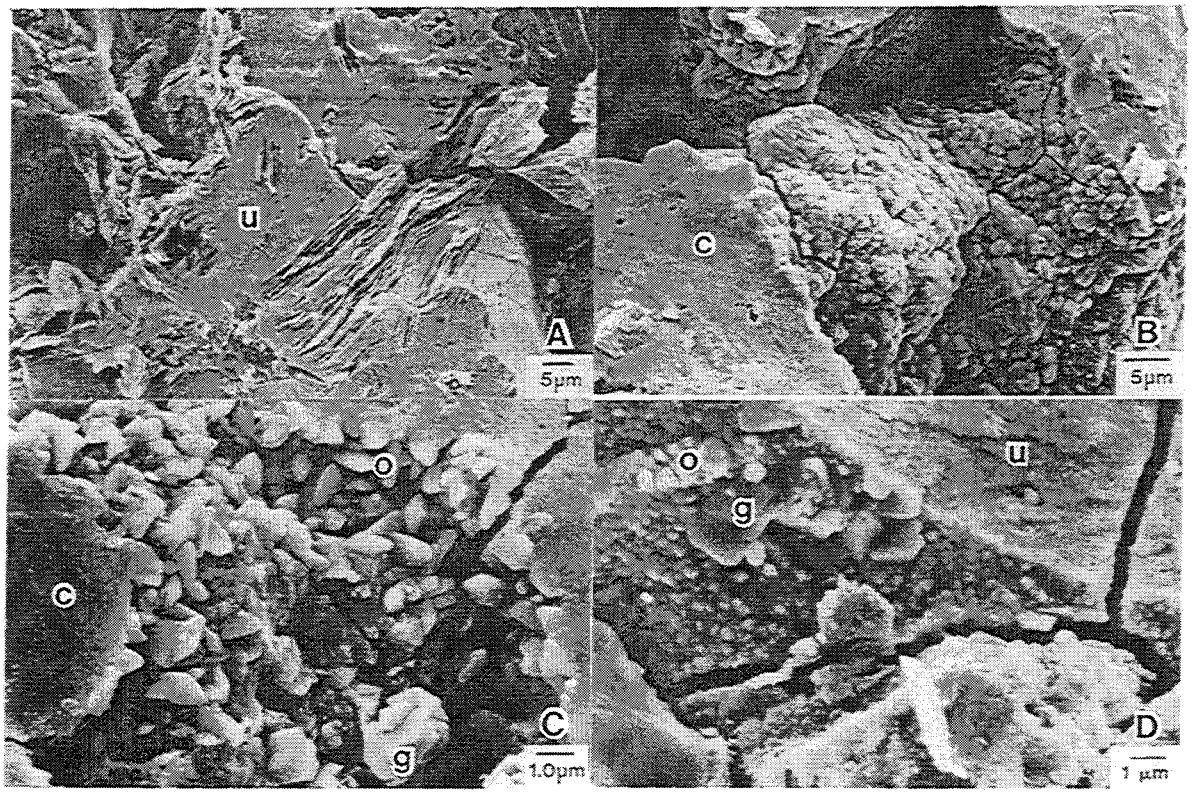

FIGURE 3.22 SEM microphotographs of uranium ore sample CS620 from drillhole 220 in the Cigar Lake deposit. The enlargements in C and D show details of cavities in the host uraninite (u) and coffinite (c), containing galena (g), coffinite and uranium oxide (o).

3.3.2.5 XRD findings

The XRD analyses were performed on an automated Rigaku instrument, model RU-220BVF with a rotating anode. The XRD patterns were obtained using a Cu-Kα beam, a 50 kV voltage and 150 mA current, and scanning speeds of between 0.1° and 10° 2θ per minute.

A summary of recent XRD work carried out on the two specimens from core of drillhole 220 is given below.

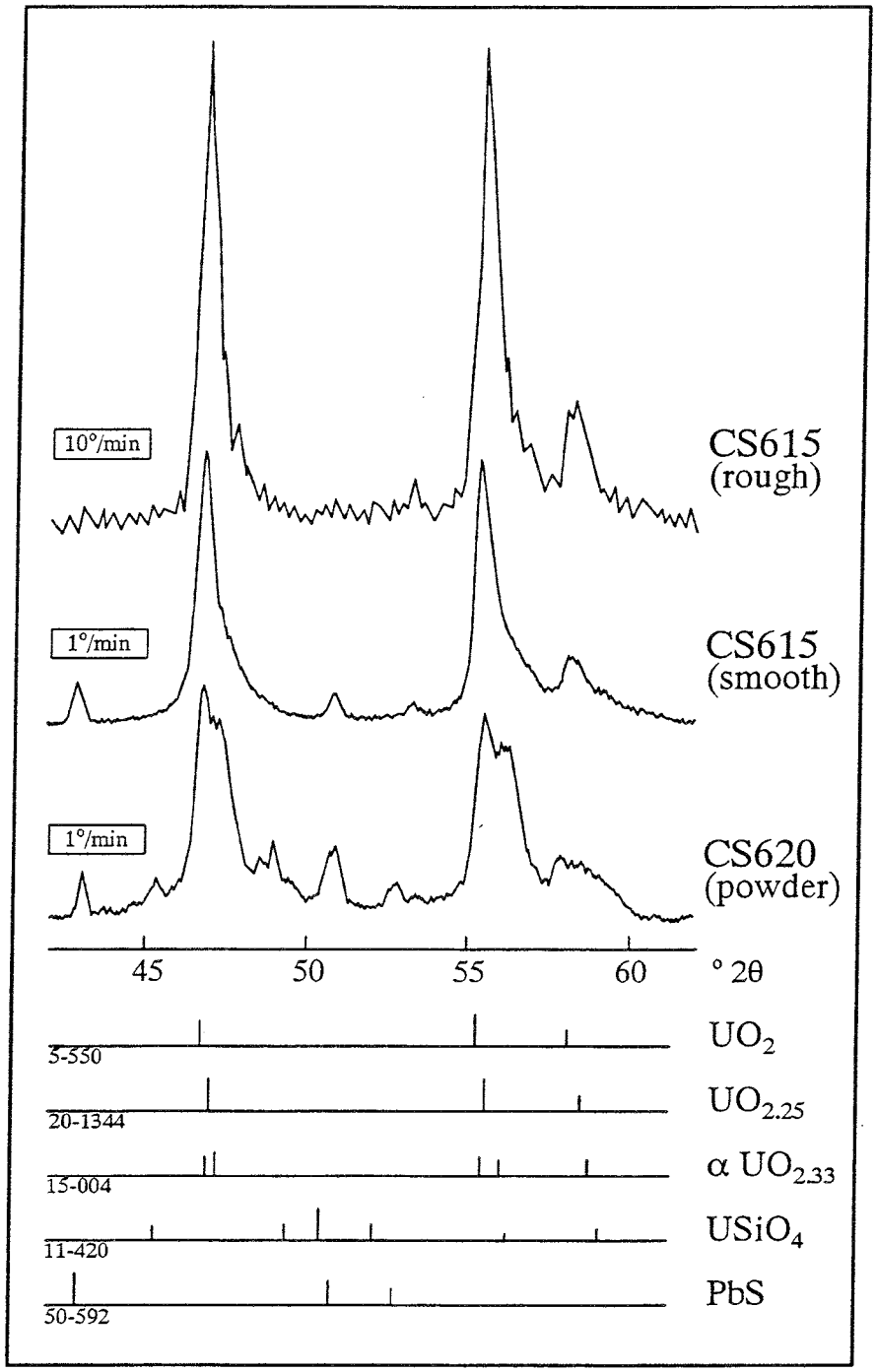

FIGURE 3.23 X-ray diffraction patterns (Cu-K_α) for uranium ore samples CS615 and CS620 from Hole 220 in the Cigar Lake deposit. The stick diagrams in the lower part of the figure show reference peak positions and relative intensities for different uranium oxides, coffinite and galena.

Figure 3.23 shows the XRD patterns for both samples CS615 and CS620. The first patttern for CS615 was obtained from the same rough break surface that was analyzed by XPS, whereas the second pattern for CS615 was obtained from the smooth saw-cut surface of the same sample. The XRD data for the CS620 specimen were obtained from two crystals that were extracted from the friable clay matrix and powdered. The dense sample CS615 contains predominantly uranium oxides and some PbS, whereas the more porous sample CS620 contains uranium oxides and silicate plus additional phases such as PbS, $CuFeS_2$ and some native copper. The following observations can be made from Figure 3.23, showing an expanded section of the XRD pattern for the (220), (311) and (222) line peaks of uraninite:

i The less oxidized material (as indicated by XPS; CS615) gives fairly sharp uraninite peaks, and we obtain cell dimensions in the range 0.5470 to 0.5476 nm. (Please note that there is a zero-angle calibration problem in the attached patterns). Peak broadening at $2\theta > 60°$ prevents more precise cell-parameter measurement, but this material appears to be similar to the Key Lake uraninite described recently by Pechmann et al. (1991).

An interesting feature of this material is the asymmetric peak shape, with a high-angle tail on each peak extending up to 2-3° 2θ higher than the extremity of a normal peak. It is not clear whether this arises from a second uraninite phase or is a consequence of the defect structure and high Pb loading. One interesting point to ponder: Pb^{2+} often has a sterically active lone-pair, and might be expected to sit off-centre in the cation sites in uraninite, in a litharge-like square-pyramidal co-ordination site. What are the crystallographic implications of this?

The significance of the slightly different profiles of the CS615 "Rough" (cleaved surface examined by XPS) and "Smooth" (saw-cut surface) is not clear at present; the possibility of some inadvertent oxidation during sample cutting should be addressed.

ii The more oxidized material (CS 620) shows more complex peaks. These appear to be a composite of the uraninite described above and a second phase with a smaller unit cell. As the diffractograms show (Figure 3.23), the material simply doesn't give a sharp enough pattern to distinguish between a tetragonal phase and some assemblage of two or even more cubic phases. We do note, however, that if the oxidized phase with the small unit cell is strongly depleted in lead, then there is less room for manoeuvring the stoichiometry away from U_3O_7.

With reference to the paper by Thomas et al. (1991), it should be noted that their work dealt with used U.S. fuel, which contains several mole percent of impurity elements (activation and fission products), and (like uraninite) is not pure UO_2. One interpretation of Thomas' findings is that tetragonal distortion in oxygen-rich uraninite-type uranium oxides is suppressed by rare-earth and/or actinide substitution. Oxidation of used

CANDU™ fuel, which typically has a lower inventory of activation and fission products than U.S. fuel, does appear to produce a tetragonal phase on prolonged oxidation at 150°C (Wasywich et al., 1993). To address the identity of U_3O_7 in the pure U—O system, we have to delve into a large body of literature not considered in our discussions to date. Furthermore, the existence or otherwise of U_3O_7 in nature may have limited relevance to its occurrence as an oxidation product on 99 %-pure UO_2 (i.e., used CANDU™ fuel).

iii U_3O_8, schoepite, uranyl or uranate have not been found in the uranium ore mineral assemblage at Cigar Lake. This observation holds true for all the samples analyzed by XRD in Pinawa as well as for all the mineralogy reports by the exploration and mining companies.

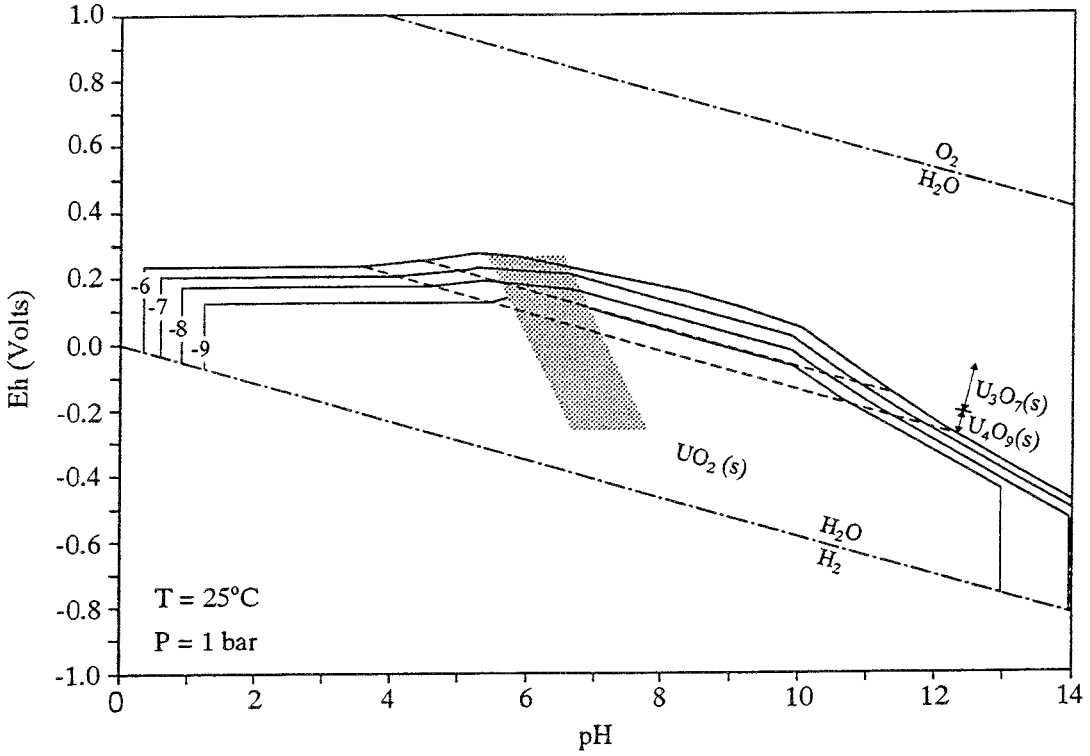

FIGURE 3.24 Isosolubility diagram for uranium oxides in Cigar Lake groundwaters. The dotted area includes all the data points for groundwaters from the ore and clay zones. The contours -6 to -9 represent dissolved-uranium concentrations from 10^{-6} to 10^{-9} mol/L U.

3.3.2.6 Geochemical discussion

The geochemical data for the water-ore interaction in the ore zone at Cigar Lake are consistent with strongly- to mildly-reducing conditions, as determined by the groundwater compositions and their uranium contents (Section 3.5.4). The shaded area in Figure 3.24

includes the measured Eh-pH data for groundwaters from the ore and clay zones. The uranium concentrations measured in these waters range from $\sim 10^{-9}$ to $\sim 10^{-7}$ mol/L U, corresponding to the solubilities of UO_2, U_4O_9 and U_3O_7 respectively. The presence of U_3O_7 along with UO_2/U_4O_9 is indicative of reducing conditions, whereas the presence of U_3O_7 along with higher U-oxides is indicative of non-reducing conditions. No U_3O_8 or other higher U-oxide phases have been found in the uranium mineralization at Cigar Lake.

Figure 3.25 reproduces Figure 2 from Garisto and Garisto (1986). The four horizontal regions in each of the solubility lines represent solubility control by the following:

i $UO_2 + U_4O_9$

ii $U_4O_9 + U_3O_7$

iii $U_3O_7 + U_3O_8$

iv $U_3O_8 + UO_3.2H_2O$ or $UO_3.2H_2O$ alone.

Thus, the sharp increase in U solubility corresponds to the point of disappearance of less oxidized phases (UO_2, U_4O_9), not the appearance of U_3O_7. We therefore prefer to use the phrase ".. the dissolution rate of the uranium oxide does not become significant until it is oxidized beyond the $UO_{2.33}$ (U_3O_7) stage." (Sunder et al. 1988, p.471).

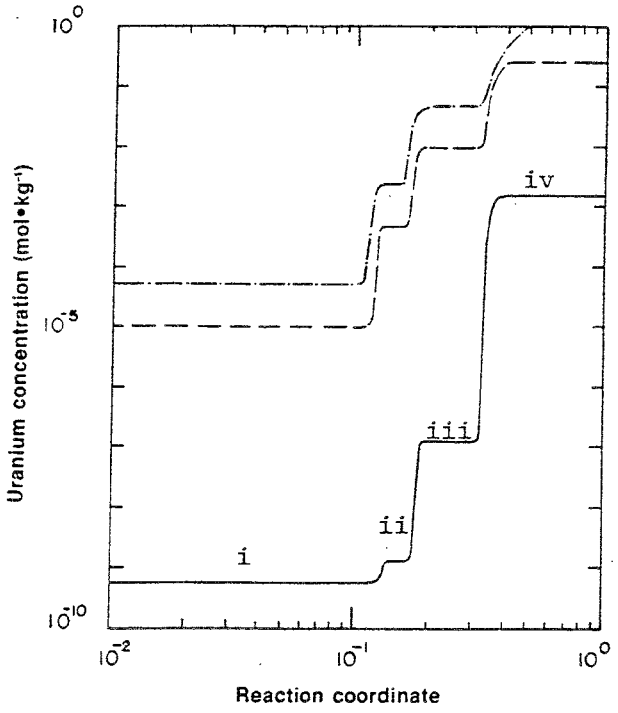

FIGURE 2. The concentration of uranium in solution at 298.15 K and pH = 10.5 as a function of the reaction coordinate, ξ, in water (solid line), in 1.61×10^{-2}-mol • kg^{-1} phosphate solution (broken line) and in 1.61×10^{-2}-mol • kg^{-1} carbonate solution (dash-dot line).

FIGURE 3.25 Reproduction of Figure 2 from Garisto and Garisto (1986).

3.3.2.7 References

GARISTO, N.C. and GARISTO, F. 1986. The dissolution of UO_2: a thermodynamic approach. Nucl. Chem. Waste Managem., **6**, 203-211.

GEORGE, E., PAGEL, M., DUSAUSAOY, Y. and GAUTHIER, J.M. 1986. Formation conditions of a tetragonal uranium oxide: α-U_3O_7 in the Brousse-Broquies Basin (Aveyron, France). Uranium, **3**, 69-89.

PECHMANN, E. von, HURTER, H., BERNHARDT, H.-J. and FRITSCHE, R. 1991. Mineralogy and crystal chemistry of anisotropic uraninite from Key Lake, Saskatchewan, Canada. In *Radioactive minerals* (ed. M. Cuney et al.). Theophrastus Publications S.A., Athens, 335-353.

SUNDER S., TAYLOR P. and CRAMER J.J. 1988. XPS and XRD studies of uranium rich minerals from Cigar Lake, Saskatchewan. In *Proc. 11th Symp. Scientific Basis for Nuclear Waste Management* Mater. Res. Soc. Proc., **112**, 465-472.

SUNDER S., CRAMER J.J. and MILLER N.H. 1992. X-ray Photo-electron Spectroscopic study of Cigar Lake uranium ore: a natural analog for used fuel. In *Proc. 15th Symp. Scientific Basis for Nuclear Waste Management.* Mater. Res. Soc. Proc., **257**, 449-457.

THOMAS, L.E., SLAGLE, O.D. and EINZIGER, R.E. 1991. Nonuniform oxidation of LWR spent fuel in air. J. Nucl. Materials, **184**, 117-126.

WASYWICH, K.M., HOCKING, W.H., SHOESMITH, D.W. and TAYLOR, P. 1993. Differences in oxidation behaviour of used candu fuel during prolonged storage in moisture-saturated air and dry air at 150 °C. Nuclear Technology, **104**, 309-329.

3.3.3 XPS studies on uranium ore from Cigar Lake

(S. Sunder and J. Cramer)

3.3.3.1 Introduction

Information about the long-term dissolution and oxidation behaviour of used UO_2 fuel in a disposal vault can be obtained by investigating the chemistry of suitable uranium minerals and their environment. The characterization of the surfaces of the uranium minerals from the ore zone in the Cigar Lake deposit provides important information with respect to the interaction of these minerals with waters in the ore zone. X-ray photoelectron spectroscopy (XPS) was used to study the uranium minerals in 24 ore samples from four different boreholes (69, 145, 220 and FH-18). XPS was used because it provides information not only about the type of the elements present in these minerals, but also on their chemical state. Furthermore, XPS is a non-destructive technique requiring no chemical preparation, and it can be used to study the composition of both crystalline and amorphous solids.

Results of the XPS studies on the samples from holes 69 and 145 have been reported by Sunder et al. (1988) and on samples from hole 220 by Sunder et al. (1992). This report summarizes the XPS work on all the samples from the four holes.

3.3.3.2 Material and methods

The 24 samples of uranium ore minerals for the XPS analysis were obtained from core of boreholes 69, 145, 220 and FH-18; sample details are listed in Table 3.12. Core sections (45 mm in diameter for holes 69, 145 and 220; 60 mm in diameter for hole FH-18) of the mineralized zone were split lengthwise, and one half was then sectioned into about 4-mm-thick coupons using a diamond-blade saw. Lake water and tap water were used for cooling during the drilling and cutting, respectively. No particular precautions were taken to prevent exposure of the uncut cores to air, but the 4-mm-thick coupons were stored under anaerobic conditions upon completion of the cutting process.

XPS studies of the samples from holes 69 and 145 were carried out using a McPherson ESCA-36 system (Sunder et al. 1988), while the samples from hole FH-18 were carried out using a PHI-5300 ESCA system (Sunder et al. 1992). The PHI system allows the transfer of samples from an inert atmosphere chamber to the evacuated sample compartment of the XPS spectrometer without exposure to atmospheric oxygen (Sunder et al. 1990a). The samples were fractured in an inert atmosphere chamber, mounted on a XPS specimen holder and analyzed. The procedure for recording the XPS spectra has been described previously by Sunder et al. (1992). The spectra were excited using Mg-Kα radiation filtered through an Al-window. Low-resolution, wide-scan survey spectra were recorded for the region 0-1100 eV. High-resolution spectra were recorded for the U 4f, C 1s, O 1s, Pb 4f, S 2p, Cu 2p and Fe 2p regions to obtain chemical-state information for these samples. The bands in the XPS spectrum of uranium that are particularly useful in determining its oxidation state result from electrons emitted from (a) the U 4f level and (b) the valence shells. Therefore, high-resolution spectra for the U 4f and valence regions were recorded to determine the oxidation state of uranium in these minerals.

TABLE 3.12
CIGAR LAKE ORE SAMPLES USED FOR XPS

Sample # CS-	Hole #	Depth m	Sample description
235C	69	419.5	Massive, black
235E	69	419.5	Massive, black
235K	69	419.5	Massive, black
372	145	441.2	Massive, black
374	145	441.1	Massive, black
615A	220	435.27	Massive, black
615B	220	435.27	Massive, black
615C	220	435.27	Massive, black
615D	220	435.27	Massive, black
620B1	220	436.36	Friable, black in white matrix
620B2	220	436.36	Friable, black in white matrix
449A1	FH-18	432.35	Mainly black with some red and white
449A2	FH-18	432.35	Black
449A3	FH-18	432.35	Reddish
449B1	FH-18	432.32	Friable, mainly white with black and red
449B2	FH-18	432.32	Black
449B3	FH-18	432.32	Red
450A	FH-18	433.89	Mixture of black and white
450B1	FH-18	433.86	Friable, mainly white with black and red
450B2	FH-18	433.86	Red
450B3	FH-18	433.86	Black
451A1	FH-18	435.07	Red
451A2	FH-18	435.07	Black
451A3	FH-18	435.07	Mixture of black, red and white

The elements seen in the XPS spectra are listed in Table 3.13. The relative abundance of the different elements seen in the XPS spectra were calculated using Equation (1) (Wagner et al. 1979; Sunder et al. 1990a).

$$C_x = \frac{I_x/S_x}{\sum_j I_j/S_j} \times 100$$

Here C_x is the atomic percentage of element x in the XPS sample, I_x represents the intensity of a band due to element x in the XPS spectrum, and S_x is the atomic sensitivity factor for that band. The summation is carried out for all elements seen in the spectrum and one band is used per element. The bands used to calculate the relative abundance of the different elements are listed in Table 3.13. These are the strongest bands in the XPS spectra of these elements, and the atomic sensitivity factors for the bands are also given in Table 3.13.

TABLE 3.13
ELEMENTS SEEN IN THE XPS SPECTRA OF CIGAR LAKE SAMPLES

Element	Main XPS Bands		
	Designation	Binding Energy	Atomic Sensitivity Factor
Na	1s	1073 eV	2.3
Cu	$2p_{3/2}$	933	4.2
O	1s	530	0.66
U	$4f_{7/2}$	380	9.00
Ca	$2p_{3/2}$	350	1.05
Th	$4f_{7/2}$	338	7.8
C	1s	280	0.25
S	2p	165	0.49
Pb	$4f_{7/2}$	138	3.82
Si	2s	155	0.19
Al	2p	120	0.17

3.3.3.3 Results and discussion

The calculated atomic concentrations for the six samples from hole 220 are given in Table 3.14. This table of the major elements seen in the Cigar Lake samples does not contain hydrogen, because H does not give a direct signal in the XPS spectra (Sunder et al. 1988). Although hydrogen cannot be determined directly, its presence can be inferred by the shift in the binding energies of the other elements, particularly oxygen. The oxygen bonded to hydrogen has higher binding energy than the oxygen present as metal oxide (Wagner et al. 1979; McIntyre et al. 1981).

The analysis of the O 1s band in the XPS spectra of samples from hole FH-18 show similar results (Table 3.15). The results for both the 220 and FH-18 samples suggest the presence of significant amounts of water in the surface of all the samples. This may reflect the exposure of the ore to aqueous environments in situ in addition to its exposure during drilling and cutting. Figure 3.26 shows the 0 1s band spectra for samples from the two sections. The O 1s bands have been resolved into O^{2-} (metal oxide), OH^- and H_2O components (McIntyre et al., 1981). The sample 620B2 shows a much higher fraction of

(H_2O + OH^-) than of O^{2-}. This is consistent with the more porous nature of this section of the core.

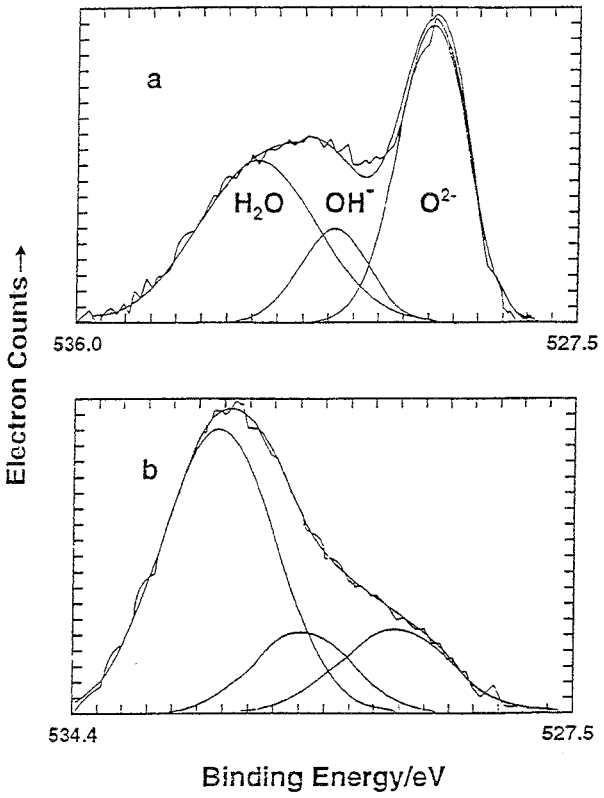

FIGURE 3.26 Resolution of the 0 ls band in the XPS spectra of two Cigar Lake samples into O^{2-}, OH^- and H_2O components (a) sample 615A and (b) sample 620B2.

TABLE 3.14
ATOMIC CONCENTRATIONS FROM XPS SPECTRA OF HOLE 220 SAMPLES

	ELEMENTS (at.%)										
Sample # CS-	Na	Cu	O	U	Ca	Th	C	Pb	Al	Si	S
620B1	-	0.7	57.3	1.7	-	0.1	16.6	0.7	9.6	13.3	-
620B2	-	0.4	47.0	2.2	-	0.14	16.8	0.37	8.06	24.5	0.49
615A	-	0.5	38.9	6.8	1.6	-	41.6	2.4	-	7.3	0.9
615B	0.5	-	40.2	4.2	3.0	-	40.5	1.2	2.1	7.3	0.9
615C	-	0.4	34.3	4.96	1.4	-	45.9	1.6	4.5	6.8	-
615D	1.2	1.2	37.8	6.1	2.6	0.3	31.1	4.1	4.0	8.2	1.5

TABLE 3.15
ANALYSIS OF THE O 1s BAND AND RELATIVE ATOMIC CONCENTRATIONS OF U, C AND O FOR FH-18 SAMPLES

Sample # CS-	Analysis of the O 1s band H_2O	OH^-	O^{2-}	Relative atomic abundances U	C	O
449A1	85.6	0.7	13.7	2.73	21.2	76.1
449A2	50.0	14.8	44.2	7.11	50.7	42.2
449A3	21.4	10.9	67.7	0.12	15.2	84.7
449B1	86.0	7.0	7.0	0.54	22.9	76.6
449B2	51.1	16.7	32.2	7.35	47.6	45.0
449B3	94.4	3.2	2.4	0.17	16.5	83.3
450A	66.5	21.0	12.5	2.64	27.4	70.0
450B1	87.1	4.8	8.1	1.56	17.9	80.5
450B2	74.1	11.2	14.7	0.10	16.0	83.9
450B3	73.9	13.5	12.6	2.13	36.0	61.9
451A1	88.5	3.4	8.1	0.02	17.6	82.3
451A2	63.7	7.6	28.7	5.75	38.0	56.3
451A3	86.0	3.7	10.3	1.46	15.2	83.4

The C 1s band was centred around 285.0 eV in all samples, indicating the presence of hydrocarbons (Wagner et al. 1979) in the ore samples. The relative atomic concentrations for U, C and O in the analysed samples from hole FH-18 are also given in Table 3.15. These data show significant abundance of organic carbon in the samples, which is in agreement with the previously reported presence of bitumen in this ore (Bruneton 1987). The signal due to inorganic carbon, i.e., carbonates, was not seen in these samples.

Lead in the ore ranges up to ~14% by weight (sample CS615B). (The composition in terms of the wt.% of different elements can be calculated from the data given in Table 3.14). The binding energies of the Pb $Uf_{7/2}$ band indicate the absence of elemental lead (Pb^0), and that all of the Pb is in the +2 (or +4) oxidation state in all samples. The lead is probably present as PbS (Bruneton 1987). The Pb present in this ore most probably arises from the radioactive decay of U and hence is dispersed throughout the uranium minerals. The crystal-chemical forces of the uranium mineral will strongly influence the oxidation state of the Pb atoms dispersed in them and would favour the formation of the Pb^{2+} state. The scatter in the atomic concentrations for different samples is indicative of the non-homogeneous nature of the ore.

The binding energy of the S 2p band seen in the XPS spectra indicates that sulphur is present in a reduced state - as sulphide. The presence of PbS in this deposit has been described by Bruneton (1987), but for most of the samples the Pb content is significantly greater than the

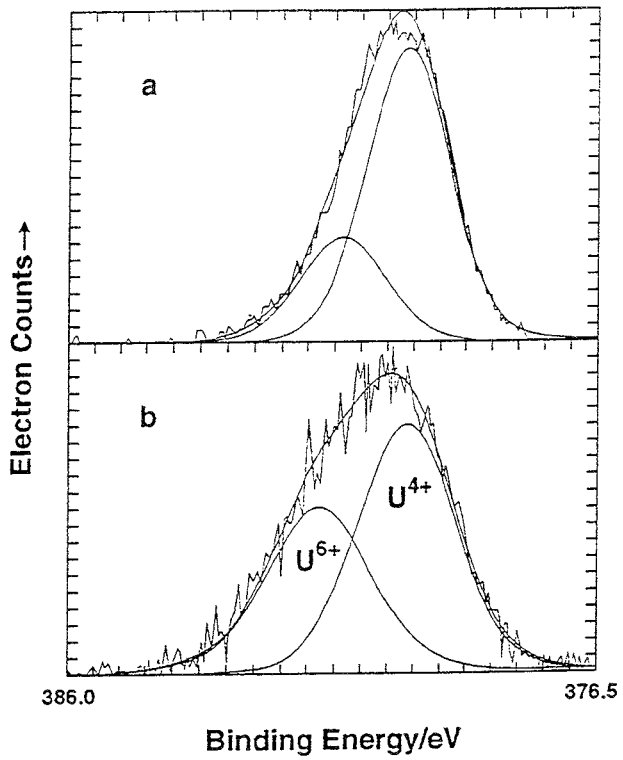

FIGURE 3.27 Resolution of U $4f_{7/2}$ band into U^{6+} and U^{4+} components for two samples from the Cigar Lake deposit; (a) sample 615A and (b) sample 620B2.

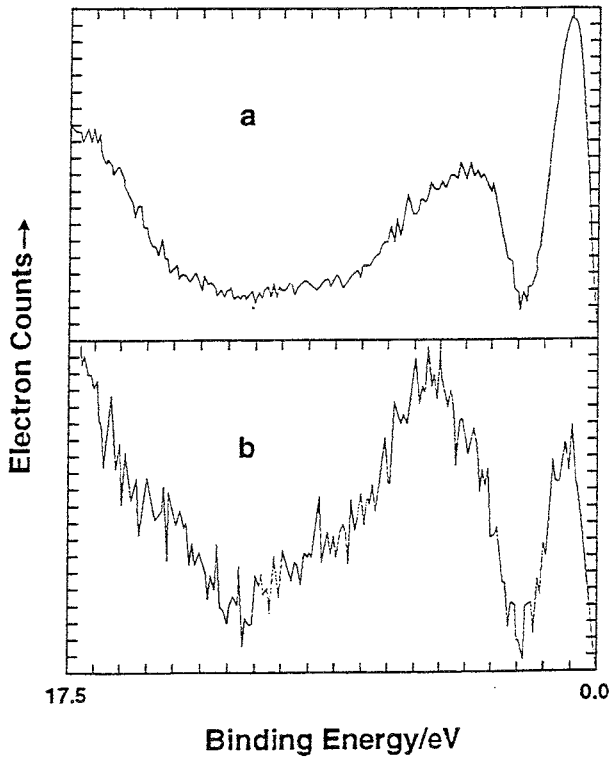

FIGURE 3.28 Comparison of the valence-band region XPS spectra of two samples from the Cigar Lake deposit; (a) sample 615A and (b) sample 620B2.

S content. Some of the Pb signal is probably arising from oxy and/or hydroxy lead moieties.

The band resulting from the U $4f_{7/2}$ core level is very sensitive to the chemical state of the uranium atom, and can be quantitatively resolved into U^{6+} and U^{4+} components to determine their relative amounts in the XPS sample (Sunder et al. 1990a; McIntyre et al. 1981). As an example, Figure 3.27 illustrates the analysis of the U $4f_{7/2}$ band in the XPS spectra of samples CS615A and CS620B2. The relative areas of the U^{6+} and U^{4+} peaks is a direct measure of the oxidation state of the uranium atoms in the sample surface. The results were verified by an analysis of the intensities of the bands in the valence region. A U^{4+} atom has two electrons in its 5f valence shell. The band seen around 1 eV in the XPS spectra of uranium compounds is assigned to these electrons. Further oxidation of U^{4+} compounds, e.g., UO_2, results in the loss of these electrons from the uranium atom and is indicated in the spectrum by a decrease in the intensity of this band. Figure 3.28 shows the valence band region spectra for the ore samples whose U $4f_{7/2}$ bands are shown in Figure 3.27. The lower intensity of the 5f band in Figure 3.28b, compared with that in 3.28a, is consistent with the results of the analysis of corresponding U $4f_{7/2}$ bands. The relative intensity measurements are not affected by any error in the binding energy scale and provide an independent check on the results from the analysis of the U $4f_{7/2}$ band.

The values for the U^{6+}/U^{4+} ratio in all samples were determined from the analysis of the U $4f_{7/2}$ band, and the results are listed in Table 3.16. The spectra due to valence bands were in qualitative agreement with the results obtained from the analysis of U $4f_{7/2}$ bands. These results show variable uranium oxidation, depending on the type of sample (see also Table 3.12). The friable samples from hole 220 (CS620B1 and 2) and the red samples from hole FH-18 show either high U^{6+}/U^{4+} ratios or a uranium signal too weak for proper analysis. The massive black ore samples and the samples with some clay matrix show U^{6+}/U^{4+} ratios between about 0.1 and 0.6, corresponding to oxidation states of the uranium equal to, or less than, that in U_3O_7. All the non-red samples from hole FH-18 and the massive black samples from hole 220 have U^{6+}/U^{4+} ratios less than 0.3, corresponding to uranium oxidation states of less than that in U_4O_9. The results for the ore samples from holes 69 and 145 are in general higher than for the samples from holes 220 and FH-18. One possible explanation may be the much longer time ($\sim$5 a) that the cores from holes 69 and 145 were exposed to the atmosphere before the XPS samples were cut and analysed. The cores from holes 220 and FH-18, on the other hand, were sampled for the XPS coupons as soon as was feasible following the drilling of these cores. Furthermore, the core from hole FH-18 was packaged and stored under N_2 gas on-site, immediately following the extraction from the core barrel.

The high U^{6+}/U^{4+} ratio seen for the samples CS620B1 and 2 probably reflects oxidation during drilling and subsequent sampling, as the rock in this section is more brittle and more permeable than the other samples. The penetration of such oxidizing waters is facilitated by the higher porosity and more friable nature of this section of the core from hole 220, where fracturing of the samples CS620B1 and 2 did follow grain boundaries rather than fresh breaks through the grains and crystals. Results of our XRD studies also support this higher oxidation of U in samples CS620B1 and 2.

TABLE 3.16
ANALYSIS OF U $4f_{7/2}$ BAND IN ALL ORE SAMPLES

Sample # CS-	U^{6+}/U^{4+}	Sample # CS-	U^{6+}/U^{4+}
235C	0.57	449A1	0.19
235E	0.37	449A2	0.20
235K	0.24	449A3	67.7
372	0.47	449B1	0.11
374	0.36	449B2	0.20
		449B3	n.a*
615A	0.29	450A	0.22
615B	0.20	450B1	0.09
615C	0.24	450B2	n.a*
615D	0.16	450B3	0.20
620B1	0.76	451A1	n.a*
620B2	0.73	451A2	0.23
		451A3	0.24

* Not analyzed because of weak U signal

Studies on the mechanism of oxidation and dissolution of UO_2 fuel have shown that the dissolution of UO_2 does not become significant until it is oxidized beyond the $UO_{2.33}$ (U_3O_7) stage (Johnson and Shoesmith 1988; Sunder and Shoesmith 1991; Sunder et al. 1981). The uranium concentrations in the groundwaters around Cigar Lake are very low (see Section 3.5). The low values of U^{6+}/U^{4+} ratio observed in this work, particularly for section CS615, are consistent with the above mechanism of UO_2 oxidation and dissolution, and explain the low uranium concentrations found in the groundwaters.

The high U^{6+}/U^{4+} ratio observed for sample CS449A3 suggests higher oxidation conditions in this section of the ore, which is supported by the presence of Fe^{3+} phases (reddish colour, Table 3.12). These local oxidized parts of the mineralization are generally found along small fractures or flanking rubble zones, suggesting that oxidizing conditions are correlated with zones of higher hydraulic conductivity than the dense clay matrix of the high-grade, low U^{6+}/U^{4+} ore.

3.3.3.4 References

BRUNETON, P. 1987. Geology of the Cigar Lake uranium deposit (Saskatchewan, Canada). In *Economic Minerals of Saskatchewan* (ed. C.F. Gilboy and L.W. Vigrass). Sask. Geol. Soc. Spec. Publ., **8**, 99-119.

JOHNSON, L.H and SHOESMITH, D.W. 1988. In *Radioactive Waste Forms for the Future* (ed. W. Lutze and R.C. Ewing). Elsevier Sc. Publ. B.V., 635-698.

McINTYRE, N.S., SUNDER, S., SHOESMITH, D.W. and STANCHELL, F.W. (1981). J. Vac. Sci. Technol., **18**, 714-721.

SUNDER, S. and SHOESMITH, D.W. 1991. Chemistry of UO_2 Fuel Dissolution in Relation to the Disposal of Used Nuclear Fuel. Atomic Energy of Canada Report, **AECL-10395**.

SUNDER, S., SHOESMITH, D.W., BAILEY, M.G., STANCHELL, F.W. and McINTYRE, N.S. (1981). Anodic Oxidation of UO_2, Part I. Electrochemical and X-Ray Photoelectron Spectroscopic Studies in Neutral Solutions. J. Electroanal. Chem., **130,** 163-179.

SUNDER, S., TAYLOR, P. and CRAMER, J.J. 1988. XPS and XRD studies of uranium rich minerals from Cigar Lake, Saskatchewan. In *Proc. 11th Symp. Scientific Basis for Nuclear Waste Management.* Mater. Res. Soc. Proc., **112**, 465-472.

SUNDER, S., BOYER, G.D. and MILLER, N.H. 1990a. XPS studies of UO_2 oxidation by alpha-radiolysis of water at 100 °C. J. Nucl. Mater., **175**, 163-169.

SUNDER, S., SAGERT, N.H., WOOD, D.D. and MILLER, N.H. 1990b. X-ray Photoelectron Spectra of γ-Irradiated Perfluorobenzene. Can. J. Appl. Spectrosc., **35**, 137-140.

SUNDER, S., CRAMER, J.J. and MILLER, N.H. 1992. X-Ray Photo-electron Spectroscopic study of uranium minerals from the Cigar Lake uranium deposit. In *Proc. 15th Symp. Scientific Basis for Nuclear Waste Management.* Mater. Res. Soc. Proc., **257**, 449-457.

WAGNER, C.D., RIGGS, W.M., DAVIS, L.E., MOULDER, J.F. and MUILENBERG, G.E. 1979. Handbook of X-ray Photoelectron Spectroscopy. Perkin-Elmer, Physical Electronic Division, Eden Prairie, Minnesota, U.S.A.

3.3.4 Uraninite from Cigar Lake: Drill Cores 220 and FH-18

(J. Janeczek and R. Ewing)

3.3.4.1 Introduction

Seven samples of the uranium ore zones of drill cores 220 and FH-18 were analysed using electron microprobe analysis (EMPA), back-scattered electron imagery (BSE), X-ray powder-diffraction analysis (XRD) and scanning-electron microscopy (SEM). Results of electron microprobe analyses of samples from drill core 220 were presented during the Forsmark meeting (Janeczek and Ewing 1991). In this report we summarize the results on the samples from drill core FH-18. The conclusions of this report are based on the analysis of all of the samples from both drill cores. The only uranium phases that we have identified using the techniques listed above are isometric uraninite (UO_{2+x}) and coffinite ($USiO_4$).

3.3.4.2 Sample descriptions

The details on the location and depth of the seven uranium ore samples from the Cigar Lake deposit are given in Table 3.17. Several morphological varieties of uraninite were distinguished in these samples, including cubic or pseudo-cubic crystals (Figure 3.29), radial aggregates (Figure 3.30), collomorphic aggregates, massive uraninite, and "brecciated" aggregates. In hand specimens, samples from drill core FH-18 differed from the samples in drill core 220 because of the presence of red hematitic clay. However, under the optical microscope, the textures of the ores are almost identical. Uranium minerals are embedded in clays (predominantly illite) and are associated with sulfides (chalcopyrite ($CuFeS_2$), pyrite (FeS_2), Cu-sulfides, Ni-sulfides and galena (PbS)). Sample CS451 contains abundant Ti-oxides, probably anatase, associated with the altered regions of uraninite.

TABLE 3.17
CIGAR LAKE URANIUM ORE SAMPLES

Sample #	Hole #	Depth interval m
CS615A1	220	435.15-435.40
CS615A3	220	435.15-435.40
CS615B2	220	435.15-435.40
CS620B3	220	436.11-436-60
CS449	FH-18	432.30-432.47
CS450	FH-18	433.84-433.93
CS451	FH-18	434.97-435.14

In samples CS449 and CS451 clusters of uraninite grains, often displaying cubic outlines, are embedded in red illite colored by a hematitic "dust". Aggregates of uraninite are rimmed by "bleached" illite. An alteration rim, distinguished in BSE images by its lower contrast, has developed along grain boundaries (Figure 3.29).

Sandwiched between the "red" samples, CS449 and CS451, is sample CS450. This sample consists of massive (in hand specimen) black uraninite embedded in white illite. Under the optical microscope, uraninite occurs as aggregates of rounded grains. Sample CS450 contains abundant elemental Cu and smaller amounts of Cu-sulfides, probably covellite (CuS). BSE images obtained at higher magnifications showed that some Cu grains are rimmed by uraninite (Figure 3.31). This suggets the cathodic precipitation of uraninite on Cu under strongly reducing conditions. Similar to samples CS449 and CS451, uraninite from CS450 displays grain embayments and other typical replacement textures. In this respect, samples from drill core FH-18 strongly resemble uraninite from drill core 220. All studied samples are altered, often severely. The replacement textures in uraninite from Cigar Lake that are indicative of dissolution of uraninite and subsequent precipitation of clays, removal of Pb, and coffinitization have been described by Janeczek and Ewing (1992). One of the most altered samples is CS620 from drill core 220. SEM images of this sample revealed the presence of micro-cavities lined with coffinite, pyrite and gypsum. A BSE image of the contact between "massive" and collomorphic aggregates of uraninite in sample CS615 from drill core 220 (Figure 3.30) suggests dissolution of the massive uraninite and the subsequent formation of clays. Lead released during this process reprecipitated as galena between the two varieties of uraninite. Galena in turn has been partially dissolved, and the space filled later by clays. This observation suggests an acidic environment, because galena is unstable at pH <7 (Janeczek and Ewing 1992). In samples from Cigar Lake, both uraninite and galena were replaced by chalcopyrite. Textural observations suggest that the dissolution of uraninite was related to the formation of illite in the range of 200 to 300 °C. Uraninite grains were also replaced by coffinite. This process was particularly pervasive along fractures and at contacts with sulfides (Janeczek and Ewing 1991, 1992).

3.3.4.3 X-ray powder diffraction analysis

The presence of sulfides, clay minerals (illite, chlorite) and coffinite in samples from Cigar Lake results in an overlapping of the diffraction maxima of their XRD patterns. This complicates detailed crystallographic studies of the uraninite. For example, there are strong peaks for uraninite, coffinite, galena, chalcopyrite and pyrite on the diffraction pattern for sample CS620B3 (clays were removed from the sample prior to analysis) (Figure 3.32). Diffraction maxima for sulfides, especially pyrite, completely or partially overlap the peaks of uraninite. High-angle tailing on the uraninite diffraction maxima reported by Cramer et al. (1991) for sample CS620B3 from drill core 220 may be caused by partial, high-angle overlapping of uraninite peaks with pyrite and chalcopyrite peaks (Figure 3.32), and cannot be taken as evidence for the presence of other uranium oxides, e.g. U_3O_7.

3.3.4.4 Chemical analysis

Averaged electron microprobe analyses of Cigar Lake uraninites are given in Table 3.18. Because of the presence of impurities (Si, Al, Fe) in most of the analysed samples, only analyses with no or little Al (less than 0.5 wt.% Al_2O_3) and with a SiO_2 content lower than 1 wt.% were considered representative of uraninite compositions. The content of UO_2 in these analyses ranges from 74.09 to 82.1 wt.%, and PbO ranges from 8.89 to 15.64 wt.%. Extreme chemical heterogeneity, even of relatively unaltered uraninite, is evident from the wide ranges of the elemental contents (Table 3.19). For instance, the content of UO_2 in CS451 varies by as much as 7.8 wt.%, and the difference between the lowest (1.8 wt.%) and the highest values (13.4 wt.%) of PbO is as large as 11.6 wt.%. Such large variations in the uranium and lead contents have also been reported from other uranium deposits in the Athabasca Basin. For example, the PbO content in samples from the Dominique-Peter deposit in the Carswell Structure ranges from 2.9 to 17.2 wt.% (Δ= 14.3 wt.%) (Pagel and Ruhlmann 1985), and the UO_2 content also varies significantly (Δ= 13.6 wt.%). The extreme heterogeneity of the Pb content can be observed in a single grain of uraninite from CS451 (Figure 3.33).

TABLE 3.18
ELECTRON MICROPROBE DATA FOR SAMPLES FROM HOLES 220 AND FH-18

220:		CS615B2			CS615A1		CS615A3	
n=		10	10	4	9	6	1	2
UO_2	wt%	81.09	81.27	78.24	77.44	80.50	75.95	75.23
SiO_2		0.36	0.72	0.32	0.23	0.56	0.23	0.29
PbO		11.46	8.48	11.27	12.04	8.73	14.13	12.92
CaO		1.54	2.03	1.48	1.30	1.80	1.09	1.70
FeO		0.38	0.48	0.29	0.32	0.48	0.13	0.22
Total		94.83	92.80	91.60	91.33	92.07	91.53	90.36

220:		CS620B3		**FH-18:**	CS449	CS450	CS451
n=		6	6	**n=**	33	21	17
UO_2	wt%	76.70	79.63		81.04	80.58	82.07
SiO_2		0.31	0.29		0.06	0.17	0.43
PbO		9.91	12.73		11.93	12.89	8.13
CaO		1.82	0.95		1.49	0.96	1.69
FeO		0.23	0.20		n.d	n.d	n.d
Total		89.06	93.80		94.52	94.60	92.64

n= number of analyses; n.d= not determined.

The relatively high Ca content, even in the least altered uraninites (from 0.6 to more than 1 wt.% CaO), suggests that this element entered the uraninite structure during its formation, substituting for uranium. This seems to be a common phenomenon in hydrothermal

uraninites, including those from the Athabasca Basin (e.g., Pagel and Ruhlmann 1985). There is a strong negative correlation between Pb and Ca in the chemical analyses of uraninites from Cigar Lake (Figure 3.34). Also, the U content tends to increase with decreasing Pb content (Figure 3.34). A poorer correlation in the latter results from the presence of a mixed-valence U that cannot be determined by EMPA. The presence of U^{6+} is suggested by the low totals in the electron microprobe analyses and by XPS results (Sunder et al. 1988, 1992). Therefore, the measured amount of U calculated in the electron microprobe analyses as UO_2 is low to the extent that U^{6+} is present. The balance of the weight fractions of UO_2, PbO and CaO suggests that the increase in U and Ca contents with decreasing Pb content was relative, and that there was no gain or loss of U during loss of Pb from the uraninite (Janeczek and Ewing 1992).

TABLE 3.19
RANGES (R) AND STANDARD DEVIATIONS (SD) FOR MAJOR ELEMENTS IN THE ELECTRON MICROPROBE ANALYSES OF URANINITES (WITH SiO_2 <0.5 wt.%) FROM DRILL HOLE FH-18

	CS449		CS450		CS451	
	R	SD	R	SD	R	SD
UO_2 wt%	78.79-83.46	1.28	78.78-84.11	1.07	77.91-85.75	2.69
PbO	7.60-13.82	1.71	7.57-14.85	1.48	1.79-13.45	4.57
CaO	1.07- 2.30	0.36	0.60- 1.40	0.28	0.78- 3.41	0.96

Several electron microprobe traverses across the cubic crystals in CS449 have not revealed any apparent chemical zoning (Figure 3.29). However, Pb seems to be slightly depleted at the margins of the crystals, suggesting preferential Pb loss at the grain boundaries (Figure 3.35). Electron microprobe analyses of altered uraninites show an enrichment in Si, Ca and Fe; whereas the Pb content decreased (Janeczek and Ewing 1991).

3.3.4.5 Chemical ages

Chemical ages of uraninites from drill core 220 range from 1309±17 Ma to 127±3 Ma (Janeczek and Ewing 1991). The oldest chemical age obtained in our study (1309±17 Ma) corresponds to the U-Pb age of the initial crystallization of the uraninite (Philippe et al. 1993). Although no rigorous calculations have been done for uraninites from drill core FH-18, estimates of the ages (Figure 3.36) may be made from the simple approximation:

Age (Ma) = 100 x %Pb (Bowles 1990).

The maximum Pb content, between 12 and 13 wt.%, corresponds to the U-Pb age of the initial uraninite crystallization. The minimum distribution of Pb, between 10 and 12 wt.% in samples from drill core FH-18 (Figure 3.36), suggests that the Pb loss is related to the crystallization of illite in the alteration halo. Illite K-Ar dates range from 1255±28 to

1148±28 Ma, whereas a sudoite+illite assemblage was dated at 815±30 Ma. The youngest stage of Pb loss may have occurred any time from most recent to about 100 Ma.

3.3.4.6 Conclusions

Based on the results summarized here and in previous work (Janeczek and Ewing 1991, 1992), we conclude the following:

1. Uraninites from drill cores 220 and FH-18 are texturally and chemically similar.

2. Uraninite in the Cigar Lake deposit underwent hydrothermal alteration under reducing conditions by dissolution, loss of lead and coffinitization. As a result of these processes, uraninite is texturally and chemically heterogeneuous on the scale of fractions of a micrometre.

3. Dissolution of uraninite was related to the formation of clays in the ore body between 1300 and 1100 Ma and was caused by saline, moderately acidic solutions at approximately 200 °C.

4. Several stages of lead loss have occurred since the formation of the deposit. These stages can be correlated with regional tectonic and magmatic events. Lead loss was not associated with significant uranium mobilization.

5. Both uranium and lead were released during coffinitization.

6. There is no mineralogical evidence for recent groundwater alteration of uraninite in the samples from drill cores 220 and FH-18.

3.3.4.7 Acknowledgements

This work was supported by the Swedish Nuclear Fuel and Waste Management Co. (SKB). The samples used in this study were obtained courtesy of Jan Cramer of AECL. The electron microprobe analyses were completed in the Electron Microbeam Analysis Facility of the Department of Geology and Institute of Meteoritics of the University of New Mexico, supported, in part, by NSF, NASA, DOE and the State of New Mexico.

3.3.4.8 References

BOWLES, J.F.W. 1990. Age dating of individual grains of uraninite in rocks from electron microprobe analyses. Chem. Geol., **83**, 47-53.

CRAMER, J.J., SUNDER, S. and TAYLOR, P. 1991. Whiteshell characterization of Cigar Lake uraninite samples. AECL/SKB/USDOE Cigar Lake Project, Internal Prog. Rep., **CLR-91-5**, 38-46.

JANECZEK, J. and EWING, R.C. 1991. Chemistry and alteration of uraninite at Cigar Lake, Canada. AECL/SKB/USDOE Cigar Lake Project, Summary Rep. Forsmark Mtg., **CLR-92-2**, Appendix.

JANECZEK, J. and EWING, R.C. 1992. Dissolution and alteration of uraninite under reducing conditions. J. Nucl. Mater., **490**, 133-156.

PAGEL, M. and RUHLMANN, F. 1985. Chemistry of uranium minerals in deposits and showings of the Carswell Structure (Saskatchewan-Canada). Geol. Assoc. Can. Spec. Paper **29**, 153-164.

PHILIPPE, S., LANCELOT, J.R., CLAUER, N. and PACQUET, A. 1993. Formation and evolution of the Cigar Lake U ore-deposit based on U-Pb and K-Ar isotope systematics. Can. J. Earth Sci., **30**, 720-730.

SUNDER, S., TAYLOR, P. and CRAMER, J.J. 1988. XPS and XRD studies of uranium rich minerals from Cigar Lake, Saskatchewan. In *Proc. 11th Symp. Scientific Basis for Nuclear Waste Management*. Mat. Res. Soc. Proc. **112**, 465-472.

SUNDER, S., CRAMER, J.J. and MILLER, N.H. 1992. X-ray photoelectron study of Cigar Lake uranium ore: a natural analog for used fuel. In *Proc. 15th Symp. Scientific Basis for Nuclear Waste Management*. Mat. Res. Soc. Proc. **257**, 449-457.

FIGURE 3.29 BSE image of cubic crystals of uraninite within illite (black) in sample CS449. Alteration rims (dark grey) in the outer portions of the crystals and embayments are indicative of dissolution of uraninite and replacement by clays. Variations in PbO and CaO contents are shown in Figure 3.35. Scale bar represents 10 μm.

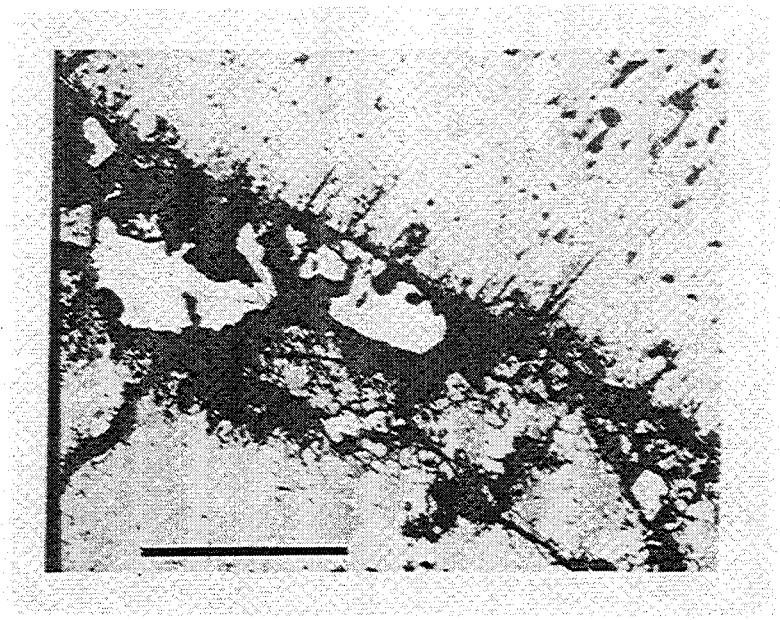

FIGURE 3.30 BSE image of the contact between radial aggregates of uraninite and "massive" uraninite in CS615. Irregular and partially dissolved grain of galena occurs in the vug between the two varieties of uraninite. The vug is filled with illite. Scale bar represents 100 μm.

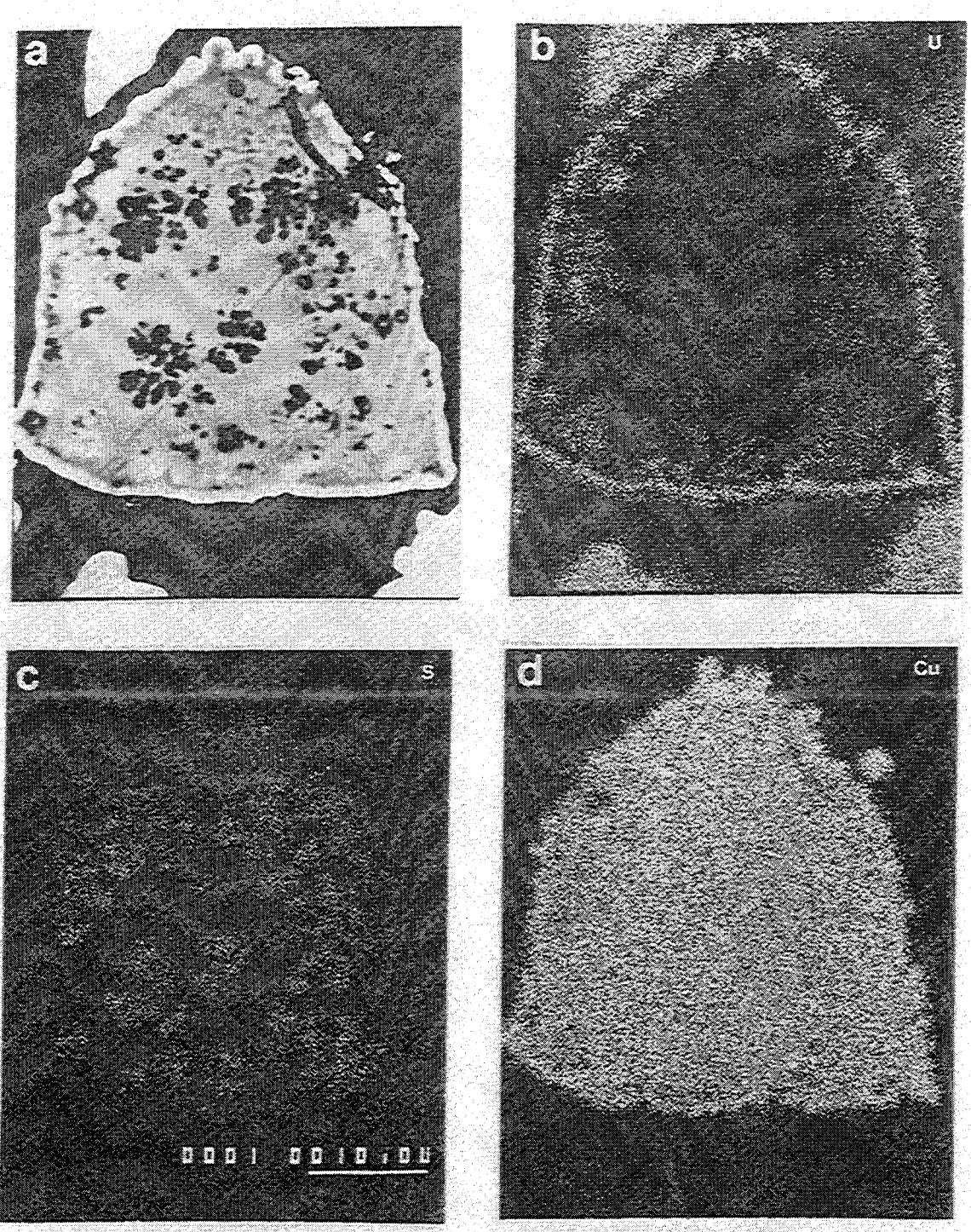

FIGURE 3.31 **A**: BSE image of a grain of elemental Cu rimmed by uraninite. Black blebs within the Cu grain consist of Cu-sulfides (covellite?). **B**: X-ray map of U-Mα. **C**: X-ray map of S-Kα. **D**: X-ray map of Cu-Kα.

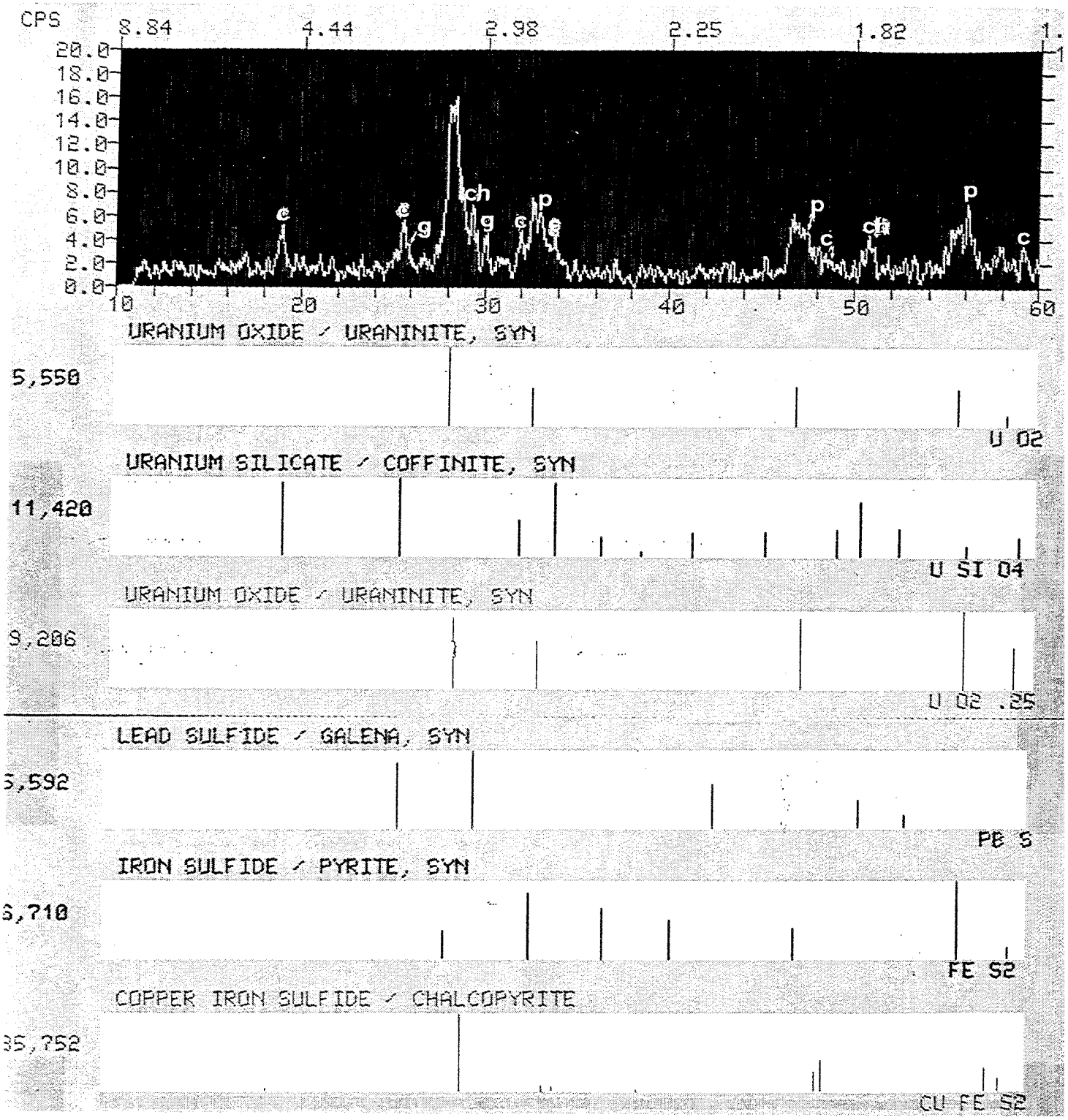

FIGURE 3.32 X-ray diffraction pattern for CS620B3. c= coffinite, ch= chalcopyrite, g= galena and p= pyrite.

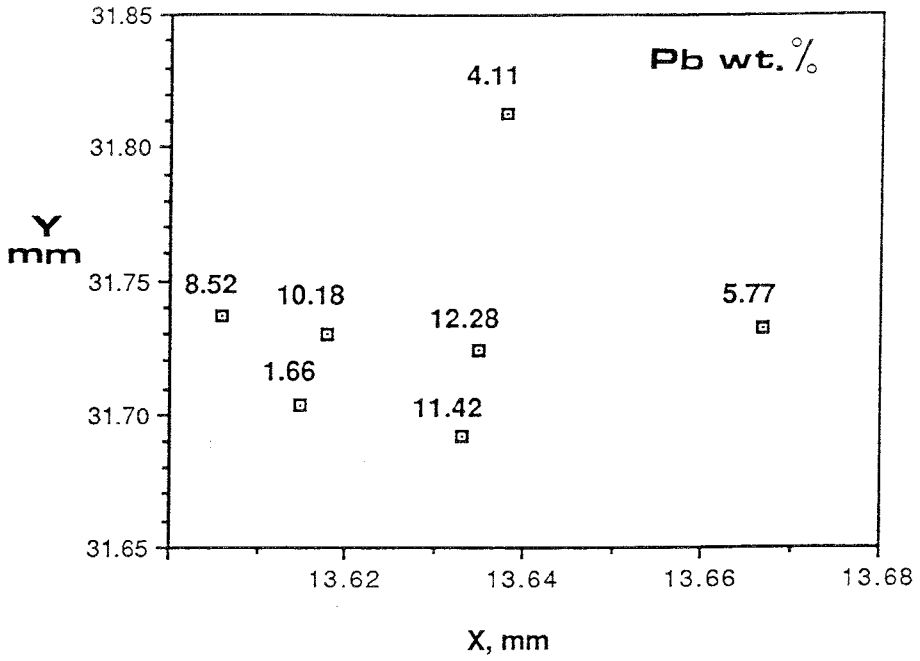

FIGURE 3.33 Lead distribution in a single grain of uraninite from sample CS451. Area covered by coordinates X and Y occurs entirely within the grain; therefore the grain boundaries are not shown.

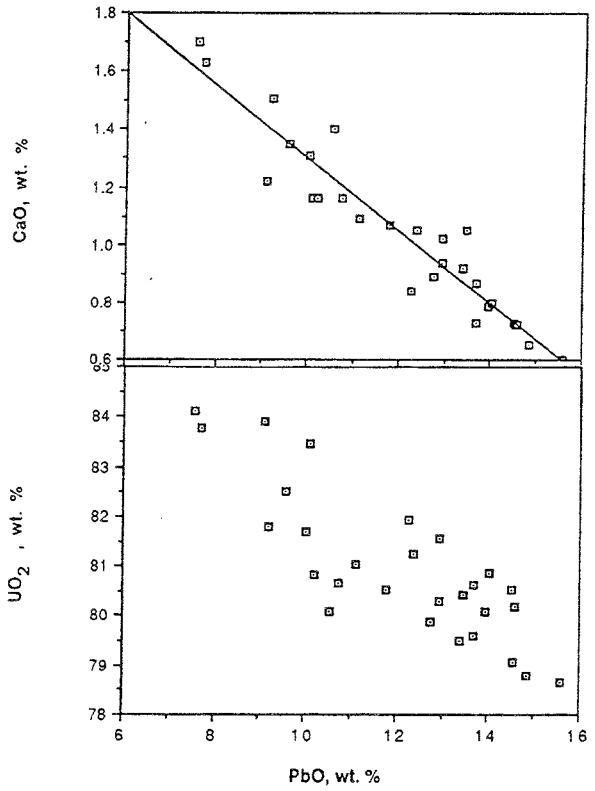

FIGURE 3.34 Plots of UO_2 and CaO contents versus PbO in sample CS450.

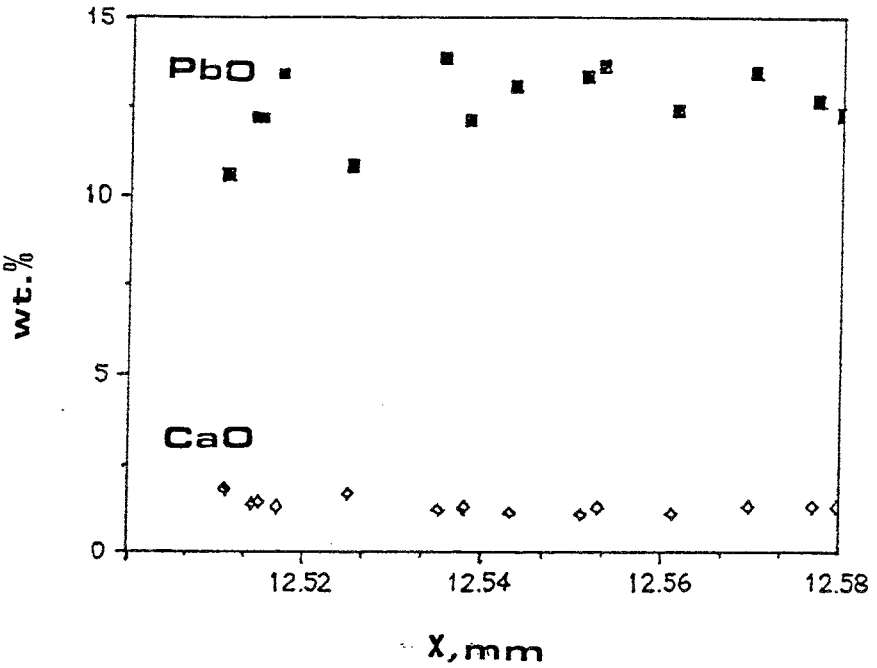

FIGURE 3.35 EPMA traverse across a crystal of uraninite in CS449 showing the distribution of PbO and CaO.

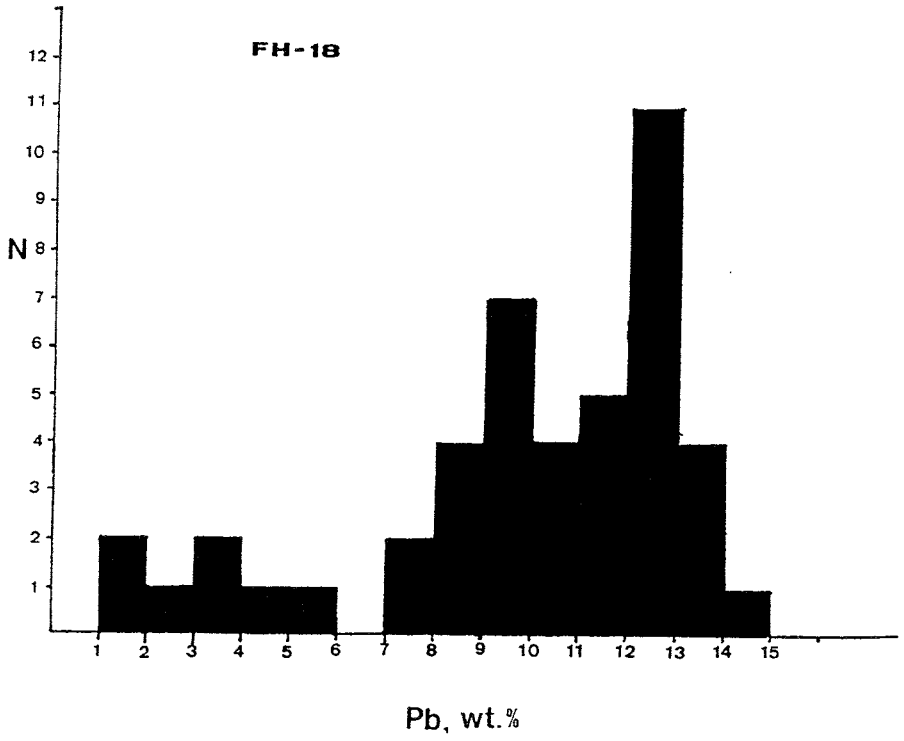

FIGURE 3.36 Histogram showing the distribution of Pb in samples from drill core FH-18.

3.4 HYDROGEOLOGICAL MODELLING
(A. Winberg and D. Stevenson)

3.4.1 Introduction

3.4.1.1 Background and scope

The Cigar Lake uranium deposit has a number of features and processes analogous to those of the concept for a high-level radioactive waste repository in crystalline rock. Notwithstanding the fact that the deposit is high-grade (up to 55 wt.% U) and is adjacent to a highly permeable sandstone, any signature of U and other radioisotopes is not detectable in sandstone groundwater some tens of metres from the periphery of the deposit. The physical and chemical properties of both the clay capsule and the groundwater around the ore deposit have been important factors in ore preservation. This report describes the overall geographical, hydrometeorological and hydrogeological framework at Cigar Lake, the types of characterization made, and the conceptualization and modelling performed.

The specific hydrogeological objectives of the project were (Cramer and Smellie 1989):

1) Characterization of the present hydrogeological environment in and around the deposit. This includes detailed modelling of the hydraulic characteristics of the deposit and adjacent rock units including the ore zone and clay zones, review of boundary conditions, calculation of flow field and estimation of overall groundwater budget. A prerequisite for this item is the establishment of a conceptual hydrogeological model at the scale studied.

2) Determination of the hydrogeologic conditions with specific regard to trace-element migration. A prerequisite is again a conceptual hydrogeological model at the scale studied. In addition, input from the established groundwater chemistry and age dating is essential.

3.4.1.2 Physical geography

Cigar Lake (464 masl) is located in a region of rolling topography created by northeastward trending, elongated hills interspersed by boggy areas and lakes (Figure 3.37). The elevated elongated hills consist primarily of Quaternary deposits in the form of eskers and drumlins with elevations reaching in excess of 500 masl. The thickness of the unconsolidated Quaternary deposits ranges between 0 and 55 m. There is an increase in topographic elevation towards the southwest. The ground surface is vegetated by small jackpine on higher elevations, whereas in the low areas close to lakes and streams, black spruce, willow, shrubs and grasses are present. Other lakes in the area are Waterbury Lake (455 masl), Sawatsky Lake (485 masl), Bizarre Lake (478 masl), Cat Lake (468 masl), Abyssmal Lake (480 masl), Aline Lake (462 masl), Thin and Tibia Lakes (461 masl) (Figure 3.37).

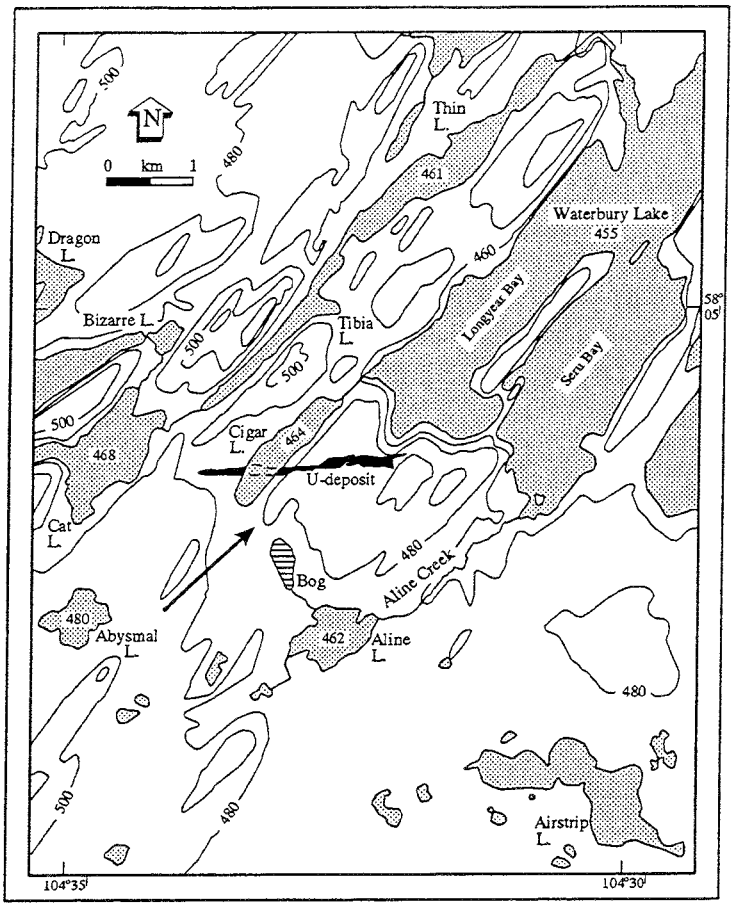

FIGURE 3.37 Map of the Cigar Lake area, showing the projected outline of the uranium mineralization and the direction of regional groundwater flow (arrow). Average water level of lakes and elevation contours are given in metres above sea level.

3.4.2 Hydrogeological data

3.4.2.1 Physical Rock Properties

3.4.2.1.1 General

This section presents the magnitude and range (variability) of the hydraulic material properties of the rock units at Cigar Lake, as inferred from the various types of hydraulic testing performed. The material properties include the hydraulic conductivity and porosity. The rock units contain both intergranular and fracture porosity, but their spatial variability is not known. Calculation of hydraulic conductivity values was based on the assumption that, over long time periods, pore spaces of the fractures and rock matrix were sufficiently interconnected to represent porous media. Subsequent groundwater-flow model simulations of water-table configuration and piezometric-level drawdown (from pumping tests) have shown the assumption to be appropriate. Representative values of these material properties have been assigned to the rock units of the conceptual model(s) presented in subsequent sections.

3.4.2.1.2 Hydraulic conductivity

The **hydraulic conductivity** ***K*** is defined as the groundwater flow rate through a unit surface ($m^3/s/m^2$ or m/s) perpendicular to the direction of flow under unit hydraulic gradient and with due consideration to the properties of the fluid. Hydraulic conductivity of all hydraulic units ranges between $4x10^{-9}$ and $3x10^{-5}$ m/s (Table 3.20; see Figures 3.40 and 3.57 for borehole locations), and up to three orders of magnitude for each of the different types of sandstone and clay units.

TABLE 3.20
RANGE OF HYDRAULIC CONDUCTIVITY IN CIGAR LAKE HYDRAULIC UNITS

Hydraulic unit	K_{min} m/s	Hole, method	K_{max} m/s	Hole, method
Basement	$4.0x10^{-9}$	WDG-137,FH_{pa}	$3.6x10^{-7}$	WDG-199,RH_{pi}
Regolith	$2.3x10^{-6}$	WDG-137,FH_{pa}	$5.6x10^{-6}$	WDG-165,FH_{pa}
UC/congl.	$3.5x10^{-9}$	WDG-165,FH_{pa}	$5.1x10^{-6}$	WDG-165,FH_{pa}
Min. ss	$2.0x10^{-8}$	WDG-79, RH_{pi}	$3.0x10^{-7}$	WDG-198,RH_{pi}
Clay	$1.1x10^{-9}$	WDG-197,RH_{pi}	$1.2x10^{-6}$	WDG-91, RH_{pi}
Clay-alt. ss	$2.0x10^{-7}$	WDG-67, RH_{pi}	$2.8x10^{-6}$	WDG-211,RH_{pi}
Lower ss	$7.8x10^{-8}$	WDG-213,RH_{pi}	$1.4x10^{-7}$	WDG-71, RH_{pi}
Upper ss	$>6.0x10^{-9}$	WDG-80, RH_{pi}	$2.0x10^{-6}$	WDG-186,FH_{pa}
Fr. alt. ss	$6.6x10^{-8}$	WDG-177,RH_{pi}	$2.8x10^{-5}$	WDG-159,FH_{pa}
OB unconsol.	$1.0x10^{-5}$	WDG-185,GD	$1.0x10^{-8}$	WDG-185,GD
OB bas. till			$<1.0x10^{-8}$	WDG-185,GD

FH= falling-head; RH= rising-head; pa= packer test; pi= piezometer test
GD= K estimated from grainsize distribution

3.4.2.1.3 Porosity

The **porosity** ***n*** is defined as the ratio of pore volume to the total volume. The kinematic (or effective) porosity n_e is defined as the ratio of pore volume actively involved in groundwater flow to the total volume. Kinematic porosity is needed to provide a means to estimate true transit times for groundwater particles, as given in the interrelation defined through Darcy's law:

$$v_p = \frac{K}{n_e} \cdot I = \frac{v_D}{n_e}$$

where v_p = particle velocity,
K = hydraulic conductivity,
n_e = kinematic porosity,
I = hydraulic gradient and
v_D = Darcy velocity.

Ideally one should use average field kinematic porosity values for particle velocity assessments, because this parameter corresponds to the porosity actually involved in the groundwater flow. Average field kinematic porosity can only be deduced from the results of tracer tests or pumping tests. Tracer tests have not been performed at Cigar Lake, and kinematic porosity can only be calculated from pumping-test data where the aquifer is homogeneous and aquifer thickness and compressibility are known. Because these conditions did not exist or were unknown for Cigar Lake rock units, a practical approach was adopted, i.e., to use the porosity values obtained from laboratory measurements made on core samples, and to assume that those numbers were close to the average field kinematic porosity values. The results from the laboratory tests indicate porosity variations between 2 and 20 %, or 0.02 and 0.2 (Smith 1983; CoreLab 1984). The porosity values assigned to each hydraulic unit are presented in Sections 3.4.3.2 and 3.4.3.3. The variation within each unit is not explicitly known but, in general, it is assumed to be within a factor of two.

3.4.2.2 Piezometry

3.4.2.2.1 General

Piezometric data were obtained from manual depth-to-water soundings and continuous fluid-pressure measurements from data loggers, made during natural piezometric-level fluctuations and during hydraulic testing in piezometer intervals and boreholes.

3.4.2.2.2 Groundwater level monitoring

Depth-to-water measurements were initially made by Beak Consultants Ltd. in 1983 (Beak 1984) in a few open boreholes and piezometers, and the data were used to construct the Beak conceptual model. Susequently, more open-standpipe piezometers were constructed in selected boreholes, and piezometric levels were measured periodically before and during the pumping test in 1987 and the flow test in 1989. From 1989 onwards, additional depth-to-water measurements in selected piezometers were made by AECL/SKB during every field trip to the site.

In 1991, continuous piezometric-level data loggers were installed by AECL/SKB in piezometers WDG-195 and WDG-79. The gauges and loggers are maintained on-site by CLMC personnel, and the data are processed by AECL in Pinawa. A comparison of water level readings made during the 1989 November field trip with those made in 1987 March indicates that the drawdown due to underground construction had generally increased by about 1 m up to that time.

An analysis of the readings performed in the AECL/SKB piezometers during the period from 1988 September to 1989 November shows decreases in piezometric levels of $\sim$0.5 m in the altered sandstone (WDG-67), almost 2 m in the basement (WDG-128), and between 0.5 and 1 m in the ore zone (WDG-79 and WDG-197). For the 1989 November to 1990 November period, piezometric levels decreased $\sim$3.5 m in the ore zone (WDG-79) and 0.86 m in the altered sandstone (WDG-67).

3.4.2.2.3 Water levels measured during hydraulic testing

Water levels in packed-off sections have been recorded during the injection/falling-head tests performed in boreholes WDG-75, 76, 137 and 139 (Beak 1984), WDG-185 (Golder 1985) and WDG-213 (Golder 1987a). These latter vertical profiles essentially show hydrostatic conditions, whereas the Beak results are more inconclusive (attributed by Beak to have resulted from the addition of drilling water to the formation).

3.4.2.3 Interference test results

A large-scale pumping test was performed in 1987 March to obtain average values of hydraulic conductivities over large volumes of rock. A new pump well (WDG-218) was drilled in the test mine area to a depth of 400 m (ending 30 m above the clay/ore zone). The entire borehole was cased, and two 25 m sections of the bottom 100 m were slotted and gravel-packed. The borehole casing above the gravel pack was cemented in.

The pumping rate during the test was 10.6 L/s, which was maintained for the duration of the 8-day test. Piezometric levels were monitored in 27 piezometers surrounding the pump well, and drawdown was observed in most of these observation holes. Time-drawdown analysis indicated that the typical aquifer response was that of a partially penetrated, leaky aquifer. The average transmissivity (T) of the aquifer was calculated to be 6.7×10^{-4} m^2/s (SIG 1987) with an associated storativity of 10^{-4}. The vertical leakage to the aquifer was calculated to be 10^{-7} m/s.

In 1989 mid-March, drilling of a suite of exploration boreholes commenced underground at the 210 m shaft station. The drilling of boreholes CLU-3 (53 °N) and CLU-4 (84 °N) yielded a combined artesian flow of 32 L/s (420 gal/min). These flows were used as a hydraulic test of the system for 1.5 days (Meneley pers. commun. 1989). The drawdown produced by this flow was monitored continuously in 4 observation piezometers, WDG-77, -79, -196 and -199. The observed responses were instantaneous and of similar magnitude, between 5 and 7 m.

3.4.2.4 Underground observations made during test mining

Hydrogeological characterization during test mining has been an integrated part of the overall geological characterization. The means for this characterization included: the probe holes that preceded excavation of underground drifts at the 420 and 480 m levels; the exploratory holes drilled from the upper shaft station; test holes for freezing and mining; and mapping subsequent to excavation. The groundwater inflow data collected from the probe holes were used to customize the pre-grouting efforts that depended on particular needs.

From the perspective of hydrogeology, one of the most important findings was that the regolith, as evidenced by the excavations at the 480 m level, appears to be much less permeable than calculated from hydraulic test data. Grouting of altered regolith and unaltered basement rocks was not required to reduce groundwater inflow into the excavation. On the basis of these observations the conceptual model was revised (see Sections 3.4.3.2.3 and 3.4.3.3.3). Maximum water inflow rates, from fractures intersected

by the excavation, measured < 19 L/h. Also, holes drilled from the 480 m level up into the ore zone produced only very small amounts of formation water (<50 L/hole), and recharge from the sandstone aquifer was not observed. These latter observations indicate that the clay-rich zone forms an efficient hydraulic barrier between the sandstone aquifer and the ore zone.

3.4.3 Conceptual models

3.4.3.1 General

On the basis of the collected geological, geophysical and hydrogeological information, a series of conceptual models of the hydrogeological system at Cigar Lake have been generated for analysis of environmental impact, dewatering schemes and alternative mining scenarios. A compilation of existing models was given by Stevenson (1989). A 2D section of the final conceptual model constructed by Golder Associates (Golder 1987b) is shown in Figure 3.38.

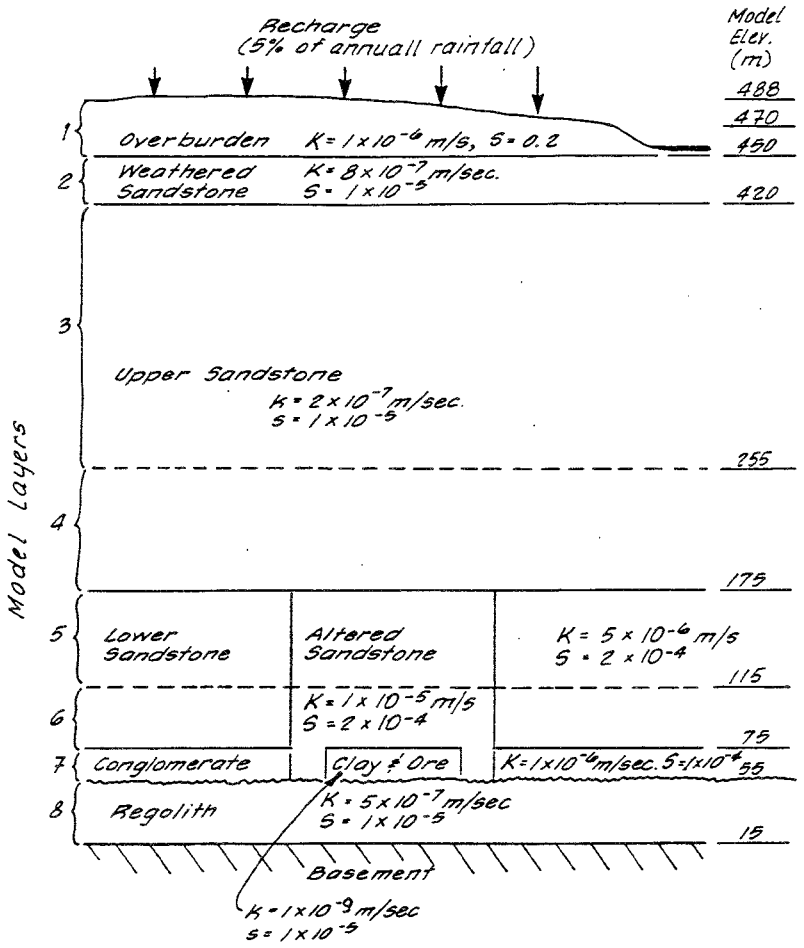

FIGURE 3.38 Golder's conceptual hydrogeological model for the Cigar Lake deposit.

3.4.3.2 AECL/SKB 2D models

3.4.3.2.1 General

The 2D-model sections described below are conceived to fit the needs and goals of the AECL/SKB Cigar Lake analog study. The conceptualization has been performed both on a regional and a local scale; in both cases the modelled domain has been regarded as a deterministic continuum. The Regional 2D-model has a larger lateral extension than the Golder 3D-model. The Regional 2D-model section, including the Local 2D-model section, is aligned with the general direction of groundwater flow, i.e., due northeast. The detail of the Local 2D-model is, however, much finer than that of the final Golder model.

3.4.3.2.2 Regional-scale 2D model

The two-dimensional Regional conceptual model has a horizontal extension of 78 km (Figure 3.39). Its southwestern boundary is located at the southern end of the Waterbury Lake catchment, whereas the northeastern boundary is located some distance northeast of Waterbury Lake. The model extends from the ground surface, as inferred from 1:50,000 map sheets, to a depth of -100 masl. The surface topography southwest-to-northeastward along the section varies between 610 masl to 454 masl. The model has three horizontal layers with different material properties (Table 3.21). The vertical and lower horizontal boundaries have been assigned as no-flow boundaries. The upper boundary, defined by the topography of the ground surface, has been assumed to coincide with the groundwater table.

TABLE 3.21
MATERIAL PROPERTIES OF THE AECL/SKB REGIONAL 2D MODEL

Elevation in model (masl)	Hydraulic conductivity K (m/s)	Kin.Poros. n_e
-100 -- 75	$1x10^{-9}$	0.05
75 -- 255	$1x10^{-6}$	0.15
255 -- surface	$1x10^{-7}$	0.02

3.4.3.2.3 Local-scale 2D model

The Local 2D conceptual-model section is aligned northeast-ward along the assumed orientation of the natural hydraulic gradient, based on topographic maps and the Golder 3D-Model results (Golder 1987b) (Figure 3.40). The geometry of the model is based on the geotechnical section 10+750E (Figure 3.41). The section is 1200 m long and extends vertically from a fixed lower coordinate at -30 masl to an upper coordinate varying between 454 and 485 masl.

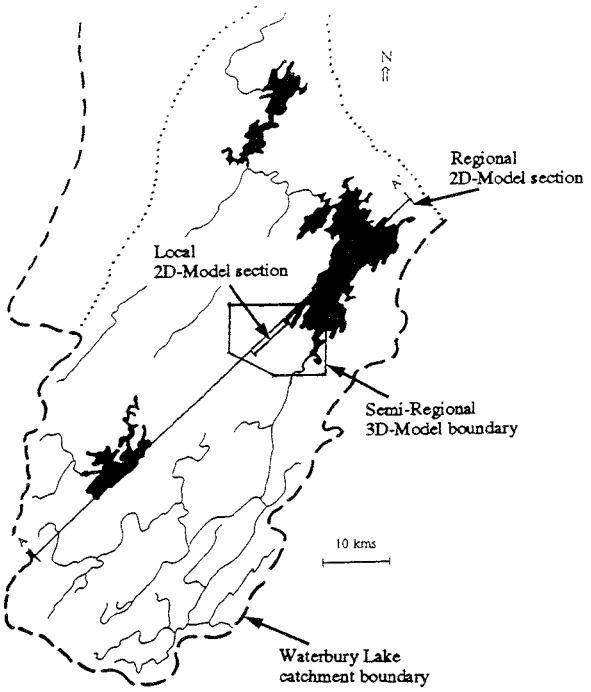

FIGURE 3.39 Location of the Regional and Local 2D-Model sections.

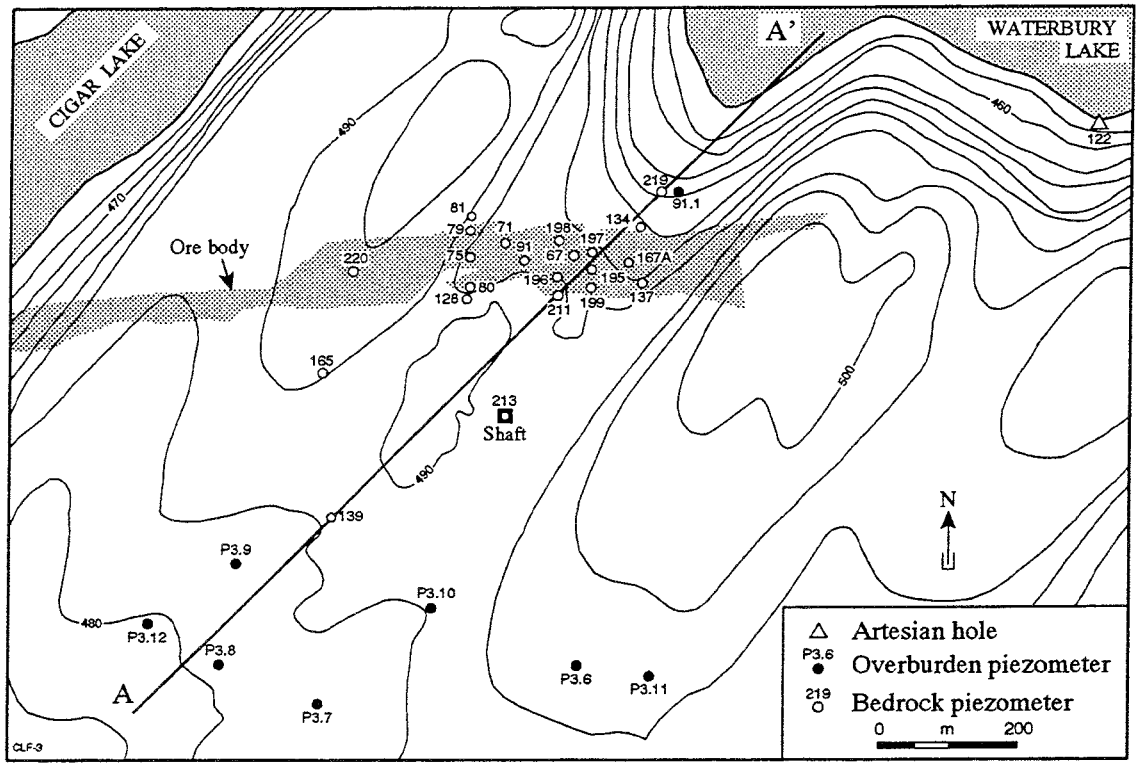

FIGURE 3.40 Map of the Cigar Lake site showing the projected outline of the uranium mineralization at the unconformity and the locations of piezometer-equipped boreholes, the shaft and the section (A-A') of the Local 2D-Model.

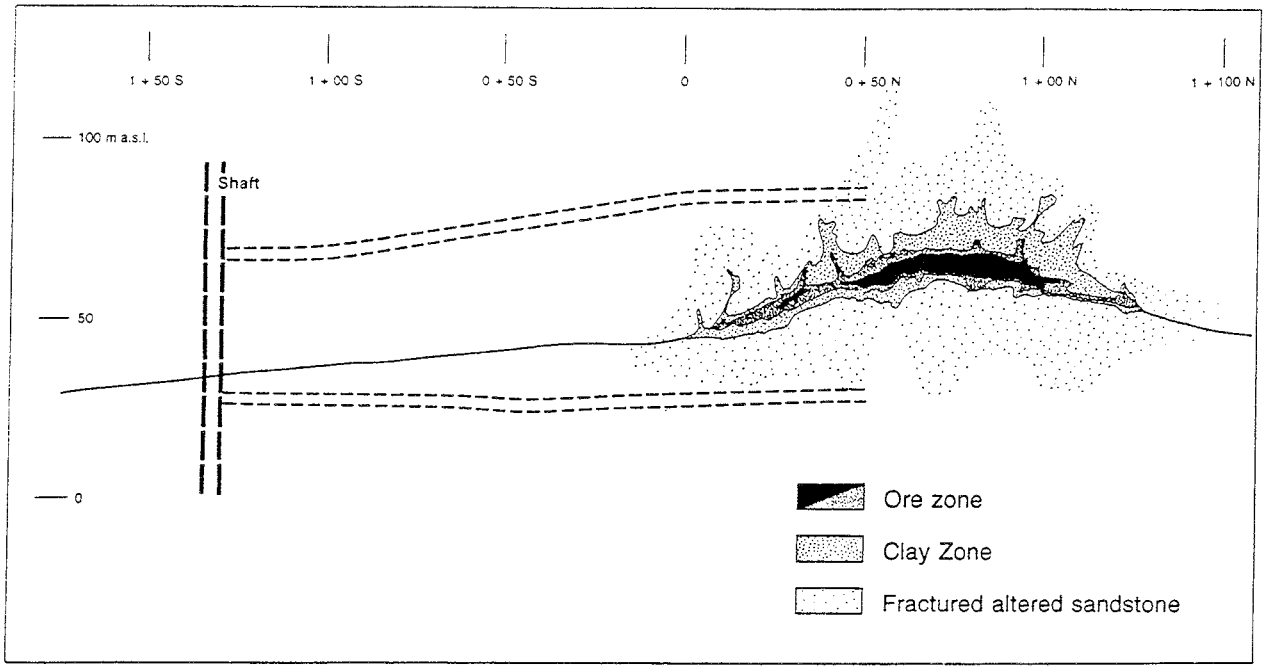

FIGURE 3.41 Vertical geotechnical base section 10+750E.

The hydraulic conductivity (K) distribution of the Local 2D model (Figure 3.42), essentially conforms to that of the final Golder model (Figure 3.38). The unaltered basement has been assumed to be essentially impervious, whereas the altered basement, or regolith, was originally labelled as a moderately-conductive unit ($K = 5x10^{-7}$ m/s). However observations underground at Cigar Lake (see Section 3.4.2.4) required this to be revised, resulting in an assigned hydraulic conductivity two orders of magnitude lower (Table 3.22). The lower sandstone constitutes the main aquifer which is semi-confined by the overlying upper sandstone.

TABLE 3.22
MATERIAL PROPERTY DISTRIBUTION OF THE AECL/SKB LOCAL 2D MODEL

Hydraulic Unit	Hydraulic conductivity K (m/s)	Kin. Poros. n_e
Overburden	$1x10^{-6}$	0.30
Weathered sandstone	$8x10^{-7}$	0.05
Upper sandstone	$2 - 5x10^{-7}$	0.01
Lower sandstone	$5x10^{-6}$	0.20
Fract. alt. sandstone	$1x10^{-5}$	0.20
Ore/clay zone	$1x10^{-9}$	0.05
Regolith	$5x10^{-9}$	0.05
Unaltered basement	$1x10^{-9}$	0.001

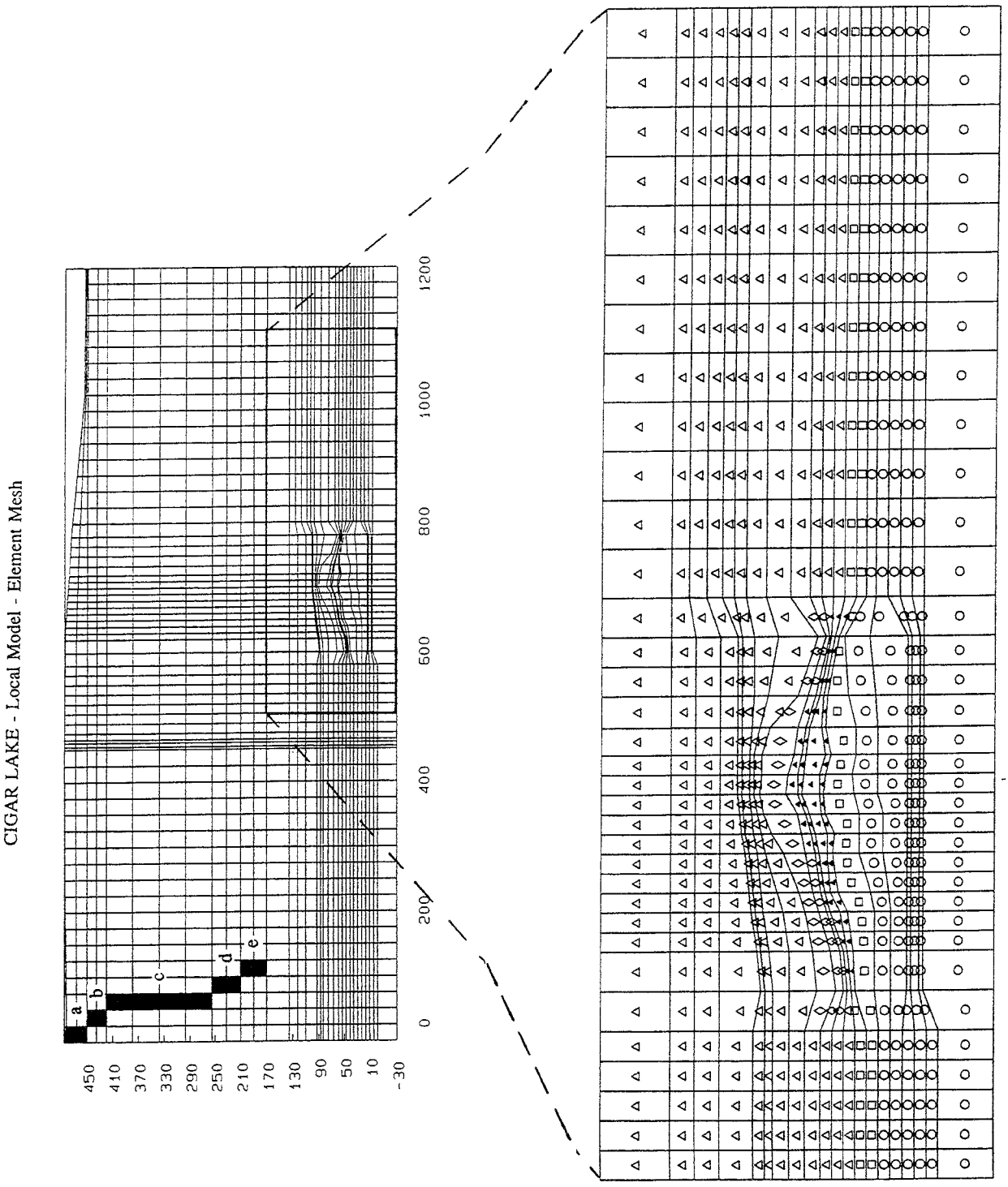

FIGURE 3.42 Local 2D-Model (Ref. material property distribution). Shaded boxes in the upper part of the Figure indicate the material properties in the upper part of the model. Hydraulic conductivities K (m/s) and kinematic porosities n_e assigned are (K; n_e): a) 10^{-6}; 0.30, b) $8x10^{-7}$; 0.05, c) $5x10^{-7}$; 0.01, d) $2x10^{-7}$; 0.01, e) $5x10^{-6}$; 0.20, o) $1x10^{-9}$; 0.001, □) $5x10^{-9}$; 0.05, ▲) $1x10^{-9}$; 0.05, △) $5x10^{-6}$; 0.20, ◇) $1x10^{-5}$; 0.20.

The weathered sandstone unit forms the shallow bedrock aquifer. The overburden Quaternary deposits are highly heterogeneous, comprising a basal, low-permeability silty till, that has a calculated (from textural analysis data) K value of $\leq 10^{-8}$ m/s, overlain by gravelly sands with hydraulic conductivities ranging up to 10^{-5} m/s. An average value of 10^{-6} m/s was assigned to the unconsolidated Quaternary materials (till and sandy gravel). Kinematic porosity (n_e) values from the analysis of the core samples are inferred to range between 0.001 to 0.30. The general material property distribution (Case 3a) is shown in Figure 3.42 and in Table 3.22.

One single set of boundary conditions inferred from the Golder 3D-Model was used in the initial modelling of 1990. In the 1991 modelling, three separate sets of boundary conditions were used. Two of these are based on boundary conditions extracted from the new Regional 2D computer-model; the third set constitutes hydrostatic boundary conditions (AECL/SKB 1991):

1) Direct boundary conditions from the Regional Model,
2) Normalized boundary conditions from the Regional Model, and
3) Hydrostatic boundary conditions.

Because the boundary conditions of set 1 are based on a Regional model where the topography of the groundwater table has been assumed to coincide with the topography of the ground surface, the hydraulic gradient across the section has been overestimated. This conclusion is based on the fact that measured depth to the groundwater table in upland areas is about 20 m below ground surface.

The boundary conditions of set 2 are normalized to provide a hydraulic head at the upstream end-position corresponding to piezometer WDG-139, approximately equal to the measured pre-excavation head. In the normalization process heads at the upstream vertical boundary of the model were reduced by the ratio of the measured pre-excavation head in WDG-139 and the head at the same position in set 1 (Winberg and Stevenson, in AECL/SKB 1991). The boundary conditions of set 3 are hydrostatic, varying between 468 and 454 masl.

3.4.3.3 AECL/SKB 3D models

3.4.3.3.1 General

This section describes the conceptual models that form the basis for the three-dimensional modelling. The models are developed entirely from the previously developed two-dimensional models described in Section 3.4.3.2. In all cases the conceptualized domain is regarded as a deterministic continuum.

3.4.3.3.2 Semi-Regional-scale 3D model

The Semi-Regional-scale 3D model has an areal coverage of approx. 145 km^2. The model area boundaries superimposed on the groundwater-level map are shown in Figure 3.43. The model is made up of four hydraulic stratigraphic units, of which two are composites of units

existing in the Local 3D Model (see next Section). A vertical section through the Semi-Regional model is shown in Figure 3.44 and the material properties of the included hydraulic units are listed in Table 3.23.

No-flow boundaries have been assigned to the vertical boundaries of the Regional 3D-Model because these are assumed to be too far from the Local 3D-Model boundaries to impose any adverse effects. The horizontal boundary is defined by the topography of the groundwater table as depicted in Figure 3.43A.

A

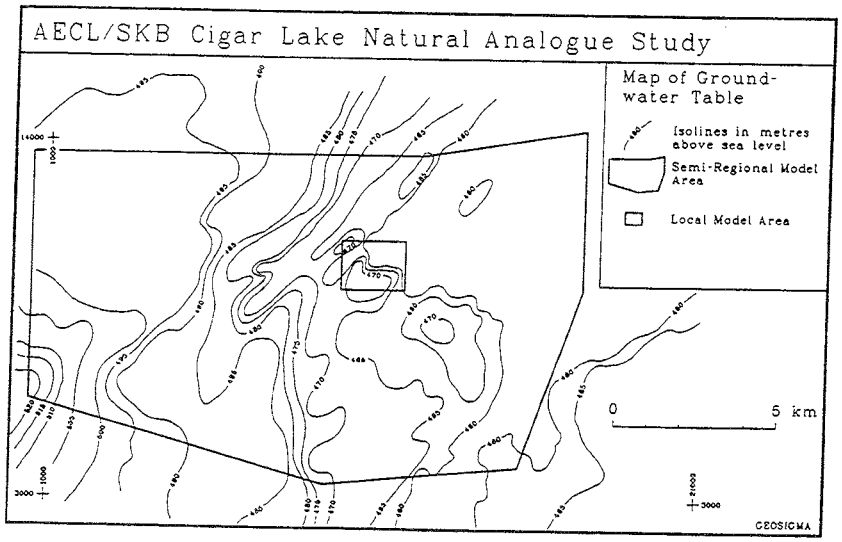

B

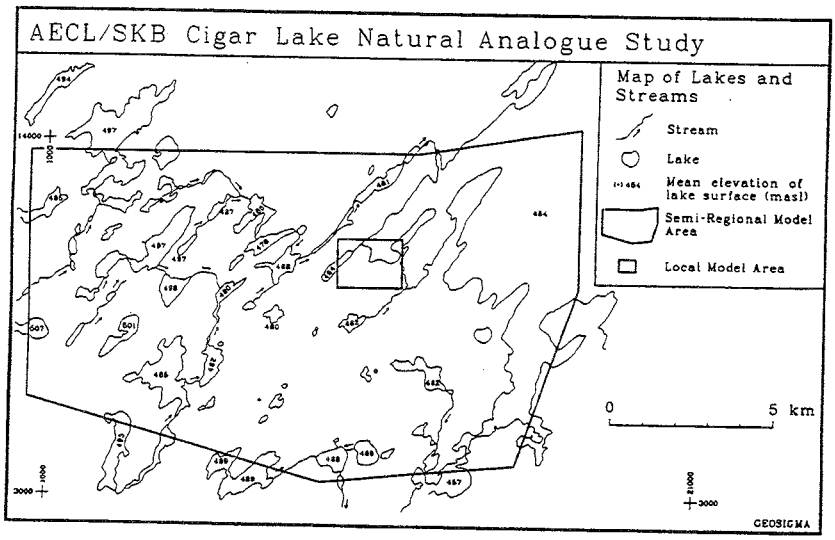

FIGURE 3.43 Plan view of the Local and Semi-Regional models superimposed on (**A**) map of groundwater table in surficial deposits, and (**B**) map showing location and elevation of bodies of surface water.

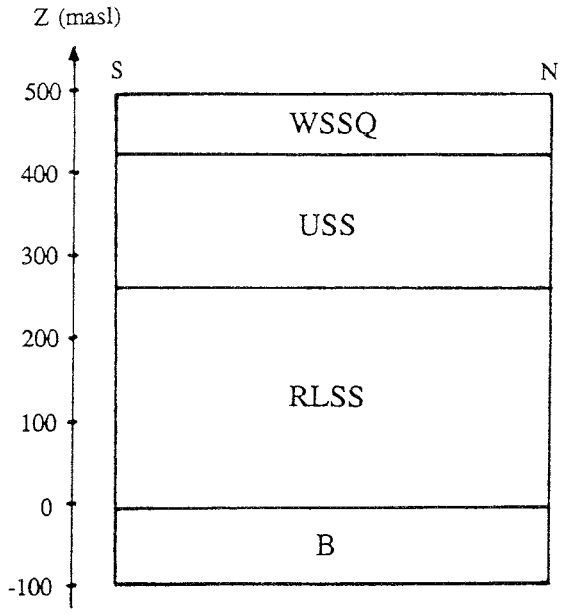

FIGURE 3.44 Stratigraphy of the Semi-Regional 3D conceptual-model.

TABLE 3.23
MATERIAL PROPERTIES OF THE HYDRAULIC UNITS
OF THE SEMI-REGIONAL 3D MODEL

Hydraulic unit	Code	K (m/s)	Kin. Por. n_e
Unweath. Basement	B	$1x10^{-9}$	$1.0x10^{-3}$
Regolith+Lower ss	RLSS	$5x10^{-6}$	$1.5x10^{-1}$
Upper sandstone	USS	$1x10^{-7}$	$1.0x10^{-2}$
W. sandstone+Qrt.	WSSQ	$1x10^{-6}$	$2.0x10^{-1}$

3.4.3.3.3 Local scale 3D model

The Local scale 3D model covers the eastern pod of the deposit (from X=10350 to X=11050 m). The main feature of the model is that it is highly detailed and allows a description of all the different alteration members in and above the ore zone. Eleven different, major hydraulic units are defined, of which four have an altered and an unaltered subunit, i.e., in all the model consists of 15 hydraulic units. The stratigraphy of the model is illustrated in Figure 3.45 and the material properties of the various units are listed in Table 3.24. A more detailed description of the regolith and ore/clay zone region is provided in Figure 3.46. Vertical boundary conditions are inferred from the Semi-Regional model and the upper horizontal boundary is defined by the pressure surface of the groundwater table defined by Figure 3.43. The lower horizontal boundary, set at Z= -100 m, is assigned no-flow conditions.

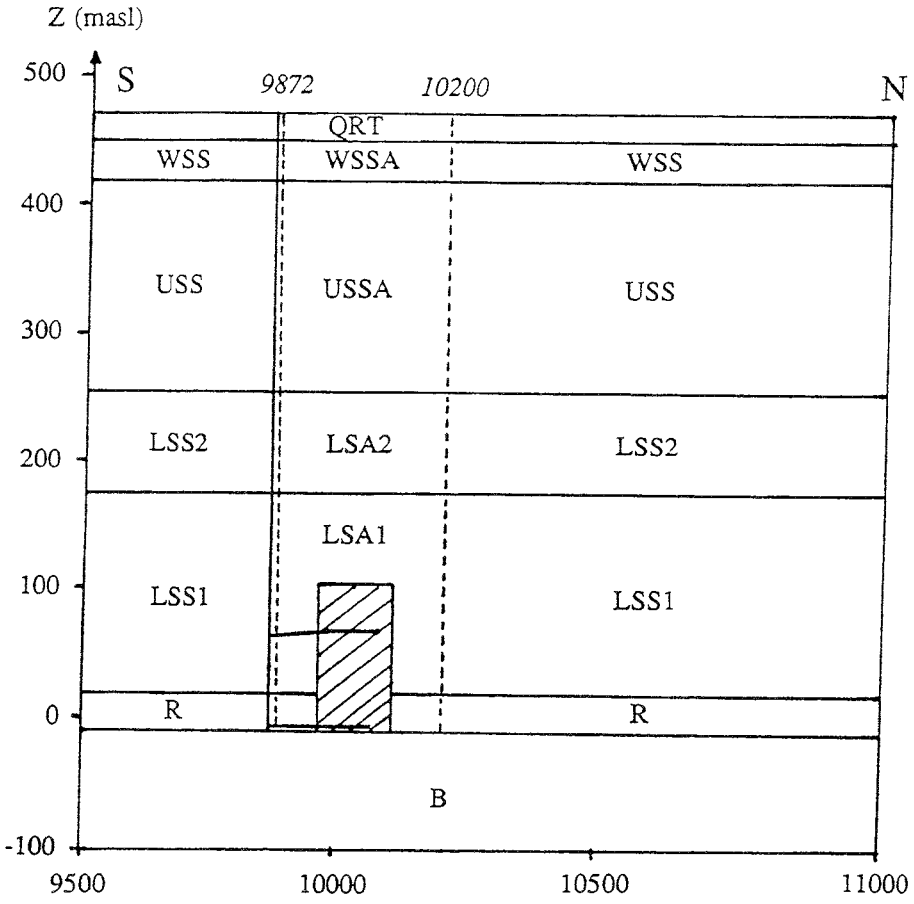

FIGURE 3.45 Stratigraphy of Section x= 10,750 m in the Local 3D Model. Shaded box corresponds to detailed close-up illustrated in Figure 3.46.

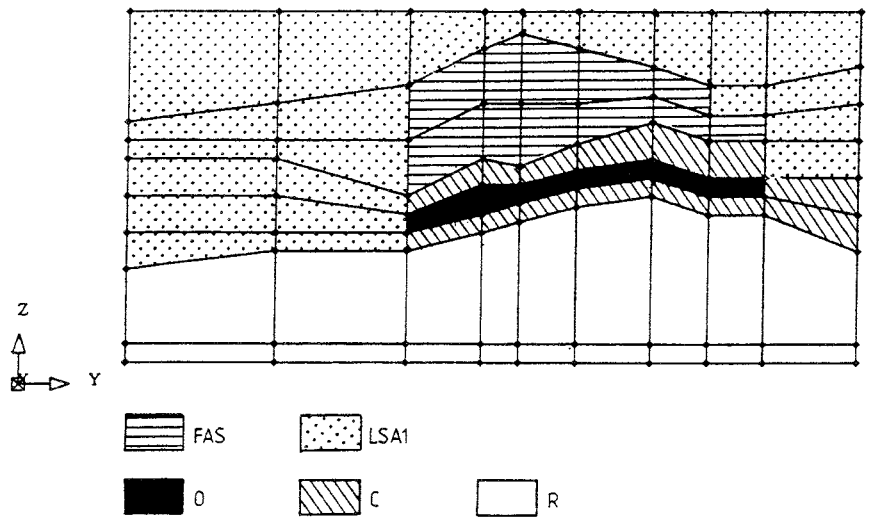

FIGURE 3.46 Close-up of regolith and clay/ore zone complex (Vertical NS section).

TABLE 3.24
LOCAL 3D MODEL: MATERIAL PROPERTIES OF THE HYDRAULIC UNITS

Hydraulic unit	Code	K (m/s)	Kin. Por. n_e
Unweath. Basement	B	$1x10^{-9}$	$1x10^{-3}$
Regolith	R	$5x10^{-9}$	$5x10^{-2}$
Lower sandstone 1	LSS1	$5x10^{-6}$	0.20
Alt. lower ss 1	LSA1	$5x10^{-6}$	0.20
Lower sandstone 2	LSS2	$5x10^{-6}$	0.20
Alt. lower ss 2	LSA2	$5x10^{-6}$	0.20
Mineralized ss	O	$1x10^{-9}$	$5x10^{-2}$
Clay, above ore	C	$1x10^{-9}$	$5x10^{-2}$
Clay, below ore	C	$1x10^{-9}$	$5x10^{-2}$
Fractured alt. ss	FAS	$1x10^{-5}$	0.20
Upper sandstone	USS	$5x10^{-8}$	$2x10^{-2}$
Alt. upper ss	USSA	$2x10^{-7}$	$5x10^{-2}$
Weath. sandstone	WSS	$3x10^{-7}$	$4x10^{-2}$
Alt. weathered ss	WSSA	$8x10^{-7}$	$5x10^{-2}$
Quaternary overburd.	QRT	$1x10^{-6}$	0.30

3.4.4 Hydraulic modelling

3.4.4.1 General

The 2D modelling performed by AECL/SKB is described in the following section, and the AECL/SKB 3D modelling results are presented in Section 3.4.4.3.

3.4.4.2 AECL/SKB 2D computer groundwater models

3.4.4.2.1 General

The computer code used for the AECL/SKB 2D model calculations is the USGS SUTRA code (Voss 1984). This code simulates fluid movement and transport of either heat or dissolved species in a subsurface environment, but was used in this study to model only fluid flow. The calculated velocity distributions for the model cases have been used to calculate trajectories and travel times for conservative, non-sorbing particles released in the models. The code used for the particle-tracking calculations is called TRACK (Vogel 1990).

3.4.4.2.2 Regional 2D model

The Regional 2D model, made up of 372x10 (3720) elements and 4103 nodes, extends 78 km laterally and approx. 550 to 710 m vertically. Plots of calculated hydraulic head and particle velocity distribution and particle tracks have been produced.

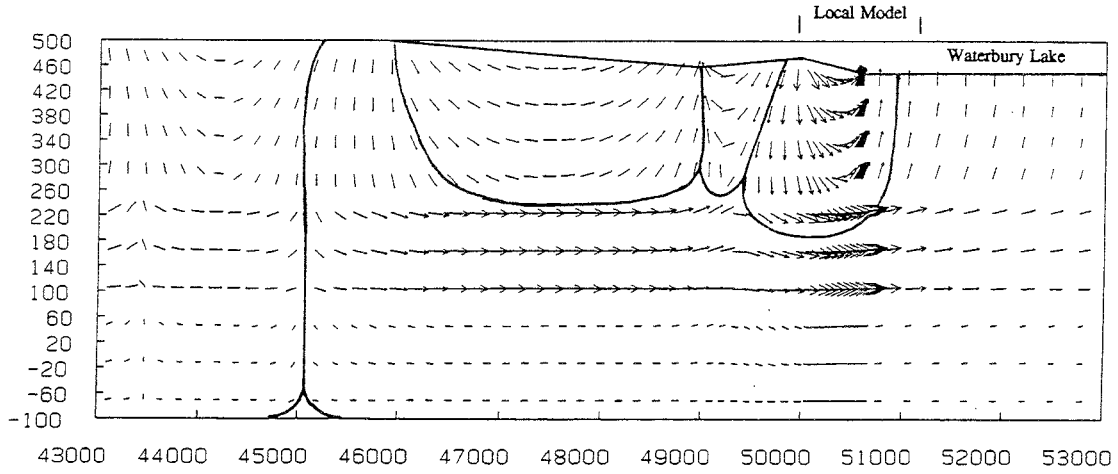

FIGURE 3.47 AECL/SKB Regional 2D Model. Detail of particle velocity field; subregional catchment including the Cigar lake deposit.

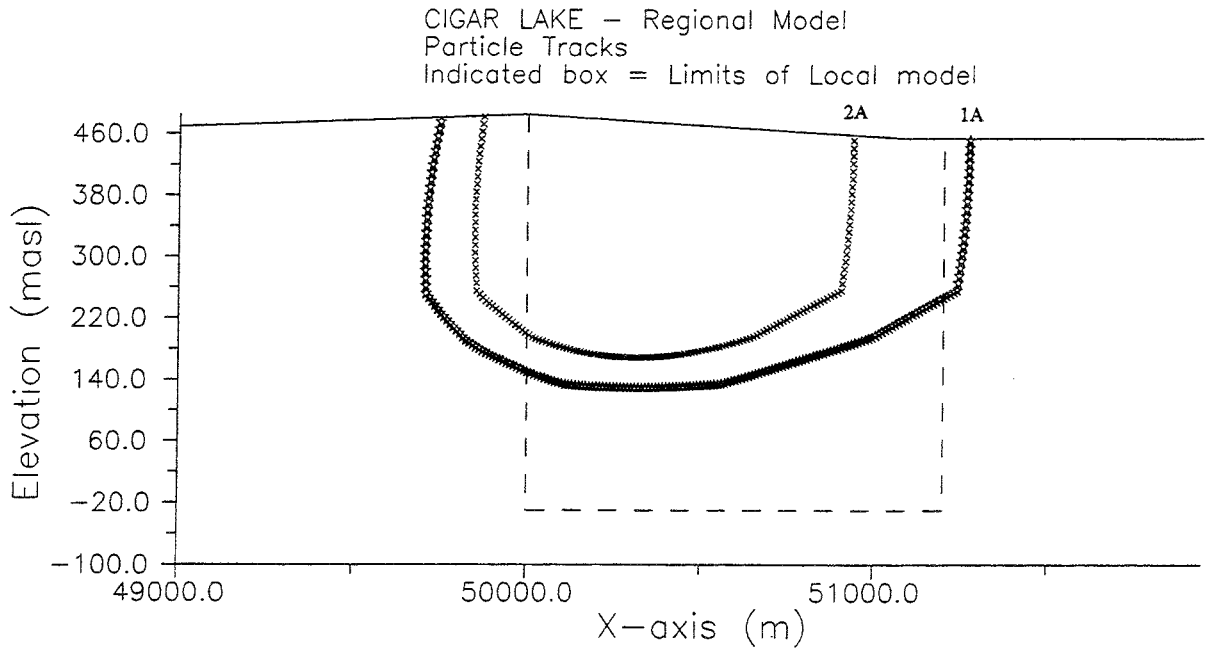

FIGURE 3.48 AECL/SKB Regional 2D Model; tracks of particles released on surface of Regional 2D Model, ( ) = 1A, ( ) = 2A.

There are weak signs of developed regional flow at depth along the subsection towards the northeast (Figure 3.47). This is also true for the complete model section. The velocity pattern in a part of the Regional 2D model (X= 43,000 - 53,000; Figure 3.47), shows a marked topographic influence, even at great depth. A number of subregional "catchments" may be identified. The developed subregional flow cell immediately south of Waterbury Lake contains the Cigar Lake deposit. This particle velocity distribution indicates recharge in the more elevated areas of the modelled domain and discharge into low points in the topography, among them, Waterbury Lake. Figure 3.48 shows particle traces of two

particles released upstream of the Local 2D model on the ground surface. The travel times of these particles 2A and 1A are 160 and 270 a, respectively.

3.4.4.2.3 Local 2D model

The Local scale 2D modelling has addressed the sensitivity in model output to: a) different boundary conditions, b) changes in geometry, and c) changes in material properties (Winberg and Stevenson in AECL/SKB 1990, AECL/SKB 1991). The model consists of 62x32 (1984) elements and 2079 nodes.

Three sets of boundary conditions were used: Set 1 boundary conditions were extracted from the Regional 2D model; Set 2 boundary conditions were normalized (see Section 3.4.3.2.3) and selected to form the base, or reference case, for further sensitivity analysis with regard to geometry and material properties, and combinations of these two; Set 3 boundary conditions were hydrostatic. The plot of the calculated hydraulic-head contours, the velocity field and resulting particle tracks for the reference case are shown in Figure 3.49.

The reference case results show a near-horizontal hydraulic gradient of approximately 1% at the depth of the deposit (Figure 3.49A). In addition, it is evident that recharge occurs upstream and discharge occurs at the downstream end, likely into Waterbury Lake (Figure 3.49B). Moreover, Figure 3.49B indicates that three flow regimes are developed in the studied section: 1) a superficial Local regime, with predominant flow in the overburden and the upper part of the weathered sandstone, which discharges into Waterbury Lake; 2) an Intermediate regime, with water recharging in the upstream end, partly discharging directly into Waterbury Lake and partly feeding the lower sandstone; and 3) a lower Semi-Regional regime that carries water in part recharged beyond the limits of the modelled section and in part being fed by water percolating through overlaying strata. The water in the lower (Semi-Regional) regime flows primarily in the lower sandstone (and to a lesser extent in the regolith and basement). The water is discharged into Waterbury Lake further downstream, beyond the limits of the model (Figure 3.48).

Nine particles have been traced through the calculated velocity field (Figure 3.49C). These particles may be divided into one set released on the surface (3A, 4A, 5A and 6A) and one set released at depth (1A, 2A, 4F, 4G and O1). The two particles released farthest upstream at the surface (4A and 6A) are carried to considerable depth, with travel times through the section ranging between 200 and 700 a. The surficial particles (3A and 5A) released in, or immediately below, the overburden show travel times between 25 and 100 a. The particles released at depth and carried through the lower sandstone (1A, 2A and 4F), show particle travel times within the 2D model area ranging between 130 and 150 a. If the paths of these particles in the Regional Model are considered, i.e., from surface release to upstream Local Model boundary and from the downstream local boundary to discharge into Waterbury Lake, the total transit time is estimated to be about 300 to 400 a. The sole particle traced through the low-permeability regolith (4G) shows a transit time of about 370,000 a, indicating an average particle velocity of 3 mm/a. The particle released in the ore zone (O1) has a long residence time in the ore zone (about 24,000 a), before passing into the more permeable lower sandstone. The results of the particle tracking calculations based on the reference case are compiled in Table 3.25.

TABLE 3.25
AECL/SKB LOCAL 2D MODEL - REFERENCE CASE: RESULTS OF PARTICLE TRACKING CALCULATIONS (FIGURE 3.49C)

Particle ID #	Path Length m	Travel Time a	Mean Velocity m/a
1A	1190	144	8.3
2A	1200	144	8.3
3A	580	100.5	5.8
4A	1320	204	6.5
4F	1160	129	9.0
4G	1160	371000	0.003
5A	180	25	7.2
6A	1150	684	1.7
O1	510	24690	0.02

Sensitivity analysis performed with regard to material properties (AECL/SKB 1990) consisted of four cases that considered variations in hydraulic conductivity in 1) the altered basement (regolith), 2) the ore zone, and 3) the fractured altered sandstone (two cases). In a second group of sensitivity analyses (AECL/SKB 1991), the sensitivity in model output to changes in boundary conditions, model geometry and material properties were carried out. The results of the initial sensitivity analysis with regard to material properties show small but consistent changes in terms of hydraulic head corresponding to type piezometers (SKB/AECL 1990). The differences in travel time between the calculated cases is within a factor of 3 if the changes in particle travel path are neglected, i.e., going over rather than under the ore zone and vice versa.

The highest sensitivity is found for particles released in and above the regolith. The travel times for the particles in the unaltered basement is essentially insensitive to the imposed variations in material properties. The highest overall impact is imposed by doubling the hydraulic conductivity in the fractured altered sandstone.

The sensitivity analysis with regard to the boundary conditions (AECL/SKB 1991) showed that the simulation with boundary conditions extracted from the 2D Regional model provided the best correlation with the measured piezometry. Hence, this set of boundary conditions was selected to be part of the reference case.

Sensitivity analysis performed with regard to geometry addressed three items (AECL/SKB 1991):

- Effect of an introduction of a low-permeability quartz cap,
- Effect of a vertical fracture zone through the ore zone, and
- Effect of a vertical fracture zone in the discharge area along the northern boundary.

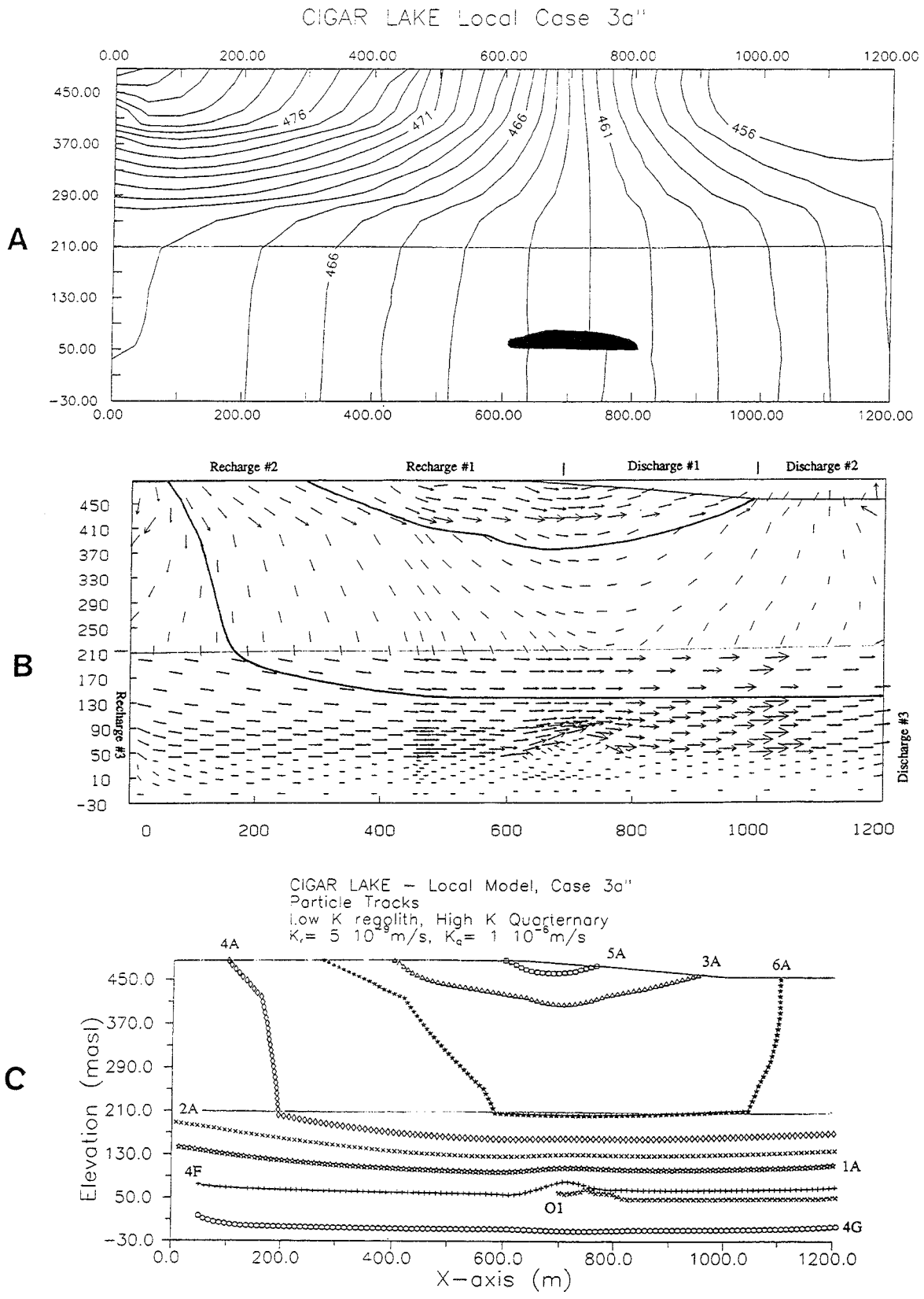

FIGURE 3.49 AECL/SKB Local 2D Model (reference case). **A**: Isopotential map of hydraulic head and location of mineralized zone. **B**: groundwater particle velocity. **C**: particle tracks (Table 3.25). The horizontal line in each diagram represents the boundary between Upper- and Lower Sandstone.

The existence, hydrogeological significance and effect of a conceived quartz mineralized zone above the ore zone were investigated by studying the evidence and modelling the effects. The extent of the zone where quartz crystals are found is known (Figure 3.42), the matrix is well cemented, and the quartz zone is highly fractured. However, the quartz zone has not shown up as a low-permeability feature in the performed packer/piezometer or pump tests. In the constructed model, the quartz zone was modelled as a low-permeability triangular pod of rock, the extent of which was inferred from borehole logs within the profile (AECL/SKB 1991). The quartz zone was assigned a hydraulic conductivity of $1x10^{-7}$ m/s (Case 3d), i.e. close to 1.5 orders of magnitude lower than the surrounding fractured altered sandstone. The resulting isopotential field showed an increase in the hydraulic gradient over the quartz zone and a subsequent relaxation in the gradient downstream. The resultant velocity field shows a preferential flow path through the fractured altered sandstone, around and above the quartz mineralized zone. The calculated transport times for this case are more than one order of magnitude longer than for the reference case.

Introduction of a vertical fracture zone through the ore zone did not produce any dramatic changes in the flow paths because of the absence of a significant vertical hydraulic gradient in that region. On the other hand, if a vertical fracture zone had been introduced in the discharge region where a significant downward gradient is present, the fracture zone would have formed the preferred travel path. Similarly, if a fracture zone was introduced below a regional high where recharge conditions prevail, downward flow would be concentrated in the fracture zone, and infiltrating water from higher parts in the stratigraphy would penetrate deep into the lower sandstone.

Finally, the sensitivity to changed conceptualization of the overburden has been investigated (AECL/SKB/USDOE 1992). As opposed to a uniform overburden with an average hydraulic conductivity and porosity, the overburden was conceptualized as a 20- to 25-m-thick sandy, gravelly, high-permeability layer overlying a thin 3 m layer of glacial silty till. Hydraulic conductivities of 10^{-6} and 10^{-8} m/s, respectively, were assigned to these layers. The results showed that the overall flow field did not change that much. This was also true for the calculated particle tracks. On the other hand, when the hydraulic conductivity of the basal glacial till was lowered to 10^{-9} m/s, the surface-released particles were transported more superficially because much steeper isopotentials in the upper and weathered sandstones (see Figures 3.50 and 3.51).

In the latter case, the bulk of local recharge is transported through the sandy overburden, whereas recharge to the semi-regional flow regime (in the Lower Sandstone unit) occurs outside the Local model in the headwater (SW) areas of the Waterbury Lake catchment. In that area recharge may occur directly into sandstone bedrock that crops out at ground surface.

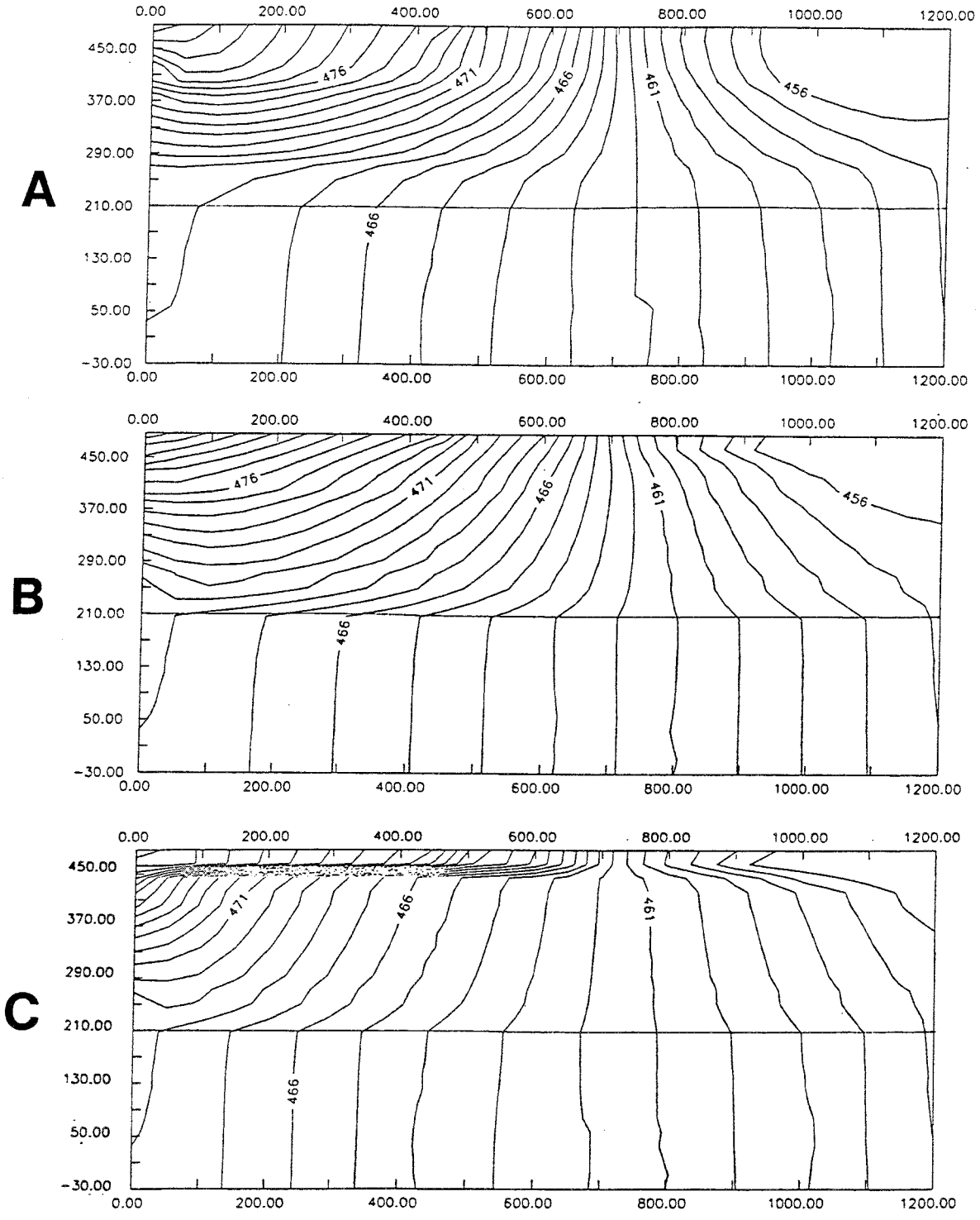

FIGURE 3.50 AECL/SKB Local 2D-Model. Distribution of equipotentials for three modelled cases, all including K_R(regolith)= $5x10^{-9}$ m/s. **A**: Case 3a"; K_{OB}(overburden: gravel+till)= $1x10^{-6}$ m/s. **B**: Case 3o; K_{SG}(sandy gravel)= 10^{-6} m/s; K_{GT}(glacial till)= 10^{-8} m/s. **C**: Case 3l; K_{SG}= 10^{-6} m/s; K_{GT}= 10^{-9} m/s.

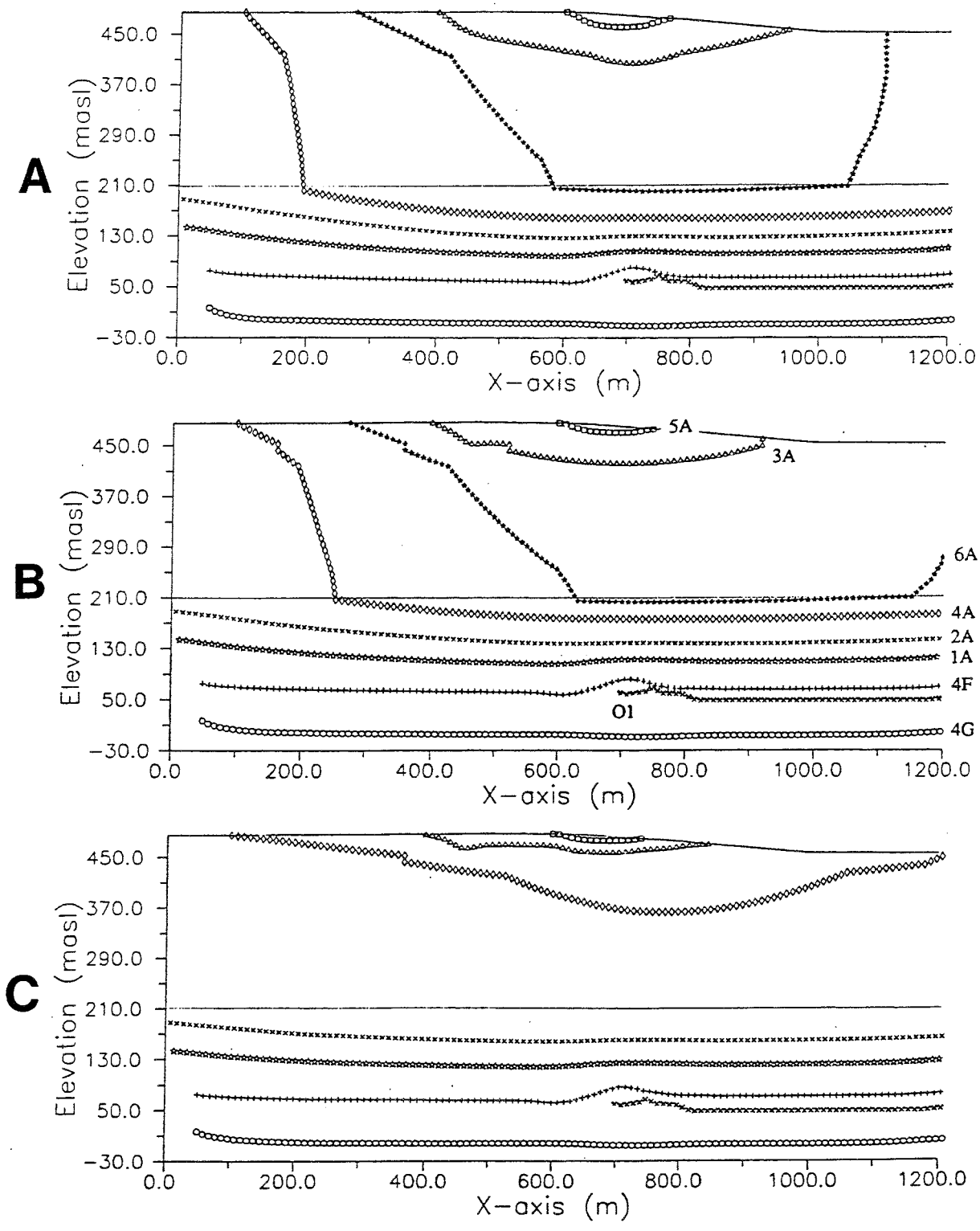

FIGURE 3.51 AECL/SKB Local 2D-Model. Particle tracks calculated for same three modelled cases as shown in Figure 3.50. **A**: Case 3a". **B**: Case 3o. **C**: Case 3l.

Groundwater flow through the Intermediate flow regime (located in the Upper Sandstone) makes up only a small part of flow through the section. Limited recharge occurs to the Intermediate flow regime from both local and regional areas.

Insufficient field data have been collected to describe permeability variations and lateral distribution within the surficial sediments in the modelled areas, but the sensitivity analysis serves to show the range of flow conditions that may exist there.

3.4.4.3 AECL/SKB 3D computer groundwater models

3.4.4.3.1 General

Three-dimensional hydraulic modelling was done at both semi-regional and local scales. The lateral extent of the Semi-Regional 3D Model was chosen to allow as good a representation of the groundwater table as possible, taking into account wet areas, lakes and the highly elevated areas in the southwest. The boundaries of the Local 3D-Model were positioned so that they would not be affected by any simulated pump test in the central parts of this model.

The 3D model calculations were performed with the groundwater flow/solute transport code NAMMU developed at Harwell, U.K. (Atkinson et al. 1989). Pre- and post-processing have been facilitated through FEMGEN/FEMVIEW (FV 1991), which interfaces with NAMMU through the program package HYPAC (Grundfelt et al. 1989). The latter package provides mesh control and optimization, assignment of material properties and boundary conditions.

The Local 3D Model has been calibrated versus piezometric data representative of the situation prior to test-mine development. The differences between calculated (base case) and measured hydraulic head are between 0.5 and 1.5 m for most piezometers.

3.4.4.3.2 Semi-Regional 3D model

The Semi-Regional 3D Model is made up of 14 layers of 400 eight-node quadrilateral elements giving a total of 5,600 elements (6615 nodes). The boundary conditions are water table constant-head conditions along the upper horizontal boundary, and no-flow conditions along the vertical and lower horizontal boundaries. One single Semi-Regional model simulation has been done. The input data for this simulation are given in Table 3.23 (Section 3.4.3.3.2). The resultant isopotential map of hydraulic head at an elevation of Z=50 masl is shown in Figure 3.52. The map indicates that the average natural groundwater flow direction is oriented nearly west-to-east in the central part of the model, and northeast-ward at the northeast and southwest corners of the model. This average flow direction in the central part of the model is a clockwise rotation of flow compared with the interpreted natural groundwater flow direction used in selecting the Regional 2D model section. The hydraulic gradient at Z= 50 masl is on the order of 0.3%.

Particle tracking calculations indicate that particles released at a depth of 50 masl below the highly elevated area in the southwest exhibit travel times on the order of 140,000 a and discharge into Waterbury Lake at the eastern extreme of the Semi-Regional model (Figure 3.53). Particles released superficially in the southwestern part show particle travel times on the order of 1,400 to 3,400 a and discharge west of the western shore of Waterbury Lake.

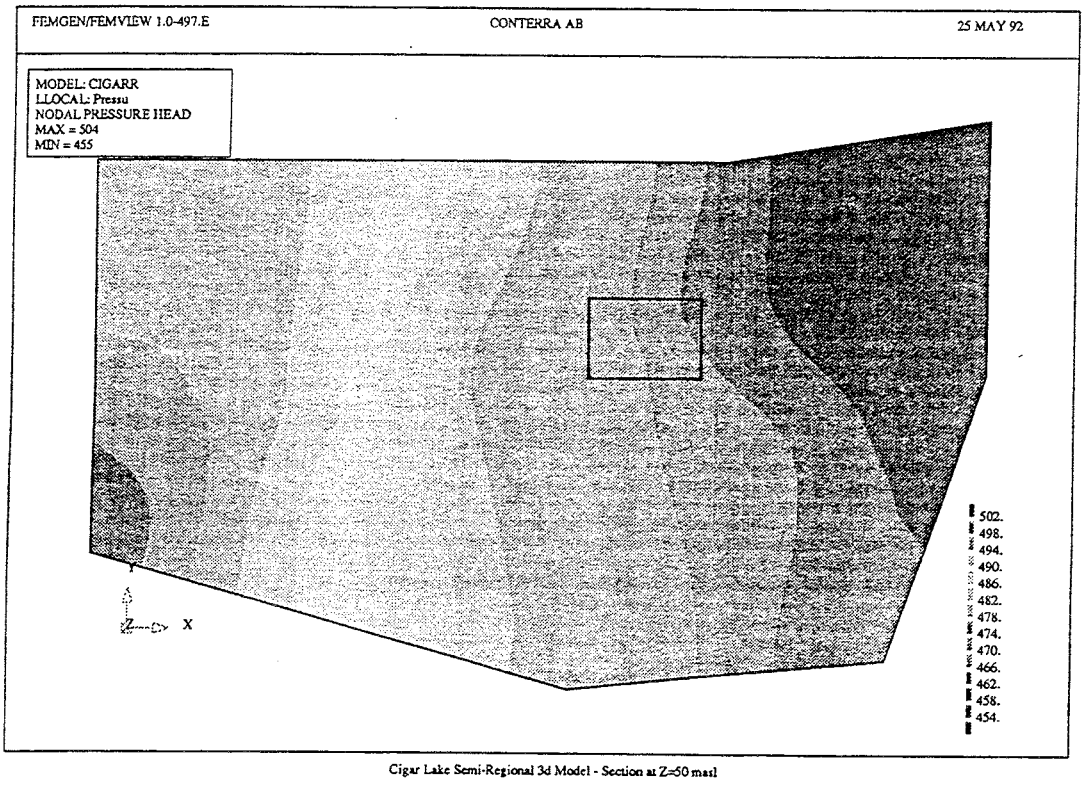

FIGURE 3.52 AECL/SKB Semi-Regional 3D Model. Horizontal isopotential map of hydraulic head at Z= 50 masl. Box represents the boundaries of the Local 3D-Model.

3.4.4.3.3 Local 3D model

The Local 3D Model is made up of 22 layers of 306 eight node quadrilateral elements giving a total of 6426 elements (7524 nodes). The model is centred on the area covering the ore deposit (with elements as small as 5x5 m) and also includes discrete description of the shaft and the two access drifts from the shaft towards the ore zone. Vertical boundary condition heads for the Local 3D Model are the values calculated for the vertical surfaces within the Semi-Regional 3D Model which correspond to those boundaries (Figure 3.53).

The data in Table 3.24 (Section 3.4.3.3.3) were used as a first set of input data to calibrate the model. Steady state simulation using this reference data set showed calculated hydraulic heads in the instrumented part of the domain which were some 1 to 1.5 m in excess of that

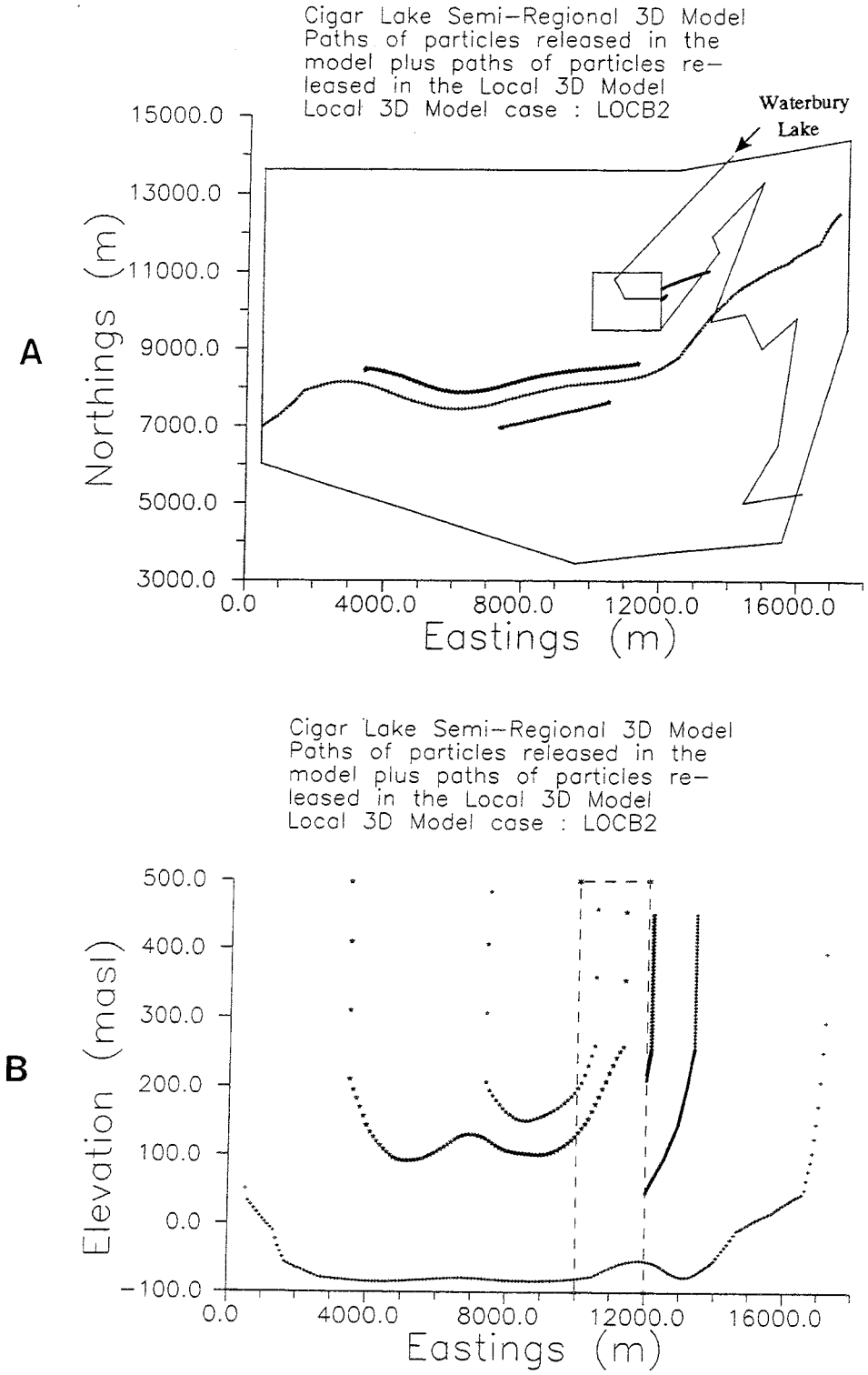

FIGURE 3.53 Cigar Lake Semi-Regional 3D Model. Trajectories of particles traced in the model domain and from the boundaries of the Local 3D Model. **A**: horizontal section. **B**: projected vertical section (----- = Local 3D Model boundary).

measured in the field. During the attempted transient calibration of the model some results appeared insensitive, and in some cases unrealistic drawdowns in neighbouring wells were calculated. A possible explanation for this behaviour can be that the resolution around the pump well (WDG-218) is not fine enough, i.e. not enough nodes have been included between the pump well and the closest observation wells. Hence, the model is presently not calibrated in the transient stage, and the results should be regarded from that perspective. A sensitivity study was performed to examine effects of changes in hydraulic conductivities on particle velocity and travel time, results are given at the end of this section.

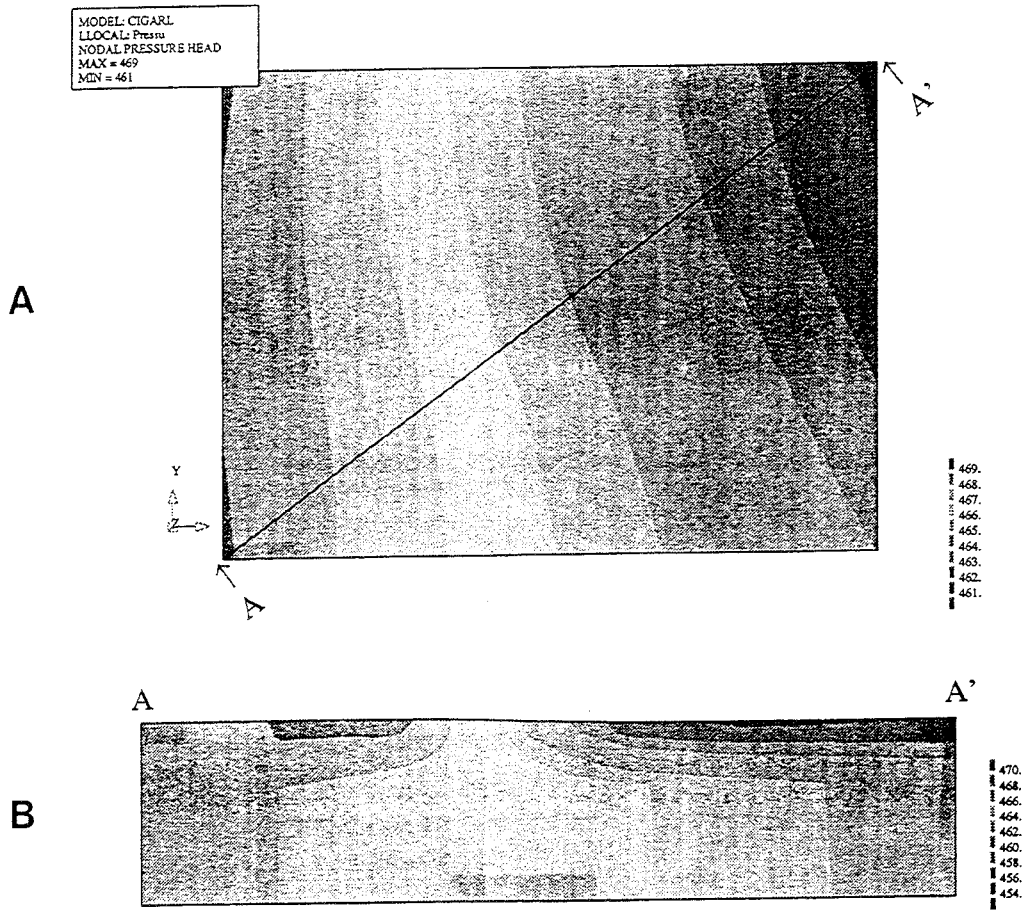

FIGURE 3.54 Cigar Lake Local 3D Model (reference case). Distribution of calculated hydraulic head in: **A**- a horizontal section at Z= 50 masl, and **B**- a vertical section oriented N45E.

Figure 3.54A shows the calculated distribution of hydraulic head in a horizontal section through the reference case Local 3D-Model at Z= 50 masl. The pattern observed in the central part of the Semi-Regional model results (Figure 3.52) are similar to those of the reference Local 3D Model results. The average groundwater flow direction is oriented

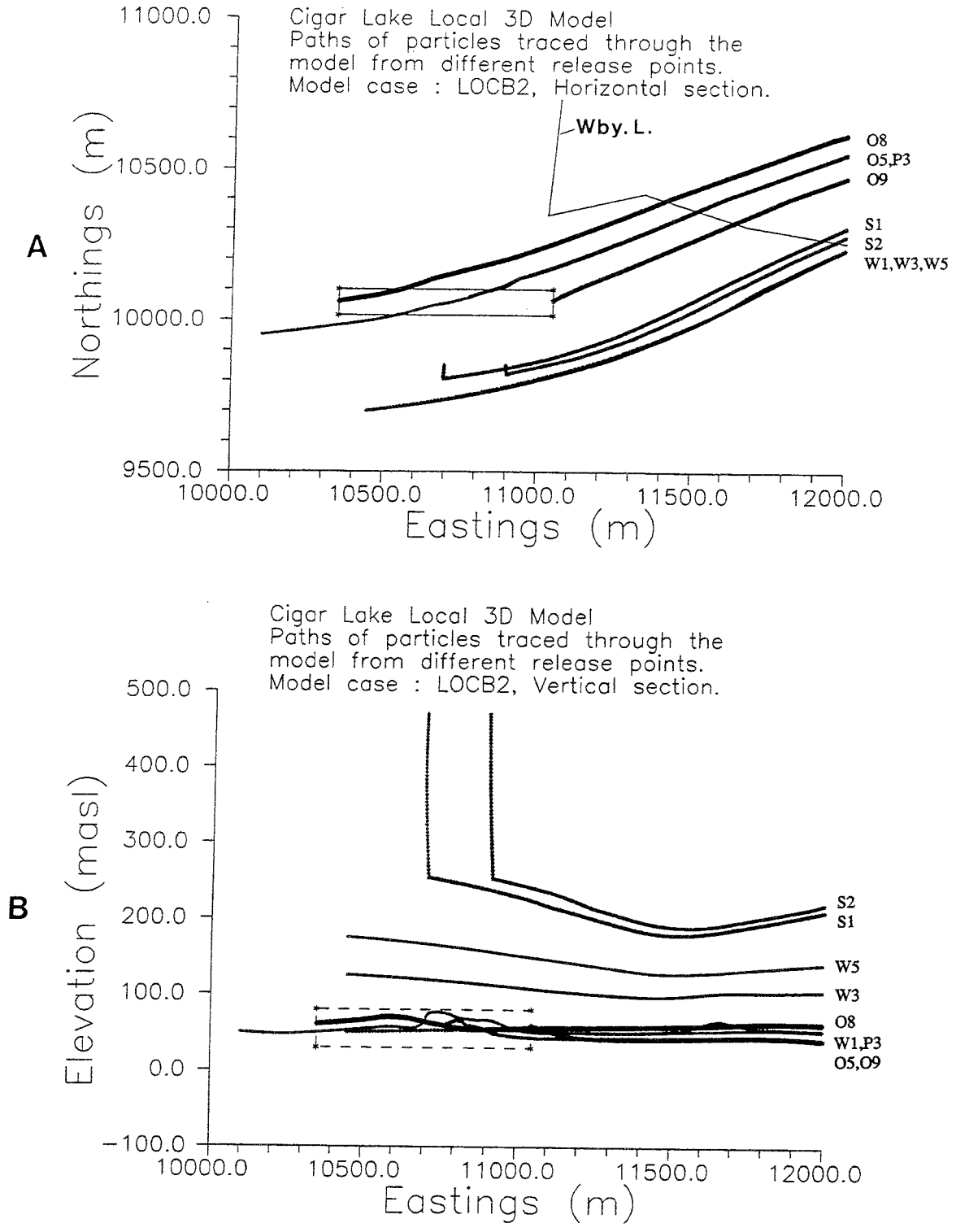

FIGURE 3.55 Cigar Lake Local 3D Model (reference case). Horizontal (**A**) and vertical (**B**) projection of trajectories of particles released in the Local 3D Model.

ENE with a mean hydraulic gradient of about 0.3%, which is about one third of the corresponding gradient calculated for the Local 2D Model. Figure 3.54B shows the distribution of hydraulic head in a vertical section through the model oriented NE, i.e., along the presumed 2D natural groundwater flow direction. The figure shows an isopotential distribution pattern very close to the corresponding reference 2D results (Figure 3.49A).

Figure 3.55A shows a horizontal projection of traces of particles (W1, W3 and W5) emanating from the location of borehole WDG-139. The groundwater chemistry of this hole is assumed to represent the input water to the studied system. Because of the noted slight rotation in the natural hydraulic gradient observed in the 3D results compared with that assumed for the 2D model, these particles are not carried to the instrumented part of the system. Instead they are deflected eastward, south of the ore zone, and northeastward, toward Waterbury Lake. The travel times of these particles are on the order of 500 a for the reference case. It should be emphasized that the groundwater composition west of borehole WDG-139 is considered to be identical to that at the WDG-139 location. A particle released north of WDG-139 (P3) passes over the ore/clay zone but shows no deflection eastward along the ore/clay zone in the highly conductive FAS.

Also included in the figure are traces of particles released at different locations within the ore/clay zone (O5, O8 and O9) and two released on the surface (S1 and S2). The calculated results for the reference case indicate that the particles released within the ore/clay zone (O1-O9) show residence times in the ore/clay zone varying between 18,000 and 85,000 a, the higher numbers being associated with particles released in the western part of the clay/ore zone (O8). The residence times of the surface-released particles (S1 and S2) within the Local 3D Model are in the order of 800 to 1,000 a for the reference case. The corresponding vertical projections of the particle traces on a plane oriented east-west are shown in Figure 3.55B.

The following issues were addressed in the subsequent sensitivity analysis:

1) LSA1 and LSS1: increase in hydraulic conductivity (x2) to 1.0×10^{-5} m/s (LOCB3),
2) LSA1 and LSS1: decrease in hydraulic conductivity (x0.2) to 1.0×10^{-6} m/s (LOCB4),
3) QRT: decrease in hydraulic conductivity (x0.01) to 1.0×10^{-8} m/s (LOCB5), and
4) O, C and CFAS: decrease in hydraulic conductivity (x0.1) to 1.0×10^{-10} m/s (LOCB6).

The results of the sensitivity analysis show that the responses to the changes in hydraulic conductivity are consistent and proportional to the changes made (see Table 3.26). The corresponding particle velocities are indicated in Table 3.27. Only minor changes in particle paths are observed for the different cases. It should be noted in this context that an order of magnitude increase in hydraulic conductivity has the same effect as an order of magnitude decrease in effective porosity.

The traces of particles from the Local 3D Model boundary through the Semi-Regional 3D

TABLE 3.26
AECL/SKB LOCAL 3D MODEL: PARTICLE RESIDENCE TIMES (a) FOR 5 CASES

Particle ID	Reference Case (R.C.) **LOCB2**	LSA1 & LSS1 2x R.C. **LOCB3**	LSA1 & LSS1 0.2x R.C. **LOCB4**	QRT 0.01x R.C. **LOCB5**	O, C, CFAS 0.1x R.C. **LOCB6**
O5*	47,290	21,360	9,775	55,520	581,700
O8	500	250	2,595	500	500
O9	290	145	2,750	295	290
W1	505	255	2,555	510	505
W3	500	250	2,560	505	500
W5	500	255	2,570	505	500
P3	582	302	2,467	574	582
S1	1,010	970	1,025	1,795	1,010
S2	850	850	860	1,830	850

* Residence time in the ore/clay zone. LOCB2 = reference case (Table 3.24)

TABLE 3.27
AECL/SKB LOCAL 3D MODEL: PARTICLE VELOCITIES (m/a) FOR 5 CASES

Particle ID	Reference Case (R.C.) **LOCB2**	LSA1 & LSS1 2x R.C. **LOCB3**	LSA1 & LSS1 0.2x R.C. **LOCB4**	QRT 0.01x R.C. **LOCB5**	O, C, CFAS 0.1x R.C. **LOCB6**
O5*	0.0036	0.0091	0.0026	0.0033	0.0003
O8	3.49	6.94	0.68	3.46	3.49
O9	3.56	7.03	0.39	3.49	3.57
W1	3.26	6.50	0.65	3.27	3.27
W2	3.28	6.50	0.65	3.29	3.28
W3	3.28	6.50	0.65	3.29	3.29
P3	3.45	6.61	0.83	3.48	3.45
S1	1.60	1.66	1.61	0.69	1.61
S2	1.65	1.65	1.65	0.41	1.65

* Velocity in the ore/clay zone. LOCB2 = reference case (Table 3.24)

Model to their discharge points are shown in Figure 3.53 in a horizontal (A) and vertical (B) projection. These figures show that the discharge points for particles from the ore/clay zone are all in Waterbury Lake, located ~2.5 km ENE of the eastern extreme of the ore zone. The added residence time for the particles exiting from the Local 3D Model at about 50 masl is about 1,000 a, and for particles released on the surface in the Local 3D Model is another 200 a.

3.4.5 Discussion

This section summarizes the integrated results of the 2D- and 3D modelling. The results are discussed and correlated to the available hydrogeochemical information. It should again be noted that the Local 3D Model is not calibrated in the transient state.

3.4.5.1 Vertical conceptual quantified 2D section

It is reiterated here that the conceptual models employed assume a continuous porous medium. This implies that even though the bulk of the occurring groundwater flow is fracture-controlled, the individual fractures in the bedrock are not explicitly represented in the model, because the exact geometry of these fractures is unknown and consequently needs to be addressed stochastically. However, the necessary geometrical and hydraulic information to facilitate such an approach is unavailable. Instead, assigned bulk material properties in terms of effective hydraulic conductivity and porosity values incorporate both the matrix and fracture properties of the hydraulic unit in question; model calibration results indicate that this approach was appropriate.

On the basis of the final conceptualization and the 2D and 3D modelling results obtained, a **vertical conceptual quantified 2D section** along the assumed natural gradient has been constructed (Figure 3.56). This section, which was previously based solely on the Local 2D Model results, has been updated using the Local 3D Model results, which are believed to describe the boundary conditions on a local scale in a better and more realistic way.

The section contains the limitations of the various defined hydraulic units and their assigned material properties in terms of hydraulic conductivity K and porosity n_e. In addition, typical values of the pointwise particle velocity v_p and the integrated particle velocity v_i are presented. The pointwise velocity v_p is defined through Darcy's law using the assigned values of hydraulic conductivity and porosity and the output hydraulic gradient obtained from the 3D modelling (about 0.3%). The integrated velocities v_i are calculated directly from the calculated integrated particle residence times and the corresponding particle travel path length through the 3D model. The presented point and integrated velocities in the upper part of the conceptual model section are considered to be representative for both 2D and 3D conditions.

Figure 3.56 shows that the integrated particle velocities in the upper part of the section, the overburden (QRT) and the altered weathered sandstone (WSSA), are on the order of 2 m/a, whereas those particles with their bulk travel path through the altered upper sandstone (USSA) and the upper part of the altered lower sandstone (LSA2), are on the order of 1 m/a and 4 m/a, respectively. In the lower part of the lower altered sandstone (LSA1) the integrated particle velocities are about 3 to 4 m/a. In the regolith (R), the particle velocity is a mere 0.001 m/a, i.e., about 0.03 % of the velocity in the lower sandstone, reflecting the high contrast in material properties between these two neighbouring hydraulic units.

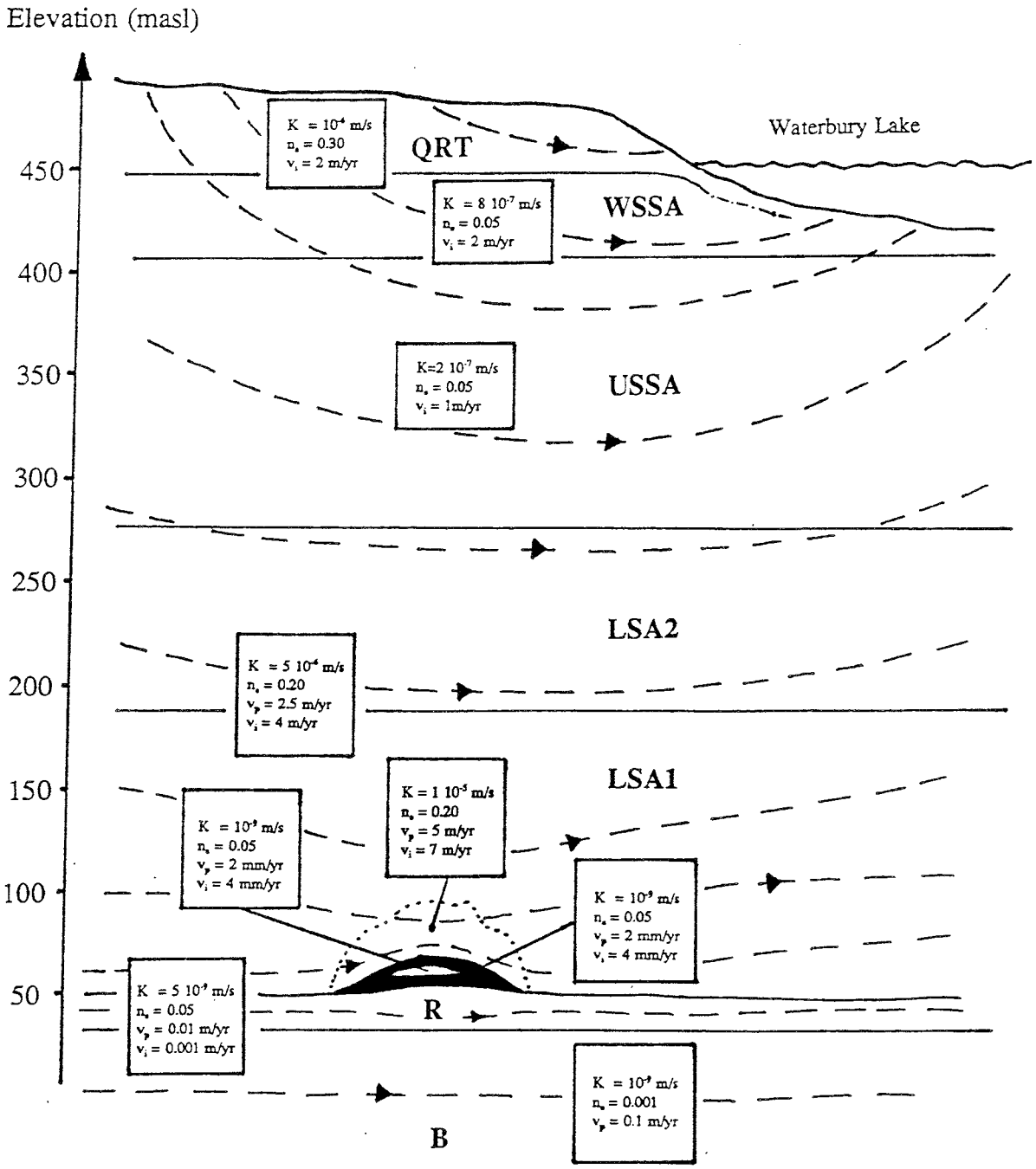

FIGURE 3.56 Conceptualised quantified 2D conceptual model in a vertical section, through the Cigar Lake deposit parallel to the semi-regional hydraulic gradient.

On the basis of the simulation results three flow regimes have been identified. These are: I) a shallow Local flow regime, II) an Intermediate flow regime, and III) a deep Semi-Regional flow regime (Figures 3.57 and 3.49B). The groundwater flow in the upper part of the stratigraphy, including the Local and Intermediate flow regimes (QRT, WSSA and

USSA), is fed through recharge occurring on a local scale, i.e., within the Local model. This recharge may be locally augmented in the surficial parts of the model via major fractures and faults, the degree of which depends on the geometry and material properties of these fractures.

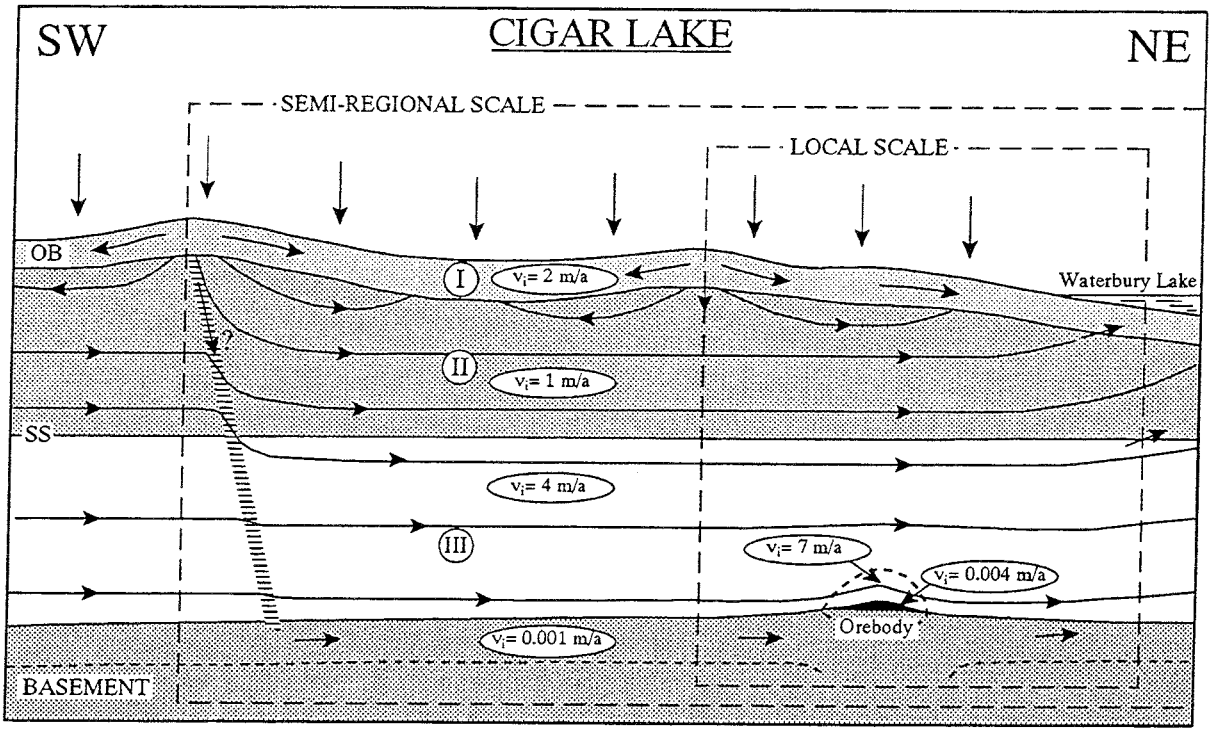

FIGURE 3.57 Schematic vertical 2D section through the Cigar Lake deposit showing defined flow regimes, their calculated particle velocities and their interaction. I= shallow Local flow regime, II= Intermediate flow regime, and III= deep Semi-Regional flow regime. An example of recharge along a fracture zone is schematically illustrated in the left side of the diagram.

The groundwater flow in the lower part of the model, i.e., the deeper flow regime (LSA1, LSA2 and R in Figures 3.56 and 3.57), is in the case of LSA1 and LSA2 partly fed by local recharge percolating through the upper strata, to a lesser degree via major fractures and faults, and in part by water migrating laterally on a semi-regional scale (Figure 3.49). The unaltered basement (B) forms the base for the deeper flow regime, because of its low hydraulic conductivity.

Recharge in the type of surficial strata that exist at Cigar Lake has not been measured, but would equal the groundwater flux through the model (15 to 35 mm/a, from Local 3D-Model) required to maintain steady-state conditions. This value should be compared with the value of 5% of the annual precipitation (27 to 30 mm/a) used both by Golder (Golder 1987b) and in this report (as a boundary flux condition in the 3D modelling).

The 3D results show that particles released within the ore zone exhibit residence times (in the ore/clay zone) of 18,000 to 85,000 a. These figures correspond well with the residence times calculated by Cornett using ^{36}Cl data (Section 3.5.5). The discharge points for these particles, all within the Waterbury Lake area, are located some 2.5 km ENE of the eastern extreme of the ore zone. The added residence time in the Semi-Regional 3D Model for particles traced through the Local 3D Model before discharge varies between 200 and 1000 a, depending on depth of exit.

The three identified flow regimes do not constitute hermetically isolated compartments in a hydraulic sense, but rather communicate either through the bounding strata or through interconnected fractures.

Overall, the 3D results support: 1) the choice of 2D model section orientation, and 2) the identification of flow regimes. The discrepancy in the direction and magnitude of calculated average hydraulic gradients at depth is not attributed to the chosen dimensions, but to possible errors when normalizing the boundary conditions assigned to the Local 2D Model.

3.4.5.2 Fractures and their significance

Very little site-specific information exists with respect to major faults and fractures, and their possible role in enhancing recharge in the upstream end of the model. Most of the data, for obvious reasons, are concentrated within the central borehole array targeted on the ore. The location and geometry of the east-west system of fractures immediately above the ore has been inferred from core logs (COGEMA 1986). An effort was also made to quantify the hydraulic properties of some of the features linked to secondary hydrothermal perched mineralizations at higher elevations (Golder 1985). The results of these tests indicated a low degree of hydraulic pervasiveness along these fractures/faults towards the surface. This was also substantiated by the absence of anomalous hydraulic conductivity values in the tested intervals. A 10 to 20 m wide (EW, 60° S) highly-permeable fracture zone (Q=75 L/s) was intercepted underground by the probe holes for one of the access tunnels at the 420 m level, indicating the presence of an east-west-trending, hydraulically conducting fracture system at depth.

3.4.5.3 Hydrochemical considerations

Normally hydrochemical parameters such as pH, HCO_3, SO_4, Cl, TOC, pCO_2 and redox potential (E_H) may be used to indicate groundwater evolutionary trends. For example, as a rule, E_H, pCO_2, HCO_3, SO_4 and TOC usually decrease, and pH and Cl increase, with increasing depth. Radioactive isotopes such as ^{3}H and ^{14}C also tend to decrease with depth as a function of increasing decay rate with time. Examination of these general parameters at Cigar Lake does not, however, reveal any simple groundwater evolutionary pattern. This may be because of the absence of ion-exchange reactions occurring in the clay-free sandstone formations. The groundwater chemistry is being determined primarily in the clay-rich overburden layers (Cramer and Nesbitt 1994b). In addition, complex groundwater interactions may be occurring in and around the orebody and in the surrounding hydrothermally altered sandstone bedrock. For example, the dissolution of salts from grain boundaries has been put forward as a possible explanation for the enhanced groundwater Cl

concentrations measured close to the deposit (Cramer and Nesbitt 1994b). Mixing of waters from basement sources has also been suggested as a contributing factor, although the general hydrogeological observations and subsequent conceptualization does not support this (Cramer and Nesbitt 1994a). Furthermore, ^{3}H and ^{14}C, produced in situ in the orebody, may result in elevated values for these isotopes in groundwaters in the ore and clay zones.

The absence of simple groundwater evolutionary patterns may also, with due respect to the limited number of sampling locations outside the basement/ore/clay complex, partly reflect the hydraulic environment. For example, in the altered upper sandstone (USSA) (i.e., in the Intermediate flow regime) ^{3}H contents of around 40 to 70 TU have been recorded (WDG-75, Figure 3.58); in the lower, more conductive sandstone (LSA1), values of 10 to 30 TU (WDG-71) occur. Lower values (<8 TU) have been obtained from a sample collected in the 210 m shaft water ring (similar elevation to that of WDG-71). The comparatively high value of ^{3}H recorded in WDG-71 suggests a sizeable component of near-surface-derived water at this level. The presence of ^{3}H generally supports the concept of non-hermetically sealed flow domains inherently described in the conceptual model.

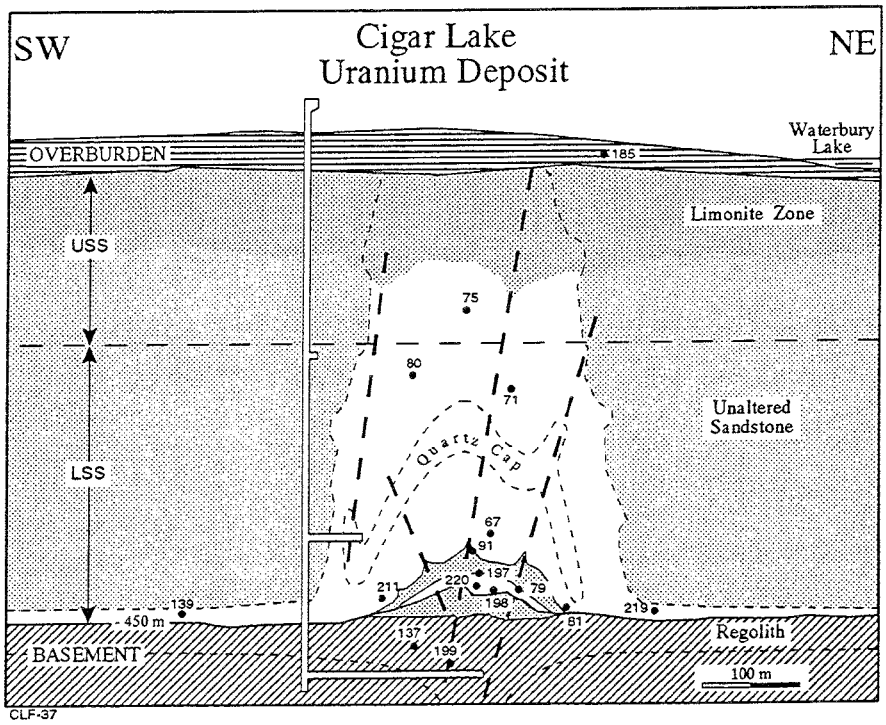

FIGURE 3.58 Schematic vertical section through the Cigar Lake deposit showing relative position of the piezometers used for groundwater sampling.

In general terms the piezometer in WDG-139, located up-gradient from the orebody and at 450 m depth, probably shows one of the best examples of tritium composition unaffected by the presence of the orebody. Here, ^{3}H is around 14 TU, which indicates a noticeable young, near-surface component (precipitation values are around 35 TU). Of the other parameters for WDG-139 water, HCO_3 (around 40 mg/L) is also somewhat high, but this

contrasts with low TOC (0.00-0.17 mg/L).

Therefore, away from the immediate vicinity of the orebody, there is a clear indication in one case, if drill-water contamination is diregarded, that a younger water component (<45 a) has penetrated to a depth of 450 m, and the most likely pathway is via subvertical fractures and faults transecting the sandstone formations. However, these features are not reproduced by the analysis based on the conceptual hydraulic model. This can in part be explained by the absence of a vertical hydraulic gradient below 200 masl (Figures 3.49A and 3.49B), and because vertical/subvertical fracture zones have not been included at local topographic highs up-gradient from borehole WDG-139. Because of the absence of drillholes or surface investigations in areas with topographic highs, such fracture zones have not been confirmed.

The hydraulic test results and the observations of piezometric disturbances from underground activities indicate a heterogeneous medium. These conditions may be present only in the vicinity of the ore zone or over much larger regions. Thus, for such a medium, a (layered) porous continuum model may seem inadequate. But, since the existing database is not large enough to enable use of the fracture network approach, nor the stochastic continuum approach, layered porous media models have been used to illustrate flow-system geometry and mean linear velocity and flow direction. In this case, the introduction of considerable amounts of surface water, grout and drilling materials during the mineral exploration and test mining activities, complicate model verification by water quality data.

3.4.6 Summary and conclusions

The available hydraulic conductivity data show a high degree of variability within identified hydraulic units, which indicates the importance of existing fractures in the overall control of the hydraulic characteristics of the studied system, and the inherent heterogeneity of the system. The hydraulic conductivity values range over 3 to 4 orders of magnitude, varying from approx. 10^{-9} to 10^{-5} m/s.

The detailed flow conditions in and around the basement/ore/clay complex at Cigar Lake has been an important focus of the analog study. In conceiving the more detailed conceptual models required for the analysis, the overall characteristics of already existing models, in some cases calibrated numerically using groundwater flow models, formed a foundation for our work.

The most important revision included in the recent AECL/SKB conceptual models is the lowering of the hydraulic conductivity in the regolith by two orders of magnitude; this was based on underground observations. The revised models also contain a higher degree of detail.

Data on kinematic porosity needed to evaluate particle velocities, particle paths and travel times are not available. In the model calculations the available porosity values measured on rock cores have been used as indicators of the kinematic porosities of the various hydraulic units.

Three different scales have been addressed in the AECL/SKB conceptual modelling: a Regional scale (2D), a Semi-Regional scale (3D), and a Local scale (2D/3D). In the case of the Local Models, the respective Regional models have been used to infer boundary conditions for the Local model scale.

Numerical modelling on the basis of the developed conceptual models has been performed in 2D using the SUTRA code and in 3D using the NAMMU code.

On the basis of existing topographic maps, an average southwest-to-northeast groundwater flow direction has been inferred, and the 2D model sections have been aligned accordingly. The results of the analysis of the Regional 2D Model indicate strong flow dependence on the surface topography, and the development of a number of sub-catchments with groundwater discharge at low points in the topography. These conditions may have been exaggerated because of the use of ground-surface elevation as the upper model boundary (versus the water-table elevation used in the Semi-Regional 3D model). Significant regional flow at depth, linking the southwestern and northeastern boundaries, was not observed.

The results of the analysis of the reference-case Local 2D and 3D Models show the development of three flow regimes within the section: a Local shallow, an Intermediate-depth, and a deep Semi-Regional flow regime, all discharging into Waterbury Lake. The former two are recharged on a local scale, whereas the latter regime is mostly recharged on a semi-regional scale (some recharge may occur locally as well). The topographic effect on groundwater flow in the 2D and 3D model is strongest in the upper 200 m. Horizontal flow prevails at depth with an average hydraulic gradient of 0.3 %. Calculated particle velocities in the upper part of the model vary between 1 and 2 m/a, whereas particle velocities in the lower altered sandstone are on the order of 3 to 4 m/a. In the regolith and unaltered basement, the corresponding velocities are 0.001 and 0.1 m/a, respectively. The results of this reference case have been compiled in a vertical quantified conceptual 2D section based on the 2D/3D model results.

Sensitivity analysis in the 2D modelling has been carried out with respect to boundary conditions, material properties and geometry (fracture zones and low-permeability quartz cap). The results show 1) that changes in travel times are consistent with changes in material properties, and 2) that these changes vary within a factor 4. The sensitivity analysis with regard to boundary conditions showed that adjusted (normalized) boundary conditions extracted from the Regional 2D Model provided the best fit with measured piezometry, when applied to the reference case. This set of conditions was chosen as the reference set of boundary conditions. Sensitivity analysis using the Local 3D Model show output results that are consistent with, and proportional to, changes made in the input data.

The inclusion of vertical fracture zones in the ore zone of the Local 2D Model did not alter the flow field or particle travel paths to any significant degree, because the hydraulic gradient is essentially horizontal. However, inclined fracture zones in the recharge and discharge end of the model may result in enhanced velocities and increase the depth of local flow systems. The incorporation of a poorly-permeable quartz cap ($K = 10^{-7}$ m/s) results in

a diversion of flow around it. Calculated transport times in the lower sandstone are in this case up to one order of magnitude higher.

A sensitivity analysis of the effect of a stratified overburden, consisting of a 20 to 25 m, highly conductive, sandy layer (K= 10^{-5} m/s) overlying a thin (approx. 3-m-thick) silty glacial-till layer (K= $\leq 10^{-8}$ m/s), showed that the output based on this conceptualization essentially corresponds to the output based on the description of the overburden in the base case, which includes an integrated sand+till layer (K= $1x10^{-6}$ m/s). On the other hand, in the case where the hydraulic conductivity of the basal-till layer was set at 10^{-9} m/s, the depth of the local flow system was much more shallow, and vertical hydraulic gradients decreased.

Even though the Local 3D Model is not fully calibrated, various qualitative and semi-quantitative inferences may be drawn from the model. The 3D results support the overall findings made on the basis of the 2D model, with the exception that the average groundwater flow direction at depth in the 3D model is oriented more ENE with a flow velocity of 1/3 that of the 2D model. This implies that the calculated residence times in 2D underestimate residence times by a factor of 3. Residence times in the ore for particles released within the ore/clay zone are on the order of 18,000 to 85,000 a, which correspond well with residence times calculated from ^{36}Cl data (Section 3.5.5).

A comparison between the 2D quantified conceptual section and the available hydrogeochemical data indicates that the relatively high tritium values (if these values are representative and do not reflect any contamination) at depth in the upstream end of the model (WDG-139 location) are incompatible with the present hydraulic conceptualization. This is because the flow below 200 masl is prevailingly horizontal, which does not allow groundwater circulation to the base of the model. Such a flow-system geometry would be changed if vertical fractures were included in the model at topographic highs where significant vertical hydraulic gradient would exist. However, the likelihood of fracture zones outcropping in topographical highs is considered to be low.

The overall hydrogeochemical indications are that the Cigar Lake deposit is located in a highly heterogeneous environment. This heterogeneity may to a large extent be attributed to the lithology, mineralogy and structure of the deposit. Heterogeneity is indicated by the large range in the measured hydraulic material properties. The hydraulic system has been conceptualized as being a layered porous continuum, because the hydraulic information is inadequate to use the fracture network or stochastic continuum approaches. Nevertheless, the good simulations of water-table configuration and piezometric-level drawdown during pumping indicate that the approach used was appropriate. The sensitivity modelling demonstrated very well the consistency of the three main flow regimes and the variability of flow-system geometries with changes in permeability distribution. Results of the modelling indicate that the presence of vertical fractures extending through the sandstone in recharge areas (where sandstones crop out at ground surface) and a poorly-permeable basal till (K= 10^{-9} m/s) would increase recharge to the Semi-Regional flow system and reduce the depth of local groundwater flow. Some effort should be made to make the necessary field observations that would determine these conditions and reduce model variability.

3.4.7 Acknowledgements

Acknowledgements are given to the Cigar Lake Mining Corporation and Golder Associates for use of their hydraulic-head data and piezometer-construction details. We thank R. Nordqvist, Geosigma AB, Sweden, and A. Boghammar, Kemakta AB, Sweden, for valuable discussions during the 2D and 3D modelling, respectively. We also thank N. Scheier, AECL Research, for his careful review of this Section of the report and his many suggestions that have improved the report quality. We are grateful as well for the numerous discussions with co-authors, particularly J. Cramer and J. Smellie.

3.4.8 References

AECL/SKB. 1990. Progress report for the period May - December 1990. Ed: J.J. Cramer. AECL Proj. Rep., **CLR-91-01**.

AECL/SKB. 1991. Second annual report of the AECL/SKB Cigar Lake Project - Year 2: 1990-1991. Eds: J.J. Cramer and J.A.T. Smellie. AECL Proj. Rep., **CLR-91-3**.

AECL/SKB/USDOE. 1992. Progress report for the period November 1991 - February 1992. Ed: J.J. Cramer. AECL Proj. Rep., **CLR-92-2**.

ATKINSON, R., HERBERT, A.W., JACKSON, C.P., ROBINSON, P.C. and WILLIAMS, M.G. 1989. NAMMU user guide (Release 4). Theoretical Physics Div., AERE Harwell, January 1989.

BEAK. 1984. Environmental impact study on COGEMA's site at Waterbury Lake, Section 3 - Hydrogeology. IEC Beak Consultants Ltd.

COGEMA. 1986. Fracturation in the sandstone above the ore zone - Cigar Lake deposit. COGEMA Canada Ltd., June 1986.

CORELAB. 1984. Core analysis - Holes WDG1-137/139. Core Laboratories - Canada Ltd.

CRAMER, J.J. and NESBITT, H.W. 1994a. Hydrogeochemistry of the Cigar Lake uranium deposit: hydrologic and isotopic constraints. Manuscript in preparation.

CRAMER, J.J. and NESBITT, H.W. 1994b. Hydrogeochemistry of the Cigar Lake uranium deposit: groundwater evolution and redox geochemistry. Manuscript in preparation.

FV. 1991. FEMGEN/FEMVIEW - The finite element pre- and post-processor: user manual, version 1. Femview Ltd., Leicester, UK, October 1989.

GOLDER. 1985. Report to Cigar Lake Mining Corporation on a revised mine inflow assessment, Cigar Lake property. Golder Associates, **1985/11**, November 1985.

GOLDER. 1987a. Report to Cigar Lake Mining Corporation presenting geotechnical and hydrogeological data from the proposed shaft location. Golder Associates, **1987/01**, January 1987.

GOLDER. 1987b. Final report to Cigar Lake Mining Corporation on 1987 hydrogeological computer model study, Cigar Lake uranium deposit, Cigar Lake, Saskatchewan. Golder Associates, **1987/08**, August 1987.

GRUNDFELT, B., BORGHAMMAR, A. and LINDBERG, H. 1989. HYPAC user's guide. Swedish Nuclear Fuel and Waste Management Co. SKB Prog. Rep., **AR-89-22**.

SIG. 1987. Cigar Lake pumping test results. Report prepared for CLMC. Stevenson International Groundwater Consultants, May 1987.

SMITH, J.D. 1983. Waterbury Lake Project - 1983 geotechnical test results (exploration boreholes WDG-75, -76, -79, -80, -81 and -91).

STEVENSON, D.R. 1989. A review of conceptual and numerical models of natural groundwater movement in Athabasca sandstone and basement rocks around Cigar Lake uranium deposit. Unpublished internal AECL report, February 1989.

VOGEL, P. 1990. TRACK - A particle tracking routine for SUTRA: a manual for its use. Bundesanstalt für Geowissenschaften und Rohstoffe, Hanover, BDR (in German).

VOSS, C. 1984. SUTRA - A finite-element simulation model for saturated-unsaturated, fluid-density-dependent groundwater flow with energy transport or chemically-reactive single-species solute transport. U.S. Geol. Survey, Water-Resources Invest. Rep., **84-4369**.

3.5 HYDROGEOCHEMISTRY

3.5.1 Introduction

(J. Cramer)

The hydrogeochemical studies at Cigar Lake started with the first field work at site in the summer of 1984. It soon became obvious that the groundwaters at depth were very reducing and dilute, and that a special effort was needed to properly collect water samples and analyze their composition. With each successive trip since 1984, improvements have been made to the methods of collecting and preparing groundwater samples, as well as in monitoring and analyzing on-site the composition of the waters upon collection. To further improve the quality of the waters and the control on their sampling location, a number of packer-equipped piezometers were installed in 1986-87. As part of the AECL/SKB collaboration, additional piezometers were installed in 1989, including those in two newly drilled holes at locations identified by the project. The Cigar Lake Mining Corporation, as part of the test-mining phase that started in 1988, provided additonal opportunities and locations for sampling and monitoring groundwater compositions. These latter activities included the installation of piezometers in the glacial overburden, access to underground sampling locations through the excavation of the shaft and horizontal developments and the drilling of underground exploration holes, and conducting several pump, flow and injection tests.

By 1990 a significant hydrogeochemical database had been obtained, and it was decided to convene a workshop to review these data and select a set of reference groundwater compositions for use in the various modelling excersises. This workshop was convened in 1990 December, in Pinawa, and resulted in the selection of two representative compositions for water obtained from each piezometer, including the overburden, and from Waterbury Lake.

The study of colloids and suspended particles in the groundwaters at Cigar Lake has been an integral part of the hydrogeochemical investigations since 1985. This integration provided opportunities for experiments to obtain additional information on the behaviour of radionuclides and trace elements, such as partitioning, sorption and coprecipitation. Starting in 1986, the groundwater samples were also analyzed for their microbial content and activity, although systematic tests and experiments were not included until 1990.

The modelling of groundwater compositions and their integration with data obtained from other disciplines, such as hydrogeology and nuclear reaction product geochemistry, required that data be obtained on additional isotopes and trace elements. The results from one of these studies, on ^{36}Cl, which involved the tandem-accelerator super-conducting cyclotron (TASCC) facility in Chalk River, Ontario, are reported in Section 3.5.5. The results of other isotope studies, including ^{129}I involving the Los Alamos National Laboratory in Los Alamos, New Mexico, is reported in Section 3.8.2.

The following sections describe the methods used in obtaining and analyzing groundwaters (Section 3.5.2), the hydrology and isotope geochemistry (Section 3.5.3), and the evolution of groundwater compositions in time and space (Section 3.5.4).

3.5.2 Water sampling and analysis

(J. Cramer, P. Vilks, H. Miller and D. Bachinski)

This section describes the methods and procedures for the collection, preparation and analysis of water samples, as well as colloid samples obtained from the filtration of these waters, from available sampling locations and piezometers at Cigar Lake. A summary is also included of the processing and selection of the hydrogeochemical data, which resulted in the set of reference water compositions (Table 3.30) for use in the various modelling activities of the analog study.

3.5.2.1 Hydrogeochemistry

3.5.2.1.1 Introduction

Initial groundwater sampling at Cigar Lake in 1984 was limited to the airlift method used by Beak Consultants, which could only collect water samples from the top of the water column inside the piezometer standpipe. A trailer-mounted downhole grab-sampler was brought on site in 1985, and this system was used to collect small samples for analysis of both water and dissolved gases. Sampling of larger volumes of groundwater started in 1986, using a downhole squeeze pump system alongside the grab-sampler. The squeeze pump system was subsequently improved by mounting it inside a small ATCO trailer, allowing for year-round sample collection under climate-controlled conditions.

In 1984-1985, the analysis of groundwater compositions and parameters of the grab samples was limited by the use of simple field methods and kits. Starting in 1986, groundwater collected by the downhole squeeze pump was monitored using an in-line flow cell inside a glovebox containing a N_2-gas atmosphere (Cramer 1986). Similarly, filtration of the water samples was initially done using tradional flow-through membranes in 1984 and 1985. A tangential-flow filtration system (Pellicon system) was introduced in 1986, and all subsequent filtration of groundwater samples has been carried out with this system, which is also located inside a N_2-gas glovebox (Cramer et al. 1987). On-site analysis of a number of components started in 1985 with the determinations of dissolved-^{222}Rn and -O_2, Fe^{++}, ortho-phosphate and sulphide. The on-site capabilities were expanded subsequently to include analysis of uranium and radium-226. The full, on-site, analytical capability was successfully used during the large-scale pump test conducted in 1987 March-April (Cramer 1988). Since 1989 AECL has installed an on-site laboratory, in addition to the mobile sampling laboratory, to carry out sample preparation (filtration, preconcentration, etc.) and analyses (anions, redox cations, uranium, radon, particle size analysis, microbial analyses (BART tests), etc.) as soon as possible following the collection of each water sample.

3.5.2.1.2 Groundwater sampling

Groundwaters from different parts of the deposit and the surrounding host rocks have been collected from piezometers installed in boreholes (Figure 3.59, Table 3.28). In addition to sampling from piezometer-equipped holes, several groundwaters have also been collected from open artesian holes, providing a mixture of waters from the sandstone formation

between the unconformity and the overburden. These artesian holes are located on the shore of Waterbury Lake to the north of the deposit and one on the shore of Cigar Lake above the deposit. The diamond-drilled holes, containing piezometers, are all vertical NQ-size exploration holes equipped with a steel casing through the overburden section at the top. The piezometers consist of a PVC pipe (3.81 cm ID) with a perforated, screened intake section at the bottom. The intake section (1-3 m long; PVC or stainless steel) collects water from a distinct interval in the borehole that is isolated either by packers (under N_2 pressure) or by bentonite seals on either side of the intake section. Before sampling the groundwater, the water column inside the piezometer was replaced with fresh formation water by flushing with N_2 gas.

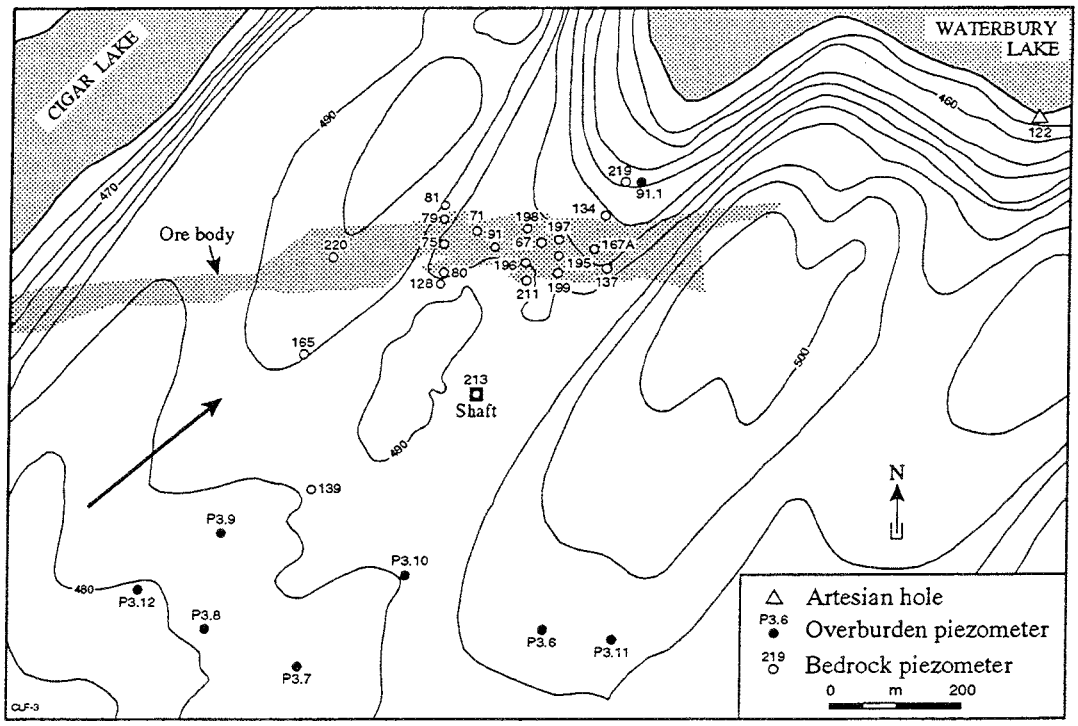

FIGURE 3.59 Map of the Cigar Lake deposit showing the projected outline of the uranium mineralization at the unconformity level and the location of piezometer-equipped boreholes, artesian holes and the shaft. The arrow indicates direction of regional groundwater flow.

Two different methods are used to collect groundwater from the piezometers, one using a downhole grab-sampler and the other using a squeeze pump. With both methods the system is lowered to the bottom of the piezometer pipe to collect the groundwater as close as possible to the borehole interval isolated for sampling. The downhole grab-sampler (Figure 3.60) collects water in stainless-steel vessels by means of N_2-gas-operated checkvalves that

isolate and preserve the sample under the ambient pressure at the sampling depth. Samples from the sealed vessels are used for the analysis of dissolved gases, bacteria and isotopes. With the other method, a N_2-driven squeeze pump is used to pump the water to the surface for on-line analysis and collection (Figure 3.61). This latter method allows the collection of large volumes of groundwater; it is used to monitor variations in composition during the pumping, to minimize changes to the compostion by immediate analysis or preparation, and to collect and preserve colloid samples.

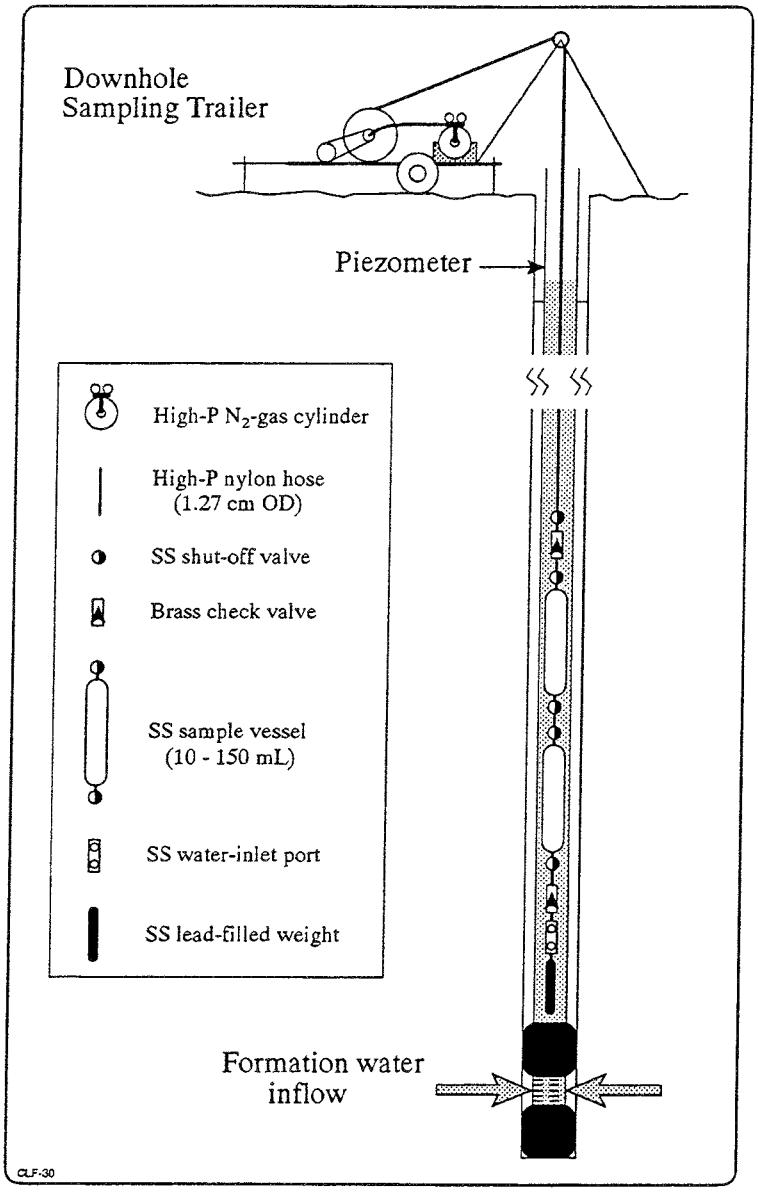

FIGURE 3.60 Schematic diagram illustrating the system used for collecting pressurized grab samples from depth in piezometers installed at Cigar Lake. Several pressure vessels can be connected in sequence providing for larger sample volumes to be collected.

TABLE 3.28
LIST OF PIEZOMETERS AND ARTESIAN WELLS
FOR WATER SAMPLING AT CIGAR LAKE

#*	Hole #	Lithology of Water inflow	Depth Interval m	Type of Piezometer
1	67	altered sandstone	345.0 - 348.6	AECL, 2 packers, van Ruth plug, sealed annulus
2	71	lower sandstone	242.3 - 245.9	AECL, 2 packers, cement plug, sealed annulus
3	75	upper sandstone	154.5 - 158.1	AECL, 2 packers on old standpipe, sealed annulus
4	79	mineralized sandstone	430.0 - 433.0	single bentonite seal, sandpack on cement plug
5	80	lower sandstone	190.5 - 208.0	single bentonite seal, sandpack on cement plug
6	81	lower sandstone discharge N-side	440.0 - 444.0	AECL, 2 packers, van Ruth plug
7	83	u+l sandstone and basement	18.3 - 477.3	open hole, artesian
8	91	clay	403.0 - 408.0	AECL, 2 packers, van Ruth plug
9	122	upper sandstone	0.0 - 200.0	open hole to cement plug, artesian
10	128	basement	463.0 - 470.9	one bentonite seal, sandpack in end of hole
11	134	clay-altered sandstone	410.0 - 422.0	two bentonite+oil seals, sandpack, van Ruth plug
12	137	basement	475.0 - 477.1	one bentonite seal, sandpack in end of hole
13	139	lower sandstone recharge S-side	439.0 - 443.0	AECL, 2 packers, van Ruth plug
14	197	ore-clay contact	415.0 - 422.0	AECL, 2 packers, van Ruth plug
15	198	ore	423.0 - 427.0	AECL, 2 packers, van Ruth plug
16	199	altered basement	445.5 - 452.0	AECL, 2 packers, van Ruth plug
17	211	altered sandstone	415.0 - 418.6	AECL, 2 packers, van Ruth plug, sealed annulus
18	219	outflow N-side	413.0 - 416.6	AECL, 1 packer, bottom of hole, sealed annulus
19	220	ore	432.0 - 439.5	AECL, 2 packers, bottom of hole, sealed annulus
20	Shaft	upper sandstone	40.0 - 210.0	water ring above shaft station at 210 m

* #s 4, 5, 10, 11, 12: installed by COGEMA prior to 1986
#s 6, 8, 13, 14, 15, 16: installed by AECL in 1986
#s 1, 2, 3, 17, 18, 19: installed by AECL in 1989
Water ring installed by CLMC in 1988

On-site analysis of the groundwater is done as much as possible to minimize changes in the composition. Since the deep groundwaters in the deposit are relatively cold (~8 °C) and reducing, rapid changes in composition occur from exposure to air, from degassing and from warming. On-site analysis or preparation may also be required because of a short half-life (e.g., ^{222}Rn), changes in the composition and abundance of colloidal particles, or the need to monitor the composition during prolonged pumping (e.g., Eh, conductivity, tracers, etc.). Up to 1987, the set-up used in the field for monitoring (of pH, ORP, temperature, conductivity, and dissolved O_2) and analysis of the pumped groundwater included a flow cell with various electrodes and an in-line conductivity sensor inside a glovebox containing a controlled N_2 atmosphere. Starting in 1989, this system was revised to include a pressurized flow cell (allowing measurements to be made under pressures up to 50 psi), additional sensors (to monitor pressure, the water level inside the piezometer during pumping, turbidity and dissolved H_2), and an on-line data acquisition system.

The water samples are also analyzed in the field for uranium, radium and radon using fluorometry, α-spectrometry and scintillometry, respectively. Filtration of the samples is carried out with a tangential-flow filtration system to concentrate particles with a size greater than 10,000 molecular weight or nominal 1 nm. Following filtration, particle-sizing of the colloid concentrate is carried out in a glovebox under a N_2-gas atmosphere.

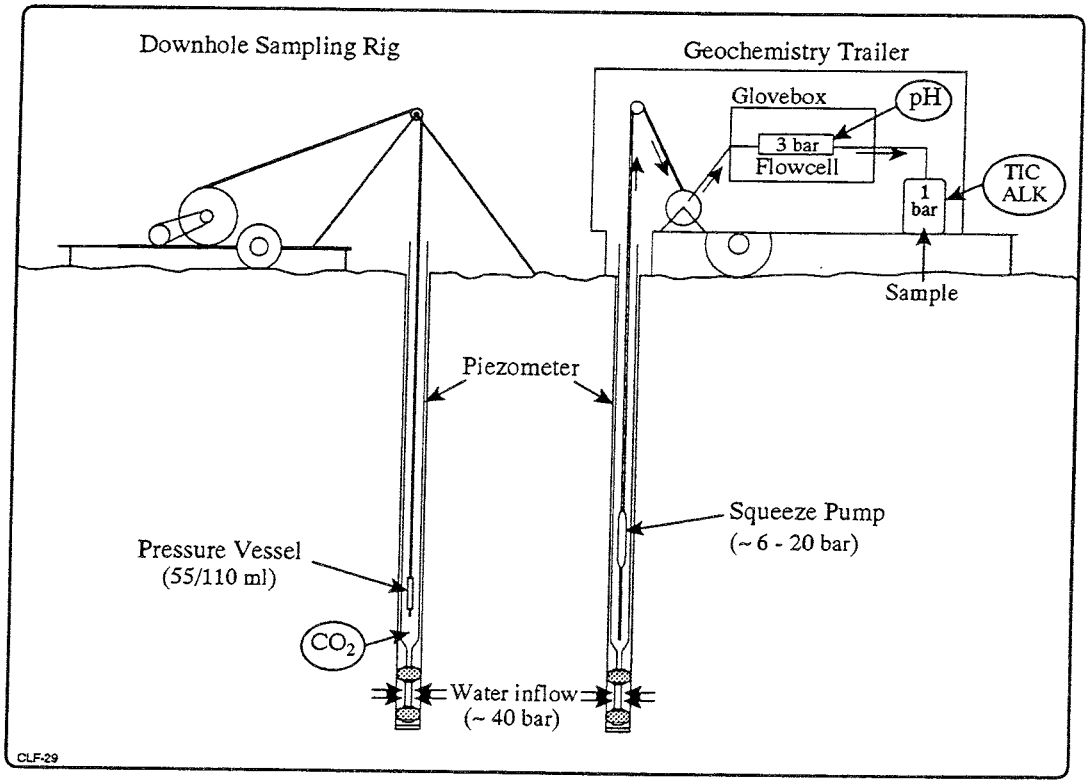

FIGURE 3.61 Diagram illustrating the setup used for groundwater sampling from deep piezometers at Cigar Lake. See text for further explanation.

3.5.2.1.3 Sample preparation

Upon collection, the total volume collected for each water sample is filtered, except for the aliquots for organic carbon and microbial analyses and the pressurized samples for dissolved gas analysis. Filtration prior to 1986 was carried out using a 5 μm prefilter, followed by, in sequence, 0.45 μm and a 0.1 μm filters. After filtration, the wet filter papers were sealed in plastic and stored in a freezer. From 1986 on, the Pellicon system was used for filtration, providing a <1 nm filtered aliquot for dissolved species and several size-fraction aliquots for colloid analysis. For further details of filtration methods and colloid sampling see Section 3.5.2.2.

The sample aliquot for cation analysis is acidified using 1 mL concentrated HCl per 100 mL of sample. The samples for anion and stable isotope analysis are not acidified, but are stored cold until they are analyzed. The sample for HS analysis is buffered with a sulphide anti-oxidant buffer and kept cold and in the dark until analyzed. Up to 1990, preparation of samples for the analysis of U, Th and Ra involved a 4 L filtered (F2) aliquot that was first acidified (1 mL conc. HCl per 100 mL sample), then spiked with 1 mL of certified Harwell ^{232}U and ^{228}Th spike solution, and subsequently concentrated by boiling down to a 1 L sample. From 1990 onwards, the preparation in the field of samples for U and Th isotopes was changed to include the Fe-coprecipitation from a 4 L filtered (F2) aliquot (the first step of the procedure for U-series isotope analysis).

The samples for organic carbon and colloid analyses, and a 1 L sample for ^{3}H and stable isotopes are stored in sterilized glass bottles with aluminum-foil seals and kept cold until analysis takes place. All other samples are stored in narrow-mouthed Nalgene HDPE bottles.

The samples collected for microbial analyses are collected with the down-hole sampling rig, and the samples are brought to surface under the ambient pressure at the sampling depth. The vessel ($\sim$55 mL) used for the collection of the microbiology sample is placed at the bottom of the vessel string directly above the intake port. This arrangement allows this vessel to be filled last after it has been thoroughly rinsed with all the formation water filling the other vessels and the pressure hose (over a length of $\sim$150-400 m). The microbiology vessel (including its two valves) is sterilized at 550 °C for $\sim$4-8 h in a muffle furnace before assembly of the vessel string. The non-sterilized components of the sampling rig that are in contact with the water below the microbiology vessel include the checkvalve (brass), intake port and weight (both stainless-steel).

Once the microbiology vessel has been isolated from the string at surface, the contents are transferred to a sterile serum bottle (glass) sealed with a sterilized septum and filled with dry N_2-gas. A sterilized stainless-steel connector and needle are attached to one end of the vessel, and a He-gas overpressure is used at the vessel's other end to transfer the water sample through the septum into the bottle. A second sterilized needle is used to bleed the gas overpressure from the bottle during the transfer. The sample bottle is then labelled and stored in the dark at $\sim$4 °C in a refrigerator in the field lab on site at Cigar Lake. Transport of the samples from Cigar Lake to elsewhere for analysis is done in coolers with dry ice added to maintain a cool temperature.

3.5.2.1.4 Sample analyses

Table 3.29 lists the elements, isotopes and gases analyzed in the water samples, as well as the analytical method, detection limit and precision.

Cations
The cations are determined by inductively coupled plasma spectrometry (#1, Table 3.29) and by atomic absorption spectrometry (#2, Table 3.29).

Anions
The anions are determined by ion chromatography (#3, Table 3.29), by titration (#4, Table 3.29) and by spectrophotometry (#5, Table 3.29).

Radioelements
The following elements and their isotopes are determined by α-spectrometry (#6, Table 3.29): total-U, ^{234}U, ^{238}U, total-Th, ^{230}Th, ^{232}Th and ^{226}Ra. Sample preparation involves chemical extraction of U, Th and Ra using coprecipitation with Fe-hydroxide (for U and Th) and Ba-sulphate (for Ra) respectively. The analysis of the gaseous element ^{222}Rn (#7, Table 3.29) involves degassing of the sample on a Rn-gas extraction line followed by measuring of the α-activity in a ZnS scintillation cell. The determinations of the ^{3}H content are done by scintillometry (#8, Table 3.29).

Stable isotopes
The contents of the stable isotopes ^{2}H and ^{18}O are determined by mass spectrometry by the Environmental Isotope Laboratory of the Department of Earth Sciences at the University of Waterloo in Waterloo, Ontario. Typical precisions in the δD and $\delta^{18}O$ are, respectively, 2 and 0.05 per mil.

Gases
The concentration of dissolved gases is determined using mass spectrometry. The vessels containing the pressurized samples are degassed on a special gas-extraction line and the total gas volume is measured gravimetrically. The resulting mass spectrum allows detection of the following gases: H_2, He, O_2, Ar, CO_2, CH_4 and N_2. The measurement of the isotope ratio for ^{12}C to ^{13}C on CO_2 or CH_4 could be made only when sufficient amounts of the gases were present in the sample. In addition, dissolved-O_2 analyses are performed in the field using an electrochemical sensor.

3.5.2.1.5 Data processing

The processing of the raw analytical data for each water sample collected involved a number of steps, depending on the type of sample collected and other considerations. All the data selected for a set of reference compositions of waters from selected locations are listed in Table 3.30.

Charge balance
The charge balance listed in Table 3.30 is calculated as the percentage difference between cation and anion equivalents divided by the cation equivalent value.

TABLE 3.29
ANALYTICAL METHODS, DETECTION LIMITS AND
PRECISIONS FOR ANALYSES OF WATER SAMPLES

Element	Method (see text)	Detection Limit	Precision (2σ)
Ca	1	0.005 mg/L	2.4% for 1.0 mg/L
Mg	1	0.001	3.4 - 1.0
Fe	1	0.010	1.1 - 0.50
Mn	1	0.005	0.47 - 0.50
Si	1	0.040	0.73 - 1.0
Al	1	0.100	4.0 - 1.0
Ba	1	0.004	0.38 - 0.50
Cu	1	0.010	0.78 - 0.50
Zn	1	0.005	7.6 - 0.50
Mo	1	0.015	1.2 - 1.0
Ni	1	0.020	2.1 - 0.50
Pb	1	0.070	5.7 - 0.50
Co	1	0.015	1.1 - 0.50
Cr	1	0.010	1.3 - 1.0
Cd	1	0.010	0.59 - 0.50
As	1	0.075	1.3 - 1.0
Se	1	0.100	2.9 - 1.0
I	1	0.400	2.0 - 10.0
Na	2	0.05 mg/L	3.3% for 1.0 mg/L
K	2	0.05	4.7 - 1.0
Li	2	0.05	5.0 - 1.0
V	2	0.012	5.5 - 0.50
F	3	0.03 mg/L	7.1% for 0.5 mg/L
Cl	3	0.13	3.2 - 5.0
HS	3	0.07	7.1 - 0.5
SO_4	3	0.1	7.1 - 0.5
NO_3	3	0.2	5.0 - 0.5
HCO_3	4	2.0	2.5 - 5.0
CO_3	4	2.0	2.5 - 5.0
HPO_4	5	0.1	5.0 - 0.5
U	6	0.1 μg/L	3.2% for10.0 μg/L
Th	6	0.5	3.5 - 10.0
Ra	6	0.02 Bq/L	5.0 - 1.0 Bq/L
Rn	7	0.02	5.0 - 1.0
^3H	8	8.0 TU	35.7 - 42.5 TU

Correction for CO_2 degassing

Although a number of parameters listed in Table 3.30 were determined at pressures of either 3 bar* (in the flow cell) or 1 bar (all bench-top analyses), the data in the table represent the composition of the groundwater under the ambient pressure at depth (* 1 bar = 100 kPa). The difference between values measured at surface and those calculated for the ambient pressure are due to the effect of the pressure differential on the dissolved gas content, primarily in the carbonate system.

Figure 3.61 illustrates the scenario of sampling and analyses for the independently determined parameters of dissolved $CO_2(g)$, pH, alkalinity and total inorganic carbon (TIC). The $CO_2(g)$ value in Table 3.30 represents the content of this gas in the sample collected under the ambient pressure at depth, whereas the original measurement of pH was made in the flow cell under a 3 bar pressure, and the determinations of alkalinity and TIC were made in the water sample under atmospheric pressure. Using these different data points, values for pH, pCO_2 and TIC can be calculated for the groundwater at depth. This calculation is based on the following assumptions:

1- chemical equilibrium in the carbonate system at depth,

2- the charges of major ionic species in solution are balanced:

$$H^+ + Na^+ + K^+ + 2Ca^{2+} + 2Mg^{2+} + 2Fe^{2+} = OH^- + F^- + Cl^- + HCO_3^- + 2SO_4^{=} + 2CO_3^{=}$$

3- alkalinity $= [HCO_3^-] + [OH^-] + 2[CO_3^{=}] - [H^+]$

is conservative under all pressures, and

4- conservation of mass balance for C:

$$C_T \text{ (TIC)} = H_2CO_3 + HCO_3^- + CO_3^{=} + CO_2(g).$$

Starting with the measured pH and Alkalinity, the measured content of $CO_2(g)$ is titrated back into the analyzed composition of the groundwater, and the composition at depth, with the dissolved CO_2, can then be calculated. These calculations have been done for 10 °C and the applicable pressure for each location, using the appropriate equilibrium constants.

The results clearly show the effects of degassing on the three parameters that have important consequences for geochemical modelling of water-rock interaction at depth. For instance, the pH value calculated for the ambient condition at depth can be lowered by as much as one unit compared with the measured pH value at surface (at 3 bar in the flowcell). This shift in pH has been assessed in terms of the criteria for chemical and thermodynamic equilibrium of the geochemical system, producing more realistic and compatible results for the observed water-rock interactions.

Thus, Table 3.30 lists the reference groundwater compositions for use in the modelling activities involving hydrogeochemical information. The data for pH, pCO_2 and TIC in this table have been assessed for their representativeness, quality and accuracy.

Representative samples

A set of typical groundwater compositions was selected by Jan Cramer, based on all available data collected since groundwater sampling and analyses were first started in 1984. This set contains compositions for two samples from each of 14 locations throughout the deposit, including one station at surface (Waterbury Lake), and these compositions are considered representative for the different rock units in the stratigraphy. The following criteria were used in the selection of these particular compositions:

- the exclusion of any compositions with obvious contamination either from poor piezometer installation (e.g., oil-contaminated bentonite seals) or broken/malfunctioning piezometers;
- the exclusion of any compositions affected by known disturbances, such as pump tests, flow tests, grouting, recent drilling (i.e., rock flour) etc.;
- the exclusion of any compositions clearly affected by sampling (pumping) parameters;
- the representation of the range of natural conditions including lithology of piezometer depth-interval, presence of fracture(s), type of piezometer, season of sampling, time since piezometer was installed etc.;
- the representation of the range of compositional variation for major cations and anions;
- the representation of the range of measured parameters, including pH, Eh, conductivity and turbidity, with emphasis on pH and Eh;
- the correlation with known lithology/mineralogy (i.e., uranium content, radon content, etc.); and
- the consideration of analytical variabilty and error.

The various compositions were reviewed and discussed in detail during the Hydrogeochemistry Review Meeting held in 1990 December in Pinawa, resulting in some modifications being made to the original selection. The final selection of representative groundwater samples, assessed for quality and accuracy, and recommended for use in the various modelling excersises, is included in Table 3.30.

3.5.2.2 Colloids

3.5.2.2.1 Introduction

The potential role of colloids in the groundwater transport of radionuclides has been addressed at Cigar Lake. As a prerequisite to understanding particle transport, research has focussed on characterizing the size distribution, concentration, composition, and natural radionuclide contents of particles throughout representative parts of the uranium deposit.

Water samples, collected periodically from piezometers, artesian wells and surface waters located in and around the Cigar Lake deposit, were filtered to obtain samples for colloid study. These samples, collected as early as 1986, were obtained using a squeeze pump with pump rates of between 2 and 20 L/h. With continued groundwater collection, the concentrations of suspended particles usually decreased with time. Although colloid

concentrations may also decrease with continued pumping during a sampling session, their concentrations may recover during periods between different sampling sessions.

3.5.2.2.2 Production of particle concentrates

The concentrations of colloids in groundwaters are often very low, and conventional dead-end ultrafiltration can process only small groundwater volumes. Consequently, only microgram quantities of colloidal material can be collected on membranes by conventional filtration. This material can be characterized only by microscopic techniques, such as scanning electron microscopy with energy dispersive X-ray analysis (SEM/EDX). Therefore, to collect enough material for a more comprehensive characterization, Millipore tangential-flow ultrafiltration systems were used to produce particle concentrates from 50 L groundwater samples. These particle concentrates contained enough material for colloid concentration and size analysis, as well as X-Ray diffraction analysis (XRD). Chemical and radiochemical analysis of particle concentrates and filtered water provided information on the size distribution of various elements and radionuclides in groundwater.

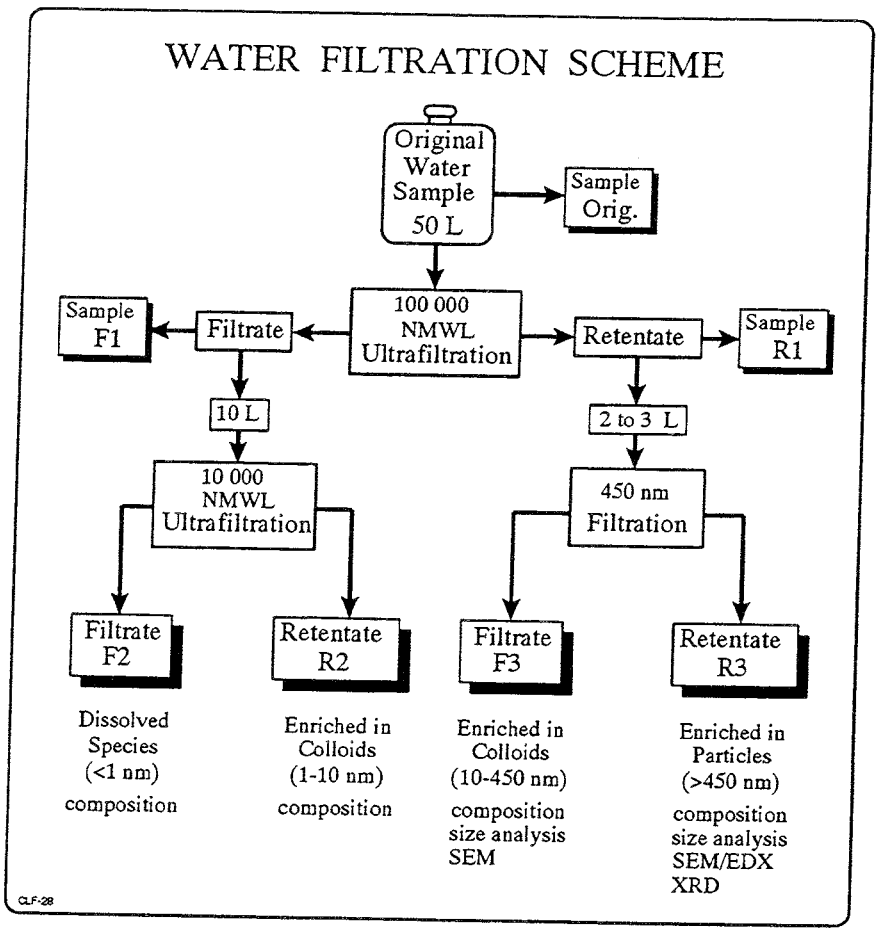

FIGURE 3.62 Filtration scheme for groundwater particles, showing the production of samples (F1, R1, F2, R2, F3 and R3) used to calculate element size distributions in groundwater.

The basic method of producing particle concentrates from Cigar Lake waters in 1989 was similar to the procedure described by Vilks and Drew (1986) and Vilks et al. (1988) (see also Section 3.6). However, since 1988 the concentration procedure has been improved in order to produce several concentrates with different particle sizes, to minimize salt retention during ultrafiltration, and to eliminate problems of irreversible membrane fouling by suspended particles. In the original procedure only one concentrate was produced using a membrane with a 10,000 nominal molecular weight limit (NMWL). No prefiltration was done to avoid loss of colloids and suspended particles. For the new procedure (Figure 3.62), groundwater is first filtered through a Pellicon system equipped with polysulfone 100,000 NMWL (about 10 nm cut-off) membrane packets, separated by retentate screens. Unlike the single-unit membrane cassettes used by the original method, the membrane packets can be disassembled for easy cleaning. The 100,000 NMWL membrane is less affected by salt retention than the 10,000 NMWL membranes. The concentrate (retentate) produced by the 100,000 NMWL filter is filtered with the Minitan tangential-flow filtration system (Millipore), equipped with a 450 nm cut-off Durapore membrane, which produced a filtrate containing colloids between 10 and 450 nm, and a concentrate enriched in suspended particles greater than 450 nm. Ten liters of filtrate produced by the initial 100,000 NMWL filtration were filtered through another Pellicon system, equipped with a polysulfone 10,000 NMWL filter cassette. This produced a sample of filtered water containing only dissolved species, and a concentrate enriched in colloids with a size range between about 1 and 10 nm. The filtrate and concentrate samples to be used for chemical and radiochemical analyses were preserved by acidifying to pH 1 with HCl.

3.5.2.2.3 Sample analysis

Particle concentrations and size distributions were measured by pressure-filtering 20 to 50 mL of particle concentrates through a series of 25 mm Nuclepore polycarbonate filters with cut off sizes of 10,000, 5000, 400, 100, 50, and 10 nm. Particle concentrations were determined by the weight of material deposited on the filters. The presence of colloidal material in the 1 to 10 nm size range could only be determined by chemical analysis of the colloid concentrates. Samples for XRD were prepared by filtering particle concentrates through a 450 nm silver membrane.

The major and trace element compositions of particle concentrates and filtered water were determined by the Analytical Science Branch at Whiteshell Laboratories in Pinawa, using atomic absorption (AAS) and inductively coupled plasma spectrometry (ICP). Inorganic and organic carbon were measured by the Astro 2001 carbon analyzer. Uranium was measured by fluorometry using the Scintrex system.

3.5.2.3 References

CRAMER, J.J. 1986. A natural analog for a fuel waste disposal vault. In *Proc. 2nd Int. Conf. Rad. Waste Manag.* Can. Nucl. Soc. Proc., 697-702.

CRAMER, J.J., VILKS, P. and LAROCQUE, J.P.A. 1987. Near-field analog features from the Cigar Lake uranium deposit. In *Natural Analogues in Radioactive Waste Disposal* (ed. B. Côme and N.A. Chapman). Com. Europ. Commun. Publ., **EUR 11037 EN**, 59-72.

CRAMER, J.J. 1988. Natural analog studies on the Cigar Lake uranium deposit: an update. In *Proc. CEC Natural analogue working group meeting in Snowbird* (ed. B. Côme and N.A. Chapman). Com. Europ. Commun. Rep., **EUR 11725 EN**, 50-56.

VILKS, P. and DREW, D.J. 1986. The effect of colloids on actinide migration. In *Proc. 2nd Int. Conf. Rad. Waste Manag.* Can. Nucl. Soc. Proc., 667-673.

VILKS, P., CRAMER, J.J., SHEWCHUK, T.A. and LAROCQUE, J.P.A. 1988. Colloid and particulate matter studies in the Cigar Lake natural-analog program. Radiochim. Acta, **44/45**, 305-310.

TABLE 3.30
REFERENCE WATER COMPOSITIONS AT CIGAR LAKE

Sample #		67C	67D	71A	71F	75B	75E	79E	79L	81H	81J	91D	91R	139C	139G
Field-ID #		67-3	67-1	71-1	71A1	75-1	75-2	79A	79A1	81E	81-2	91A	91-1	139-1	139-2
Date		89/6/8	89/11/4	89/6/13	90/5/13	89/6/18	89/11/16	87/9/6	90/5/23	87/9/10	89/6/14	87/3/8-9	89/11/4	89/6/16	89/11/12
DH/SP/AT**		SP	SP	SP	SP	SP	SP	SP	SP	SP	SP	SP	SP	SP	SP
Cations :															
Na	mg/L	11.80	12.10	14.00	15.50	3.21	2.36	19.80	19.20	3.70	5.58	18.00	6.61	2.87	2.69
K		2.19	2.26	2.07	2.21	1.18	1.25	7.60	5.64	1.20	1.25	2.10	1.24	1.16	1.12
Ca		6.70	6.80	6.50	11.30	4.70	3.20	14.80	11.80	5.60	3.00	2.08	2.43	4.30	3.70
Mg		1.53	1.41	1.62	1.14	1.08	0.87	5.30	4.90	1.41	1.37	0.81	0.92	2.28	2.09
Fe++		2.50		2.20	*0.35	1.95	*2.10		2.70		1.40			0.05	
Fe(T)		3.40	1.56	4.10	0.01	3.50	4.50	5.50	4.10	0.81	1.86	<0.01	0.56	0.04	0.01
Mn		0.38	0.31	0.39	0.03	0.16	0.14	0.46	0.26	0.18	0.26	0.30	0.28	0.26	0.22
Si		5.30	5.50	4.90	4.40	4.90	5.10	6.10	5.80	8.40	7.80	6.32	8.00	13.80	14.40
Al		<0.15	<0.10	<0.15	<0.10	<0.15	<0.10	<0.10	<0.10	<0.10	<0.15	<0.085	<0.10	<0.15	<0.10
Anions :															
F	mg/L	0.13	0.19	0.12	0.25	<0.025	0.14	0.39	0.34	0.54	0.05	0.15	0.12	0.06	0.09
Cl		17.03	15.03	17.35	16.94	0.42	0.38	24.90	20.75	2.48	4.86	8.26	5.92	0.23	0.24
Br		0.28	0.23	0.28	0.17	<0.01	<0.01	<0.01	0.18	<0.01	<0.01	<0.01	<0.01	<0.01	<0.01
S*		0.009	<0.002	<0.002	<0.002	0.040	0.088				0.058	<0.07	<0.002	0.021	<0.002
SO4		3.74	3.84	1.02	1.28	4.34	3.00	0.65	0.17	2.65	3.10	4.09	4.88	3.63	3.34
NO3		<0.065	1.11	<0.065	<0.065	<0.065	<0.065	0.48	<0.065	<0.065	<0.065	<0.065	1.44	<0.065	<0.065
HPO4		<0.05	<0.05	<0.05	<0.05	<0.05	<0.05	<0.05	<0.05	<0.05	<0.05	0.50	<0.05	<0.05	<0.05
H2CO3		19.45	10.23	7.57	2.49	27.60	44.85	35.75	67.70	12.77	47.60	44.02	35.77	24.51	33.48
HCO3		39.04	37.19	45.08	59.48	32.95	20.18	95.11	85.39	23.79	28.70	45.15	15.91	48.79	34.18
CO3		0.01	0.01	0.03	0.14	0.00	0.00	0.03	0.01	0.00	0.00	0.00	0.00	0.01	0.00
Trace elem. :															
Ba	ug/L	8.4	16.0	46.0	22.9	57.0	60.0	170.0	116.0	<10	8.7	18.0	13.5	27.3	9.6
Li		<40	<50	<40	7.0	<40	<50	<50	47.0	<50	<40	<60	<0.05	<40	<50
B		46.0	35.0	63.0	55.0	<25	<15	192.0	191.0	<10	26.6	35.2	<15	<25	<15
Cs					<50				70.0						
Sr		41.0	44.0	46.0	58.0	39.0	38.0		242.0		18.6		28.5	17.3	15.1
Cu		<2	2.0	<2	<2	<2	<2	64.7	10.6	<2	5.0	6.8	<2	2.0	<2
Zn		2.4	11.0	9.0	2.1	37.0	15.6	3.1	24.8	1.6	10.8	<1	5.9	27.5	6.6
Mo		<12	<10	15.1	33.0	<12	<10	26.2	20.3	<6.5	<12	36.7	<10	<12	<10
Cr		<12	<9	<12	<9	<12	<9	<4.5	<9	<4.5	<12	<4.5	<9	<12	<9
Co					<20			<10	<20	<10		<10			
Ni					<50			<15	<50	<15		<15			
Pb		<1	2.2	<1	<1	<1	<1	<1	<1	<1	<1	<1	<1	<1	<1
V								<10		<10		<10			
Cd		<1	1.3	<1	<1	<1	<1	<1	<1	<1	<1	<1	<1	<1	<1
As								<30		<30		16.0			
Se								<30		<30		<20			
I		140.0	4.0	4.0	2.8	<1	<1	4.0	2.8	<1	1.5	<1	<1	<1	<1
Hg								<0.05		<0.05		0.07			
U	ug/L	7.00	29.81	1.40	1.33	0.31	0.49	5.81	7.71	1.58	0.30	54.74	14.79	0.28	0.49
Th		0.04	0.21	0.15	0.27	0.11	0.34	0.10	0.20	<0.02	0.15	0.11	<0.02	<0.02	0.03
Ra-226	Bq/L	0.49	0.65	0.61	0.25	0.09	0.48	1.38	2.83	0.33	0.21	0.34	0.44	0.06	0.16
Rn-222		1952.0		1442.3	267.7	777.4			2739.3		2109.7	545.3		5.70	

10-Feb-94 * Analysis on "original" groundwater sample
CLT-45

TABLE 3.30
REFERENCE WATER COMPOSITIONS AT CIGAR LAKE (Continued)

Sample #	67C	67D	71A	71F	75B	75E	79E	79L	81H	81J	91D	91R	139C	139G
Field-ID #	67-3	67-1	71-1	71A1	75-1	75-2	79A	79A1	81E	81-2	91A	91-1	139-1	139-2
Date	89/6/8	89/11/4	89/6/13	90/05/13	89/6/18	89/11/16	87/9/6	90/05/23	87/9/10	89/6/14	87/3/8-9	89/11/4	89/6/16	89/11/12
DH/SP/AT**	SP	SP	SP	SP	SP	SP	SP	SP	SP	SP	SP	SP	SP	SP
Field meas. :														
pH	6.73	6.99	7.22	7.82	6.52	6.10	6.85	6.53	6.71	6.22	6.45	6.09	6.74	6.45
Eh mV	29	-9	-304	-150	65	77	78	80	174	16	255	209	150	235
T oC	8.7	5.3	10.2	8.6	6.6	7.0	16.1	15.0	10.4	9.7	10.6	8.3	8.5	4.9
P bar	33.0	33.0	22.3	22.3	13.2	13.2	41.1	41.1	42.2	42.2	38.8	38.8	42.9	42.9
Alkal. meq/L	0.64	0.61	0.74	0.98	0.54	0.33	1.56	1.40	0.39	0.47	0.74	0.26	0.80	0.56
Cond. uS/cm	131	119	149	195	82	64	271	200	75	86	114	80	81	72
Turb. NTU	4	11	4	25	52	16		25		118		16	70	42
Diss. O2 ug/L	0	29	0	65	10	45	490	300	0	1	990	560	125	83
Diss. H2 ug/L	50	68	45	70		62		50		65		69	60	65
Calc. data :														
TDS mg/L	110.98	97.78	105.07	115.37	84.10	86.03	217.04	226.35	63.53	105.44	131.80	84.10	101.97	95.57
Ionic strength	0.0015	0.0014	0.0016	0.0018	0.0009	0.0007	0.0031	0.0026	0.0008	0.0008	0.0012	0.0007	0.0010	0.0008
Log pCO2 bar	-2.23	-2.51	-2.64	-3.13	-2.08	-1.87	-1.97	-1.69	-2.42	-1.85	-1.88	-1.97	-2.13	-2.00
Log pO2 bar	-54.24	-55.77	-74.78	-61.98	-52.65	-53.55	-50.44	-51.59	-44.52	-57.16	-40.08	-44.66	-46.02	-41.45
Cation meq/L	1.16	1.11	1.28	1.39	0.62	0.53	2.44	2.13	0.62	0.61	1.02	0.55	0.57	0.51
Anion	1.21	1.14	1.26	1.49	0.64	0.41	2.30	2.01	0.54	0.67	1.08	0.56	0.89	0.64
Charge bal. %	-3.69	-3.37	1.70	-7.54	-2.88	22.71	5.78	5.60	12.72	-9.97	-5.76	-2.26	-55.98	-25.62
Isotopes :														
H-3 TU	38	44	11	30	69	38	48	73	87	78	96	98	15	13
SD o/oo	-150.57	-151.45	-147.08	-147.57	-153.49	-154.31	-149.80	-151.78	-152.82	-155.20	-147.36	-151.36	-155.89	-153.30
SO-18	-19.42	-19.43	-18.99	-19.13	-19.96	-20.61	-19.27	-19.61	-19.44	-20.10	-18.16	-19.80	-19.94	-19.75
U234/U238	2.20	1.40	4.00	2.30	5.00	5.00	1.50	1.80	1.60	5.00	1.49	1.28	5.00	2.80
+-	0.02	0.02	1.00	0.80	4.00	3.00	0.20	0.30	0.22	3.00	0.02	0.07	2.00	0.80
(In)organ. C :														
TIC mg/L	11.45	9.30	10.34	12.21	11.83	12.65	25.64	29.90	7.15	14.86	17.40	10.05	14.34	13.20
TOC	0.18	0.32	1.76	1.00	0.47	0.00	13.20	10.56	5.72	0.32	1.21	0.00	0.17	0.00
Gases :														
H2 cm3/L	0.01		0.03		0.01			<0.026		0.01		0.01	0.01	
He	0.01		0.04		<0.02			0.18		<0.03		0.11	<0.01	
O2	0.02		0.07		<0.004			<0.026		<0.007		0.03	<0.004	
Ar	0.71		0.62		0.58			0.67		0.56		0.79	0.61	
CO2	1.21		1.31		1.54			6.42		0.96		1.37	2.03	
CH4	0.62		1.00		0.42			48.43		0.43		3.40	0.02	
N2	38.32		56.47		36.15			203.06		64.99		64.79	38.90	
Tot.Gas	40.90		59.50		38.70			259.00		67.00		70.50	41.60	
Solids :														
>0.45um mg/L	5.49	3.04	2.91	0.83	11.82	0.50		2.03		17.63	41.90	3.66	16.59	0.42
>0.01<0.45um	0.66	0.53	0.65	1.01	0.89	0.38		1.04		0.76	3.23	0.14	0.84	0.25
Tot.Solids	6.15	3.57	3.56	1.84	12.71	0.88		3.07		18.39	45.13	3.80	17.43	0.67

** Collection mode: DH= down hole, SP= squeeze pump, AT= artesian flow + nd= not detected

TABLE 3.30
REFERENCE WATER COMPOSITIONS AT CIGAR LAKE (Continued)

Sample #		197I	197O	198G	198J	199B	199D	211C	211D	219D	219F	220A	220B	WL1	WL3	3.7A	3.8A
Field-ID #		197C	197-1	198B	198D	199A	199C	211-3	211-1	219-1	219A1	220-1	220-2	200	Wbry L	P3.7	P3.8
Date		87/9/14	89/11/7	87/9/12	87/9/13	87/3/28	87/4/1	89/6/12	89/11/9	89/11/8	90/5/15	89/6/20	89/6/21	87/9/17	90/05/20	90/10/26	90/10/27
DH/SP/AT**		SP	SP	SP	SP	SP	SP	SP	SP	SP	SP	SP	SP			PP	PP
Cations :																	
Na	mg/L	3.40	4.91	2.70	3.40	55.00	59.00	34.30	33.30	14.80	16.30	31.20	28.90	1.61	1.16	1.76	6.05
K		1.39	1.26	1.23	1.80	5.60	5.50	4.99	4.29	3.23	3.31	8.81	8.51	0.34	0.43	0.35	1.77
Ca		2.85	2.30	1.86	1.65	6.76	5.40	3.10	3.20	4.50	5.10	11.40	10.90	0.54	1.22	1.00	3.40
Mg		1.07	1.10	0.94	0.86	3.09	2.75	1.73	1.89	2.66	2.92	3.60	3.40	0.22	0.42	0.20	0.49
Fe++								1.60			2.40					0.01	1.30
Fe(T)		0.60	0.25	0.62	0.34	0.49	<0.01	1.87	1.97	3.70	4.10	<0.012	<0.012	<0.06	0.05	0.04	0.58
Mn		0.06	0.03	0.05	0.03	0.70	0.05	0.34	0.53	0.38	0.46	0.11	0.08	<0.01	0.05	0.02	0.184
Si		8.80	9.80	8.70	8.70	4.29	4.30	3.50	3.80	4.50	4.60	4.30	4.40	2.04	1.25	8.00	7.30
Al		<0.10	<0.10	<0.10	<0.10	<0.085	<0.085	<0.15	<0.10	<0.10	<0.10	<0.15	<0.15	<0.10	<0.10	<0.1	<0.1
Anions :																	
F	mg/L	0.05	0.09	0.67	0.06	0.53	0.56	0.65	0.67	0.20	0.21	0.69	0.69	<0.03	<0.025	0.08	0.39
Cl		2.87	6.04	1.23	2.63	86.50	86.10	40.53	38.92	26.50	26.93	37.79	38.83	0.47	0.43	0.51	0.71
Br		0.02	<0.01	<0.01	0.04	1.14	1.03	0.61	0.52	0.36	0.32	0.56	0.56	<0.01	<0.01		
S*			<0.002			<0.07	<0.07	<0.002	<0.002	<0.002		<0.002	<0.002				0.117
SO4		<0.10	3.65	0.55	1.10	1.02	<0.035	0.26	1.29	0.10	<0.035	25.97	26.35	<0.10	0.35	0.27	0.05
NO3		<0.065	1.35	<0.065	<0.065	<0.065	<0.065	0.73	<0.065	<0.065	<0.065	0.35	0.54	<0.20	<0.065	0.55	0.37
HPO4		<0.05	<0.05	<0.05	<0.05	3.50	0.80	<0.05	<0.05	<0.05	<0.05	<0.05	<0.05	<0.07	<0.05	0.01	
H2CO3		151.04	70.43	47.40	17.42	2.43	3.51	24.96	17.28	42.29	42.81	3.27	3.51				
HCO3		23.33	22.03	12.29	17.10	46.77	67.43	50.01	51.83	35.40	34.80	23.14	31.05	7.00	7.93	9.76	32.33
CO3		0.00	0.00	0.00	0.00	0.09	0.14	0.01	0.02	0.00	0.00	0.02	0.03				
Trace elem. :																	
Ba	ug/L	78.0	19.3	184.0	121.0	36.0	29.0	<8	11.7	19.5	11.4	35.0	33.0	<10	<5	<5	<5
Li		<50	<0.05	<50	<50	60.0	60.0	<40	<0.05	<0.05	<2	<40	<40		<2	4.0	6.0
B		<10	<15	<10	<10	790.0	840.0	520.0	540.0	113.0	111.0	740.0	750.0	<10	<10	<15	<15
Cs											<50						
Sr			16.3					62.0	62.0	81.0	94.0	220.0	198.0		11.2	6.7	15.8
Cu		26.5	32.9	<2	<2	9.4	5.0	<2	<2	<2	<2	<2	<2	<2	<2	<17	<17
Zn		43.2	40.9	5.7	4.7	42.5	19.0	17.3	18.7	19.2	8.4	5.6	2.2	29.07	5.8	8.9	13.6
Mo		<6.5	11.4	<6.5	13.8	12.8	6.5	<12	14.7	<10	<10	187.0	150.0	14.10	<10	<10	<10
Cr		<4.5	<9	<4.5	<4.5	4.5	8.3	<12	<9	<9	<9	<12	<12	<4.5	<9	<6	<6
Co		<10		<10	<10	10.0	10.0				<20			<10	<20	<20	<20
Ni		<15		<15	<15	15.0	15.0				<50			<15	<50	<50	<50
Pb		<1	<1	<1	<1	<1	25.0	<1	<1	<1	<1	<1	<1	<1	<1	<100	<100
V		<10		<10	<10	10.0	10.0							<10			
Cd		<1	<1	<1	<1	<1	0.3	<1	<1	<1	<1	<1	<1	<1	<1		
As		<30		<30	<30	59.0	50.0							<30			
Se		<30		<30	<30	20.0	20.0							<30			
I		<1	<1	<1	<1	5.6	5.6	6.3	1.6	4.7	5.2	7.6	8.7	<1	<1		
Hg		<0.05		<0.05	<0.05	<0.05	<0.05							<0.05			
U	ug/L	1.05	1.12	0.36	0.32	5.44	12.39	3.20	2.31	2.66	0.44	25.50	7.80	0.32	1.36	0.17	0.64
Th		<0.02	<0.02	<0.02	<0.02	0.09	0.17	0.35		0.34	0.04	0.23	<0.02				
Ra-226	Bq/L	0.53	0.35	0.59	0.39	0.20	0.39	0.47	0.42	0.32	0.41	4.30	4.28	0.16	0.14		
Rn-222			496.0	1631.5		21.7	n.d	1096.6			197.6	5992915.0					

10-Feb-94 * Analysis on "original" groundwater sample
CLT-45

TABLE 3.30
REFERENCE WATER COMPOSITIONS AT CIGAR LAKE (Concluded)

Sample #	197I	197O	198G	198J	199B	199D	211C	211D	219D	219F	220A	220B	WL1	WL3	3.7A	3.8A
Field-ID #	197C	197-1	198B	198D	199A	199C	211-3	211-1	219-1	219A1	220-1	220-2	200	Wbry L	P3.7	P3.8
Date	87/9/14	89/11/7	87/9/12	87/9/13	87/3/28	87/4/1	89/6/12	89/11/9	89/11/8	90/5/15	89/6/20	89/6/21	87/9	90/5/20	90/10/26	90/10/27
DH/SP/AT**	SP	SP	SP	SP	SP	SP	SP	SP	SP	SP	SP	SP			PP	PP
Field meas. :																grab
pH	5.63	5.93	5.85	6.43	7.71	7.71	6.73	6.91	6.35	6.34	7.27	7.37			7.50	7.30
Eh mV	312	238	130	188	98	109	44	70	124	108	-243	-242			298	197
T oC	10.5	9.9	12.3	8.9	11.2	14.5	8.6	12.3	9.4	5.5	11.0	7.4			8.3	11.4
P bar	40.5	40.5	41.2	41.2	43.5	43.5	39.8	39.8	41.0	41.0	41.0	41.0				
Alkal. meq/L	0.38	0.36	0.20	0.28	0.77	1.11	0.82	0.85	0.58	0.57	0.38	0.51	0.11	0.13	0.16	0.53
Cond. uS/cm	60	68	44	52	419	425	207		126	215	270	265			64	35
Turb. NTU		7					4	10	1	1	500	408				280
Diss. O2 ug/L	1	610	2	5	0	<0.01	<1	14	179	14	750	3				
Diss. H2 ug/L		63					50	62	61	76	1900	1400				
Calc. data :																
TDS mg/L	195.56	123.14	78.42	55.26	217.95	236.60	167.59	159.51	138.64	141.87	151.24	157.78	12.22	13.28	22.55	53.63
Ionic strength	0.0006	0.0007	0.0004	0.0005	0.0036	0.0037	0.0022	0.0022	0.0016	0.0017	0.0029	0.0029	0.0001	0.0002	0.0002	0.0007
Log pCO2 bar	-1.34	-1.68	-1.85	-2.28	-3.14	-2.98	-2.13	-2.29	-1.90	-1.89	-3.01	-2.98			-3.58	-2.86
Log pO2 bar	-39.52	-43.31	-50.95	-44.73	-45.69	-44.91	-53.23	-50.75	-49.36	-50.46	-70.46	-69.99			-32.98	-40.61
Cation meq/L	0.44	0.46	0.34	0.36	3.17	3.20	2.00	1.96	1.32	1.45	2.45	2.30	0.12	0.16	0.15	0.55
Anion	0.47	0.63	0.28	0.38	3.34	3.59	2.02	2.01	1.34	1.34	2.03	2.20	0.13	0.15	0.19	0.58
Charge bal. %	-6.61	-36.74	17.50	-5.75	-5.38	-12.06	-1.25	-2.63	-2.13	7.41	17.03	4.24	-3.24	6.69	-25.40	-5.86
Isotopes :																
H-3 TU	74	75	105	102	25	30	8	10	22	11	201	281	76	54	30	57
SD o/oo	-150.37	-151.43	-154.43	-154.10	-152.59	-153.86	-150.80	-150.46	-152.28	-151.43	-149.72	-153.95	-128.55	-147.55	-153.69	-154.87
SO-18	-19.39	-19.81	-19.92	-20.09	-19.28	-19.55	-19.49	-19.41	-19.09	-19.41	-19.86	-19.66	15.39	-18.54	-20.26	-20.41
U234/U238	1.70	1.80	2.00	1.00	2.04	1.89	4.70	2.90	1.60		2.70	2.90				
+-	1.10	0.50	2.00	2.00	0.13	0.08	0.60	0.50	0.30		0.10	0.30				
(In)organ. C :																
TIC mg/L	33.82	17.97	11.59	6.74	9.69	13.97	14.67	13.54	15.15	15.13	5.19	6.79	3.35	2.17	0.75	3.80
TOC	12.90	0.00	6.96	2.10	5.19	4.73	0.00	0.00	0.72	1.53	3.97	0.86	1.18	3.42	1.52	1.46
Gases :																
H2 cm3/L		<0.03					0.04		0.03	0.01	0.04					
He		1.24					0.74		0.31	0.11	0.19					
O2		<0.03					0.01		0.09	1.77	0.02					
Ar		0.78					0.81		1.48	0.68	0.75					
CO2		1.67					1.44		3.86	1.80	1.07					
CH4		1.96					3.06		1.57	0.60	1.06					
N2		282.24					98.91		77.69	54.93	46.57					
Tot.Gas		288.00					105.00		85.00	59.90	51.40					
Solids :																
>0.45um mg/L		0.31			127.34	95.81	2.23	5.25	0.47	0.99	154.47	59.54				
>0.01<0.45um		0.50			4.05	1.81	0.53	0.67	1.04	0.80	0.28	0.68				
Tot.Solids		0.81			131.39	97.62	2.76	5.92	1.51	1.79	154.75	60.22				

** Collection mode: DH= down hole, SP= squeeze pump, AT= artesian flow + nd= not detected

3.5.3 Hydrologic and isotopic constraints
(J. Cramer and W. Nesbitt)

3.5.3.1 Introduction

The Cigar Lake uranium deposit (at ~430 m depth in the Athabasca Sandstone Formation) occurs inside a clay-rich matrix, where it has remained well preserved for 1.3 Ga despite being surrounded by a major aquifer. Migration of groundwater and its evolution through water-rock interaction play an important role in maintaining the stability of the UO_2-$USiO_4$ mineralization. Three distinct flow regimes have been identified in the local stratigraphy on the basis of geologic, hydrologic, major element and isotopic data for the present-day system. The uppermost, local flow regime is unconfined and includes waters of the glacio-fluvial sands and basal till of the Quaternary deposits. The intermediate flow regime, in the Upper Sandstone unit, is confined above by the basal till of the Quaternary deposits and below by the comparatively impermeable base of the Upper Sandstone. The semi-regional flow regime, in the permeable Lower Sandstone unit, is confined above by the base of the Upper Sandstone and below by the regolith of the Aphebian basement and the clay-rich matrix surrounding the mineralization. The three regimes provide a useful framework within which to discuss the geochemical evolution of these waters.

Although waters from the three regimes, basement and mineralization have similar low-temperature meteoric δD and $\delta^{18}O$ values, the waters can be distinguished on the basis of their ^3H contents. Recharge from the local to the intermediate regime occurs locally, whereas recharge to the semi-regional regime occurs mainly outside the immediate Cigar Lake area. The dilute groundwaters in the two sandstone regimes change composition (increased TDS and Cl^- contents) as they pass through the hydrothermal alteration halo of the deposit. Water-rock interaction, rather than mixing with basement-derived waters, are responsible for these changes. Compositions of waters and clay minerals are also used to demonstrate that the flux of water through the clay-hosted mineralization is apparently very low; estimated water-residence times are $>10^4$-10^5 a. Thus, the chemical stability of the uranium mineralogy appears to be controlled by diffusive, rather than advective, processes, allowing reducing conditions to be buffered by interaction of water with the host rock mineralogy.

3.5.3.2 Hydrologic considerations

Most of the information for establishing the hydrologic regime in the vicinity of the Cigar Lake deposit (Figure 3.63) has been collected as part of the environmental impact studies coordinated by the mining company (CLMC 1987). The hydraulic data were obtained both during borehole installation and from measurements and tests in piezometers installed in and around the deposit (Figure 3.64). Two- and three-dimensional numeric modelling of the available hydrogeological data has been carried and reported by Winberg and Stevenson (Section 3.4). Details of the hydrologic regime on the scale of the deposit (Figure 3.65) are discussed here using data from hole 213 (the pilot hole for the shaft), as illustrated in Figure 3.66.

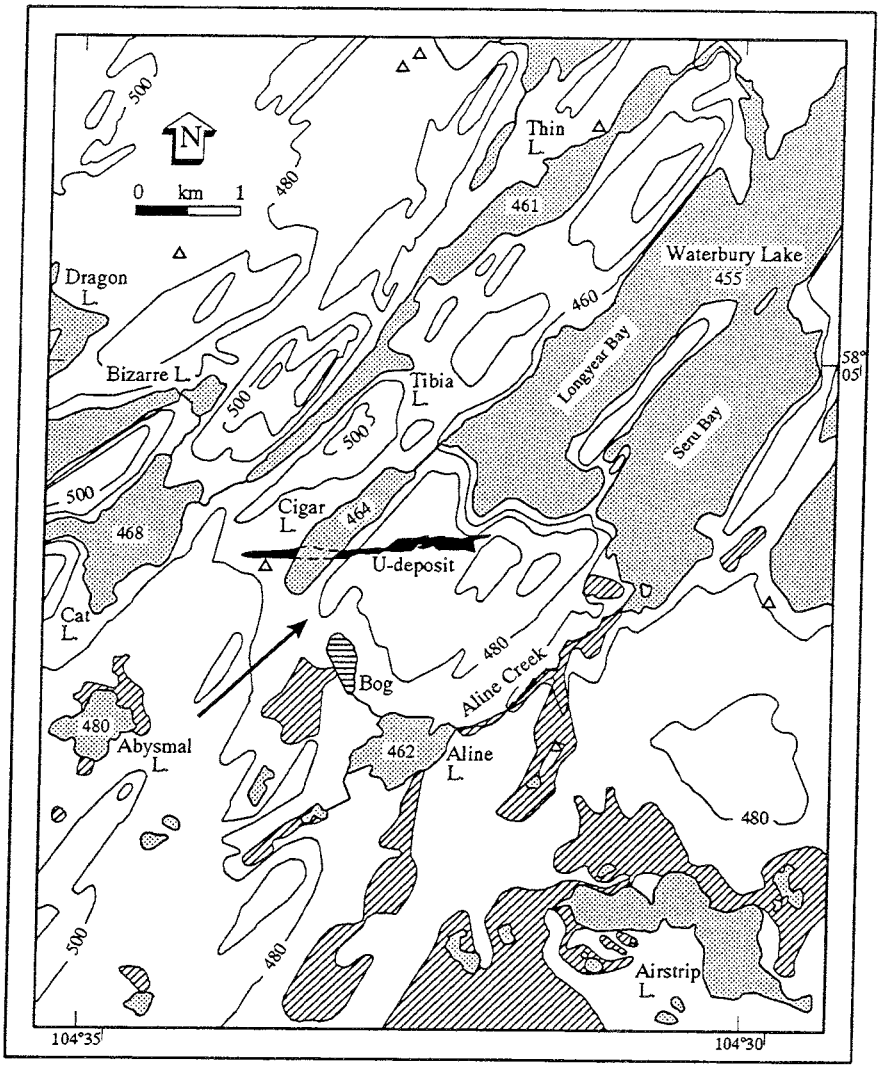

FIGURE 3.63 Plan view of the Cigar Lake area, showing the projected outline of the uranium deposit, the direction of regional groundwater flow (arrow) and the numerous bodies of surface water. Also marked (diagonal lines) are areas where permafrost has been observed in the Quaternary deposits, and where sandstone outcrops occur (Δ).

3.5.3.2.1 General

Regional groundwater flow is from SW to NE, with waters flowing over and possibly through and beneath the mineralization (Figure 3.65). The overburden consists of permeable unconsolidated glacio-fluvial sands (hydraulic conductivity (K) 10^{-4} to 10^{-6} m/s) overlying the basal till, an aquatard with $K < 10^{-8}$ m/s (CLMC, 1987). Between the till and Upper Sandstone (US) is a thin, highly permeable zone of glacio-fluvial conglomerate (referred to as Pleistocene Conglomerate) and fractured Upper Sandstone (locally rubble). The hydraulic conductivity of this zone is approximately 10^{-5} m/s (Figure 3.66). The Upper

Sandstone is subdivided into an upper Limonitic Upper Sandstone unit (LUS) and a lower Unoxidized Upper Sandstone unit (UUS). These units, LUS and UUS, correspond to units 'D' and 'C' respectively of the Manitou Falls Formation (Ramaekers, 1981). The LUS is typically more permeable than the unoxidized portion of the sandstone (UUS), as indicated on Figure 3.66 (see Permeability Index). The UUS is less permeable than either the LUS or the Pleistocene Conglomerate-rubble zone underlying the till as shown by Figure 3.66.

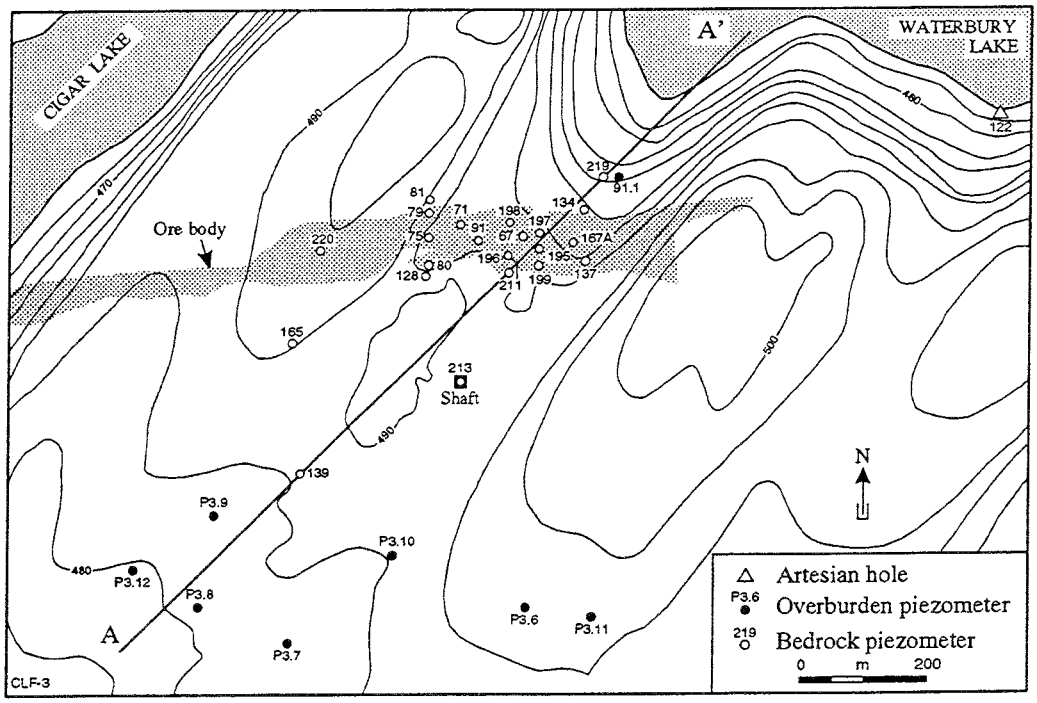

FIGURE 3.64 Map of the Cigar Lake deposit showing the projected outline of the uranium mineralization at the unconformity level and the location of piezometer-equipped boreholes, the shaft and the vertical section A-A' shown in Figure 3.65.

Differences in permeability and hydraulic conductivity are also demonstrated by procedures followed during construction of the shaft. The shaft was lined and sealed from surface to a depth of 40 m below the overburden-US contact to seal off the permeable overburden, Pleistocene conglomerate and the uppermost part of the LUS. The lower 20 m of the LUS and the entire UUS did not require grouting. From this we conclude that the lower part of the LUS and the UUS have comparatively low hydraulic conductivities. The Upper Sandstone extends from approximately 40 m to 210 m depth, and the boundary between LUS and UUS is at approximately 100 m; hence the LUS is approximately 60-70 m thick. The Lower Sandstone (LS) extends from the base of the US (at 210 m) to approximately 450 m depth. It is more permeable ($K \sim 5 \times 10^{-6}$ m/s) than the overlying UUS, as shown by hydraulic conductivities and Permeability Index (Figure 3.66). A coarse grained, highly permeable Basal Conglomerate ($K \sim 1 \times 10^{-5}$ m/s) separates the LS from the much less permeable Aphebian basement. The top of the basement consists of a regolith, composed of

clays and quartz primarily, and is an effective lithologic aquatard. This conclusion is based on the sonic logs (Figure 3.66) and observations made while sinking the shaft and excavating the horizontal drifts: there was no need to grout the regolith, since it was sufficiently impermeable to prevent all flow except for minor seeps (flow rates <20 L/h). The unaltered basement is also highly impermeable, as observed during construction of the shaft bottom and the 480-m-level drift.

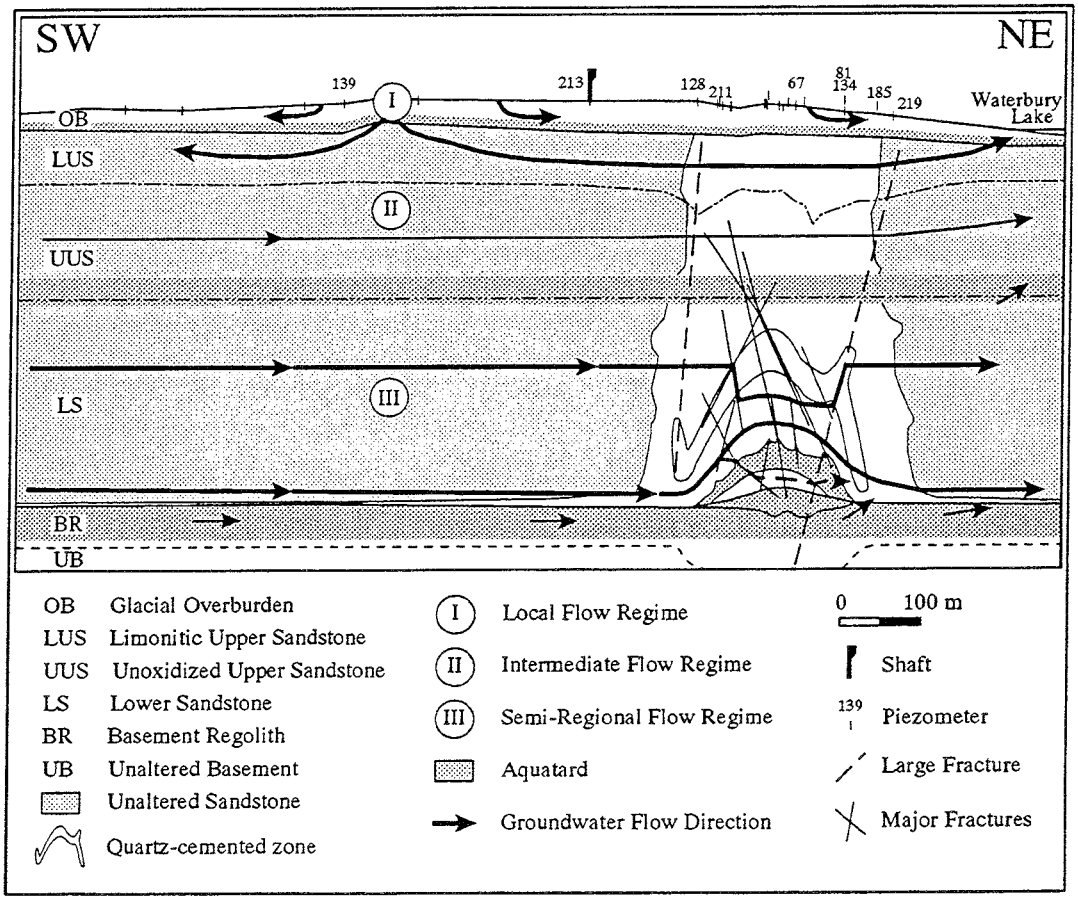

FIGURE 3.65 Cross section A-A' (see Figure 3.64) parallel to the direction of regional groundwater flow. Flow lines are illustrated on the diagram, and although hypothetical, they are constrained by the available hydrologic and geologic data.

3.5.3.2.2 Flow regimes

Theoretical analysis of groundwater flow demonstrates that numerous flow regimes are likely to exist within sedimentary basins where they are accentuated by variations in permeability and hydraulic conductivity of the various lithologic units (Freeze and Cherry, 1979). The hydrologic regime at Cigar Lake can be separated into at least three sub-

regimes. A "local" flow regime exists in the overburden at Cigar Lake, an "intermediate" regime in the Upper Sandstone, and a "semi-regional" regime in the Lower Sandstone.

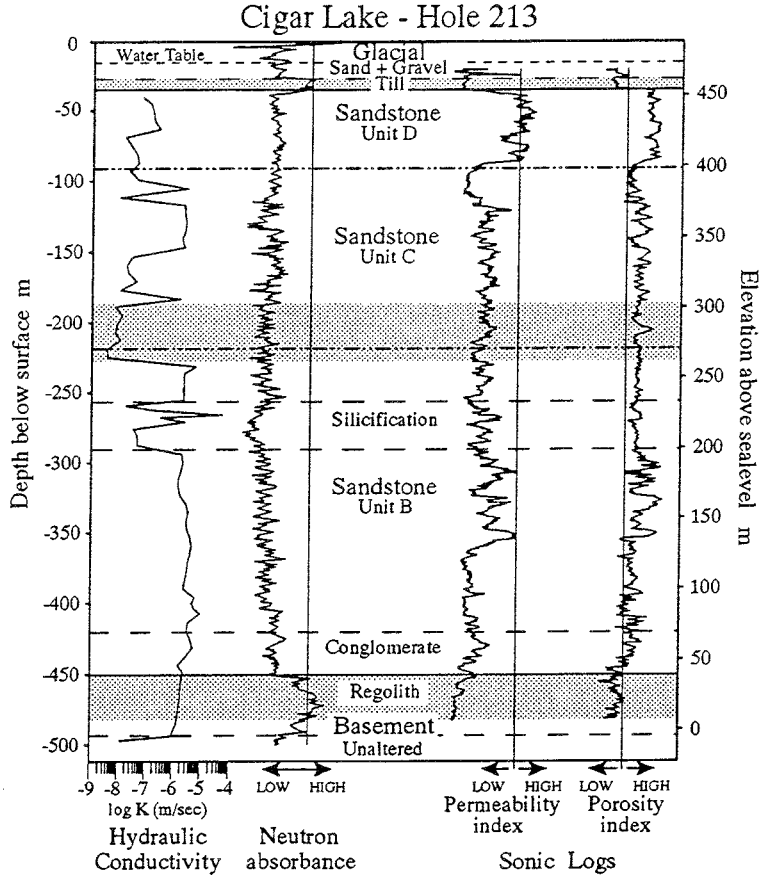

FIGURE 3.66 Vertical profile at shaft Hole 213 with various hydrologic and logging data included.

The three regimes are separated on the basis of lithological properties, topography, groundwater compositions, observations during drilling, and hydraulic conductivities (Figures 3.65 and 3.66). The uppermost, local flow regime is unconfined and includes waters of the glacio-fluvial sands and till. The basal till is an effective aquatard and its base is taken as the base of the local flow regime. It is a perched regime, separated from other flow regimes by the till, as demonstrated by the different heads measured in the overburden and in the flow regime immediately below the till. The head in the overburden is consistently much greater than in the flow regime immediately below the till. Apparently, there is little communication between the two regimes in the vicinity of the Cigar Lake deposit, and whatever communication there is will result in transport from the local flow regime to the flow regime below the till. The intermediate flow regime is confined above by the base of the till, and below by the base of the comparatively impermeable UUS (Figure 3.66). It is composed of an uppermost very permeable zone (Pleistocene Conglomerate and dismembered sandstone), the LUS and the UUS. Both the conglomerate and LUS display

high hydraulic conductivities compared with the overlying till and underlying UUS, as observed during drilling of the >200 boreholes on this deposit. There is a zone of high hydraulic conductivity within the UUC (note *K* in Figure 3.66) and there may be grounds to subdivide the intermediate flow regime into two sub-regimes. For simplicity they are here treated as one regime. The semi-regional flow regime includes the permeable Lower Sandstone, the highly permeable Basal Conglomerate and the effectively impermeable regolith, clay zone and Aphebian basement rocks. Thus, the base of each flow regime is an aquatard (till, UUS and regolith+clay zone). The three regimes provide a useful framework within which to discuss the geochemical evolution of these waters.

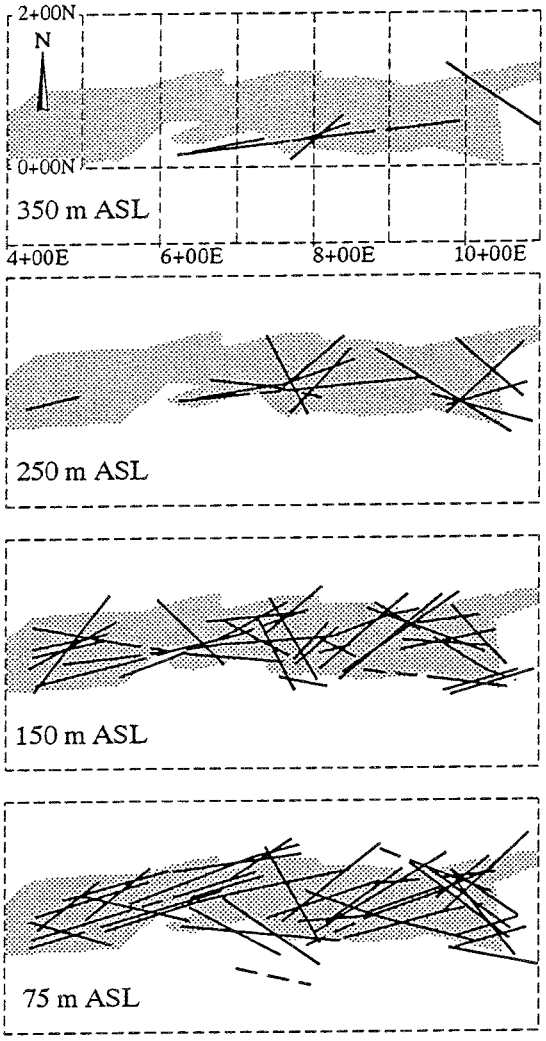

FIGURE 3.67 Location and density of fractures at four different elevations above the mineralization (see Figure 3.66 for reference elevation). Outline of mineralization is shown for reference.

3.5.3.2.3 Fractures

As indicated by stable- and radioisotope data and major-element compositions, there is some communication among the three flow regimes. Communication is most likely facilitated by localized fractures and fracture systems (Figures 3.65 and 3.67), which extend through the till, and areas without an overburden cover, allowing recharge to deeper flow regimes. Again the differential heads between local and intermediate flow regimes suggest that these features are localized, and therefore the hydrologic regimes may be more or less isolated in different regions.

The diagrams in Figure 3.67 illustrate the localized nature of the fracturing immediately above the ore and clay zones. This fracturing, in the highly altered sandstone and quartz-cemented zone, resulted from local volume adjustments caused by the hydrothermal alteration and associated mass transport. Because of the high density of fractures in the quartz-cemented zone in the altered sandstone, this zone is considered "transparent" to the movement of groundwater rather than causing significant deflection, as illustrated schematically in Figure 3.65. However, there is also evidence for pockets of "old", non-tritiated water (<5 TU); such pockets were encountered during shaft sinking and drilling in the LS and AS around the southern part of the quartz-cemented zone. These pockets may represent relatively stagnant water between zones where water flow is deflected against or behind less-fractured rock.

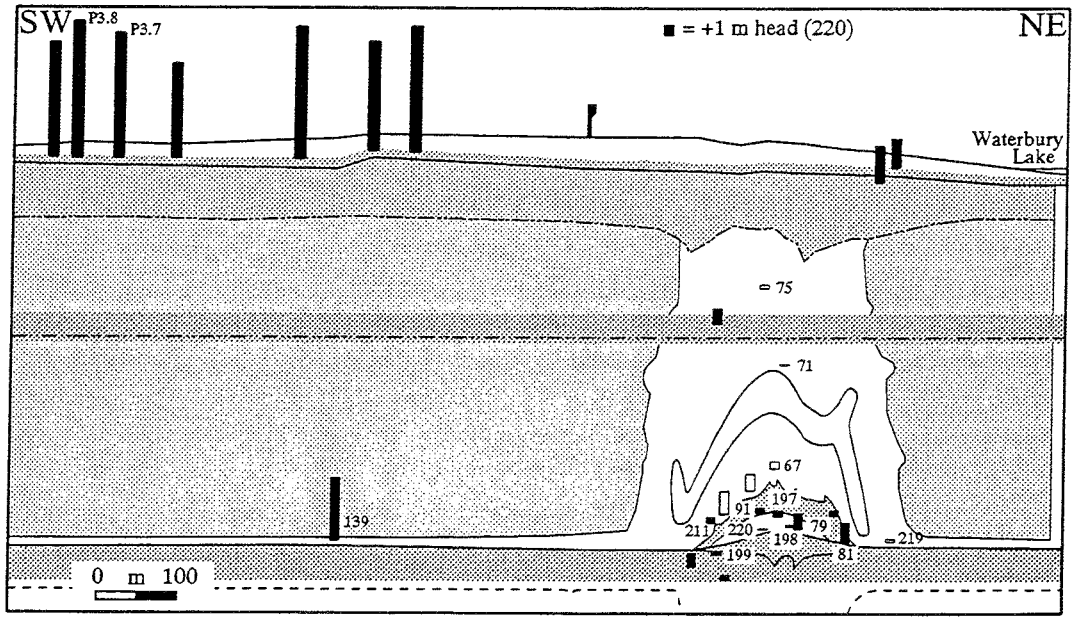

FIGURE 3.68 Same section as in Figure 3.65, showing the difference in hydraulic head (black bars) for each piezometer relative to the head in piezometer 220 (in mineralization). The base of each bar is located at the correct elevation and location at which the head is generated. Piezometer numbers refer to compositions listed in Table 3.31.

3.5.3.2.4 Hydraulic heads

Heads in the local flow regime above the till aquatard are much higher than the head of the underlying intermediate regime (Figure 3.68). The difference in heads across the till indicates that advection (where it occurs) is from the local to the intermediate flow regime: the local flow regime recharges the deeper intermediate regime. Where advection does not occur, diffusion is the only means for transporting solvent and solute from one regime to the other. Since the water compositions are similar in both regimes, the chemical potentials (concentration gradient) of the major solutes is minimal across the till, as is transport by diffusion. Although advection may not occur within the bulk of the till, the till is saturated. Furthermore, feldspars and mafic minerals are more abundant in the till than in the sandstones or in the overlying unconsolidated sands. Because of the increased proportions of feldspars and mafic minerals, and because "water/rock" ratios are much lower in the till, waters of the till are likely to dissolve greater quantities of feldspars and mafic minerals, increasing the solute content of enclosed waters. Where this occurs, solutes derived from the till will diffuse into the more dilute waters of the local and intermediate flow regimes. Undoubtedly this aquatard, and probably the others, is a physical barrier to bulk transport; it is also a barrier to diffusion of major constituents from one regime to another. Generally, however, transport by diffusion requires detailed analyses of chemical potentials and concentration gradients before substantial conclusions can be made about transport of solutes by diffusion.

Similar arguments are applicable to the base of the intermediate flow regime where the UUS acts as an aquatard. Heads measured across this aquatard are few, but they indicate that where advection occurs, transport is from intermediate to regional regime. The mineralogical composition of UUS is similar to the sandstones above and below it, thus diffusion is unlikely to be significant.

The regolith and the mineralization plus clay envelope represent the base of the semi-regional flow regime. The head in the LS (piezometer station 139) is much higher than heads in the regolith, basement, mineralization or clay envelope. Heads surrounding the mineralization are similar. If advection occurs within the regolith, clay zone or mineralization, the potential for transport is from the semi-regional flow regime to the regolith, mineralization and clay envelope: the semi-regional flow regime recharges the aquatards. The conclusion based on head differential (potentials) is supported by the compositions of waters from the regolith and basement immediately below the regolith. These "basement waters" are very dilute compared with other basement waters of the Canadian Shield collected from similar depth. The basement waters at Cigar Lake contain up to 90 mg/L Cl^-, whereas waters of similar depth elsewhere in the Shield typically contain 50,000-140,000 mg/L (Gascoyne et al. 1987). The exceptionally dilute basement waters in the basement underlying the Cigar Lake region are most simply explained by recharge of the basement waters (where possible) by waters of the overlying semi-regional flow regime. As argued for the till aquatard, decreased "water/rock" ratios in the aquatards result in higher solute content of solutions enclosed in the aquatard, as a result of greater contact time with all phases.

Although heads surrounding the ore and clay zones are similar (Figure 3.68), groundwater migrating through the clay envelope into the mineralization and out on the other side, along the SW-to-NE gradient, also have a longer contact (or residence) time because of the lower hydraulic conductivity of the clay and mineralized zones. The calculated results for the reference case of Winberg and Stevenson (Section 3.4) indicate that residence times of groundwater in the clay and mineralized zones would more than double, ranging between 18,000 and 85,000 a, depending on the location where the water enters through the clay envelope. Such long residence times mean that diffusion is certainly the more likely mechanism for mass transport within the clay and mineralized zones.

3.5.3.3 Geochemical considerations

Samples of precipitation, surface waters and groundwaters have been collected at Cigar Lake over an 8-a period from 1984 to 1992. Details on the methods used for collection and analysis of these water samples have been reported in Section 3.5.2 of this report. In addition to measurements and analyses of critical parameters in the field, the waters have been analyzed for the contents of major and trace elements, selected isotopes, dissolved gases, total inorganic and organic carbon (TIC and TOC) and suspended particles and colloids. A critical review of all the data was carried out as part of the AECL/SKB program, and a set of representative water compositions was selected (Section 3.5.2). Table 3.31 gives selected analytical data for some cations, anions and isotopes of both surface waters and groundwaters from Cigar Lake (see Figures 3.64 and 3.68 for sample locations).

3.5.3.3.1 Stable isotope data

Surface waters include samples from Waterbury Lake, Cigar Lake, Aline Creek and precipitation (snow and rain), and their δD and $\delta^{18}O$ values are plotted in Figure 3.69a. They define a meteoric water line (MWL_{CL}: $\delta D = 6.85\delta^{18}O - 19.08$) for the Cigar Lake locality. The standard error of coefficient has been applied to the slope and intercept to calculate the "error envelope" for the meteoric water line (see also Figure 3.69b). Also plotted on this diagram is the average meteoric water line for Wynyard (Saskatchewan) and The Pas (Manitoba) (MWL_{WTP}: $\delta D = 7.53\delta^{18}O - 1.91$), the two locations nearest Cigar Lake for which long-term precipitation data have been reported by the International Atomic Energy Agency (IAEA 1983, 1986). The waters from the glacial overburden all plot on or near the Cigar Lake meteoric water line (Figure 3.69a), indicating their meteoric origin but with a slightly more fractionated (colder) D and ^{18}O signature compared with the lake waters.

Figure 3.69b shows the δD and $\delta^{18}O$ values for groundwaters from the deep formation piezometers. This diagram shows that the deep groundwaters also plot entirely within the envelope, suggesting that the variations in the isotopic signatures observed for the groundwaters result entirely from variation in meteoric water compositions. The simplest explanation for these isotopic trends is that they reflect (moving) averaged meteoric water compositons of the Cigar Lake area. As discussed below, major-element compositions of the surface and groundwaters support this conclusion.

TABLE 3.31. COMPOSITION OF REPRESENTATIVE WATERS FROM CIGAR LAKE

SAMPLE *		Rain1	Snow2	CL3	WL3	3.7A	3.8A	67C	67D	71A	71F	75B	75E	79E	79L	81H	81J
Na	mg/L	0.38	0.19	1.30	1.16	1.76	6.05	11.80	12.10	14.00	15.50	3.21	2.36	19.80	19.20	3.70	5.58
K		0.50	0.06	0.50	0.43	0.35	1.77	2.19	2.26	2.07	2.21	1.18	1.25	7.60	5.64	1.20	1.25
Ca		0.82	0.26	0.59	1.22	1.00	3.40	6.70	6.80	6.50	11.30	4.70	3.20	14.80	11.80	5.60	3.00
Si		0.07	<0.03	0.86	1.25	8.00	7.30	5.30	5.50	4.90	4.40	4.90	5.10	6.10	5.80	8.40	7.80
F		0.24	0.09	0.67	<0.03	0.08	0.39	0.13	0.19	0.12	0.25	<0.03	0.14	0.39	0.34	0.54	0.05
Cl		0.66	0.38	1.12	0.43	0.51	0.71	17.03	15.03	17.35	16.94	0.42	0.38	24.90	20.75	2.48	4.86
Br		<0.01		<0.01	<0.01			0.28	0.23	0.28	0.17	<0.01	<0.01	<0.01	0.18	<0.01	<0.01
SO_4		0.78	0.18	0.17	0.35	0.27	0.05	3.74	3.84	1.02	1.28	4.34	3.00	0.65	0.17	2.65	3.10
HCO_3		4.88	0.01	3.66	7.93	9.76	32.33	39.04	37.19	45.08	59.48	32.95	20.18	95.11	85.39	23.79	28.70
B	µg/L	<20	<15	<20	<10	<15	<15	46	35	63	55	<25	<15	192	191	<10	26.6
U		0.18	0.08	0.09	1.36	0.17	0.64	7.00	29.81	1.40	1.33	0.31	0.49	5.81	7.71	1.58	0.30
^3H	TU**	22	<6	32	55	31	60	37	44	10	31	67	52	42	74	76	75
δD	‰	-120	-183	-133	-147	-154	-155	-151	-151	-147	-148	-153	-154	-150	-152	-153	-155
$\delta^{18}O$		-16.0	-25.1	-16.5	-18.5	-20.3	-20.4	-19.4	-19.4	-19.0	-19.1	-20.0	-20.6	-19.3	-19.6	-19.6	-20.1
pH		7.24	6.80	6.38	7.16	7.50	7.30	6.73	6.99	7.22	7.82	6.52	6.10	6.85	6.53	6.71	6.22
Alk	meq/L	0.08	0.08	0.06	0.13	0.16	0.53	0.64	0.61	0.74	0.98	0.54	0.33	1.56	1.40	0.39	0.47
Cond	µS/cm		101	16	20	64	35	131	119	149	195	82	64	271	200	75	86
TDS	mg/L	9.0	6.2	9.2	13.3	22.5	53.6	111.0	97.8	105.1	115.4	84.1	86.0	217.0	226.3	63.5	105.4

SAMPLE *		91D	91R	139C	139G	197I	197O	198G	198J	199B	199D	211C	211D	219D	219F	220A	220B
Na	mg/L	18.00	6.61	2.87	2.69	3.40	4.91	2.70	3.40	55.00	59.00	34.30	33.30	14.80	16.30	31.20	28.90
K		2.10	1.24	1.16	1.12	1.39	1.26	1.23	1.80	5.60	5.50	4.99	4.29	3.23	3.31	8.81	8.51
Ca		2.08	2.43	4.30	3.70	2.85	2.30	1.86	1.65	6.76	5.40	3.10	3.20	4.50	5.10	11.40	10.90
Si		6.32	8.00	13.80	14.40	8.80	9.80	8.70	8.70	4.29	4.30	3.50	3.80	4.50	4.60	4.30	4.40
F		0.15	0.12	0.06	0.09	0.05	0.09	0.67	0.06	0.53	0.56	0.65	0.67	0.20	0.21	0.69	0.69
Cl		8.26	5.92	0.23	0.24	2.87	6.04	1.23	2.63	86.50	86.10	40.53	38.92	26.50	26.93	37.79	38.83
Br		<0.01	<0.01	<0.01	<0.01	0.02	<0.01	<0.01	0.04	1.14	1.03	0.61	0.52	0.36	0.32	0.56	0.56
SO_4		4.09	4.88	3.63	3.34	<0.10	3.65	0.55	1.10	1.02	<0.035	0.26	1.29	0.10	<0.035	25.97	26.35
HCO_3		45.15	15.91	48.79	34.18	23.33	22.03	12.29	17.10	46.77	67.43	50.01	51.83	35.40	34.80	23.14	31.05
B	µg/L	35.2	<15	<25	<15	<10	<15	<10	<10	790	840	520	540	113	111	740	750
U		54.74	14.79	0.28	0.49	1.05	1.12	0.36	0.32	5.44	12.39	3.20	2.31	2.66	0.44	25.50	7.80
^3H	TU**	82	97	14	13	65	74	92	89	21	26	7	10	22	11	195	272
δD	‰	-147	-151	-156	-153	-150	-151	-154	-154	-153	-154	-151	-150	-152	-151	-150	-154
$\delta^{18}O$		-18.2	-19.8	-19.9	-19.7	-19.4	-19.8	-19.9	-20.1	-19.3	-19.5	-19.5	-19.4	-19.1	-19.4	-19.9	-19.7
pH		6.45	6.09	6.74	6.45	5.63	5.93	5.85	6.43	7.71	7.71	6.73	6.91	6.35	6.34	7.27	7.37
Alk	meq/L	0.74	0.26	0.80	0.56	0.38	0.36	0.20	0.28	0.77	1.11	0.82	0.85	0.58	0.57	0.38	0.51
Cond	µS/cm	114	80	81	72	60	68	44	52	419	425	207		126	215	270	265
TDS	mg/L	131.8	84.1	102.0	95.6	195.6	123.1	78.4	55.3	217.9	236.6	167.6	159.5	138.6	141.9	151.2	157.8

* **Surface**= Rain, Snow, Cigar Lake, Waterbury Lake; **Overburden**= 3.7 and 3.8; **Bedrock**= piezometer # (Figure 3.64). ** normalized to 1990 Jan 1.

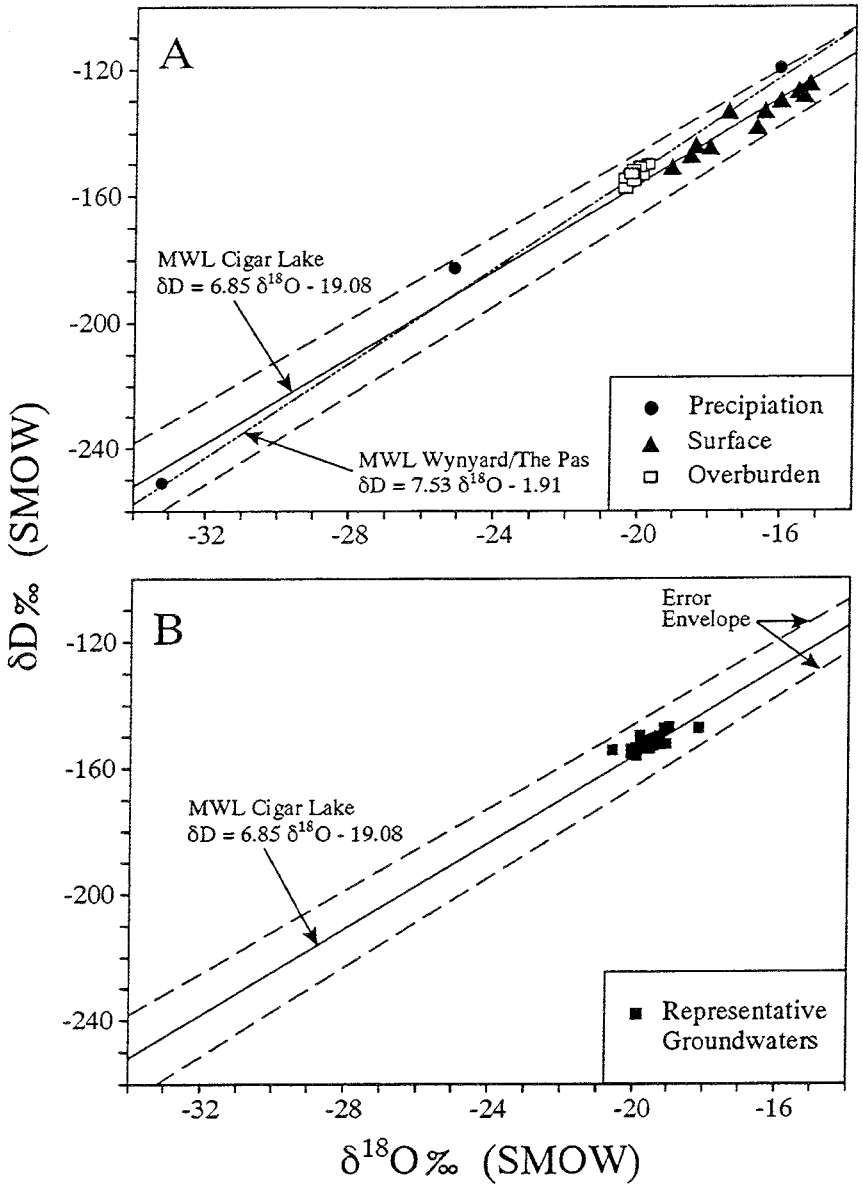

FIGURE 3.69 Diagrams showing δD and $\delta^{18}O$ values for surface and groundwaters from Cigar Lake. **A:** Plot showing values for precipitation and surface waters, and the calculated meteoric water line (MWL) for Cigar Lake. The average MWL for Wynyard and The Pas is shown for reference. **B:** Plot showing values for the overburden and formation waters from Cigar Lake. The error envelope in both plots represents the standard deviation of the calculated MWL_{CL}.

3.5.3.3.2 Tritium data

Tritium data for the representative surface, overburden and deep groundwaters from Cigar Lake are given in Table 3.31. The analyzed ^3H contents of the water samples have all been

normalized to 1990 January 1 to compensate for radioactive decay during the 8-a sample collection period. The tritium values have been plotted in Figure 3.70 according to the sample location within the local stratigraphy and the boundaries of the three flow regimes. These data show several trends with regard to the recharge, evolution and mixing of waters, which are discussed here, together with other geochemical data, for each regime separately. The elevated ^{3}H contents in waters from the ore and clay zones, resulting from the generation of ^{3}H by neutron capture on ^{7}Li in the vicinity of uranium minerals, are also discussed separately in Section 3.8.2 of this report.

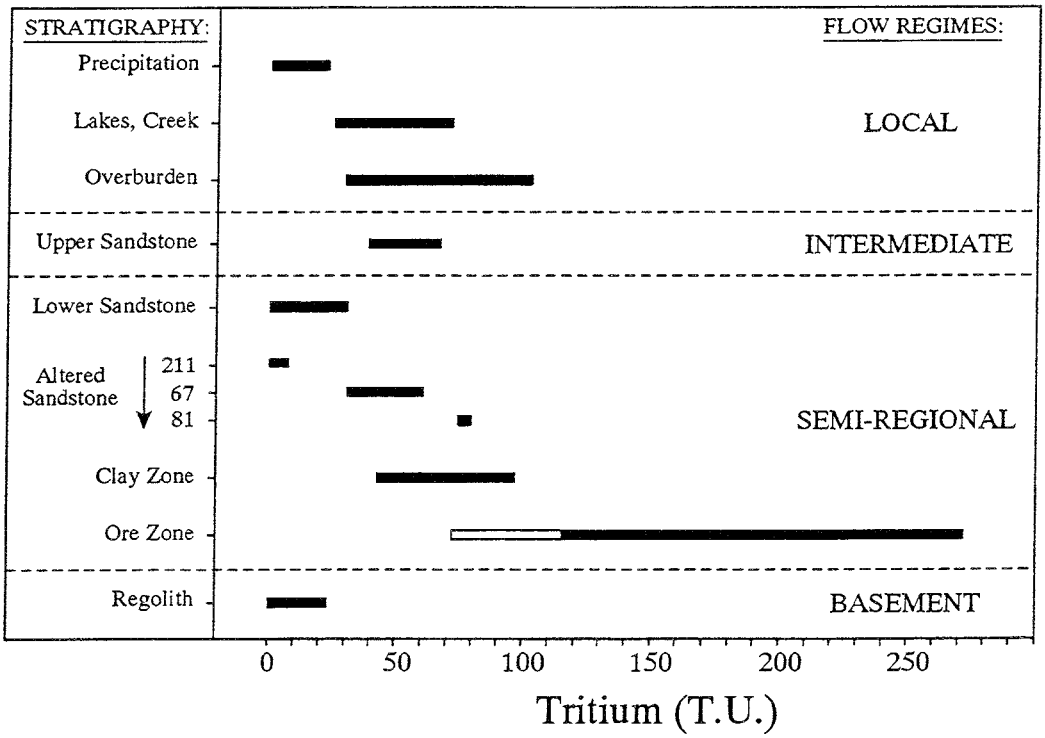

FIGURE 3.70 Tritium values for waters sampled at Cigar Lake. All ^{3}H data have been normalized to 1990 January 1 and plotted according to their location within the different flow regimes. The arrow indicates the direction of water flow in the Altered Sandstone: from station 211 to 67 to 81.

Local Flow Regime

In the overburden at Cigar Lake, the base of the sand unit directly overlying the basal till is stained a rusty colour within 1 to 2 m of the sand-till contact. The sand aquifer is unconfined, with saturated conditions existing within 2 m of the contact with the basal till, as exemplified by the ~1.5-m-deep Aline Lake. The local flow regime seems to be perched, in that heads are generally much higher in the local regime than in the underlying intermediate regime (Figure 3.68). Rain and meltwater recharge maintain the local water table within the sand at ~20-25 m depth in the vicinity of the shaft. Solute concentrations are low in precipitation (rain+snow) at Cigar Lake. Calcium is the dominant cation and sulphate is the dominant anion, although carbonic acid is more abundant than either of these.

Compared with precipitation, Waterbury Lake and Cigar Lake waters contain an order of magnitude more cations and anions (aqueous silica contents ~1-2 orders of magnitude greater), see Table 3.31. Silica must therefore be derived from the overburden or bedrock of the drainage basin. Although lake waters are very dilute, surface runoff and subsurface input apparently provide the bulk of solutes in the lake waters.

Soilwaters and groundwaters from the overburden (Table 3.31) contain still more solutes than lake waters. Sodium, potassium and calcium are typically 1-5 mg/L ($5x10^{-4}$ M/L), with bicarbonate the dominant anion (10-40 mg/L). Bicarbonate, followed by $SiO_2(aq)$, are the most abundant solutes. They indicate that dissolution of silicates occurs within the overburden. Total dissolved solids (TDS) are ~30 mg/L in overburden waters (n= 13), about 15 mg/L in lake waters (n=12), and precipitation has ~7 mg/L (n=4). Mixing of overburden water with sub-equal amounts of precipitation yields total dissolved solids, chloride, $SiO_2(aq)$, cation and anion contents similar to lake-water values. If overburden waters and precipitation are the major components of lake water, the calculation suggests that the components contribute approximately equally to lake-water composition.

Stable isotope δD and $\delta^{18}O$ values for precipitation, lake and overburden waters are similar, demonstrating a common source of H_2O. There are greater isotopic fluctuations for precipitation (seasonal) than for lake or groundwaters. Isotopic excursions probably are damped in the two reservoirs, because of mixing during residence in the aquifers, and probably reflect season-averaged values of precipitation at this locality. Overburden waters generally contain a slightly greater proportion of the lighter isotopes than Waterbury or Cigar lakes. Overburden waters may have on average a somewhat greater proportion of winter snows contributing to the reservoir (spring melt) than does Waterbury Lake. Alternatively there is some contribution from permafrost, which may be isotopically lighter than recent precipitation.

Tritium of precipitation at the Cigar Lake site is low (Figure 3.70), both for snow (<6 TU) and rain (~22 TU). Tritium measurements of precipitation at Wynyard, Saskatchewan, and The Pas, Manitoba, indicate that precipitation had an average of 40-50 TU in 1979 (IAEA 1983), and now should be about 20-25 TU. Waterbury Lake, Cigar Lake and Aline Creek contain detectable tritium (av.=47.7, σ=13.5, n=11), and the overburden waters contain similar levels (av.=68.1, σ=27.6, n=10). Additional analyses are needed to determine if the differences between the two reservoirs are statistically significant. Despite the statistical ambiguities, the average values for the two reservoirs are similar enough to indicate that both have similar reservoir residence times, and that the same components contribute in similar proportions to each reservoir. These reservoirs undoubtedly contain older waters where tritium was initially much higher. For instance, permafrost occurs in the glacial overburden (Figure 3.63), where layers of clear ice have been reported (CLMC 1987). Although ^3H data are not available, it is possible that older water containing bomb-puls tritium is part of this permafrost, which could now contribute tritium to the overburden waters. The ^3H-enriched waters have been mixed with recent precipitation to yield the observed average values of 48 and 68 TU in lake and overburden waters. The major-

element data suggest that Waterbury Lake waters contain subequal contributions from precipitation and runoff/overburden leakage. Precipitation (av.=15 TU) and overburden waters (68 TU) mixed in subequal proportions yields a lake-water value of 42 TU, which is close to the average value (48 TU). Additional data and a more sophisticated interpretation may provide constraints on residence times and mass balances for the overburden and lake-water reservoirs.

Intermediate Flow Regime

Station 75 is located witin this flow regime. The TDS value of water 75 is approximately 85 mg/L (Table 3.31), a value three to four times greater than the TDS of waters from the local flow regime. The δD, $\delta^{18}O$ and ^3H values for station 75 are similar to those of the local regime, indicating that the two regimes have the same source of H_2O. The average ^3H value of water from piezometer 75 is 52.6 TU (σ=11.2, n=3), which is close to the average of the ^3H-values for overburden waters plus surface waters (Figure 3.70). Furthermore, the residence times and components contributing to the reservoir are similar for the two flow regimes. There is either very good communication between the two regimes, intimate mixing of the two reservoirs, or they are separated but recharged by the same components, affected by the same reactions and discharged at similar rates (to yield similar residence times). The latter seems more likely in view of the low hydraulic conductivity and permeability of the till aquatard. This aspect is explored further in a subsequent section on fractures.

The Limonitic Upper Sandstone is characterized by iron staining, which results from oxidation of pyrite and marcasite to produce limonite and goethite. Waters sufficiently oxygenated to cause this reaction obviously permeate the upper parts of the intermediate flow regime. The Unoxidized Upper Sandstone also contains pyrite/marcasite but there is no evidence for oxidation to ferrihydrites. The lack of reaction attests to the low rate of flow through the UUS. The "oxidation front" separates the LUS from the UUS and is now about 100 m below ground surface, hence oxygenated waters have penetrated overburden and LUS to a depth of no more than, and possibly less than, 100 m since glaciation. Preservation of the UUS at this shallow depth provides strong evidence that the "intermediate flow regime" (Pleistocene Conglomerate, LUS and UUS) is effectively separated from the underlying "semi-regional flow regime", and that communication is limited by the low hydraulic conductivity of the UUS.

Semi-Regional Flow Regime

Station 139 is within the Basal Conglomerate of the semi-regional flow regime. The TDS value for waters from this location is ~100 mg/L, about 10-15 % greater than waters from station 75 of the intermediate regime. These data suggest that the waters of the regional regime have acquired slightly more solutes during their residence in the semi-regional regime than have waters of the intermediate regime. We emphasize, however, that waters from the two stations are similar, an aspect that is emphasized subsequently. The D and ^{18}O data indicate that H_2O of the semi-regional regime has local meteoric water as recharge, hence the same source as waters of the other regimes. The isotope values are indistinguishable from waters at station 75. Tritium values from 139 are constant and low with an average value of 22.7 TU (σ=7.8, n=8). The constant values suggest a stable, well

mixed, reservoir. The properties mitigate against any appreciable contamination during sampling. Certainly continual sampling over a number of years would lead to variable amounts of contamination with each sampling episode, and consequently to variable tritium results.

The low average tritium value is similar to recent precipitation, but the water would have to be almost entirely recent precipitation (e.g., the only component contributing to this reservoir) to achieve the low value. Waters of the intermediate flow regime, overburden waters (local flow regime) and surface waters (Waterbury and Cigar Lakes) have appreciably higher tritium levels (Figure 3.70). One or more of these reservoirs (particularly overburden waters) are likely to be a major recharge component of the regional regime, yielding higher tritium contents. We conclude that the waters of station 139 are not derived directly from precipitation; more likely the low tritium values reflect a mixture of an effectively non-tritiated component (exclusive of recent precipitation) and a tritiated component. The non-tritiated source is predominant, as now shown. If overburden water (68 TU) is the tritiated component and it is mixed with a non-tritiated component to yield a water with 14 TU (water at station 139), then the non-tritiated component constitutes approximately three quarters of the mixed solution (water 139). The conclusion holds, regardless of when mixing occurred (anytime during the last 50 a). The result demonstrates that the non-tritiated component represents by far the larger contribution to waters of the semi-regional flow regime (provided the proper components have been chosen).

The tritium values reflect three important properties of the semi-regional flow regime. First, its reservoir properties are different from those of the local and intermediate flow regimes; residence times are different and most likely the components contributing to the reservoir are different from the components contributing to the other reservoirs. Secondly, there is a tritiated component to these waters. The component is less than 50 a old (assuming bomb tritium), hence it has migrated to more than 400 m depth in less than 50 a and the vertical component to flow rate is necessarily 8-10 m/a. If, within the hydraulically conductive Basal Conglomerate, waters migrates a similar distance horizontally ($\sim$400 m per 50 a), then the bulk flow rate would be near 20 m/a within the Basal Conglomerate. The second mixing component is non-tritiated water and of meteoric origin, as demonstrated by stable isotopes, and most likely has been introduced to the regional reservoir before 1950. If so, this component has remained in the reservoir for more than 50 a. Since it is the major component, the residence time for H_2O in the reservoir probably is greater than 50 a as well.

The tritium data demonstrate that the semi-regional flow regime has some characteristics quite distinct from those of the intermediate regime (Figure 3.70). Specifically, tritium at stations 75 and 139 reflect little or no mixing of the two reservoirs. Although their major-element compositions are strikingly similar, we conclude that there is little communication between the two regimes. Apparently, the Unoxidized Upper Sandstone is an effective aquitard. As well, the heads in the Upper and Lower Sandstones are within a few cm of each other, hence there is little potential for cross-boundary flow. There is an important

corollary to this conclusion. If the waters of the two regimes do not mix appreciably, their similar major solute contents must be the result of the similar solution-mineral reactions occurring in both flow regimes. This is addressed separately by Cramer and Nesbitt (in prep.).

Water from the Unaltered Sandstone in the semi-regional regime enters the hydrothermal alteration halo of the deposit on the south side and is deflected up and over the clay-rich rocks of the clay and mineralized zones (Figure 3.65). The water passing, over the deposit and into the clay and mineralized zones becomes progressively more enriched in ^{3}H (Figure 3.70). Uranium mineralization occurs throughout the clay-rich rocks, ranging in concentration from >10 ppm in the Altered Sandstone, to >100 ppm in the clay zone, to $>10{,}000$ ppm in the mineralization (Bruneton 1987; Section 3.2.2). The production of ^{3}H from the reaction $^{7}Li(n,\alpha)$ in rock containing uranium minerals can lead to elevated ^{3}H contents in the associated groundwater (Section 3.8.2). Depending on the lithium content of the rock and on the degree of mixing and exchange of ^{3}H between the water and rock, Fabryka-Martin (Section 3.8.2) estimates that in-situ ^{3}H production, for an average 15 wt.% uranium in the rock, can contribute from a few TU to >500 TU in the water. The high ^{3}H-contents in groundwaters from the clay and mineralized zones may thus have a significant component of in-situ produced ^{3}H. Alternatively, the low hydraulic conductivity of these zones may have caused the retention of water enriched in bomb-puls ^{3}H (i.e., <40-a-old water). As discussed subsequently, this latter explanation appears unlikely, at least for the mineralization, based on estimated residence times for water in these clay-rich rocks. The low ^{3}H content of waters from the downstream piezometer 219 (11.6 TU, $\sigma=5.3$, $n=5$) further suggests that the elevated ^{3}H-contents are local isolated occurences in the clay zone, and do not contribute ^{3}H to the bulk formation water passing through the deposit.

3.5.3.4 Discussion

3.5.3.4.1 Fractures and their influence on hydrology

The tritium results suggest that the semi-regional flow regime is separated from the intermediate regime. Till separating the local and intermediate regimes has a lower hydraulic conductivity than the UUS, indicating that it should be the more effective aquatard (Figure 3.63). If so, reservoirs of the intermediate and semi-regional regimes must be recharged in regions where the till cover is absent, and/or by fractures through the aquatard. Although exposures of the sandstone bedrock occur locally in the Cigar Lake area (Figure 3.63), they are small and sporadic compared with the larger bedrock exposures found in the upland area further south and west towards Close Lake and McArthur River. In addition to recharge at breaks in the till cover, recharge from the local to the intermediate flow regime in the Cigar Lake area must therefore also occur along fractures and fault zones. The occurence and depth of the limonite alteration in the matrix and along fractures in the US indicate that active recharge of waters from the local regime occurs before these waters lose their oxidation potential. This local recharge is supported both by the ^{3}H data for the US waters and by uranium-series isotopic data for LUS samples. As discussed previously and as illustrated in Figure 3.70, the ^{3}H values of waters collected in the intermediate regime

correspond to the average values of ^{3}H in waters from the local regime, suggesting recharge on a relatively short time scale. The uranium-series data for samples collected from the LUS (Section 3.2.2) show that oxidative bulk dissolution of uranium occurs in these rocks (i.e., $^{234}U/^{238}U$= 0.87-0.88 and $^{230}Th/^{234}U$= 1.10-1.29). These observations suggest that local recharge to the intermediate regime occurs mainly along fractures under local topographic highs, as illustrated schematically in Figure 3.65.

Similarly the lower, semi-regional regime must be recharged through the comparatively impermeable UUS. There are major fault zones and fractures within the basin that penetrate the Upper and Lower Sandstones, as shown in Figure 3.65. These fractures or fault zones occur throughout the Athabasca Basin, as described by Ramaekers (1981), Kotzer and Kyser (1990a) and Sibbald et al. (1990). Major transport of groundwater along such fractures causes retrograde alterations to occur. These alterations include late fault-controlled kaolinization where the regular clay mineral stratigraphy of the sandstones is locally transected and destroyed. As a result the total clay mineral content and the illite/kaolinite ratio are decreased, in extreme cases leading to an incoherent sandy material (Sibbald et al., 1990). This kaolinization process involves hydration, leaching of soluble cations (primarily K and Si from the illite-quartz matrix) and mass transport, requiring considerable advection of groundwater through the system. Similar retrograde alteration (late kaolinization) has been reported for other sedimentary basins where it has been interpreted as being related to erosion and uplift, allowing acidic surface waters to percolate downwards along reactivated open fault zones and regaining access to the deeper aquifers (e.g., Kish 1983; Nesbitt 1985).

In fact, fault-related kaolinization in the Athabasca sandstones is most commonly described in relatively shallow settings, such as the near-surface uranium deposits at Key Lake (De Carle 1986), Midwest (Hoeve 1984), Rabbit Lake (Hoeve and Sibbald 1978) or in the fracture-hosted mineralizations at McArthur River (Kotzer and Kyser 1990b). The extent of distinct fault-related kaolinization in the sandstones at Cigar Lake is limited and is mainly confined to the Upper Sandstone, where it occurs in association with the perched uranium mineralizations (Bruneton 1987). The extensive drilling program on the Cigar Lake deposit has not identified any major faults or fracture zones with continuous kaolinization reaching down beyond the Upper Sandstone deep into the Lower Sandstone. However, small (cm-scale) kaolinite alterations occur sporadically along some of the many fractures within the upper 70 m of the LS (see Figure 3.67), of which some are associated with minor perched mineralizations of uranium. Smellie et al. (Section 3.2.2) report on one such occurence (depth 270 m; ~5000 ppm U) where the uranium-series activity ratios indicate some remobilization of uranium (i.e., $^{234}U/^{238}U$= 0.92 and $^{230}Th/^{234}U$= 1.24). In contrast, the uranium-series isotopes in samples from deeper within the deposit have close to equilibrium activity ratios for $^{234}U/^{238}U$ and $^{230}Th/^{234}U$ (Section 3.2.2). These observations suggest that some minor recharge from the intermediate to the semi-regional regime may occur along fractures in the upper part of the LS, at least in the highly fractured zone above the Cigar Lake deposit.

TABLE 3.32
URANIUM CONTENTS AND ACTIVITY RATIOS FOR URANIUM AND THORIUM ISOTOPES IN CIGAR LAKE WATER AND ORE SAMPLES

SAMPLE	TYPE+LOC	U*	$^{234}U/^{238}U$ ±		$^{230}Th/^{234}U$ ±	
67C	water, AS	7.00	2.20	0.02	**	
67D	water, AS	29.81	1.40	0.02		
71F	water, LS	1.33	2.30	0.80		
79E	water, O	5.81	1.50	0.20		
79L	water, O	7.71	1.80	0.30		
81H	water, AS	1.58	1.60	0.22		
91D	water, C	54.74	1.49	0.02		
91R	water, C	14.79	1.28	0.07		
139G	water, LS	0.49	2.80	0.80		
197O	water, C/O	1.12	1.80	0.50		
199B	water, B	5.44	2.04	0.13		
199D	water, B	12.39	1.89	0.08		
211C	water, AS	3.20	4.70	0.60		
211D	water, AS	2.31	2.90	0.50		
219D	water, LS	2.66	1.60	0.30		
220A	water, O	25.50	2.70	0.10		
220B	water, O	7.80	2.90	0.30		
83A	ore	37.2	1.00	0.01	1.05	0.02
83C	ore	46.8	0.98	0.01	1.09	0.01
235L	ore	55.4	0.99	0.01	1.11	0.01

* In water: μg/L; in ore: wt.%. ** Dissolved-Th is too low.

Kaolinization is also observed in the highly conductive Altered Sandstone (between the clay/mineralized zones and the quartz-cemented zone) where it is associated with fractures. However, the uranium contents and the uranium-series activity ratios measured in groundwaters (Table 3.32), in ore samples (Table 3.32) and in hostrock samples (Section 3.2.2) indicate that bulk dissolution of uranium is not now occurring in the AS and other locations deep in the deposit. The low concentrations of dissolved uranium in the waters combined with the equilibrium ratios of both $^{234}U/^{238}U$ (0.95-1.00 $\pm$0.05) and $^{230}Th/^{234}U$ (0.95-1.05 $\pm$0.05) in the ore and rock samples indicate reducing conditions for both current and recent water-rock interaction. The elevated $^{234}U/^{238}U$ ratios in the groundwaters can then be explained by α-recoil of ^{234}U from the solid into the aqueous phase rather than bulk dissolution of uranium from the rocks. The prevailing reducing conditions of waters in the LS result from interaction with the reduced-iron minerals within the hydrothermal alteration halo surrounding the deposit (Cramer and Nesbitt in prep.). The general distribution of these ferrous phases, particularly of pyrite/marcasite (Bruneton 1987), suggests that dominating lateral, rather than downward, flow of groundwater has occurred over time. These observations and the absence of a significant vertical hydraulic gradient across the

US/LS boundary (Figure 3.65; Section 3.4), at least in the present-day system, argue against major recharge along fractures from the intermediate to the semi-regional regime in the immediate Cigar Lake area. This is again supported by the ^{3}H data (Figure 3.70) which show a clear distinction between these two flow regimes. Thus, major recharge to the semi-regional flow regime occurs probably along major fractures or fault zones located under topographic highs (Section 3.4), which generally are outside the immediate Cigar Lake area (Figure 3.63).

As discussed elsewhere (Cramer and Nesbitt in prep.), the influence of these faults on hydrology also explains why the major-element compositions of waters of the three flow regimes (outside the influence of the deposit) are similar. All are recharged by the same type of waters (rainwater and snow melt that have migrated through organic and soil zones), and since the mineralogy of the overburden, Upper and Lower Sandstones are similar, they contact the same mineral assemblages during recharge and migration.

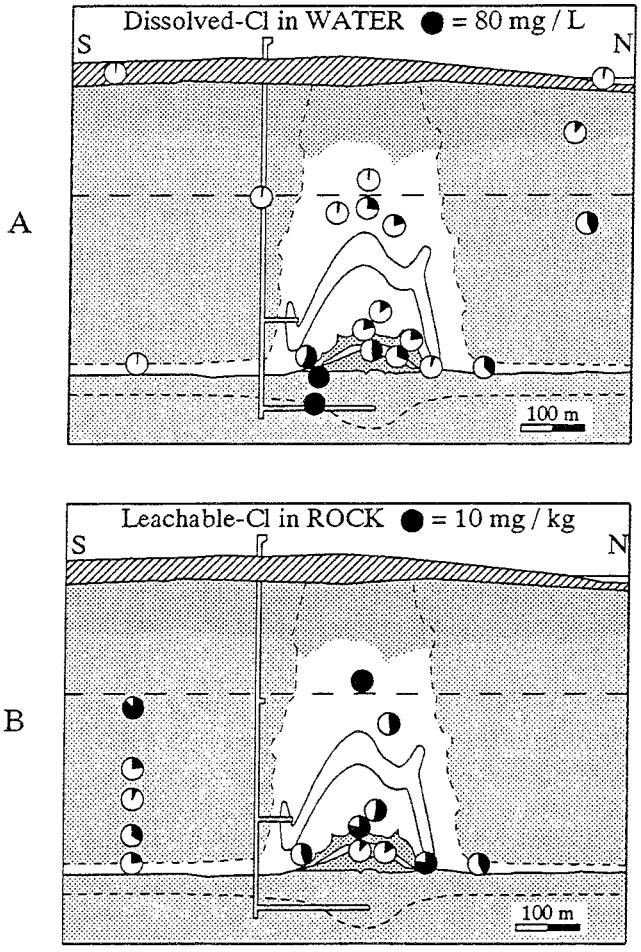

FIGURE 3.71 Sections showing distribution of Cl across Cigar Lake deposit. **A**: Dissolved-Cl in water samples. **B**: Leachable-Cl in rock from whole-rock leaching experiments.

3.5.3.4.2 Chloride contents and mixing

The compostions of groundwaters from the sandstone formation in and around the deposit show a range in chloride contents of between 0.2 and 40 mg/L. The Cl contents of waters farthest removed from the centre of the deposit are the lowest, whereas the highest Cl-contents are generally found in and around the clay and mineralized zones (Figure 3.71a). The chloride content of basement waters (from piezometer 199 and from a fracture discharge at the 480 m level underground) is distinctly higher than the sandstone waters, averaging about 86 mg/L (Table 3.31).

The relationship between Cl content of the sandstone waters and sampling distance relative to the centre of the deposit could be explained by mixing of the low-Cl regional sandstone water with basement-derived waters. These latter waters would then be discharged along fractures from the basement into the semi-regional aquifer of the lower sandstone, where these fractures are most abundant in the centre of the deposit (or centre of the hydrothermal paleo-system). The mixing of sandstone and basement-derived waters may possibly also explain the values of other constituents (e.g., Na, Br) in some of the groundwaters within the deposit. However, the following observations argue against such mixing as the origin of the compositions for the sandstone groundwaters:

- Hydrologic observations from the ungrouted excavations in the basement show that, even where fractures are intersected, groundwater discharge into the excavation is minimal to non-existent. The highest observed discharge rate of water (under a hydraulic-pressure differential of ~ 5 MPa between the rock and the excavation) is ~ 20 L/h, from a fracture intersected in the west drift.

- Hydrogeological modelling by Winberg and Stevenson (Section 3.4) indicates that waters from the semi-regional flow regime are recharging into the regolith aquatard (Figure 3.65), rather than discharging in and around the deposit. Also, the dominating hydraulic gradient in the semi-regional regime is horizontal, arguing against discharges of huge volumes of water from the basement into the lower sandstone. Such large discharges would be required to explain a mixed composition for water from, for instance, piezometer 71 (see Table 3.31), which is located about 200 m above the unconformity.

- Although mixing of (up to equal proportions) basement water with waters in the lower sandstone may produce selected cation and anion contents similar to those analyzed in the sandstone water, values for ^{3}H (Figure 3.70) and several other parameters (e.g., pH, TIC/TOC etc.) can not be reproduced by this mixing.

An alternate explanation for the elevated Cl-contents in the analyzed waters may be mixing of dilute recharge waters with relicts of the hydrothermal formation waters. Bray et al. (1988) and Wilson et al. (1987) report estimated values for δD and $\delta^{18}O$ of such formation waters (or basinal brines) for several sandstone-hosted uranium deposits in the Athabasca

Basin. These estimates ($\delta D \sim -45$ °/$_{oo}$, $\delta^{18}O \sim +6$ °/$_{oo}$ and $\delta D \sim -60$ °/$_{oo}$, $\delta^{18}O \sim +5$ °/$_{oo}$, respectively) are based on analyses of fluid inclusions of brines (with temperatures of around 200 °C) associated with the clay mineralization in these deposits. The plot in Figure 3.72 shows these formation waters (rectangles) plotting close to the (extended) regression line through the present-day groundwaters from Cigar Lake (solid rectangles). This relationship suggests that at least the isotopic trend of the Cigar Lake groundwaters may be explained by mixing of meteoric waters with residual formation water. However, this explanation seems unlikely for the reasons given below.

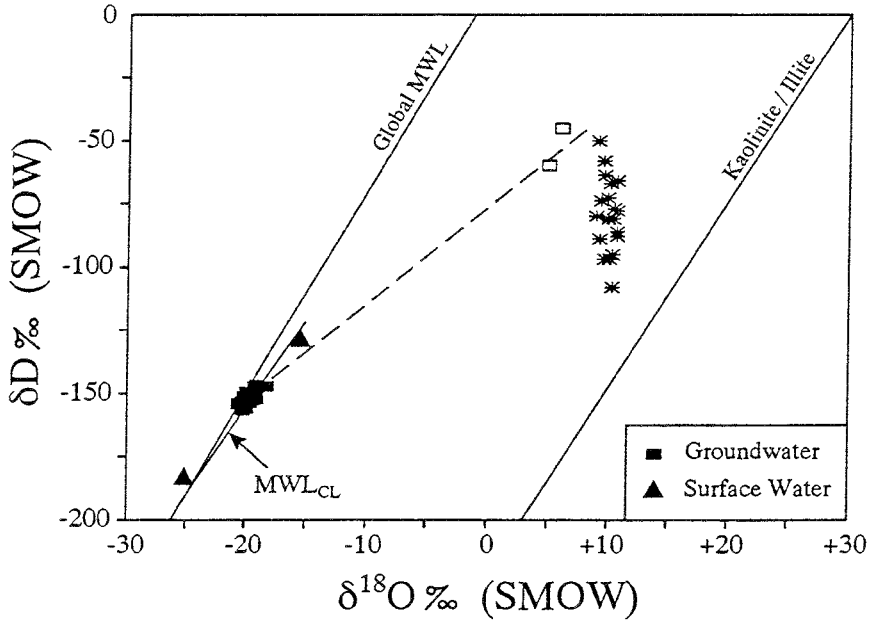

FIGURE 3.72 Diagram showing δD and $\delta^{18}O$ values for representative groundwaters and for the clay mineral data (*) from Percival (1990). Also shown are the Cigar Lake (MWL_{CL}) and global meteoric water lines, and the Kaolinite/Illite line. The linear regression line for the Cigar Lake groundwaters (dashed) is extended through the plots of the estimated values (Bray et al. 1988; Wilson et al. 1987) for two formation waters (rectangles) associated with clay mineral genesis.

The intersection of the regression line for the Cigar Lake groundwaters with the Global meteoric water line gives $\delta D = -153$ °/$_{oo}$ and $\delta^{18}O = -20.0$ °/$_{oo}$, values similar to those for meteoric recharge water from piezometer 139, located up-gradient from the deposit. The mixing of about 15 % of the estimated composition for formation water (Table 3.33) with 139 groundwater would shift these values along the regression line to δD and $\delta^{18}O$ values similar to those for groundwater from piezometer 71, located in the LS above the deposit. However, the calculated contributions of Ca, Na, Cl and Br from the formation water result in a composition for the mixed water (last column Table 3.33) that is quite different from the compositon of the 71 groundwater. Similar calculations for the other groundwaters from

the deposit show that mixing of residual formation water with present-day groundwater from 139 cannot explain the variation in compositions of these waters.

TABLE 3.33
CALCULATED COMPOSITIONS OF GROUNDWATER UPON MIXING WITH RELICT FORMATION WATER

	Form. Water (FW)*	139 (C+G)av.	71 A	139 + 15 % FW
δD	-53	-155	-147	-147
$\delta^{18}O$	+5.5	-19.9	-19.0	-19.0
Ca	29,487	4.00	6.50	4,427
Na	117,949	2.75	14.00	17,695
Ca/Na	0.25	1.45	0.46	0.25
Cl	182,051	0.25	17.35	27,308
Br	3,310	<0.01	0.28	497
Cl/Br	55	>250	62	55

Mixing of 15 %(av.) of FW with 139 equals shift in δD and $\delta^{18}O$ values from 139 to 71:

$$(\delta D_{139}-\delta D_{71})/0.1\delta D_{FW} = 14.3\ \%$$

$$(\delta^{18}O_{139}-\delta^{18}O_{71})/0.1\delta^{18}O_{FW} = 15.6\ \%$$

* Data from Pagel et al. (1990), Wilson et al. (1987) and Bray et al. (1988).

Nordstrom and Olsson (1987) investigated the contribution of chloride to groundwaters from fluid inclusions in the Stripa granite in Sweden. With a granite porosity of 0.5 % and an average fluid inclusion salinity of 3 wt.% equivalent NaCl, only 1 to 2 % of the fluid inclusions need to leak to obtain groundwater chloride concentrations of 600 to 700 mg/L. The porosity of the altered and unaltered sandstone at Cigar Lake are significantly higher than that of granite (by at least an order of magnitude), whereas reported salinities of fluid inclusions from unconformity-related deposits are typically an order of magnitude greater than found in the Stripa granite (about 30 wt.% equivalent NaCl, Pagel et al. 1980; Kotzer and Kyser 1990a,b). Thus, a comparable 1 to 2 % of fluids, trapped in inclusions in the sandstone and leaking into the groundwater, should contribute at least 1 to 40 mg/L Cl to groundwaters, which spans the range of Cl in groundwaters of the sandstones at Cigar Lake. This explanation requires fluid inclusions to make an exceedingly small volume contribution to groundwaters; the contribution is too small to produce significant variations in the stable isotope signatures.

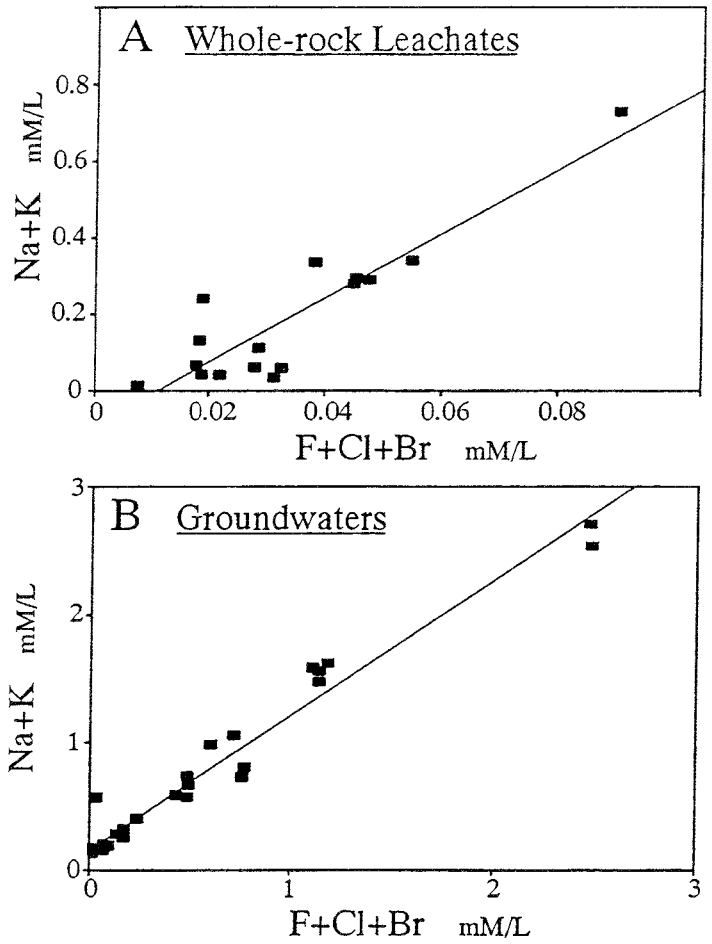

FIGURE 3.73 Na+K vs. F+Cl+Br in leachates of whole rock samples (A), and in groundwaters (B) from the Cigar Lake deposit. Regression lines have been drawn through the data points.

A third explanation involves the leaching of residual salts from the hydrothermal and/or diagenetic formation waters that are still present on grain boundaries and in intergranular pores within the rock matrix. Although the members B, C and D of the Manitou Falls Formation have been classified as fluviatile sandstones (Ramaekers 1981), local marine transgressions have occurred in the eastern part of the Athabasca Basin. Furthermore, the fluid inclusion data show that highly saline formation waters were common around the time of ore formation in this part of the Basin. Natural access by water to these salts would be gradual, facilitated by the opening up of pathways as a result of lithostatic decompression during erosion; drilling may also open up access paths for water. To evaluate the leaching of Cl from salts within the rock, leaching experiments were conducted. Whole-rock and coarsely-ground samples from drill core were contacted with double-distilled deionized water (water/rock weight ratio of 5:1) for 1 week under static conditions. The results of these experiments with whole-rock samples are illustrated in Figure 3.71b, showing the Cl-contents of the leachates. The results indicate that leachable-Cl contents are significant in all the rocks. In fact, calculated Cl-contents for water in contact with intact rock, having a 10 % porosity and between 20 and 40 mg/kg Cl, range between 50 and 100 mg/L. The

linear correlation between Na+K and F+Cl+Br in the leachates (Figure 3.73a) suggests simple halide salt compositions corresponding to those observed in primary fluid inclusions in associated hydrothermal quartz (Pagel et al. 1980; Wilson et al. 1987; Bray et al. 1988; Kotzer and Kyser 1990a,b). A similar linear correlation exists for the groundwaters compositions (Figure 3.73b). Thus, the salts being leached are probably the solid residues of the same saline hydrothermal system from which liquid residues were preserved in the fluid inclusions. However, the leaching experiments also showed that leachable-Cl values for the coarsely-ground samples are 2 to 7 times higher than the whole-rock values. This suggests that the interstitial salts, rather than fluid inclusions, account for most of the leachable-Cl from the intact rock in the natural system.

TABLE 3.34
COMPOSITION OF ILLITE SAMPLES FROM CIGAR LAKE
DATA FROM PERCIVAL (1990)

Sample #	Litho code	Clay min. % I	C	K	K_2O wt.%	LOI wt.%	U ppm	δD ‰	$\delta^{18}O$ ‰	K-Ar Ma
44-01	AS	100	0	0	8.98	7.24	42	-67	10.2	
44-04	AS	100	0	0	9.96	6.12	66	-77	10.5	
44-06	AS	100	0	0	9.94	5.74	104	-95	10.3	1210
44-08	AS	100	0	0	9.52	6.48	245	-86	10.7	
44-11	AS	99	0	1	10.40	5.31	233	-81	10.4	
44-18	C	88	0	12	9.56	6.60	116	-88	10.7	
49-12	C	100	0	0	9.02	8.47	318	-80	9.0	
49-13	C	100	0	0	9.78	6.45	110	-66	10.7	
53-02	AS	100	0	0	7.42	4.73	3	-97	9.7	
53-15	B	53	47	0	6.36	8.98	52	-50	9.1	815
60-03	C	100	0	0	9.82	6.11	71	-78	10.7	1255
60-04	C	95	0	5	10.00	7.39	189	-89	9.3	
113-02	AS	100	0	0	10.20	5.68	245	-81	10.0	
113-04	C	100	0	0	10.18	5.69	100	-73	9.9	
118-03	C	99	0	1	8.56	6.51	177	-97	10.1	
118-06	C	100	0	0	8.62	6.48	146	-108	10.3	
137-01	AS	100	0	0	8.58	6.90	185	-64	9.7	1148
139-12	LS	100	0	0	8.30	4.49	2	-74	9.4	
139-18	B	68	32	0	7.94	7.37	8	-58	9.6	

This latter explanation is feasible in that it is compatible with the major-element composition of groundwaters and is entirely compatible with the stable isotope data. The isotopic trends of the Cigar Lake groundwaters result from variations of their recharge waters, meteoric surface waters and precipitation.

3.5.3.4.3 Groundwater flux through the mineralization

The fact that clay-rich hostrock forms the matrix to the mineralization, is one of the main reasons the uranium mineralization has been so well preserved since its hydrothermal formation 1.3 Ga ago. This clay-rich matrix and, in particular, the clay zone surrounding the economic-grade ore provide efficient sealing of the groundwaters from the main aquifer in the altered sandstone, allowing water to migrate mainly through tight and tortuous flowpaths along fractures. A low flux of groundwater through the clay-rich zones of the Cigar Lake deposit is supported by data on the hydraulic conductivity, and on the compositions of illite, the dominant clay mineral in these zones.

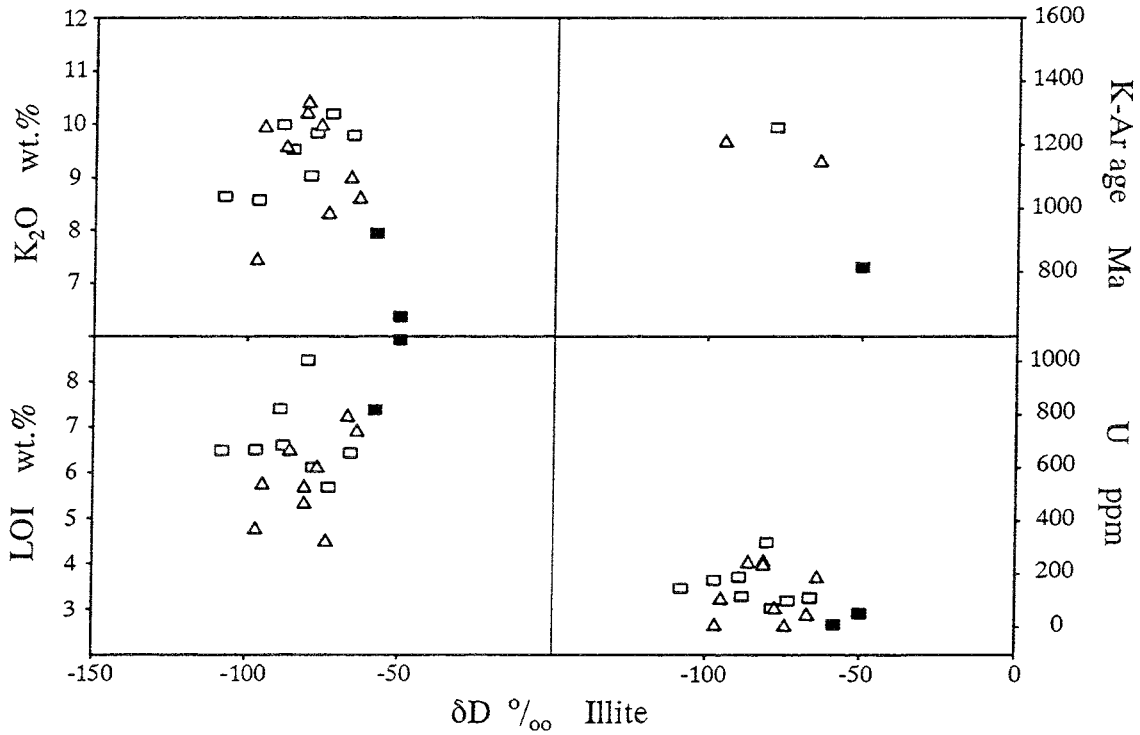

FIGURE 3.74 Composition of illite samples from Cigar Lake. Variation in K_2O, water content (LOI), K-Ar age and U content of illites plotted as a function of δD (Table 3.34). Rectangles are samples from the Clay and Mineralized zones, triangles are samples from the Altered Sandstone and Lower Sandstone, and filled rectangles are samples from the Basement.

All the illite samples analyzed by Percival (1990) (Table 3.34 and Figure 3.72) have δD and $\delta^{18}O$ values and K-Ar ages (between 1257 and 813 Ma) similar to those reported for diagenetic clay minerals from other uranium deposits in the Athabasca Basin (Wilson et al. 1987; Kotzer and Kyser 1991). Wilson et al. (1987) found a correlation between the decrease in δD and K-Ar age with an increase in interlamellar water content for illites from the relatively shallow Key Lake, Midwest, Collins Bay and McLean Lake deposits. Similar results are also reported by Kotzer and Kyser (1991) for illites from the McArthur River

deposit. They interpret this as reflecting low-temperature alteration of the illites by meteoric waters with δD and $\delta^{18}O$ values similar to those of surface waters found at present in the Athabasca Basin. This retrograde alteration caused a decrease in δD values upon replacement of K_2O by H_2O in the illite structure, resulting in kaolinite formation, and a corresponding decrease in the (measured) K-Ar age (Kotzer and Kyser 1991).

The diagram in Figure 3.74 shows the absence of any correlation between the contents of K_2O, water (measured as loss on ignition, LOI) and uranium, and the K-Ar ages, with the variation in δD values for the Cigar Lake illites. The XRD data for the Cigar Lake illites indicate that they formed under conditions of high-grade diagenesis up to low-grade metamorphism (anchizone), corresponding to 2M and 3T illite polytypes, without evidence for low-temperature 1M polytype or I/S mixed layer phases (Percival 1990). Although the characteristic clay-mineral assemblage in the more hydraulically conductive bleached and altered sandstones includes both illite and kaolinite (up to subequal amounts in the permeable altered sandstone), kaolinite is absent or rare in the mineralization (Bruneton 1987). The absence of significant alteration of illite to kaolinite indicates very limited mass transport, particularly of potassium, within the mineralization. Any significant leaching and removal of K from illite, resulting in kaolinite formation, would require significant advection over time.

Thus, the narrow range of $\delta^{18}O$ values (9.3 to 10.7 $^{o}/_{oo}$), the high-grade crystallinity of the Cigar Lake illite samples (Percival 1990) and the absence of any significant kaolinite in the ore/clay zone suggest that the range of illite δD values reflects preferential exchange of hydrogen isotopes with meteoric groundwaters rather than recrystallization during low-temperature (retrograde) alteration. However, since Cenozoic times (i.e., for the past ~ 60 Ma) the Athabasca Basin has been at a latitude of 60 °N (Fahrig et al. 1978), where the meteoric waters had much lower δD and $\delta^{18}O$ values than meteoric waters at low altitudes, and possibly similar values to modern-day meteoric waters from the same location (Cigar Lake latitude is 58 °N, Figure 3.63).

A number of additional arguments suggest also that groundwater flux through the clay and mineralized zones has been low, at least during the deposit's most recent history. The low hydraulic conductivity measured today for the bulk clay and mineralized zones was likely even lower during the deposit's geological history, because of the higher lithostatic pressure at greater depths and the plastic texture of the clay-rich rocks. Furthermore, the uranium-series isotopic data (Section 3.2.2) for samples from the clay and mineralized zones, showing near-equilibrium activity ratios or true secular equilibrium (in clay-filled fractures), indicate that reducing and non-advective conditions have prevailed for at least the past 1 Ma. It is thus possible that relatively old waters with "modern" meteoric isotopic signatures have been in contact with the illites for long periods of time (i.e., $>10^6$ to $\sim 6 \times 10^7$ a). The very limited alteration of illite, restricted to the preferential exchange of hydrogen isotopes, indicates that diffusion rather than advection was the dominant mass transport mechanism during prolonged periods of time. The hydrogen isotopic trend of the Cigar Lake illites may then simply reflect the variations in meteoric water compositions during the past $\sim 10^7$ to 10^8 a.

A low flux of groundwater through the mineralization during the deposit's recent geological history is further supported by the following observations:

- Direct hydrologic observations were made during drilling from the underground excavation up into the mineralization, as part of the test mine development. Only very small volumes of formation water from the mineralization were recovered in each hole (<50 L/hole) that was terminated in the mineralization, without noticeable subsequent recharge from the altered sandstone aquifer through the clay zone. However, when drilling was continued upwards through the overlying clay zone, water inflows of several thousand litres per minute were encountered.

- In-hole measurements of hydraulic conductivity give values for the ore and clay zones of $\leq 10^{-9}$ m/s. The numeric modelling by Winberg and Stevenson (Section 3.4) shows that, using such low K values and a local hydraulic gradient of 0.3% in their reference case, calculated minimum residence times for groundwater in the mineralization range between 2×10^4 and 8×10^4 a.

- Uranium-series isotopic data for particles suspended in groundwaters collected from the mineralization (Vilks et al. 1993) show calculated ages for the particles of up to 8×10^3 a.

- Measurements of ^{14}C contents in the humic fraction dissolved in groundwaters extracted from the mineralization (Section 3.7.2) show calculated ages for the humics of $> 1.5 \times 10^4$ a.

- Measurements and production-rate calculations of ^{36}Cl contents (Sections 3.5.5 and 3.8.2) confirm the production of ^{36}Cl (through neutron-capture by ^{35}Cl) inside the mineralization, and lead to calculated residence times for groundwaters in the mineralization of $> 10^5$ a.

The flux of groundwater through the clay and mineralized zones may vary somewhat locally, depending on fracture density and stratigraphic and/or structural anisotropy, with preferred pathways being along weaker structural elements. During the deposit's history, major tectonic disturbances may have opened up these pathways temporarily, allowing groundwater advection to cause uranium mobilization from the mineralization along fractures into the host rocks. This may explain the local alteration of primary uraninite and pitchblende in and around more permeable zones within the ore and their age-correlation with the perched mineralizations, of which the youngest has been dated at 293 Ma (Cumming and Krstic 1992). However, the combined evidence of water and rock compositions in the present-day system strongly suggests that diffusive, rather than advective, processes have controlled water-rock interaction under reducing conditions during the recent ~ 1 Ma.

3.5.3.5 Conclusions

Based on available geological, hydrological and geochemical data, we have studied the hydrologic framework for water-rock interaction at the site of the Cigar Lake deposit, and we conclude the following:

- Three distinct flow regimes have been identified in the local stratigraphy, including a local regime in the surficial Quaternary deposits, an intermediate regime in the Upper Sandstone and a semi-regional regime in the Lower Sandstone.

- Recharge from the local to the intermediate regime occurs locally, along fractures and in places where the overburden cover is absent, whereas recharge to the semi-regional regime occurs mainly outside the immediate area surrounding the Cigar Lake deposit, probably along fractures under local topographic highs. Estimated flow rates for groundwater in the semi-regional regime are ≥ 10 m/a.

- Evolution of water compositions, from precipitation to groundwater in the clay and mineralized zones, involves interaction with similar mineralogies in all three regimes, as well as leaching of interstitial salts. These salts are probably relicts of the ancient, saline diagenetic-hydrothermal fluids responsible for ore formation and host rock alteration.

- The flux of groundwater through the clay-rich matrix hosting the uranium mineralization is very low, with estimated residence times for water in contact with the ore of $> 10^4$-10^5 a. Therefore, diffusive, rather than advective, processes are likely involved in controlling the redox conditions within the mineralization.

3.5.3.6 References

BRAY C., SPOONER E.T.C. and LONGSTAFFE F.J. 1988. Unconformity-related uranium mineralization, McClean deposits, northern Saskatchewan, Canada: Hydrogen and oxygen isotope geochemistry. *Can. Mineral.* **26**, 249-268.

BRUNETON P. 1987. Geology of the Cigar Lake uranium deposit (Saskatchewan, Canada). In *Economic Minerals of Saskatchewan* (ed. C.F. GILBOY and L.W. VIGRASS). *Sask. Geol. Soc. Spec. Publ.* **8**, 99-119.

CLMC 1987. Cigar Lake test mine - Environmental Impact Statement. Public documents available from Environment Canada.

CRAMER J.J. and NESBITT H.W. In prep. Hydrogeochemistry of the Cigar Lake uranium deposit: groundwater evolution and redox conditions.

CUMMING G.L. and KRSTIC D. 1992. The age of unconformity-related uranium mineralization in the Athabasca Basin, northern Saskatchewan. *Can. J. Earth Sci.* **29**, 1623-1639.

DE CARLE a.l. 1986. Geology of the Key Lake deposits. In *Uranium deposits of Canada* (ed. E.L. Evans). *Can. Inst. Min. Metal. Spec. Vol.* **33**, 170-177.

FAHRIG W.F., CHRISTIE K. and FREDA G. 1978. The Paleolatitude and Paleomagnetic age of the Athabasca Formation, northern Saskatchewan. In *Current Research, part C. Geol. Surv. Can. Paper* **78-1C**, 1-6.

FREEZE R.A. and CHERRY J.A. 1979. *Groundwater.* Prentice-Hall.

GASCOYNE M., DAVISON C.C., ROSS J.D. and PEARSON R. 1987. Saline groundwaters and brines in plutons in the Canadian Shield. *Geol. Assoc. Canada Spec. Pap.* **33**, 53-68.

HOEVE J. 1984. Host rock alteration and its application as an ore guide at the Midwest Lake uranium deposit, northern Saskatchewan. *Can. Inst. Min. Bull.* **77**, 63-72.

HOEVE J. and SIBBALD T.I.I. 1978. On the genesis of Rabbit Lake and other unconformity-type uranium deposits in northern Saskatchewan, Canada. *Econ. Geol.* **73**, 1450-1473.

IAEA. 1983. Environmental isotope data No. 7: World survey of isotope concentrations in precipitation (1976-1979). *Int. Atom. Energy Agency Tech. Rep. Ser.* **226**.

IAEA. 1986. Environmental isotope data No. 8: World survey of isotope concentrations in precipitation (1980-1983). *Int. Atom. Energy Agency Tech. Rep. Ser.* **264**.

KISH H.J. 1983. Mineralogy and petrology of burial diagenesis (Burial Metamorphism) and incipient metamorphism in clastic rocks. In *Developments in sedimentology #25B: Diagenesis in sediments and sedimentary rocks, 2* (ed. G. LARSEN and G.V. CHILINGAR), pp. 189-493. Elsevier.

KOTZER T. and KYSER T.K. 1990a. The use of stable and radiogenic isotopes in the identification of fluids and processes associated with unconformity-type uranium deposits. In *Modern exploration techniques* (ed. L.S. BECK and C.T. HARPER). *Sask. Geol. Soc. Spec. Publ.* **10**, 115-131.

KOTZER T. and KYSER T.K. 1990b. Fluid history of the Athabasca Basin and its relation to uranium deposits. In *Summary of investigations 1990. Sask. Geol. Surv. Misc. Rep.* **90-4**, 153-157.

KOTZER T. and KYSER T.K. 1991. Retrograde alteration of clay minerals in uranium deposits: radiation catalyzed or simply low-temperature exchange? *Chem. Geol.* **86**, 307-321.

NESBITT H.W. 1985. A chemical equilibrium model for the Illinois Basin formation waters. *Amer. Jour. Sci.* **285**, 436-458.

NORDSTROM D.K. and OLSSON T. 1987. Fluid inclusions as a source of dissolved salts in deep granitic groundwaters. In *Saline water and gases in crystalline rocks* (ed. P.FRITZ and S.K. FRAPE). *Geol. Assoc. Can. Spec. Pap.* **33**, 111-119.

PAGEL M., POTY B. and SHEPPARD S.M.F. 1980. Contributions to some Saskatchewan uranium deposits mainly from fluid inclusion and isotopic data. In *Uranium in the Pine Creek Geosyncline* (ed. S. FERGUSON and A.B. GOLEBY). *Int. Atom. Ener. Agency*, Vienna, 639-654.

PERCIVAL J.B. 1990. Clay mineralogy, geochemistry and partitioning of uranium within the alteration halo of the Cigar Lake uranium deposit, Saskatchewan, Canada. Ph.D. dissertation, Carleton Univ., Ottawa, Canada.

RAMAEKERS P. 1981. Hudsonian and Helikian basins of the Athabasca Region, northern Saskatchewan. In *Proterozoic Basins of Canada* (ed. F.H.A. CAMPBELL). *Geol. Surv. Can. Pap.* **81-10**, 219-233.

SIBBALD T.I.I., QUIRT D.H. and GRACIE A.J. 1990. Uranium deposits of the Athabasca Basin, Saskatchewan. *Geol. Surv. Can. Open File* **2166**.

VILKS, P., CRAMER, J.J., BACHINSKI, D.B., DOERN, D.C. and MILLER, H.G. 1993. Studies of colloids and suspended particles, Cigar Lake uranium deposit, Saskatchewan, Canada. *Appl. Geochem.*, **8**, 605-616.

WILSON M.R., KYSER T.K., MEHNERT H.H. and HOEVE J. 1987. Changes in the H-O-Ar isotopic composition of clays during retrograde alteration. *Geochim. Cosmochim. Acta* **51**, 869-878.

3.5.4 Groundwater evolution and redox geochemistry
(J. Cramer and W. Nesbitt)

3.5.4.1 Introduction

Understanding the evolution of water compositions, from precipitation (rain and snow) to ore zone waters, is very important with regard to modelling the long-term stability of the uranium mineralization in the Cigar Lake deposit. Precipitation and surface waters (lakes and streams) provide the recharge to the local aquifer in the overburden, where these oxidizing waters evolve through interaction with the mineralogy of the glacial deposits. Subsequent recharge from the local aquifer to the intermediate, followed by the semi-regional aquifer, would again modify the compositions of these waters through water-rock interaction. Finally, the groundwater composition is affected by interaction with the minerals in the halo of hydrothermally altered host rocks surrounding the ore, before coming in contact with the uranium mineralization.

Reactions affecting waters of the local, intermediate and semi-regional flow regimes are similar, involving primarily the Al-silicates, kaolinite and illite, which are common to the rocks and sediments in all three regimes. The dissolution of kaolinite and illite, and the conversion of illite to kaolinite yields very dilute groundwaters of near neutral pH, with SiO_2(aq) more abundant than most cations. The waters also precipitate Fe-oxyhydroxides as they leave the local flow regime to recharge deeper regimes. Waters that enter altered and bleached sandstones may undergo additional reduction through dissolution of Fe-sulphides and carbonates. The iron sulphides, pyrite and marcasite (Bruneton 1987) within the hydrothermally altered sandstones and ore zone affect the oxidation potentials of associated solutions. In fact, these sulphides play a very important role in providing the redox buffering capacity to maintain the strongly reducing conditions prevailing in the ore zone.

This section summarizes the conceptual model for evolution of groundwater compositions through analysis of the water-rock interaction processes for each regime, including the redox geochemistry. The numerical modelling of these processes is not included and will be dealt with in a seperate paper.

3.5.4.2 Overburden waters

3.5.4.2.1 Local equilibrium model

The interpretation is based on the classical studies of Bricker and Garrels (1967), Garrels and Mackenzie (1967), Garrels (1967) and Helgeson et al. (1969). The arguments that follow are based on local equilibrium concepts as presented by Helgeson (1968) and Helgeson et al. (1970).

Rainwaters plot in the gibbsite field (Figure 3.75), but they contain little or no Al(aq), and hence are undersaturated in the gibbsite phase. The waters are acidified by passage through the organic zone of the soils. The initial downward evolutionary trend (Figure 3.75, segment A-B) reflects acidification of rainwater. Upon entering the mineral zones (below the organic zone), all silicates dissolve, including quartz, feldspars, kaolinite and illite. As a

result, SiO_2(aq) increases in solution, H^+ is consumed and cations are released to solution. The evolutionary trend is shown on Figure 3.75 (segment B-C). These reactions proceed until gibbsite (crystalline or amorphous) saturation is achieved or exceeded, resulting in precipitation. There is an inflection point in the evolutionary path where gibbsite begins to precipitate (Figure 3.75, point C). However, saturation with respect to gibbsite may not occur, depending on the initial solution composition and relative rates of dissolution of the various solid phases. The subsequent path (Figure 3.75, segment C-D) represents the evolution of the water as the Al-silicates dissolve and a gibbsitic phase precipitates. These reactions continue until the gibbsite-kaolinite boundary is encountered (Figure 3.75, point D). Aqueous silica values greater than that indicated by point D result in stability of kaolinite relative to gibbsite, and continued dissolution of Al-silicates (excluding kaolinite) results in formation of kaolin (or amorphous Al-Silicate resembling kaolin, Paces (1973)) rather than gibbsite (Helgeson et al. 1970). The evolutionary path during this phase is illustrated on Figure 3.75 (segment D-E). At point E (Figure 3.75) the waters are equilibrated with respect to kaolinite and illite, hence the solution is saturated in both phases and they cease to dissolve. Since these are comparatively abundant Al-silicates in the overburden sands, and are also reactive, their dissolution probably has contributed substantially to dissolved aqueous silica and consumption of H^+. The solutions, however, remain undersaturated with respect to the feldspars. Where feldspars are absent, reactions cease and the waters remain, at point E (Figure 3.75), equilibrated with respect to illite and kaolinite, supersaturated with respect to quartz and undersaturated with respect to the feldspars. Where feldspars are present and are contacted by solution, they will dissolve, releasing SiO_2(aq) and alkalis to solution and consuming H^+(aq). The solution then tends to evolve through the illite field towards the feldspar illite-feldspar boundary (Figure 3.75, dashed segment E-F).

There is, however, another reaction that affects the reaction path of the solutions. It is the conversion of kaolinite to illite and results from continued consumption of H^+ and release of K^+ to solution during feldspar dissolution. Where clay minerals react rapidly with solution, the solution composition remains on, and evolves along, the solution-illite-kaolinite boundary as long as kaolinite is present to react with solution (Figure 3.75, segment E-G or E-H). (The segment followed by the waters depends upon other phases formed, particularly the smectite phases that consume large amounts of SiO_2 during their formation, Helgeson et al. 1970.) Segments E-G or E-H are more likely to be followed than the dotted segment E-F for reasons related to mass balances. Kaolinite probably is much more abundant in the overburden sands than feldspars, hence feldspars will be consumed before all kaolinite is converted to illite; consequently the solution evolves along the solution-illite-kaolinite boundary while feldspar is consumed.

Application of local equilibrium concepts provides a reasonable working hypothesis for the genesis and evolution of the major alkali, alkaline earth, aqueous Al and SiO_2 of the overburden waters.

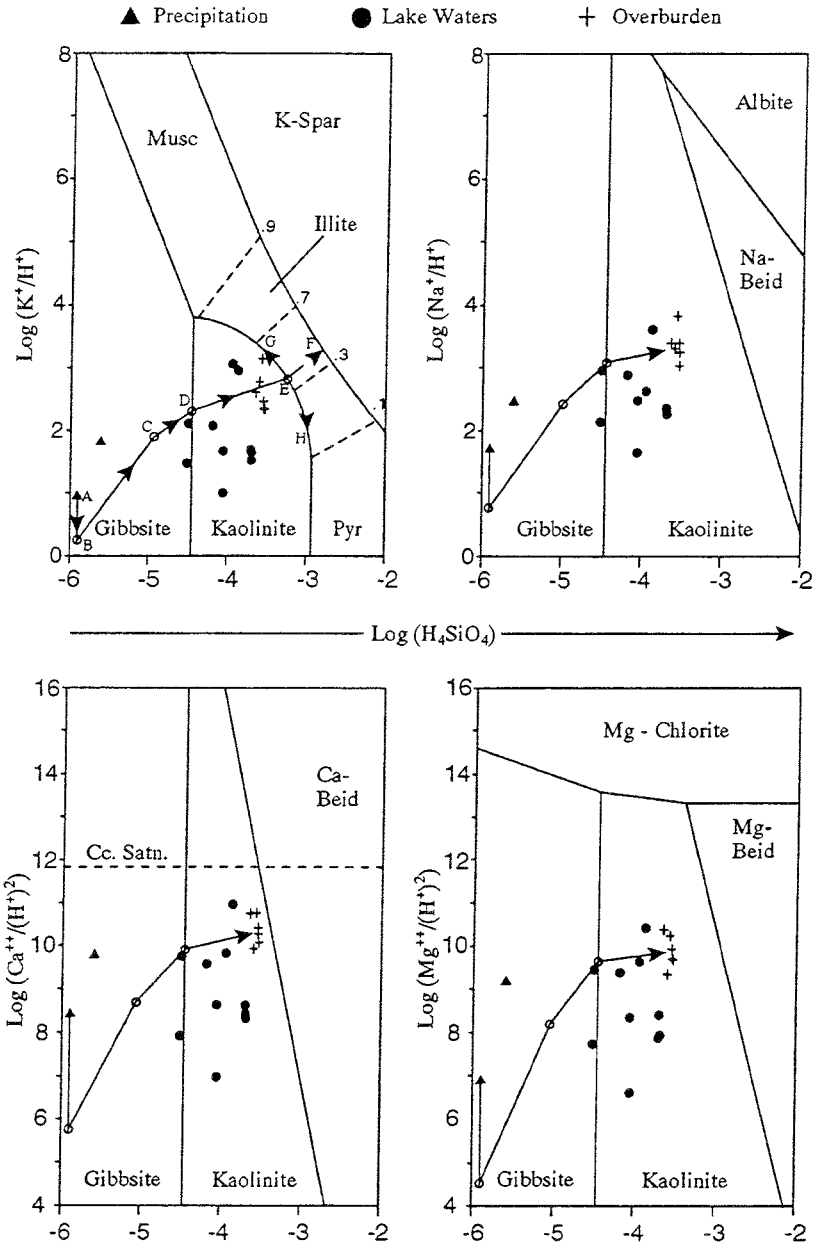

FIGURE 3.75 Activity-activity diagrams for the systems Na-, K-, Ca- and Mg-Al-Si-O-H systems. Precipitation (triangles) overburden waters (crosses) and surface waters (dots) are plotted on the diagrams. The labelled trends emanating from precipitation (triangle) traces the evolutionary path of overburden waters as precipitation first enters the organic zone and dissolves inorganic and organic acids (segment A-B), then the mineral zones of soils and the sandy overburden beneath the soils. Reactions driving the solution composition from point B to point E is dissolution of kaolinite and illite primarily, but possibly feldspars and quartz. Thermodynamic data are taken from Helgeson (1969), Helgeson et al. (1978) and Nesbitt (1977).

3.5.4.2.2 Oxidation and reduction in the overburden

The overburden sands are stained a rusty colour within a few metres of the till contact, and typically, staining occurs at and below the water table. Presumably Fe of the secondary Fe-oxyhydroxides is derived from the overburden sands and transported by overburden waters to the site of deposition. Some Fe may be derived from the underlying till, although its low permeability does not permit significant transport by mass flow.

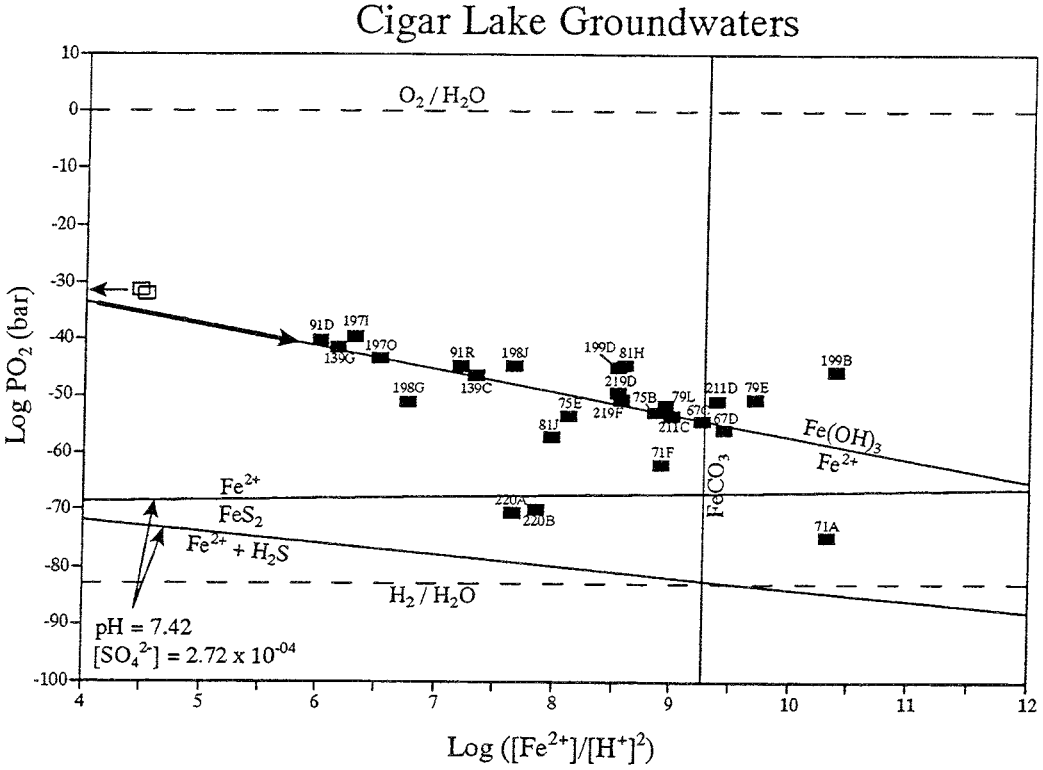

FIGURE 3.76 Diagram illustrating the redox relations among waters of the overburden (open rectangles) and formation waters (solid rectangles). The diagram is constructed for 25 °C, 1 bar total pressure and H_2O activity of 1.0.

Diffusion may be operative. The overburden groundwaters carry 0.04 to 0.6 mg/L of total dissolved Fe ($Fe_T(aq)$). In Figure 3.76, the waters are plotted on an Fe-activity-Log[$P(O_2)$] diagram (open rectangles), along with groundwaters from the sandstones (solid rectangles) and saturation boundaries for $Fe(OH)_3$, $FeCO_3$ and FeS_2. Most formation waters plot near the solution-$Fe(OH)_3$ saturation boundary, indicating that an Fe-oxyhydroxide controls Fe(aq) and is the major control of redox potentials in the subsurface. By contrast, the overburden waters plot well above the boundary; hence the waters are supersaturated with respect to the same phase that controls redox conditions in the formation waters. The relationship is surprising in that most water compositions from the overburden and Upper and Lower Sandstones are similar in other respects. Explanations include error in analyses of Fe and/or Eh. Alternatively, supersaturation may be apparent rather than real, due to formation of Fe-complexes that have not been considered in speciation calculation. Also,

Fe-oxyhydroxides forming in the overburden may be different from those of the other regimes. The first explanation (error in analyses) is unlikely in that all waters were analyzed using the same techniques. The second explanation is a possiblility. Formation of complexes not yet considered, such as organic complexes of Fe, may result in apparent saturation, as argued for Al systematics. The last possiblity can be resolved only by conducting detailed studies of the oxyhydroxides from the various flow regimes.

Regardless of the reasons for (apparent) supersaturation in Fe-oxyhydroxides, there is no doubt that these form within the overburden, as proved by the rusty stain. Undoubtedly, Fe(III)-oxyhydroxides have precipitated from solution since deposition of the glacio-fluvial debris. The overburden waters (Figure 3.76), upon precipitation of Fe(III)-oxyhydroxides, must evolve to lower $\log[p(O_2)]$ values as Fe(t) decreases (i.e., Fe(II)aq/Fe(III)aq increases):

$$Fe^{2+} + 2\frac{1}{2}H_2O + \frac{1}{4}O_2 = Fe(OH)_3 + 2H^+.$$

Kaolinite and illite control pH values at equilibrium, thus the waters are effectively buffered with respect to pH. Formation of $Fe(OH)_3$ therefore results in decrease in Fe^{2+}, hence decrease in $\log[Fe^{2+}/(H^+)^2]$ and decrease in $\log[P(O_2)]$. Typical evolutionary paths are illustrated by the solid arrows on Figure 3.76. The overburden waters are oxidizing (high $\log[p(O_2)]$ values) relative to most formation waters from the lower flow regimes. Upon precipitation the waters evolve towards the saturation boundary of $Fe(OH)_3$ and towards the compositions of the formation waters.

3.5.4.3 Intermediate and semi-regional flow regimes

3.5.4.3.1 Major solutes and isotopes

The major-element compositions of formation waters from the Upper and Lower Sandstones are, in most respects, strikingly similar to the overburden waters. The similarity suggests that waters from the local, intermediate and semi-regional flow regimes have undergone many of the same solution-mineral interactions. As a result, discussion of waters from the deeper regimes is brief. Redox reactions, however, are for some formation waters different in the overburden waters.

Goundwaters from stations 75 and 139 are very dilute, with $SiO_2(aq)$ an abundant constituent of both waters (Table 3.30). The range of chloride concentrations is similar at both stations (Table 3.30) and similar to overburden waters and precipitation waters collected at Cigar Lake. The concentrations of major cations and anions are likewise similar. Hydrogen and oxygen stable isotopic data for stations 139 and 75 and overburden waters are effectively the same as local precipitation (Table 3.30), suggesting that H_2O molecules of all regimes have a common origin. Tritium values for precipitation and station 75 are the same, indicating that source and residence times are similar, but tritium for 139 is lower. Although some young waters (<50 a) mix with the waters from station 139, it is predominantly old water, hence the residence time of waters in the semi-regional flow regime is greater than for local or intermediate regimes (see hydrogeology section). Similar Cl-contents of groundwaters (stations 139 and 75, Table 3.30) and precipitation, the stable

isotope and tritium data, all indicate that the formation waters are derived ultimately from precipitation; their solute contents are determined largely by reaction with the enclosing sediments and sedimentary rocks.

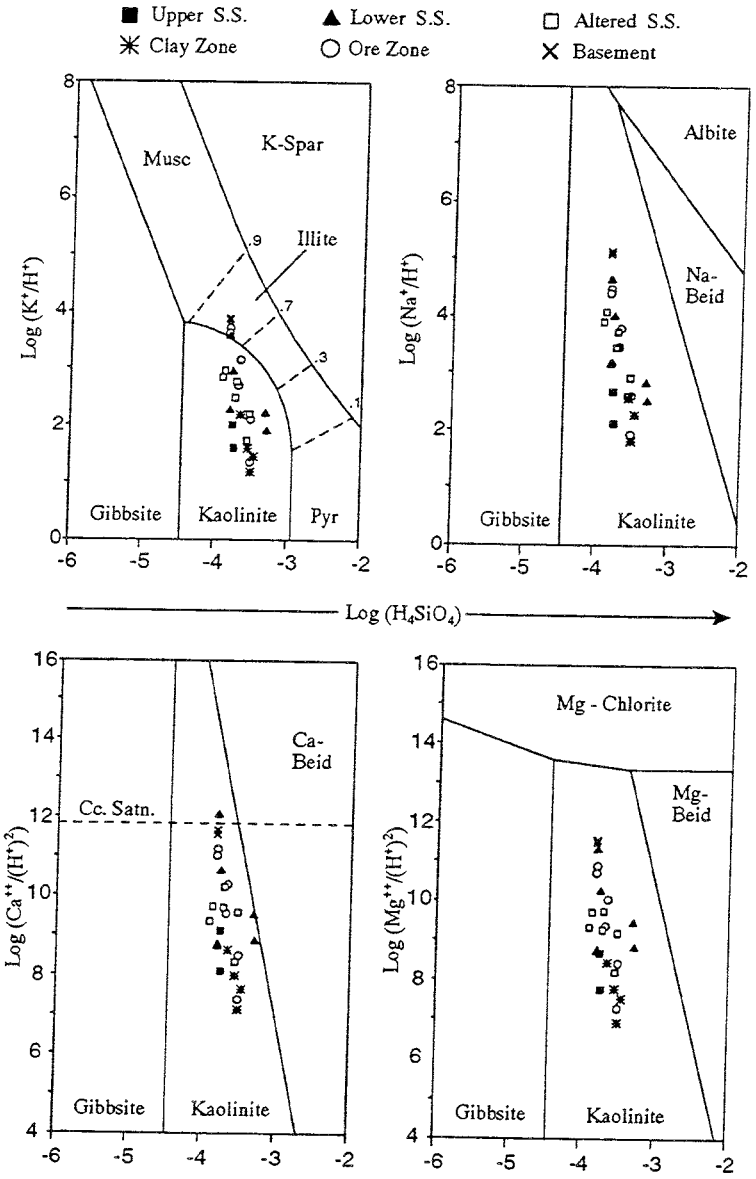

FIGURE 3.77 Activity-activity diagrams for the Na-, K-, Ca- and Mg-Al-Si-O-H systems with all formation waters plotted. Overburden waters, surface waters and precipitation are excluded.

3.5.4.3.2 Reaction with silicates

Thermodynamic properties of groundwaters are assessed using the computer program SOLMIN88, WATEQF and SPECIATE. The ionic strength of waters from 139 and 75 (Table 3.30) is less than 0.001, hence activity coefficients for most species are close to

unity. Major cations, Na, K, Mg and Ca, and detected trace metals (Ba, Sr, Mn and Zn), are largely uncomplexed; uranium is an exception. Measured Eh and pH values, applied to the iron system, indicate that dissolved Fe is in the ferrous state, predominantly (Fe^{2+}aq).

The abundance of aqueous silica in solutions from stations 139 and 75, combined with low concentrations of Na, K, Mg and Ca suggest that silicates containing only low concentrations of alkalis and alkaline earths have reacted with the groundwaters. Quartz and its polytypes, and kaolinite and illite are likely candidates in that they are low in alkalis and alkaline earths. They are also common minerals of the Manitou Falls Formation (Percival 1989; Smellie et al. 1991). The formation waters plot near or on the kaolinite-illite boundary and close to the kaolinite-beidellite boundaries (Figure 3.77), just as do the overburden waters. As argued for the overburden waters, illite and kaolinite are the most likely phases to control water compositons because, relative to other Al-silicates, they are abundant and they react with the formation waters as indicated by the activity-activity diagrams. Some waters may also have reacted with a smectitic phase. Furthermore, and as for the overburden waters, much of the SiO_2(aq) may be drived by conversion of illite to kaolinite as discussed below. Feldspars are absent from, or very scarce in, the standstones; consequently they cannot affect these formation water compositions significantly. In fact, there is generally little evidence for appreciable dissolution of minerals other than kaolinite and illite.

Groundwater 139 is close to saturation with respect to chalcedony and cristobalite: it is supersaturated in quartz and undersaturated with respect to amorphous SiO_2. Although chalcedony and cristobalite have not been observed in the formation, they may be present in small amounts as cement of the sandstone. If so, the groundwaters may dissolve one or both of these phases until saturation is achieved. Quartz is not a significant source of SiO_2(aq) because it can contribute at most 6 mg/L SiO_2(aq) (saturation value). Clay minerals are a possible source of SiO_2(aq). Illite and kaolinite are the dominant phases of the unmineralized sandstone at stations 75 and 139 (Percival, 1989; Smellie et al., 1991; Hoeve et al., 1981). If kaolinite is the source, a secondary aluminous phase must be produced at the expense of kaolinite because the waters, although high in SiO_2(aq), contain low total dissloved Al (Table 3.30). Gibbsite forms at the expense of kaolinite in many sedimentary environments, but neither mineral has been reported from the Manitou Falls Formation. Electron microprobe analyses of illite (Smellie, et al., 1991) indicates that stoichiometric (congruent) dissolution of illite produces approximately 30 mg/L SiO_2 (observed value in 139G, Table 3.30), 10-15 mg/L Al(aq) and 5-7 mg/L of K^+(aq). There is, however, little dissolved K or Al in solution (Table 3.30); kaolinite may be a "sink" for Al(aq). Three petrographic observations support the suggestion. Sibbald et al. (1990) observe that the clay mineral stratigraphy of the basin is transected by kaolinitized zones, which are localized about faults and fractures that intersect all formations and the surface. Kaolinization is intensive adjacent to these faults and leads to complete destruction of the original assemblages, which include illite and chlorite. They also note that similar late kaolinization occurs in other sedimentary basins where it is interpreted to be the result of acidic surface waters percolating down the faults and reacting with adjacent rocks. On a regional scale Hoeve et al. (1981) note that, in the lower unit of the Manitou Falls Formation, the clay mineral assemblage is dominated by kaolinite, whereas in the upper unit of the same

formation illite predominates. The lower unit is 10^2-10^3 more permeable than the upper unit, and the change in proportions may be a result of much greater volumes of dilute, acidic solutions migrating through the lower unit. There is evidence that the same reaction occurs in the upper unit. The most recent reaction (i.e., last retrograde reaction) observed in the upper Manitou Falls sandstone is formation of kaolinite after illite (Sibbald et al. 1990). The observations demonstrate that kaolinite has formed after illite in the Manitou Falls Formation, and in highly permeable fault zones cutting all formations. The reaction probably proceeds today (Kotzer and Kyser 1991), driven by disequilibrium between the solids of the sandstones and the acidic, near-surface waters introduced to the subsurface.

Dissolved potassium (6.5 mg/L) is sufficiently low that K released from illite during dissolution may be exchanged onto other clay minerals (illite or kaolinite) or incorportated into the 12-fold lattice site of these potassium-deficient illites. Identification of the "sink" for K^+ awaits study of the cation exchange properties of the clay minerals and detailed compositional studies of the illite, particularly documentation of the K contents of 12-fold coordination sites of illites. Groundwaters 139 and 75 are significantly undersaturated in all other minerals excluding quartz, chalcedony and cristobalite. Al(aq) was below detection limits; consequently saturation indicies of Al-silicates were not tested.

Cation exchange and sorption reactions are rapid (Helfferich 1962), and as is evident from procedures to determine soil exchange capacities, exchange equilibrium is rapidly achieved. Small quantities of clay minerals are present in the Manitou Falls Formation and undoubtedly exchange of cations occurs among the various clays and formation waters. Although the quantity of clay minerals and their exchange capacities are small, these waters are so dilute that exchange may affect the proportions of cations.

All formation waters from the intermediate and semi-regional flow regimes have been plotted on activity-activity diagrams (Figure 3.77). The waters are near the kaolinite-illite boundary and within the kaolinite field close to, and parallel to, the kaolinite-beidellite field boundaries; they are strikingly similar to the characteristics of the overburden waters. The silica contents of the overburden waters are similar to waters from station 75 and 139. If, as indicated by the stable- and radioisotopes, these waters are derived from surface, much of the reaction may have occurred very near the surface, and possibly in the overburden. In fact, if the local flow regime feeds the intermediate and semi-regional regimes, and waters of the local flow regimes are similar to the overburden waters (Table 3.30), little reaction occurs in the two deeper regimes. Whether or not the overburden waters recharge the lower regimes, the genesis/evolution of waters from the intermediate and semi-regional flow regimes are similar to that of overburden waters. The overburden and formation waters, however, are somewhat different with respect to redox characteristics.

3.5.4.4 Redox geochemistry

3.5.4.4.1 Redox reactions during evolution of waters

Observations, hydrologic data and groundwater isotopic and major-element compositions indicate that the intermediate and semi-regional flow regimes are recharged at surface by

dilute meteoric waters, perhaps similar to the present-day overburden waters. Overburden waters have high oxidation potentials compared with the oxidation potential of the Fe^{2+}-$Fe(OH)_3$ couple that controls redox conditions in the unaltered and bleached sandstones. The overburden waters, as they recharge the lower regimes, must precipitate $Fe(OH)_3$ to achieve saturation as observed in waters from the sandstones. Precipitation decreases $\log[p(O_2)]$ and $Fe_T(aq)$; Fe^{2+}/Fe^{3+} increases sympathetically in solution. The evolutionary trends shown on Figure 3.78 (arrows) illustrate, qualitatively, the changes that occur as the overburden waters enter the intermediate and semi-regional flow regimes. Once saturation is achieved with respect to $Fe(OH)_3$, oxidation potentials are maintained and controlled by the Fe^{2+}-$Fe(OH)_3$ redox couple.

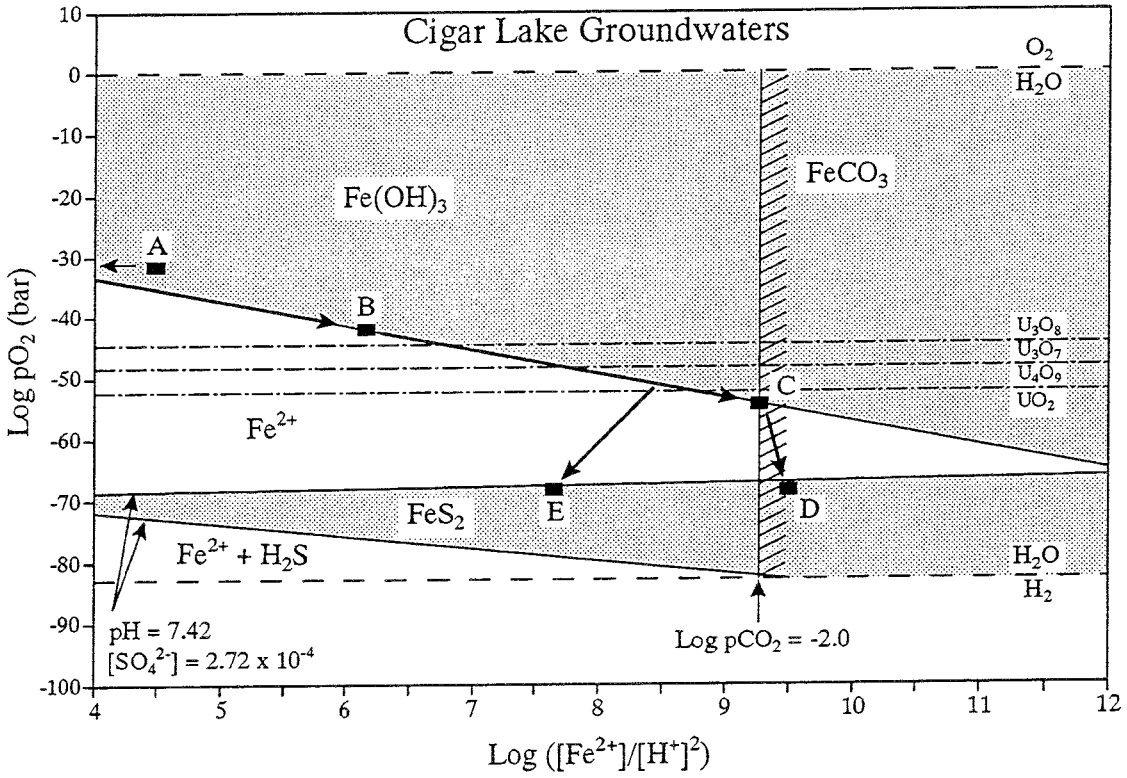

FIGURE 3.78 Redox diagram for water-rock interaction in the Cigar Lake deposit. Groundwater compositions evolve from A (overburden) to B (unaltered sandstone and limonite zone), to C (altered sandstone), to D/E (clay and ore zones). Semi-dashed lines represent stability boundaries for various solid uranium oxides. See text for further explanation.

The concentration of total dissolved Fe was included in the modelling (SOLMIN88, SPECIATE), along with measured Eh and pH values (Table 3.30). Groundwaters 75 and 139 are undersaturated in siderite but close to saturation with respect to $Fe(OH)_3$ (Figure 3.76). $Fe^{2+}(aq)$ is calculated to be the dominant aqueous species. Although errors associated with measuring total dissolved Fe, Eh and pH of the waters are potentially large, the results shown in Figure 3.77 suggest that the data are reliable and imply that the measured Eh value reflects the equilibrium oxidation potential of the Fe^{2+}-$Fe(OH)_3$ redox

couple. This redox couple controls the oxidation potential of waters from stations 75 and 139 (Figure 3.76 and point B in Figure 3.78). Furthermore, most of the formation waters plot on or close to the $Fe(OH)_3$ saturation boundary; apparently the same reaction controls the oxidation potential of the majority of waters.

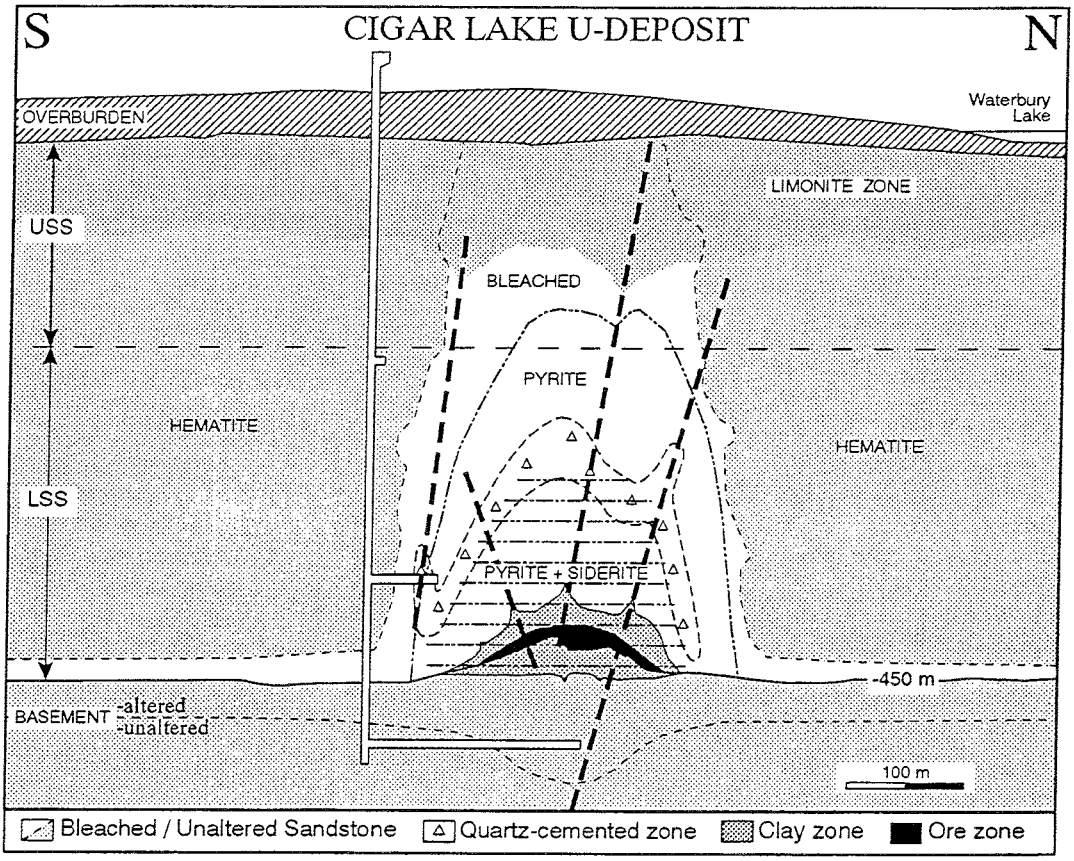

FIGURE 3.79 Schematic cross section through the Cigar Lake deposit showing the uranium mineralization and its host rocks, including the lithologic characteristics related to hydrothermal alteration and weathering. (USS= upper sandstone; LSS= lower sandstone).

As the waters from up-gradient of the deposit enter the halo of hydrothermally altered rock surrounding the deposit, they encounter little or no ferric mineral phases in the bleached rocks, but rather increasing amounts of pyrite/marcasite (Figure 3.79). The corresponding change in composition of these waters is shown by the arrow from point B to C in Figure 3.78. Whereas the waters up-gradient were in equilibrium with hematite (139) or limonite/ferrihydrite (75), they become increasingly more undersaturated with respect to ferrihydrite as they penetrate further into the bleached halo. Similarly, the waters are undersaturated with respect to pyrite/marcasite when they first enter the bleached halo. Consequently, dissolution of both ferrihydrite and pyrite will change the water composition towards lower $\log[p(O_2)]$ and higher $\log[Fe^{2+}/(H^+)^2]$ values, as illustrated in Figure 3.80. If at some point along the flowpath inside the bleached halo ferrihydrite is no longer available for dissolution, the dissolution of pyrite only will change the water composition

away from the $Fe(OH)_3$ stability line towards the pyrite field (arrow towards point E, Figure 3.78).

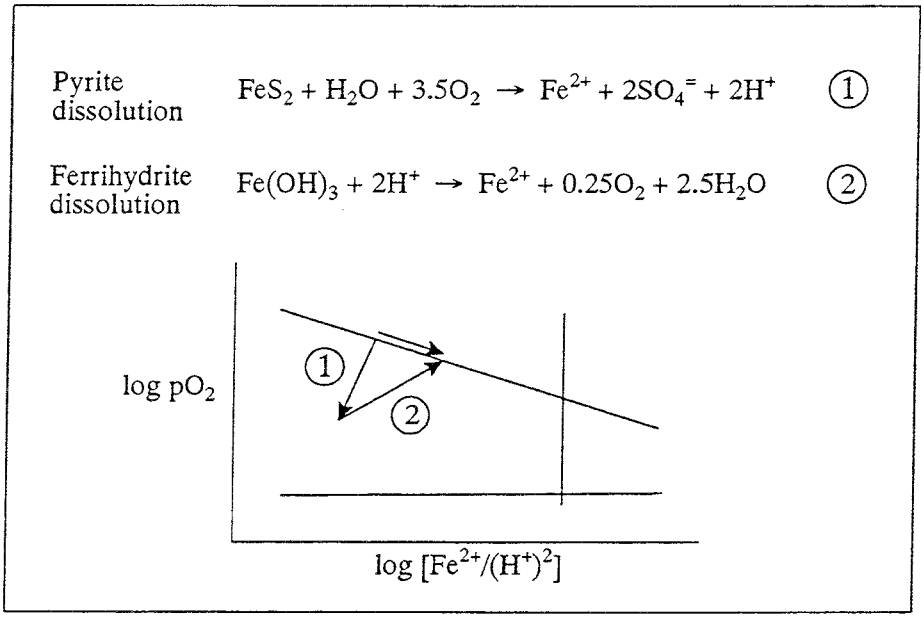

FIGURE 3.80 Diagram illustrating schematically the change in composition of groundwaters entering the bleached halo of the Cigar Lake deposit. The result of dissolution of both ferrihydrite and pyrite is a successive change in water compositions from point B to C in Figure 3.78.

Some waters that plot at high $\log[Fe^{2+}/(H^+)^2]$ values are saturated with respect to siderite. The vertical boundary (Figure 3.78) represents siderite saturation for average CO_2 partial pressure of the formation waters. The boundary shifts to higher $\log[Fe^{2+}/(H^+)^2]$ values where CO_2 is lower than the average, and to higher $\log[Fe^{2+}/(H^+)^2]$ values where CO_2 is greater than average value. Siderite, although not found in the unaltered sandstone is present locally in the bleached sandstones, particularly in the Lower Sandstone near the ore deposit. When siderite is encountered, dissolution of the carbonate increases $\log[Fe^{2+}/(H^+)^2]$ (pH is buffered as discussed previously), and $FeCO_3$ saturation may occur where siderite is dissolved in quantity. Carbonate dissolution affects the Fe^{2+}-$Fe(OH)_3$ redox couple by increasing $\log[Fe^{2+}/(H^+)^2]$, resulting in precipitation of $Fe(OH)_3$ and reduction in the partial pressure of oxygen (lower oxidation potentials). Although these reactions may occur wherever siderite is present, they may be particularly important in and around the clay envelope, where siderite is reported to be locally abundant.

However, when the water has penetrated into the clay-rich halo where siderite and pyrite are encountered, but ferrihydrite is no longer available for dissolution, the water composition will change away from the $Fe(OH)_3$ stability line towards the pyrite field. This is illustrated in Figure 3.81.

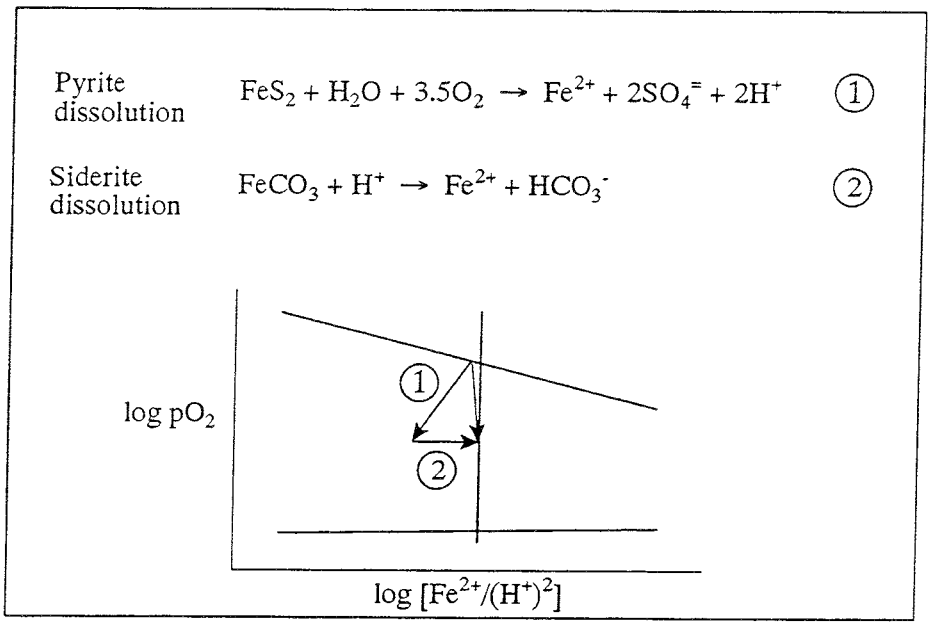

FIGURE 3.81 Diagram illustrating schematically the change in composition of groundwaters penetrating the clay-rich halo of the Cigar Lake deposit. The result of dissolution of both pyrite and siderite is a successive change in water compositions from point C to D in Figure 3.78.

Waters from stations 220 and 71 plot below the Fe^{2+}-$Fe(OH)_3$ boundary (Figure 3.76), indicating that other reactions affect the oxidation potential of these waters. Where waters from the unaltered or bleached sandstones enter the ore zone, they will be reduced by reaction with sulphides. The reaction, however, results from oxidation/reduction of sulphur in the solids and solution. Dissolution of pyrite, for example, consumes oxygen to produce SO_4(aq) at the expense of S, nominally in the -1 state. The waters from station 220 plot very close to the Fe^{2+}-FeS_2 boundary. This sample is from the ore zone, which contains significant amounts of sulphide minerals but contains no Fe-oxyhydroxides. The groundwater and mineralogy of the ore zone are entirely compatible in that they indicate sulphide mineral control of oxidation potentials. The buffering effect of this sulphide control on any influx of oxidizing water is illustrated in Figure 3.82A. Depending on the value for the CO_2 partial pressure, Fe^{2+}(aq) from the dissolution of pyrite may result in the precipitation of siderite in the ore zone, as illustrated in Figure 3.82B. In both cases the redox-buffering capacity of the sulphides in the ore zone is extremely important, because the log[p(O_2)] will be maintained at low values by the sulphide dissolution/oxidation as long as sulphide minerals are available to react.

Station 71 is within the bleached, hydrothermally altered Lower Sandstone. These rocks contain Fe-sulphides such as marcasite and/or pyrite. Their dissolution results in oxidation of the sulphide to SO_4 by the comparatively oxidizing solutions. During reaction the oxidation potentials of the waters are reduced (compare waters 75B, 139C and 71F and 71A, Figure 3.76) and sulphate is accumulated in solution. Some waters are reduced sufficiently

to become saturated in pyrite (Figure 3.76, stations 220 and 71). The pyrite boundary has been constructed using typical pH and SO_4 values, and additional detailed study of waters from station 71 are required before conclusions are drawn. The waters of Station 71, however, demonstrate that the minor amounts of sulphides, where present in the altered and bleached sandstones, may have a major effect on the geochemistry of the solutions, particularly transition metal geochemistry.

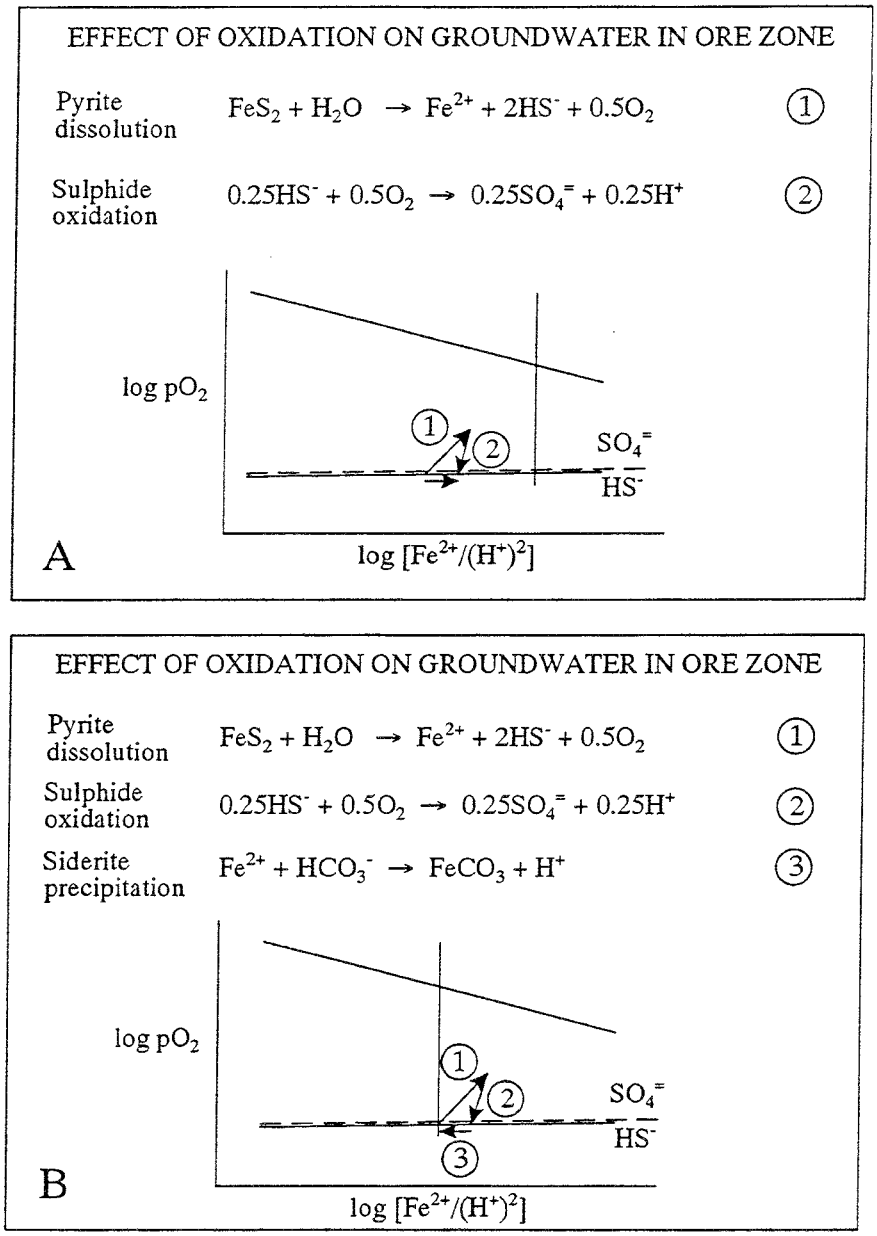

FIGURE 3.82 Diagram illustrating schematically the redox buffering by sulphide dissolution/oxidation in the ore zone of the Cigar Lake deposit. **A**: The result of pyrite dissolution and subsequent oxidation of dissolved sulphide buffers the log[p(O_2)] at the low values of pyrite stability. **B**: Same as in A but with pCO_2 values sufficiently high to also form siderite.

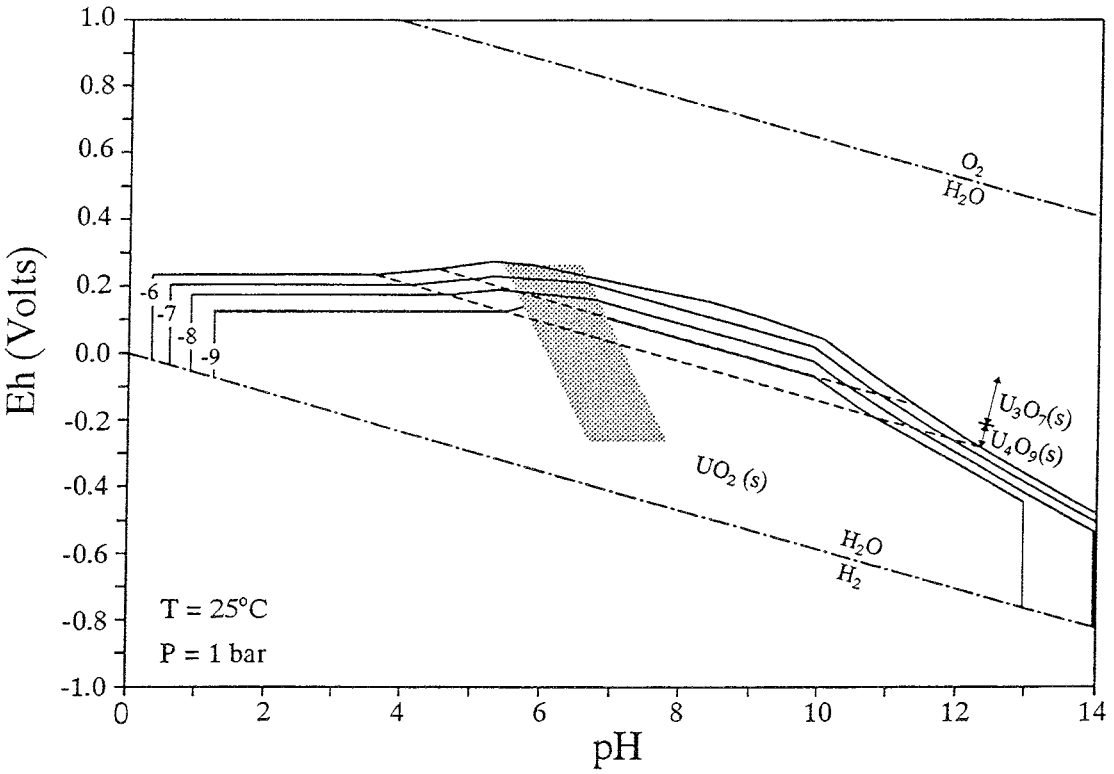

FIGURE 3.83 Isosolubility diagram for uranium oxides in Cigar Lake groundwaters. The dotted area includes all the data points for groundwaters from the ore and clay zones. The contours -6 to -9 represent dissolved-uranium concentrations from 10^{-6} to 10^{-9} mol/L U.

3.5.4.4.2 Uranium dissolution

The stability fields for UO_2, U_4O_9, U_3O_7 and U_3O_8 in the groundwaters with respect to the log[$p(O_2)$] are shown in Figure 3.78. On the basis of the measured values for pH, Eh and Fe^{2+}(aq) in the waters, the majority of groundwaters from inside the bleached halo of the deposit plot below the U_3O_7-U_3O_8 stability boundary. These latter waters have corresponding total-uranium contents ranging from 10^{-7} to 10^{-9} mol/L, in good agreement with the thermodynamic data for the solubilities of UO_2 to U_3O_7 under those conditions. Plotting the compositions of all ore- and clay-zone waters on a regular Eh-pH diagram (Figure 3.83) shows similar agreement between the measured total-uranium contents of the waters, their location in the deposit and the uranium solubility data.

Reducing conditions, as indicated by the low concentrations of dissolved uranium in the waters, are further supported by the U-series equilibrium data for the rocks and minerals in contact with these waters. The activity ratios for $^{234}U/^{238}U$ and $^{230}Th/^{234}U$ of the ore and rock samples show equilibrium values (0.95-1.00 $\pm$0.05 and 0.95-1.05 $\pm$0.05, respectively) for samples from within the bleached sandstone halo (Section 3.2.2). The elevated $^{234}U/^{238}U$ ratios in the corresponding groundwaters (Table 3.32) are then explained by α-recoil of ^{234}U from the solid into the aqueous phase rather than by bulk dissolution of uranium from the rocks.

The measured redox conditions, uranium contents and general composition for the groundwaters from the deposit support the results from the characterization of the uranium ore minerals as obtained by XPS, SEM and XRD (see Section 3.3). This characterization has found no evidence for U_3O_8 or other higher U-oxide phases, nor have any been reported by others (e.g., Bruneton 1987; Percival 1989). Thus, the dissolution, and therefore the stability, of UO_2 appears to be controlled by a thin surface layer of higher oxides (up to U_3O_7). This is supported by **a**) experimental work (e.g., Shoesmith et al. 1984; Garisto and Garisto 1986) showing that the dissolution rate of UO_2 does not become significant until it is oxidized beyond the $UO_{2.33}$ (U_3O_7) stage, and by **b**) the predictive calculations (using measured groundwater compositions) of the uranium phases at equilibrium, which mostly give U_3O_7 with some overlap to U_4O_9 (see also Section 3.9.3).

3.5.4.5 Conclusions

The composition of surface and groundwaters at Cigar Lake evolve through interaction with the reactive mineral phases in the various lithologies of the deposit and its host rocks. A conceptual model for both groundwater evolution and redox geochemistry has been presented here. The conclusions from this study include the following:

- interactions with clay minerals control the bulk composition of groundwater in all litholgies;

- waters recharging the intermediate and semi-regional flow regimes from the local regime in the overburden have already equilibrated with the same clay minerals (illite and kaolinite) as are found in the sandstones of the lower regimes;

- the extent of illite-to-kaolinite conversion throughout the deposit is a good indicator for advective mass transport caused by bulk groundwater movement;

- the absence of significant kaolinite in the ore zone supports measured values of low hydraulic conductivity for this zone, and suggests that mass transport in the ore zone is controlled by diffusion;

- the redox geochemistry in the deposit is strongly controlled and buffered by the iron and sulphur redox couples; and

- the measured redox conditions and uranium geochemistry are in good agreement with accepted uranium thermodynamic data and observed uranium mineralogy.

3.5.4.6 References

BRICKER, O.P., and GARRELS, R.M. 1967. Mineralogical factors in natural water equilibria. In *Principles and Applications of Water Chemistry* (ed. S.D. Faust and J.V. Hunter). Wiley & Sons, New York, 449-469.

BRUNETON P. 1987. Geology of the Cigar Lake uranium deposit (Saskatchewan, Canada). In *Economic Minerals of Saskatchewan* (ed. C.F. GILBOY and L.W. VIGRASS). Sask. Geol. Soc. Spec. Publ., **8**, 99-119.

GARISTO, N.C. and GARISTO, F. 1986. The dissolution of UO_2: a thermodynamic approach. Nucl. Chem. Waste Manag., **6**, 203-211.

GARRELS, R.M. 1967. Genesis of some ground waters from igneous rocks. In *Researches in Geochemistry, II* (ed. P.H. Abelson). Wiley & Sons, New York, 405-420.

GARRELS, R.M., and MACKENZIE, F.T. 1967. Origin of the chemical compositions of some springs and lakes. In *Equilibrium Concepts in Natural Water Systems* (ed. R.G. Gould). Adv. Chem. Series, **67**. Amer. Chem. Soc., 222-242.

HELFFERICH, F. 1962. Ion Exchange. McGraw-Hill Book Co., New York.

HELGESON, H.C. 1968. Evaluation of irreversible reactions in geochemical processes involving minerals and aqueous solutions: I. Geochim. Cosmochim. Acta, **32**, 853-877.

HELGESON, H.C. 1969. Thermodynamics of hydrothermal systems at elevated temperatures and pressures. Amer. Jour. Sci., **267**, 729-804.

HELGESON, H.C., GARRELS, R.M., and MACKENZIE, F.T. 1969. Evaluation of irreversible reactions in geochemical processes involving minerals and aqueous solutoins: II. Geochim. Cosmochim. Acta, **33**, 455-481.

HELGESON, H.C., BROWN, T.H., NIGRINI, A., and JONES, T.A. 1970. Calculation of mass transfer in geochemical processes involving aqueous solutions. Geochim. Cosmochim. Acta, **34**, 569-592

HELGESON, H.C., DELANEY, J.M., NESBITT, H.W., and BIRD, D.K. 1978. Summary and critique of the thermodynamic properties of rock-forming minerals. Amer. Jour. Sci., **278-A**, 229p.

HOEVE, J., RAWSTHORNE, K. and QUIRT, D. 1981. Uranium metallogenic studies: clay mineral stratigraphy and diagenesis in the Athabasca Group. In *Summary of Investigations 1981* Saskatchewan Geol. Survey, Misc. Rep. **81-4**, 76-89.

KOTZER, T. and KYSER, T.K. 1991. Retrograde alteration of clay minerals in uranium deposits: radiation catalyzed or simply low-temperature exchange? Chem. Geol., **86**, 307-321.

NESBITT, H.W. 1977. Estimation of the thermodynamic properties of Na- Ca- and Mg-beidellites. Canadian Mineral., **15**, 22-30.

PACES, T. 1973. Steady-state kinetics and equilibrium between groundwater and granitic rock. Geochim. Cosmochim. Acta, **37**, 2641-2664.

PERCIVAL, J.B. 1989. Clay mineralogy, geochemistry and partitioning of uranium within the alteration halo of the Cigar Lake uranium deposit, Saskatchewan, Canada. Carleton Univ., Ottawa, PhD-Thesis, 343p.

SHOESMITH, D.W., SUNDER, S., BAILEY, M.G., WALLACE, G.J. and STANCHELL, F.W. 1984. Anodic oxidation of UO_2 Part IV: X-ray photelectron spectroscopic and electrochemical studies of film growth in carbonate-containing conditions. Appl. Surf. Sci., **20**, 39-57.

SIBBALD, T.I.I., QUIRT, D.H. and GRACIE, A.J. 1990. Uranium deposits of the Athabasca Basin, Saskatchewan, Field Trip 11. In *Field Trip Guidebook, 8th IAGOD Symposium* Geol. Surv. Canada, Open file **2166**, 56 p.

SMELLIE, J.A.T., PERCIVAL, J.B., and CRAMER, J.J. 1991. Mineralogical and Geochemical database for the major lithological and hydrothermal subdivisions of the Cigar Lake Uranium Deposit. Cigar Lake Project Report, **CLR-91-4**, AECL, Pinawa, Canada, 74 p.

3.5.5 ^{36}Cl at Cigar Lake

(J. Cornett and J. Cramer)

3.5.5.1 Introduction

The objectives of measuring the concentration of ^{36}Cl in ore and water samples from the Cigar Lake uranium deposit are

1- to compare the measured ^{36}Cl concentrations with those calculated by J. Fabryka-Martin (see Section 3.8.2) using a Monte Carlo neutron transport code, and

2- to estimate the residence time of groundwater within the ore zone by comparing the ^{36}Cl concentration in the groundwater with that in the ore.

This report summarizes the results of the ^{36}Cl determinations in ore and water samples, and of the leaching experiments carried out on whole-rock ore samples.

3.5.5.2 Samples and methods

Seven uranium ore samples from the Cigar Lake deposit were selected for analysis. The uranium content of the samples ranges from 4 to 55 wt.% U, and five of the samples come from Hole 220 (Table 3.35). These latter samples are from the same profile section of the ore zone in Hole 220 that is being studied in detail by D. Curtis, J. Fabryka-Martin and P. Dixon at the Los Alamos National Laboratory (see Section 3.8.2).

Fifteen samples of groundwater and one surface water from the site of the Cigar Lake deposit were selected for ^{36}Cl analysis. These samples come from the main stratigraphic units in the hydrologic section through the deposit (Table 3.36 and Figure 3.84).

Chlorine contents of the Hole 220 ore samples were determined by X-ray fluorescense (X-Ray Assay Laboratories Ltd. (XRAL), Don Mills, Ontario), and Cl in all ore samples was measured gravimetrically during the preparation of samples for $^{36}Cl/Cl$ measurement by accellerator mass spectrometry (AMS). All samples were diluted to ensure that they were within the linear range of the calibration curve. Ore and rock samples were crushed and ground using a puck and ring shatter box. Then 20 g subsamples were leached with boiling H_3PO_4 and HNO_3 to extract the Cl. The digestion was performed in a sealed glass system connected to a vented, water-cooled distillation trap (Phillips et al. 1986). The HCl gas evolved was collected as AgCl in the trap solution containing 50 mL of double-distilled water, 0.5 mL HNO_3 and 100 mg $AgNO_3$. Each digestion was continued for 0.5 to 1.0 h until the formation of fresh AgCl precipitate ceased. The AgCl precipitate was centrifuged and purified by discarding the supernatant, adding NH_4OH to dissolve the AgCl, and removing any precipitate by centrifugation. The purification process was repeated twice, after which the AgCl precipitate was washed twice with dilute HNO_3 and then with ethanol. The precipitate was transferred to a vial and dried under a vacuum at 60 °C and weighed.

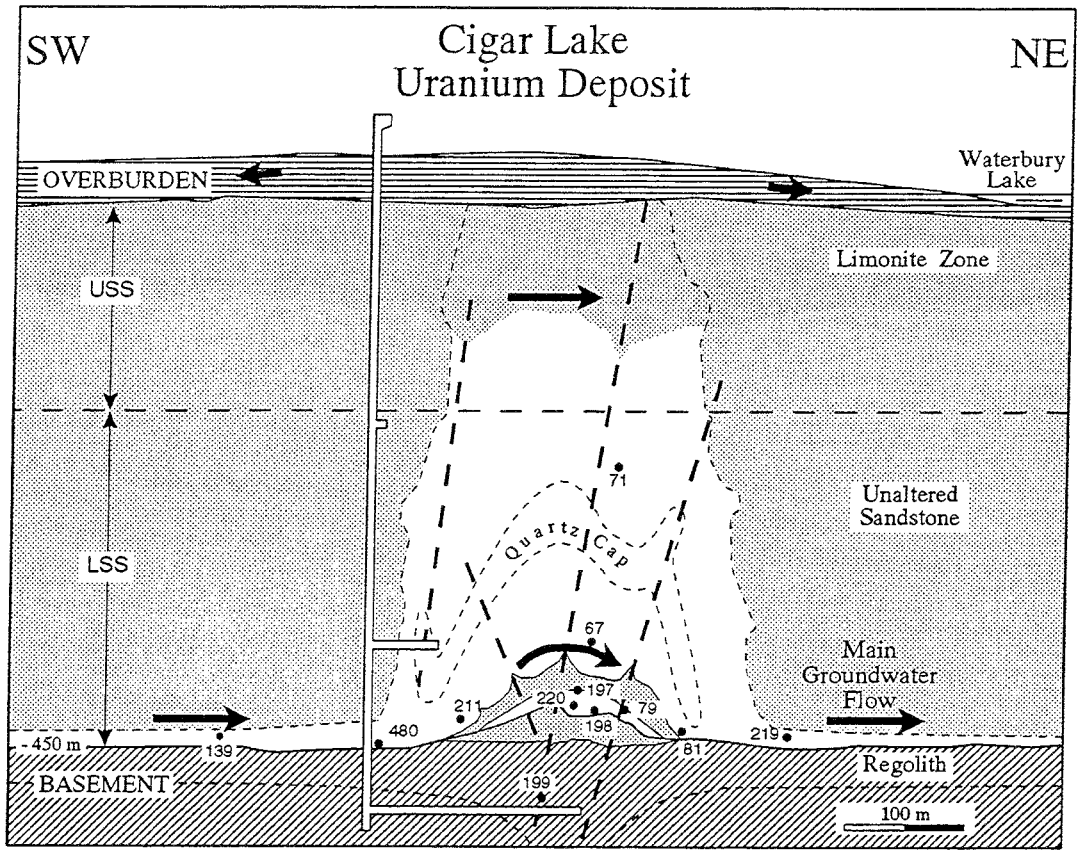

FIGURE 3.84 Cross section through the Cigar Lake deposit showing sample locations of waters used for ^{36}Cl analyses. Groundwater flow direction is indicated with heavy arrows.

Anion concentrations in the water samples were measured by ion chromatography using a Dionex system. The Cl from the water samples was also collected by precipitating and purifying AgCl, using the same steps described for the distillate collected from the rock dissolution.

Chemical yields ranged from 50 to 80 % and are similar to those described for AgCl preparation from other types of samples (Conard et al. 1986). Blanks were prepared using a few mg of Cl from reagent-grade KCl or seasalt, and these samples were handled identically to the actual samples.

The $^{36}Cl/Cl$ ratios were measured by AMS using the Tandem Acellerator Super-Conducting Cyclotron (TASCC) facility at Chalk River Laboratories (Andrews et al. 1990). The ^{36}Cl was measured using a Bragg type detector. The ^{36}S interference was minimized using a gas-filled magnet (Milton 1992; Andrews et al. in prep.). Machine background was monitored using KCl and seasalt blanks, which had a $^{36}Cl/Cl$ ratio of $<2x10^{-15}$. The accuracy of the measurments was assessed by a ^{36}Cl intercalibration with URNSL and by measuring $^{36}Cl/Cl$ ratios in the diluted ^{36}Cl NBS standard (Sharma et al. 1990).

The $^{36}Cl/Cl$ activity ratios are expressed in relative units (CLU) that are normalized to an atom ratio of $1x10^{-15}$. For example, a $^{36}Cl/Cl$ atom ratio of $5x10^{-12}$ is equivalent to a value of 5,000 CLU. The ^{36}Cl atom ratios in the water samples were converted to concentrations (mg/L) using the measured stable Cl values.

3.5.5.3 ^{36}Cl in Cigar Lake Ore Samples

Five samples were selected from Hole 220 to study the small-scale spatial variation in ^{36}Cl concentration, and two samples with high concentrations of U were selected from other cores collected within the main ore pod. The ^{36}Cl content of these samples ranged from 7,000 to 48,000 CLU (Table 3.35). These concentrations within the ore are $>10^2$ higher than the ^{36}Cl content of a sandstone sample collected from the LS unit, and they are $>10^3$ higher than values calculated for sandstone with an average U and Th content (Bentley et al. 1986). ^{36}Cl is being produced in the ore by neutron activation of ^{35}Cl in the high neutron-flux as are other nuclear reaction products. The ^{36}Cl content of the Cigar Lake ores falls within the range of values reported by Fabryka-Martin et al. (1988) for the Ranger-3 and Koongarra ore deposits (2,700 to 167,000 CLU) and from Great Bear Lake (5,0000 CLU) and from deposits in Zaire (9,0000 CLU) (Kenna and Kuroda 1960).

TABLE 3.35
^{36}Cl IN CIGAR LAKE ORE SAMPLES

Sample #	Hole #	Sample description	Cl mg/kg	U wt.%	$^{36}Cl/^{35}Cl$ CLU	± CLU
CS-235H	113	Massive, black		56.0	24393	2150
CS-371	145	Massive, black		37.2	47817	4950
CS-604	220	Massive, black	850	39.4	37000	2480
CS-605	220	U minerals in red clay	700	14.0	30100	2180
CS-609	220	Clay-rich matrix	1300	6.7	18200	2000
CS-610	220	Red clay-rich matrix	1900	3.9	7000	34
CS-615B	220	Massive, black	1100	52.9	29007	3640

The spatial variation in ^{36}Cl in Hole 220 was examined in 5 samples collected from the 433 to 435.5 m interval (Figure 3.85). In this hole, as in other sections of the ore deposit, the U content varies from ~1 to >50 % in interbedded layers of clay-rich, U-mineral-rich and massive U ore deposits. Over this 2.5 m depth range, the ^{36}Cl concentration also varies by ~5 times from 7,000 to 37,000 CLU (Table 3.35). The average ^{36}Cl of the five samples in this interval is 23,000 CLU. The average U content in the five samples from Hole 220 and in this entire section of Hole 220 is 16.0 and 14.6 %, respectively. The average in the main deposit is 12-14 % U. Therefore, ignoring edge effects, the average ^{36}Cl in Hole 220 and in the main deposit is 21,060 CLU and 17,310 to 20,200 CLU, respectively.

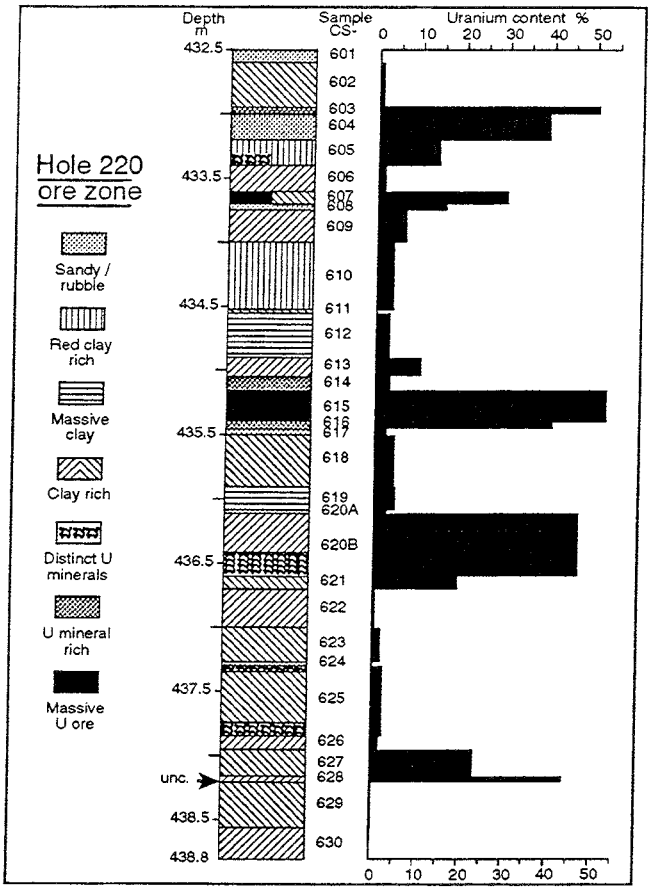

FIGURE 3.85
Diagram showing the lithographic profile and the corresponding uranium distribution (wt.%) through the ore intersection in Hole 220.

The variation in ^{36}Cl content in samples from Hole 220 is 10 times less than that of U. This likely reflects the geometry of the deposit. The mean path length of the neutrons is greater than the thickness of most layers of massive U ore. As a result, neutrons leak out of these layers and produce more ^{36}Cl in zones with lower U content than we expected apriori. Some of the variation in ^{36}Cl production may also be attributed to the different elemental composition of the rock matrix and variations in the total neutron cross section of the rock from different layers.

3.5.5.4 ^{36}Cl in precipitation and groundwater

Measured ^{36}Cl concentrations in the water samples ranged from 170 to 8,200 CLU. ^{36}Cl values in the sandstone basement and surface waters were less than concentrations measured in the groundwaters collected from the ore zone. The meteoric ^{36}Cl input from the atmosphere was calculated to be 3.5×10^{-5} atoms $^{36}Cl/L$ using the fallout rate ($F = 4.4$ atoms/m^2.s) for the geomagnetic latitude of 74 °N (Bentley et al. 1986), and a precipitation input of 0.4 m/a (Environment Canada 1977). This value was converted to an atom ratio using the mean Cl^- concentration of 0.18 mg/L. This value is based on 0.09 mg/L Cl^- measured in wet deposition at the CAPMoN precipitation study site located at Cree Lake, located approximately 200 km southwest, and an estimated input of 0.09 mg/L in dry deposition (Vet et al. 1988). The Cl^- content of precipitation (0.44 ± 0.18 mg/L) is less than that measured in shallow piezometers (see Section 3.5.3). Cl^- in these overburden waters is

likely representative of Cl^- in recharge after it has been concentrated ~2.4 times by evaporation. The average ^{36}Cl atom ratio in atmospheric inputs, prior to the weapons tests was calculated to be 185±46 CLU.

TABLE 3.36
^{36}Cl IN CIGAR LAKE WATERS

Sample #	Description *	Cl mg/L	$^{36}Cl/^{35}Cl$ CLU	±	^{36}Cl atoms x10^6/L	±	^3H NTU
WL	Waterbury Lake	0.45	794	281	6	2	56
71A	US above deposit	17.35	174	9	51	3	10
480-C1	LS up-gradient	70.13	168	18	200	21	<6
67C	AS above clay/ore	17.03	179	2	52	1	37
211C	AS near clay/ore	40.53	1705	176	1172	121	7
211D	AS near clay/ore	38.92	1008	100	665	66	10
81K	AS/C down-gradient	7.23	843	88	103	11	77
219D	LS down-gradient	26.50	861	231	387	104	22
219F	LS down-gradient	26.93	280	26	128	12	11
197F	C/O contact	11.20	4456	242	846	46	75
197O	C/O contact	6.04	2328	1129	238	116	74
198B	O	4.41	1429	273	2097	400	51
79F	O	24.90	2247	71	911	29	52
79L	O	20.75	1088	483	383	170	74
220A	O	37.79	6049	938	3876	601	195
220B	O	38.83	8267	183	5439	120	272

* US, LS, AS= Upper-, Lower-, Altered Sandstone; C= Clay zone; O=Ore zone.

The mean ^{36}Cl atom ratio in lake water used for drill water was 790±280, approximately 4 times higher than the calculated meteoric ^{36}Cl input. The difference between these two values is hypothesized to be due to fallout from weapons testing that has not been completely washed from the lake's catchment. A residue of only ~5 % of the total fallout input to the catchment could explain the higher measurements. ^{36}Cl in samples measured from the two deeper sandstone aquifers also suggests small amounts of weapons-test fallout is present. Samples 67C and 71C from in the sandstone contain about the $^{36}Cl/Cl$ ratio expected from meteoric fallout. However, when these results are expressed per litre (Table 3.37), the ^{36}Cl concentration is 300 times higher than expected, and shows clearly that some weapons-test fallout has mixed with these samples. This hypothesis is supported by the presence of ^3H, from weapons-test fallout (11-50 Tu) in these samples (see Section 3.5.3). In addition, the ^{36}Cl concentrations in the Athabasca sandstone are higher than those measured in the Milk River Aquifer located ~8 ° latitude south (Fabryka-Martin 1988), despite the fact that meteoric ^{36}Cl deposition is estimated to be about 4 times higher in the Milk River area than at Cigar Lake (Bentley et al. 1986).

Inside the clay halo ^{36}Cl atom ratios range from 1100 to 8300 CLU, and from $1x10^8$ to $5.4x10^9$ atoms/L ^{36}Cl (Table 3.36). The highest concentrations were measured in groundwater samples from Hole 220. The $^{36}Cl/Cl$ atom ratios in all the groundwater samples were less than those measured in the ore samples. This suggests that the ^{36}Cl in the groundwater did not result solely from the dissolution of Cl in rock flour produced during drilling.

The importance of the temporal history of sample collection was tested by analyzing duplicate samples from five piezometers that were collected up to 2.5 a apart. ^{36}Cl concentrations were lower in the second sample in all of the samples except 220A and 220B. The duplicate samples from Hole 220 were collected only 1 d apart, and the second sample is ~ 25 % greater than the first. In other cases, the difference between the first and second sample represented a decline of up to 70 % compared with the original ^{36}Cl concentration. We attribute the decrease in ^{36}Cl to the removal of water and ^{36}Cl during sample collection and pumping tests, coupled with the heterogeneous spatial distribution of ^{36}Cl. The removal of groundwater from the small ore zone has resulted in the replacement of this water with water from outside the main ore zone, or from areas within the ore body that contain less ^{36}Cl.

^{36}Cl is produced in the rock and water in direct proportion to the ^{35}Cl concentration. Since the path length of the neutrons is long (~ 1 m), ^{35}Cl in both the rock and water in the ore deposit should be irradiated by the neutron flux. ^{36}Cl concentrations in the water are less than those in the ore. Therefore, Cl in the groundwater has not resided in the high neutron flux long enough to reach equilibrium between production and decay.

^{36}Cl measurements in boreholes located up-gradient from the ore (211), in the metamorphic basement (199), and down-gradient from the ore (219) are less than concentrations measured in the centre of the deposit (220). However, they are all elevated above the regional meteoric ^{36}Cl concentration. This suggests that some ^{36}Cl is transported from the deposit by groundwater advection and diffusion, or that there is a significant source of ^{36}Cl in the clay and sandstone outside of the main ore deposit.

3.5.5.5 Ore leaching

Whole-rock leaching experiments on ore samples were carried out to assess potential ^{36}Cl-leaching by groundwater from the solid ore and its contribution to the measured $^{36}Cl/Cl$ in the groundwaters. Small intact samples of high-grade ore from different boreholes and double-distilled deionized water (DDW) were used in each experiment; the experiments were carried out under static conditions at room temperature and lasted for 7 to 10 d. The results are summarized in Table 3.37, together with data from two high-temperature leaching experiments on ore samples from Hole 220 (S. Stroes-Gascoyne pers. commun. 1993) and the average anion composition in water from Hole 220.

The Cl^- contents are low (<1 mg/L) in all the whole-rock leachates of the high-grade ore samples in the room-temperature experiments. The 100 °C leachates (from experiments that ran for >100 d) are significantly richer in Cl^- (because of the enhanced access by water to interstitial salts in the rock under these conditions), but their Cl^- contents remain below that

of the formation water (CLW). Because water-rock interaction in the natural system takes place under low-temperature conditions (~8 °C), the leaching experiments suggest that only a small amount of Cl from the rock is added to the Cl in the groundwater.

TABLE 3.37
ANION CONTENTS IN LEACHATES FROM CIGAR LAKE ORE

Sample #	Hole #	U wt.%	Weight g	Water mL	mg/L F	Cl	Br	NO_3	HPO_4	SO_4
Low-T Leaching: 25 °C in DDW										
CS615a	220	52.9	20.86	51.75	0.58	0.26	<0.01	0.83	0.04	4.71
CS615b	220	52.9	8.40	51.10	0.63	0.17	<0.01	0.38	<0.04	55.21
CS460a	FH-18	34.4	20.09	47.62	0.12	0.57	<0.01	0.77	0.06	5.54
CS460b	FH-18	34.4	11.60	54.51	3.91	0.39	1.15	0.45	<0.04	14.13
CS472a	FH-18	33.3	16.47	50.18	4.22	0.51	<0.01	0.84	0.15	4.37
CS472b	FH-18	33.3	10.10	53.30	4.35	<0.01	<0.01	0.42	0.28	4.55
High-T Leaching: 100 °C in DDW										
CS615	220	52.9	1.91	500	0.81	22.35	<0.01	4.30	<0.04	2.83
High-T Leaching: 100 °C in CLW										
CS615	220	52.9	2.23	500	0.51	34.31	0.41	1.64	<0.04	5.55
Cigar Lake water (CLW)										
220A+B220		16.65 μg/L			0.69	38.31	0.56	0.45	<0.05	26.16

The potential contribution of ^{36}Cl from the solid ore to that in the groundwater can be assessed with some simple calculations, which are summarized for two examples in Table 3.38:

1- Hole 220: a consistent data set that includes results for the ore, groundwater and leachate from the same hole.

2- Conservative "mix": results for the ore containing the lowest content of Cl and the highest $^{36}Cl/Cl$, for the groundwater with the lowest content of Cl and $^{36}Cl/Cl$, together with the leachate with the highest content of Cl.

The contribution to the $^{36}Cl/Cl$ of the water is calculated using the ratio of the Cl contents in the leachate and the ore times the $^{36}Cl/Cl$ of the ore, and the results are given as the percentage of the $^{36}Cl/Cl$ in the groundwater (Table 3.38). The calculated contribution to $^{36}Cl/Cl$ of the groundwater from leaching of the ore appears to be small (<4 %) under static leaching conditions, simulating the diffusion-controlled water-rock interaction in the low-permeability clay matrix of the ore zone.

TABLE 3.38
CALCULATED CONTRIBUTIONS (*) TO THE $^{36}Cl/Cl$ IN GROUNDWATER FROM LEACHING OF CIGAR LAKE ORE

Sample ID	Hole #	Cl content mg/kg	Cl content mg/L	$^{36}Cl/Cl$ CLU	Calc. contribution to $^{36}Cl/Cl$ in water
Hole 220					
CS615 ore	220	1100		29007	
CS615 DDW leach	220		0.26	7*	0.1 %
220A+B groundwater	220		38.30	7158	
Conservative "mix"					
CS605 ore	220	700		47817	
CS460 DDW leach	FH-18		0.57	39*	3.6 %
79L groundwater	79		20.75	1088	

* Calculated values.

The leaching of Cl^- from salts on grain boundaries and in microfractures contributes to the Cl^- content of groundwaters in the different lithological units of the deposit and its host rocks (see Section 3.5.3). The Cl^- content in the dilute groundwaters of the main sandstone aquifer increases when these waters encounter and transect the halo of hydrothermally altered rock, and Cl^- leaching from the host rocks accounts for this increase in Cl^- in the waters. However, the groundwaters in the ore zone have similar Cl^- contents (av. = 30.6 mg/L, σ= 9.1) to the waters in the surrounding altered sandstone and clay zone (av. = 27.9 mg/L, σ= 13.7), suggesting little additional leaching of Cl^- from the rocks in the ore zone. This is supported by the results of the leaching experiments, including those run at 100 °C where the Cl^- content of the leachate (34.3 mg/L) does not vary significantly from its starting value (38.3 mg/L in Cigar Lake water 220).

We conclude from these experiments that the contribution to the $^{36}Cl/Cl$ of the water from Cl^- leaching of the rocks in the ore zone is small, and is insignificant in comparison with the contribution from ^{36}Cl production by n-capture on the ^{35}Cl already dissolved in the water.

3.5.5.6 Residence time of water in the ore zone

The $^{36}Cl/Cl$ atom ratio is independent of the total Cl concentration and Cl distribution between the ore and water. Within the ore, the $^{36}Cl/Cl$ ratio will be at equilibrium because the Cl^- in the ore has been irradiated for a long period (1.3 Ga), relative to the half-life of ^{36}Cl (3.01 ka). The same ratio will be found in the water as in the ore, provided they both have been subject to the neutron flux over the same time period. However, if groundwater has a residence time within the ore deposit shorter than the time required to reach equilibrium (~2.7 Ma), the residence time (T, a) of the Cl can be calculated from the ingrowth of ^{36}Cl using

$$T = \frac{1}{\lambda} \ln \left(1 - \frac{A_{gw}}{A_{ore}} \right)^{-1}$$

where A_{ore} and A_{gw} are the measured $^{36}Cl/Cl$ atom ratios in the ore and in the groundwater within the ore deposit, and λ is the radioactive decay constant for ^{36}Cl.

There are several assumptions inherent in the calculation of T. First, the background ^{36}Cl content of the groundwater before it enters the ore zone must be subtracted from A_{gw} so that only ^{36}Cl ingrowth within the ore body is included in the calculations. The value from sample 67C, collected within the altered sandstone just above the ore (179±2 CLU), was used as the background ^{36}Cl correction. Additional assumptions include the following:

i) The behaviour of ^{36}Cl and $^{35,34}Cl$ within the ore zone is coupled so that the atom ratio can be used in the calculations and interpretation.

ii) ^{36}Cl production and groundwater flow are assumed to occur continuously rather than as episodic, discrete events.

iii) The Cl is subject to the average neutron flux in the ore zone and heterogeneity in the ore and neutron flux is unimportant.

iv) The ^{36}Cl input into the ore from in-situ leaching is small. It is estimated to be <4 % based on the results of the leaching experiments (Section 3.5.5.5).

v) The Cl^- and groundwater must move at the same velocities if the values of T_{Cl} are to be used to infer T for the groundwater.

The residence times of Cl in the groundwater within the ore zones ranged from 14 to 282 ka. The longest residence times are from Hole 220 (155 to 282 ka) in the middle of the ore deposit. The lowest values are calculated for Hole 79. The latter samples may be biased low since they were influenced by the leakage of water and Cl from outside the ore zone into these samples.

The importance of the heterogeneous neutron flux described in the third assumption can be evaluated using data collected from Hole 220. The ^{36}Cl content was measured in groundwater and in several rock samples collected from the same sample intervals in Hole 220. The mean U and $^{36}C/Cl$ atom ratio in the ore within the interval were 16 % and 23,000 CLU, respectively. These values are only slightly higher than the average values for the entire deposit. The residence times based on the direct comparison were 132 and 193 ka, slightly shorter than that based on the average neutron flux in the deposit. The heterogeneity of the flux is not that important because the path length of the neutrons is long relative to the thickness of various mineral sequences within the ore body. As a result, the production rate of ^{36}Cl is averaged over a larger volume, and this minimizes the influence of individual strata.

3.5.5.7 References

ANDREWS, H.R., BALL, G.C., BROWN, R.M., CORNETT, R.J., DAVIES, W.G., GREINER, B.F., IMAHORI, Y., KOSLOWKSY, V.T., MCKAY, J., MILTON, G.M. and MILTON, J.C.D. 1990. Development of the Chalk River program for ^{36}Cl. Nucl. Instrum. Meth. Phys. Res., **B52**, 243-248.

ANDREWS, H.R., CORNETT, R.J., DAVIES, W.G., GREINER, B.F., IMAHORI, Y., KOSLOWKSY, V.T., MCKAY, J., MILTON, G.M. and MILTON, J.C.D. Measurement of ^{36}Cl by AMS using the CRL TASCC facility. AECL Research Rep. (in preparation).

BENTLEY, H.W., PHILLIPS, F.M. and DAVIS, S.N. 1986. Chlorine-36 in the terrestrial environment. In *Handbook of Environmental Isotope Geochemistry, Vol. 2, The Terrestrial Environment* (ed. P. Fritz and J-Ch. Fontes). Elsevier, New York, p.427.

CONARD, N.J., ELMORE, D., KUBIK, P.W., GOVE, H.E., TUBBS, L.E., CHRUNYK, B.A. and WAHLEN, M. 1986. The chemical preparation of AgCl for measuring ^{36}Cl in polar ice with accelerator mass spectrometry. Radiocarbon, **28**(2A), 556-560.

ENVIRONMENT CANADA. 1977. Hydrologic Atlas of Canada. Environment Canada Publ., p.34.

FABRYKA-MARTIN, J. 1988. Production of radionuclides in the earth and their hydrogeologic significance, with emphasis on chlorine-36 and iodine-129. Unpubl. Ph.D. dissertation, Dept. of Hydrology and Water Resources, Univ. of Arizona, Tucson AZ, U.S.A., 400 p.

FABRYKA-MARTIN, J., DAVIS, S.N., ROMAN, D., AIREY, P.L. and KUBIK, P.W. 1988. Iodine-129 and chlorine-36 in uranium ores, 2. Discussion of AMS measurements. Chem. Geol. (Isot. Geos. Sect.), **72**, 7-16.

KENNA, B.T. and KURODA, P.K. 1960. The ratio of induced fission vs. spontaneous fission in pitchblends, and natural occurrence of radiochlorine. J. Inorg. Nucl. Chem., **16**, 1-7.

MILTON, J.C.D. 1992. Possibilities and limitations of a gas-filled magnet for separating neighboring isobars in AMS work: Calculation of the trajectories of heavy ions. AECL Research Rep., **RC-900**.

PHILLIPS, F.M., LEAVY, B.D., JANNIK, N.D., ELMORE, D. and KUBIK, P.W. 1986. The accumulation of cosmogenic chlorine-36 in rocks: a method for surface exposure dating. Science, **231**, 41-43.

SHARMA, P., KUBIK, P.W., FEHN, U., GOVE, H.E., NISHIIZUMI, K. and ELMORE, D. 1990. Development of ^{36}Cl standards for AMS. Nucl. Instrum. Meth. Phys. Res., **00**, 1-6.

VET, R.J., SUKLOFF, W.B., STILL, M.E., MARTIN, J.B., KOBELKA, W.F and GAUDENZI, A. 1988. Canadian Air Precipitation Monitoring Network (CAPMoN), Precipitation chemistry data summary. Environment Canada, Atmos. Envir. Serv. Rep., **AQRB-88-01**.